

I. Abstract

The cyclin-dependent kinases (CDKs) are a well-conserved family of serine/threonine protein kinases that drive mammalian cell cycle progression. The transition of cells through the early G1 stage of the cell cycle is co-ordinated by CDK4 and CDK6 following mitogen-dependent expression of D-type cyclins. Irregular CDK activity results in abnormal cell cycle control and is a significant indicator of poor cancer prognosis. The chaperone Hsp90, with the adaptor co-chaperone Cdc37, plays a key role in regulating the stability and function of a substantial proportion of the kinome including CDK4 and CDK6. However, the mechanism of CDK4(6)-cyclin D complex formation and regulation via the Hsp90 chaperone system remains poorly understood.

A range of biophysical and biochemical techniques have been used to investigate the mechanism of CDK4(6)-cyclin D complex formation and regulation by the D-type cyclins and cyclin-dependent kinase inhibitors (CKIs) via the Hsp90 chaperone system. These have revealed that Cdc37 complexes can distinguish D-type cyclins, with CDK6 being more readily relinquished to cyclin D3 than cyclin D1, while the presence of p27KIP1 can stabilise the CDK-cyclin complexes against re-distribution into complexes with Cdc37, potentially providing an assembly role for CDK-cyclin complexes. In contrast to the D-type cyclins the CDKs were found to be readily relinquished by Cdc37 to members of the INK family, potent inhibitors of CDK4 and CDK6. However, this potency can be greatly reduced by the introduction of clinically significant INK point mutations, one of which differs greatly in its ability to bind and displace CDK4 and CDK6. In addition, co-crystal structures of selected CDK4/6 inhibitors bound to CDK2-cyclin A have been determined to gain a greater understanding of inhibitor selectivity and binding modes. Taken together these results suggest the Cdc37-Hsp90 chaperone system provides an opportunity to fine tune the regulation of CDK4 and CDK6 activities during G1.

II. Acknowledgements

First and foremost I would like to thank my supervisor Jane Endicott for her continual help and support throughout the project. I would also like to thank the rest of my supervisory team Martin Noble and Craig Robson for their expertise and guidance. In particular, I would like to thank Martyna Pastok who has been my mentor throughout the project and has been exceptional fun to work with.

I would also like to thank the rest of the Endicott/Noble lab, past and present, for their invaluable help and advice during my time here. Particular thanks must go to Judith Reeks for her assistance in setting up the HTRF assay which has played such a large part in this project and to Mat Martin for his advice thereafter. Thanks goes to Claire Jennings for her mass spectrometry data collection and analysis and to Richard Heath for his expertise on molecular biology, music and his laugh.

A special thank you goes to Laurence Pearl, Marc Morgan and the rest of our collaborators from the University of Sussex for their knowledge and guidance in the field of Hsp90 chaperones. I also thank Arnaud Baslé for all his help and expertise on X-ray crystallography, data collection and structure solution as well as the rest of my friends in the structural biology lab.

Finally, I would like to thank my funders the Medical Research Council for their financial support which has allowed me to carry out this research and of course the whole of the DDI lab for making my time at the NICR so enjoyable and for keeping me well supplied with cakes.

III. Table of Contents

I. Abstract	i
II. Acknowledgements	ii
III. Table of Contents	iii
IV. List of Figures	ix
V. List of Tables	xiv
VI. Abbreviations	xv
Chapter 1. Introduction	1
1.1 General principles of signalling pathways.....	1
1.1.1 Intrinsic signalling mechanisms	1
1.2 The eukaryotic cell cycle	2
1.2.1 The cell cycle CDKs	5
1.3 CDK4/6-cyclin D complexes regulate the G1 phase of the cell cycle.....	6
1.3.1 Differential expression of cyclin D isoforms	6
1.3.2 Passing the restriction point	8
1.3.3 Further regulation by binding partner association	9
1.3.4 Roles outside the cell cycle	11
1.4 The CDK structural paradigm	13
1.4.1 CDK4-cyclin D breaks the structural paradigm	15
1.4.2 CDK-cyclin-CKI structures reveal the molecular details of CDK inhibition.....	17
1.5 The Hsp90 chaperone system	19
1.5.1 The Hsp90-Cdc37-client structure and mechanism.....	20
1.6 CDK deregulation in cancer	22
1.6.1 CDK4 and CDK6 dysregulation in cancer.....	23
1.6.2 Hsp90 dysregulation in cancer	25
1.7 Aims of the Thesis	27
Chapter 2. Reagent generation	28
2.1 Introduction	28
2.1.1 Recombinant protein expression systems	28
2.1.2 Tailoring protein expression	30
2.1.3 Design of truncated CDK6, cyclin D1 and cyclin D3	33
2.1.4 Design of constructs to express cyclin-dependent kinase inhibitor p27KIP1	37
2.2 Biophysical methods to characterise proteins.....	39

2.2.1 Mass spectrometry	40
2.2.2 Differential scanning fluorimetry	41
2.3 Materials and methods	42
2.3.1 Construct generation	42
2.3.2 Cloning	42
2.3.3 E. coli transformation.....	44
2.3.4 Virus production and amplification	44
2.3.5 Expression tests	46
2.3.6 Protein expression in E. coli	47
2.3.7 Protein expression in Insect cells.....	47
2.4 Protein purification by column chromatography	48
2.4.1 Glutathione-affinity chromatography.....	48
2.4.2 Ni-NTA chelate chromatography	48
2.4.3 Size exclusion chromatography	48
2.4.4 Subtractive affinity purification	49
2.4.5 Biotinylation	49
2.4.6 Mass Spectrometry	49
2.4.7 Differential scanning fluorimetry	50
2.5 Examples of protein purification from recombinant E. coli cells.....	50
2.6 CDK6-cyclin D3 expression in insect cells	53
2.6.1 Conversion to the MultiBac™ system for complex expression	55
2.6.2 Building larger complexes.....	61
2.6.3 Purification of CDK2-cyclin A2	63
2.7 Quality control (QC) of protein samples	65
2.7.1 SDS-PAGE and silver staining to assess protein complexes for use in homogeneous time-resolved fluorescence assays.....	66
2.7.2 Characterisation of CDK6-cyclin complexes by mass spectrometry.....	66
2.7.3 Thermal melt buffer screen to optimise buffer conditions	68
2.8 Discussion.....	72
Chapter 3. The CDK-Cdc37 interaction	73
3.1 Introduction	73
3.1.1 Hsp90 regulates a large proportion of the protein kinome	73
3.1.2 Kinase sequence features that identify a Cdc37 client.....	74

3.1.3 Cdc37 sequence features that identify a client kinase	76
3.1.4 Molecular details of the interaction of Cdc37-Hsp90 with a client kinase....	79
3.2 Biophysical methods to measure protein-protein interactions.....	84
3.2.1 Homogenous Time Resolved Fluorescence (HTRF)	85
3.2.2 Surface plasmon resonance	89
3.2.3 Microscale Thermophoresis.....	90
3.3 Materials and methods	92
3.3.1 Protein production	92
3.3.2 Biotinylation of Avi-tagged constructs.....	92
3.3.3 Streptavidin pull-downs	93
3.3.4 Microscale thermophoresis	93
3.3.5 Optimisation of the HTRF direct binding mode assay	94
3.3.6 HTRF direct binding mode assay	95
3.4 Results	96
3.4.1 Optimisation of the HTRF protocol	96
3.4.2 Optimisation of reagents	98
3.5 Determining Cdc37 affinity for CDK4 and CDK6	102
3.5.1 Cdc37 interactions confirmed by MST	104
3.5.2 Cdc37 ^{S13E} does not show an enhanced interaction with the CDKs.....	105
3.6 Formation of a CDK-Cdc37-Hsp90 complex in vitro.....	107
3.6.1 The Q247R mutant did not enhance CDK interactions with Hsp90	108
3.7 Discussion.....	110
Chapter 4. CDK regulation by the Hsp90 chaperone system	112
4.1 Introduction	112
4.1.1 Viral cyclins are surrogates for canonical D-type cyclins.....	112
4.1.2 The CIP-KIP family as assembly factors.....	116
4.1.3 HTRF in competition mode	119
4.2 Materials and Methods.....	120
4.2.1 Protein production	120
4.2.2 Biotinylation of Avi-tagged constructs.....	120
4.2.3 HTRF in direct binding mode.....	120
4.2.4 HTRF in Competition mode.....	121
4.2.5 Competitive pull-downs	122

4.3 Results	122
4.3.1 Competition mode optimisation.....	122
4.3.2 The viral cyclins bind tightly to CDK4 and CDK6.	125
4.4 Trends in D-type cyclin binding to CDKs	127
4.4.1 The viral cyclins differ in their ability to displace the CDKs from Cdc37	127
4.4.2 Assessment of the ability of Cdc37 to displace viral cyclins from their CDK partners.....	128
4.4.3 D-type cyclins vary in their affinities for CDK4 and CDK6.....	130
4.5 p27KIP1 can act as an assembly factor	133
4.5.1 p27KIP1 and p21CIP1 stabilise CDK-cyclin complexes to disruption by Cdc37	133
4.5.2 p27M is not sufficient to prevent Cdc37 binding	135
4.5.3 Viral cyclin containing complexes are not affected by p27KIP1	136
4.6 Analysis of the p27KIP1 interactions involved in Cdc37 displacement	137
4.6.1 p21CIP1/p27KIP1 fragments weakly disrupt CDK-Cdc37 complexes	137
4.6.2 The RXL binding motif is not required for p27 stabilisation of CDK-cyclin D complexes	139
4.6.3 Phosphomimetic mutants do not decrease p27KIP1 stabilisation	140
4.6.4 Extended p27KIP1 C-terminal truncations weaken the stabilisation effects of p27KIP1	141
4.7 Discussion.....	143
Chapter 5. INK regulation	146
5.1 Introduction	146
5.1.1 INK mutations drive cancer progression.....	146
5.2 Materials and methods	151
5.2.1 Protein production.....	151
5.2.2 Biotinylation of Avi-tagged constructs.....	151
5.2.3 HTRF in direct binding mode.....	151
5.2.4 HTRF in competition mode	152
5.2.5 Microscale thermophoresis	152
5.2.6 Surface plasmon resonance	152
5.2.7 Differential Scanning Fluorimetry	152
5.3 Determining INK affinity for G1 CDKs	153

5.4 INK mutants affect CDK affinity	158
5.4.1 The D108N mutation had no effect on CDK binding	158
5.4.2 Mutation of Asp84 to asparagine reduces the affinity of p16 for CDK4 and CDK6.....	160
5.4.3 p16 Met53 mutants can differentiate between CDK4 and CDK6.....	161
5.5 p19 mutants also reduce CDK binding.....	165
5.6 Competition assays	167
5.6.1 The INKs rapidly disrupt the CDK-Cdc37 complex	167
5.6.2 The p16 M53 mutants show a difference in ability to disrupt CDK4-Cdc37 and CDK6-Cdc37 complexes.....	168
5.6.3 p19 displaces CDK4 from Cdc37.....	170
5.7 Discussion.....	171
Chapter 6. CDK-cyclin inhibition by ATP-competitive inhibitors	173
6.1 Introduction	173
6.1.1 Structure based design of kinase inhibitors.....	173
6.1.2 The CDK binding pocket	176
6.1.3 ATP-competitive inhibitors cause kinase-Cdc37-Hsp90 complex disruption	178
6.2 Materials and methods	180
6.2.2 Protein production	180
6.2.3 Biotinylation of Avi-tagged constructs.....	180
6.2.4 HTRF in competition mode	180
6.2.5 Crystallisation trials and structure determination.....	180
6.2.6 Data collection and processing.	182
6.3 CDK4/6-specific inhibitors disrupt Cdc37 complex formation.....	182
6.4 CDK6 crystallisation trials.....	186
6.5 ATP-competitive inhibitor crystallisation trials using a CDK2 surrogate	187
6.6 Comparison of CDK4/6 inhibitor interactions.....	191
6.6.1 LY2835219 vs Lee011 binding to CDK2-cyclin A	193
6.6.2 Alternate packing of the P-loop	195
6.6.3 Comparison of Lee011 and PD0332991 binding to CDK2-cyclin A2.....	196
6.6.4 Modelling PD0332991 into CDK6 active site	198
6.6.5 Why is Lee011 so much weaker a competitor?	199

6.7 Discussion.....	201
Chapter 7. Conclusions and future directions	204
Appendix A.	209
A.1 Additional techniques.....	209
A.1.1 Polymerase chain reaction	209
A.1.2 Transformations.....	209
A.1.3 Agarose gels.....	209
A.1.4 Sequencing.....	209
A.1.5 SDS-PAGE	210
A.1.6 Determining protein concentration	210
A.2 Primers.....	210
A.2.1 Additional constructs.....	212
A.3 Table of protein constructs.....	213
A.4 Media and buffers.....	215
A.5 CDK2-cyclin A2 optimised crystallisation screen	216
Bibliography.....	218

IV. List of Figures

Figure 1-1 Cyclin expression profiles	2
Figure 1-2 Diagram of the eukaryotic cell cycle.....	3
Figure 1-3 Comparison of the D-type cyclins.....	7
Figure 1-4 The role of CDK4/6-cyclin D.....	9
Figure 1-5 INK amino acid sequence alignment and key structural features.....	10
Figure 1-6 CIP/KIP amino acid sequence alignment and key structural features.....	12
Figure 1-7 Quintessential structures described by CDK2 vs CDK2/cyclin A.....	14
Figure 1-8 Comparison of CDK4/cyclin D3 and CDK9/cyclin T structures.....	16
Figure 1-9 The binding and inhibition mechanism of p27 on CDK2-cyclin A.....	18
Figure 1-10 Structure of p16 bound to CDK6 showing mechanism of inhibition	19
Figure 1-11 An overview of the structure of the CDK4-Cdc37-Hsp90 complex	21
Figure 1-12 Schematic of Hsp90 client regulation	22
Figure 1-13 Chart of amplifications/ deletions in various cancers	24
Figure 2-1 Schematic of the MultiBac system.....	30
Figure 2-2 Cyclin D1 and D3 secondary structure alignment	34
Figure 2-3 CDK4 and CDK6 alignment.....	35
Figure 2-4 CDK6 has short predicted disordered regions at the N and C-termini.....	36
Figure 2-5 The D-cyclins show an extended disordered region towards the C-terminus	36
Figure 2-6 p21 and p27 sequence and constructs	38
Figure 2-7 Schematic of a quadrupole TOF instrument.....	40
Figure 2-8 Diagram of thermal melt assay.....	41
Figure 2-9 Example purification of a Cdc37 construct.....	51
Figure 2-10 Example of p27M purification	52
Figure 2-11 Thrombin cleavage of the GST tag is incomplete and is accompanied by cyclin D3 degradation.....	53

Figure 2-12 3C protease completely cleaves the GST tag from GST3CCDK6 without degrading cyclin D3.....	54
Figure 2-13 PCR amplification of DNA sequences to express truncated constructs of CDK6 and cyclin D	56
Figure 2-14 Successful Cre-LoxP reactions to generate transfer vectors to co-express various CDK6 and cyclin D proteins were confirmed by PCR	57
Figure 2-15 Successful transfections were identified by YFP expression levels.....	58
Figure 2-16 GSTCDK4 and GSTCDK6 expression from the MultiBac system	58
Figure 2-17 GSTCDK4 and GSTCDK6 co-expression with the D-type cyclins using the MultiBac™ system.....	59
Figure 2-18 Truncated CDK6-cyclin D constructs proved challenging to express	60
Figure 2-19 CDK6-cyclin D3 expression using the MultiBac™ system	61
Figure 2-20 Formation of ternary CDK6-cyclin D3-p27S complexes.....	62
Figure 2-21 Purification of CDK2-cyclin A2. CDK2 is co-expressed with <i>S. cerevisiae</i> CAK1 to generate CDK2 phosphorylated on Thr160.....	64
Figure 2-22 SDS-PAGE analysis of purified proteins	66
Figure 2-23 Analysis of CDK6-cyclin D3 by mass spectrometry.....	67
Figure 2-24 Differential scanning fluorimetry to assess CDK6 stability in different buffers	69
Figure 2-25 CDK6-cyclin D3 has two distinct melting events	70
Figure 3-1 Hsp90 dependency varies considerably across the kinome.....	73
Figure 3-2 Regions of CDK4 identified for Cdc37 interactions.....	75
Figure 3-3 Cdc37 structural features	77
Figure 3-4 Hsp90 interactions with CDC37	78
Figure 3-5 Cdc37 dimer interactions in crystal structure	79
Figure 3-6 The CDK4-Cdc37-Hsp90 complex.....	80
Figure 3-7 High resolution cryo-EM structure of CDK4-Cdc37-Hsp90.....	82
Figure 3-8 Schematic of an HTRF experiment.....	85
Figure 3-9 The HTRF assay format for determining CDK interactions with Cdc37.....	87
Figure 3-10 The Avi-tag can be repositioned to measure alternative interactions.....	88

Figure 3-11 Diagram of SPR set-up	89
Figure 3-12 Diagram of typical MST experiment	91
Figure 3-13 Performing the HTRF assay at 4 °C greatly enhances the size and reliability of the fluorescent signal obtained	96
Figure 3-14 The N-Avi Hsp90 interaction is weak at high temperatures.....	97
Figure 3-15 The change in fluorescent signal was assessed over time	98
Figure 3-16 Biotinylation levels assessed by streptavidin pull-downs	99
Figure 3-17 Concentration dependent conditions.....	101
Figure 3-18 Potential Hook effect	102
Figure 3-19 CDK4 binds tighter than CDK6 to Cdc37	103
Figure 3-20 Cdc37 does not interact with GST or CDK2	104
Figure 3-21 MST confirms CDK4/Cdc37 ₁₋₃₄₈ interaction strength	105
Figure 3-22 Interactions with Cdc37 ^{S13E} are comparable to wild-type.....	106
Figure 3-23 GST-CDK-Cdc37-N-Avi Hsp90 complex formation measured by HTRF.....	108
Figure 3-24 The Cdc37 ^{Q247R} mutant does not dramatically affect the GSTCDK4-N-Avi Hsp90 interaction.....	109
Figure 4-1 The viral cyclins share high structural homology canonical cyclins.....	113
Figure 4-2 Comparison of CDK2-cyclin A to CDK6-Vcyclin and CDK4-cyclin D3.....	115
Figure 4-3 The interaction of p27KIP1 with CDK2-cyclin A.....	117
Figure 4-4 Diagram of the HTRF assay in competition mode	119
Figure 4-5 Optimisation of detection reagents for the GSTCDK4-C-Avi Cdc37 interaction	123
Figure 4-6 Optimisation of the GSTCDK concentrations for use in the HTRF assay in competition mode.....	124
Figure 4-7 Vcyclin binds very tightly to CDK4 and CDK6.....	125
Figure 4-8 Kcyclin binds very tightly to CDK4 and CDK6	126
Figure 4-9 Assessment of the non-specific binding between Vcyclin and GST	127
Figure 4-10 The viral cyclins strongly compete with Cdc37 for CDK6 but not CDK4.....	128
Figure 4-11 Viral cyclin containing CDK6 complexes are resistant to Cdc37 displacement whereas those containing CDK4 are not.....	129

Figure 4-12 Cyclin D1 is readily displaced from CDK4 and CDK6 by Cdc37	131
Figure 4-13 The CDK6-cyclin D3 complex is more stable to Cdc37 disruption	131
Figure 4-14 Cyclin D1 and D3 can be distinguished by their displacement from CDK4 and CDK6 by CDC37	132
Figure 4-15 p27 stabilised CDK4-cyclin D1 and CDK6-cyclin D1 complexes against Cdc37	134
Figure 4-16 p27KIP1 and p21CIP1 stabilise CDK4-cyclin D3 and CDK6-cyclin D3 complexes against Cdc37	134
Figure 4-17 p27M is not sufficient to prevent CDK4-Cdc37 complex formation	135
Figure 4-18 p27M addition does not stabilise viral cyclin complexes against Cdc37... ..	136
Figure 4-19 p21CIP1 and p27KIP1 fragments can weakly disrupt CDK-Cdc37 complexes	138
Figure 4-20 The RXL binding site is not required for complex stabilisation	140
Figure 4-21 p27KIP1 phosphomimetic mutants can still stabilise CDK-cyclin D3 complexes against Cdc37	141
Figure 4-22 p27 ₁₋₇₅ does not stabilise GSTCDK4-cyclin D3 against Cdc37	142
Figure 5-1 The structural makeup of p16 and p19	147
Figure 5-2 Mechanism of INK inhibition	148
Figure 5-3 p16 point mutations map to the interface with CDK6	150
Figure 5-4 Avi-tagged INKs do not interact with GST	153
Figure 5-5 p16 bound tightly by HTRF	154
Figure 5-6 p19 binding was weaker than p16.....	155
Figure 5-7 The CDK6-p16 interaction could not be accurately determined by MST	156
Figure 5-8 p16 binding to CDK4 and CDK6 is very tight and is characterised by a very slow off rate.....	157
Figure 5-9 p16 ^{D108N} binding by SPR	159
Figure 5-10 p16 ^{D84N} binding by SPR	160
Figure 5-11 p16 ^{M53E} interaction by HTRF	162
Figure 5-12 p16 Met53 mutants binding by SPR	163
Figure 5-13 Direct binding of p19 mutant M50E to CDK4 and CDK6	165

Figure 5-14 Direct binding of p19 mutant G19D to CDK4 and CDK6	166
Figure 5-15 All INKs can effectively compete with Cdc37 for the CDKs	168
Figure 5-16 INK4 mutants show a weakened ability to displace Cdc37	169
Figure 5-17 p19 mutants showed a reduced ability to displace CDK4 from Cdc37.....	170
Figure 6-1 The structure of CDK2-cyclin A to highlight key conserved structural elements	174
Figure 6-2 Classification of protein kinase ATP-competitive inhibitors.....	175
Figure 6-3 Conserved residues in ATP binding site	176
Figure 6-4 Conserved sequence features in the CDK2, CDK4 and CDK6 ATP binding sites residues	177
Figure 6-5 ATP-competitive inhibitors can disrupt the Hsp90 complex in vivo.....	179
Figure 6-6 kinases not bound to the Hsp90 complex are degraded.....	179
Figure 6-7 ATP does not disrupt the interaction of CDK4/6 with Cdc37	183
Figure 6-8 ATP-competitive inhibitors disrupt CDK-Cdc37 complexes.....	184
Figure 6-9 Determination of the ability of LY2835219 to displace CDK4 from CDK4-Cdc37	185
Figure 6-10 CDK6-cyclin D3 crystallisation trials.....	186
Figure 6-11 CDK2-cyclin A2 used in crystallisation trials was phosphorylated on Thr160.	187
Figure 6-12 Images of CDK2-cyclin A2 crystals used for structure determination	188
Figure 6-13 Chemical structures of LY2835219, Lee011 and PD0332991	191
Figure 6-14 Structures of LY2835219 and Lee011 bound to the CDK2-cyclin A2 ATP binding site	192
Figure 6-15 Inhibitor overlay.....	193
Figure 6-16 A structural comparison of the binding of LY2835219 and Lee011 to CDK2	194
Figure 6-17 LY2835219 orders the CDK2 P-loop.....	196
Figure 6-18 A comparison PD0332991 binding to CDK2-cyclin A2 and CDK6-Vcyclin..	197
Figure 6-19 Comparative inhibitor interactions between CDK active sites.....	199

Figure 6-20 Comparison of the binding of LY2835219, Lee011 and PD0332991 to CDK2-cyclin A	200
Figure 6-21 Lee011 binding to CDK2 is accompanied by a shift in Lys33	201

V. List of Tables

Table 2-1 CDK6 and cyclin D truncated constructs	37
Table 2-2 Truncated CIP/KIP constructs designed for this study.....	39
Table 2-3 Buffer compositions that stabilised CDK6.	69
Table 2-4 Buffer compositions that stabilised CDK6-cyclin D3.....	71
Table 3-1 Table of Cdc37 affinities.....	106
Table 3-2 Table of Hsp90 affinities	109
Table 3-3 Table of CDK4 and CDK6 affinities	111
Table 4-1 Optimisation of the competition assay at 4 °C has greatly reduced the concentrations of reagents required	124
Table 5-1 Summary of SPR kinetic analysis.....	164
Table 5-2 Thermal stability of p16 point mutants	169
Table 6-1 Crystal growth conditions	182
Table 6-2 Data collection and refinement statistics for determination of the CDK2-cyclin A2-LY2835219 complex structure	189
Table 6-3 Data collection and refinement statistics for determination of the CDK2-cyclin A2-Lee011 complex structure	190
Table A-1 Primers for Avi-tagged constructs	211
Table A-2 Primers for truncated CDK6 and D-type cyclins for MultiBac™ system	212
Table A-3 Protein constructs produced	215
Table A-4 Table of media and buffer components	216
Table A-5 DSF buffer screen conditions.....	217

VI. Abbreviations

3C	Human Rhinovirus (HRV) 3C Protease
ADP	Adenosine di-phosphate
ATP	Adenosine tri-phosphate
CAK	CDK-activating kinase
CCP4	Collaborative Computational project 4
Cdc37	Cell Division Cycle 37
CDK	Cyclin Dependent Kinase
CKI	Cyclin Dependent Kinase Inhibitor
C-terminal	Carboxy-terminal
cv	Column volume
Da	Dalton
DNA	Deoxyribonucleic acid
DSF	Differential Scanning Fluorimetry
DTT	Dithiothreitol
<i>E. Coli.</i>	<i>Escherichia coli</i>
EDTA	Ethylene Diamine Tetra-acetic Acid
FL	Full-length
FRET	Förster resonance energy transfer
GST	Glutathione-S-transferase
HEPES	4-(2-Hydroxyethyl)piperazine-1-ethanesulphonic acid
His ₆	Hexahistidine tag
Hsp90	Heatshock protein 90
HTRF	Homologous Time Resolved Fluorescence
INK4	Inhibitors of CDK4
IPTG	Isopropyl β -D-1-thiogalactoside
ITC	Isothermal titration calorimetry

K _{off}	Off rate
K _{on}	On rate
K _d	Binding constant
K _{d-app}	Apparent affinity
kDa	KiloDalton
LB	Lysogeny Broth
LC-MS	Liquid chromatography-mass spectrometry
M	Molar
m/z	Mass charge ratio
MEFs	Mouse embryonic fibroblasts
MS	Mass spectrometry
Ni ²⁺ -NTA	Nickel-nitotriacetic acid
N-Terminal	Amino-terminal
OD ₆₀₀	Optical density at $\lambda = 600$ nm
PAGE	Polyacrylamide Gel Electrophoresis
PCR	Polymerase chain reaction
PDB	Protein Data Bank
Rpm	Revolutions per minute
RT	Room temperature
SAXL665	Streptavidin bound XL665 dye
SDS	Sodium dodecyl sulphate
SEC	Size exclusion chromatography
Sf9	<i>Spodoptera frugiperda</i> 9
siRNA	Short interfering RNA
SOC	Super optimal broth with catabolic repressor
SPR	Surface plasmon resonance
TAE	Tris-acetate-EDTA

Tb	Terbium
TCEP	Tris(2-carboxyethyl)phosphine
T _m	Melting temperature
UV	Ultraviolet
WT	Wild-type

Amino acids

Alanine	A	Ala
Arginine	R	Arg
Asparagine	N	Asn
Aspartic acid	D	Asp
Cysteine	C	Cys
Glutamic acid	E	Glu
Glutamine	Q	Gln
Glycine	G	Gly
Histidine	H	His
Isoleucine	I	Ile
Leucine	L	Leu
Lysine	K	Lys
Methionine	M	Met
Phenylalanine	F	Phe
Proline	P	Pro
Serine	S	Ser
Threonine	T	Thr
Tryptophan	W	Trp
Tyrosine	Y	Tyr
Valine	V	Val

Chapter 1. Introduction

1.1 General principles of signalling pathways

Cellular processes in response to both internal and external stimuli are tightly regulated to elicit the appropriate response from multiple stimuli. External signals typically formed by small excreted proteins such as growth factors including Epidermal Growth Factor (EGF) must be recognised by receptors at the surface of the cell and the message relayed to the nucleus to prompt the required transcriptional changes (Morgan, 2006). In the majority of cases this message is relayed down intricate networks of signalling cascades, such as the Ras/MAP kinase pathway, which operate via a succession of phosphorylation events (Coleman *et al.*, 2004). The stimulus by external signals must be balanced against internal cellular conditions to prevent incorrect or damaged cells from commencing a process they are ill prepared for. For example, damage such as breaks in the DNA triggers a signalling network leading to rapid expression of cell-cycle inhibitors such as p21CIP1 and the activation of DNA repair pathways (Bartek and Lukas, 2001; Bartek and Lukas, 2007).

1.1.1 *Intrinsic signalling mechanisms*

Multiple cellular mechanisms allow the size and timeframe of a response to be tailored to the situation. Protein expression leads to a gradual increase in activity as the concentration in the cell rises. The increase in activity can be delayed by low levels of potent inhibitory molecules. A signal will only be triggered once this lower inhibitor threshold is reached (Morgan, 2006). Inhibitory mechanisms prevent activity and can act as checkpoints preventing progression until a sufficiently high signal is received. Protein expression is slow and results in a gradual increase in activity. Posttranslational modifications of proteins, such as phosphorylation, allow for a more rapid as well as reversible switching between active and inactive states. Ubiquitin-dependent proteolytic degradation results in an irreversible switch thereby provoking a prolonged delay in activity until cellular protein levels rise again through expression, often requiring further stimulating signals. In eukaryotes further control is provided by subcellular localisation which can be used to limit the activity of a newly expressed protein until

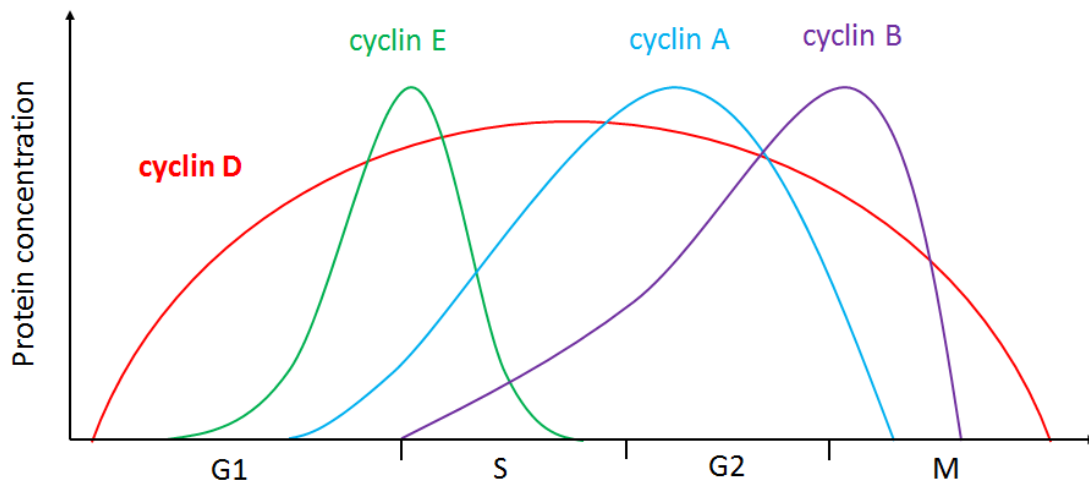


Figure 1-1 Cyclin expression profiles

The cyclin levels vary throughout the cell cycle. Cyclin D (red) is present during the whole cell cycle while the other cyclins are periodically expressed and then degraded.

triggered by a phosphorylation or protein binding event. For example, the nuclear uptake of CDK1-cyclin B is triggered by the phosphorylation of the cyclin (Morgan, 2006).

Positive feedback mechanisms, whereby the activity of a protein stimulates further activity, either through direct interactions such as phosphorylation or by stimulating further expression, is employed by the cell to produce rapid gains in activity (Morgan, 2006). The addition of further positive and negative regulators results in a stable all or nothing response whereby a protein is either fully stimulated at the maximum level or inactive. The use of positive feedback loops means that signals can be maintained even after the initial stimulus is lost. For the cell cycle this ensures that cyclin dependent kinase (CDK) activity rises and is maintained until the next stage of the cell cycle is activated. Negative feedback mechanisms, which downregulate activity when a threshold is exceeded, quench excess activation of a protein and maintain control (Morgan, 2006). The careful balance of positive and negative feedback loops results in the oscillation of cyclin levels observed with each round of cell division (Figure 1-1).

1.2 The eukaryotic cell cycle

The eukaryotic cell cycle is divided into four main stages: an initial growth phase, G1, the S phase where DNA replication occurs, a second growth phase, G2, and then M phase when the duplicated chromosomes are divided and the cell separates into two daughter cells (Figure 1-2) (Pines, 1993). An additional quiescent state, G0, exists outside of the cell cycle where cells remain in a non-proliferative state. Multiple checkpoints regulate

the transitions between each stage to ensure the cell is properly prepared for the next step in division. This process is tightly controlled by the cyclin dependent kinases (CDKs), a family of serine/threonine protein kinases (Morgan, 2006). In the budding yeast *Saccharomyces cerevisiae* and the fission yeast *Schizosaccharomyces pombe*, all cell cycle events are controlled by a single CDK, CDK1 (Beach *et al.*, 1982). However, in higher eukaryotes, the family has expanded and cells contain in addition CDK2 which regulates entry into S-phase, and CDK4 and CDK6 which both regulate entry into the cell cycle at G1 (Figure 1-2).

The concentrations of the CDKs remain fairly constant throughout the cell cycle and instead their activity is dictated by the expression profiles of cyclins, their binding partners. The CDKs are always in excess of overall cyclin levels (Arooz *et al.*, 2000). The cyclins were first identified in sea urchin eggs and gained their name from the cyclic nature of expression and degradation observed with each cell division (Evans *et al.*, 1983). Mammalian cells express four cyclins D, E, A and B whose expression and ubiquitin-mediated degradation profiles correspond with the transitions between each stage of the cell cycle (Figure 1-1) (Arellano and Moreno, 1997). While each cyclin member predominantly activates a particular CDK, there is a great level of redundancy built into the cell cycle, as the cyclins are also capable of binding to and activating other

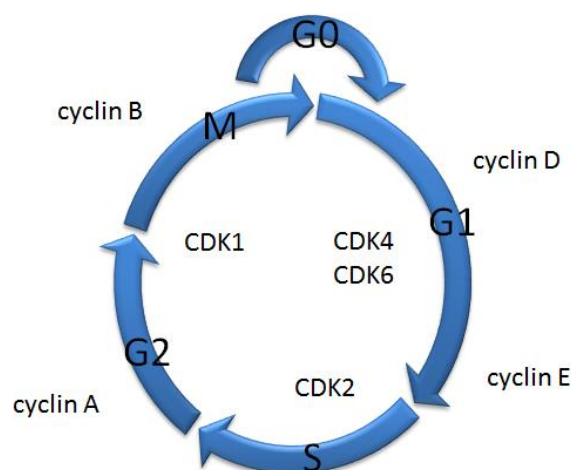


Figure 1-2 Diagram of the eukaryotic cell cycle.

Schematic overview of the eukaryotic cell cycle to highlight the temporal expression of members of the CDK and cyclin families. Under certain conditions, cells can exit the cell cycle and enter a quiescent state, termed G₀. CDK7 and cyclin H are not included in the Figure but are required for CDK activation. CDK7 activity does not oscillate throughout the cell cycle.

CDKs (Satyanarayana and Kaldis, 2009). For full activity the CDKs require cyclin binding and phosphorylation of a threonine residue near the active site on the activation segment, which is performed by CDK activating kinase (CAK) (Fesquet *et al.*, 1993; Kato *et al.*, 1994; Wu *et al.*, 1994). Each CDK is responsible for phosphorylating specific downstream targets, often aided by the cyclin partner, stimulating progression to the next stage of the cell cycle and in turn promoting the activation of the next cyclin (Morgan, 2006).

To adapt CDK-cyclin activity to changes in cellular environment further regulation is provided by the cyclin dependent kinase inhibitors (CKIs). The CKIs in particular suppress the G1 phase to promote cell cycle arrest due to unfavourable cellular conditions such as DNA damage (Morgan, 2006). The CKIs are divided into two classes: the Inhibitors of CDK4 (INK) family and the CIP/KIP family. CDK regulation by the CKIs is discussed further in Section 1.3.3.

Additional CDK regulation is supplied by phosphorylation within the activation segment by CAK as previously mentioned, but also by inhibitory phosphorylation of conserved residues within the glycine-rich loop by Wee1, first identified in yeast (Aligue *et al.*, 1997) and Myt1 (Morgan, 2006). CDK activity can be restored through dephosphorylation of the glycine-rich loop by Cdc25 (Gu *et al.*, 1992) This mechanism has been shown to be particularly important for the CDK2 stress response (Hughes *et al.*, 2013). Additional binding partners, such as cyclin-dependent kinase regulatory subunit 1 (CKS1), can also be recruited to help target the CDKs to specific substrates, such as those that have previously been phosphorylated (McGrath *et al.*, 2013).

At the end of the cell cycle the Anaphase Promoting Complex/Cyclosome (APC/C) targets S and M phase cyclins for degradation by the proteasome returning the cell to its quiescent state. The APC/C remains active during G1 to inhibit CDK activity until a mitogenic signal is received (Morgan, 2006).

Other CDK-cyclin complexes perform alternative essential regulatory roles outside of direct cell cycle regulation. These include CDK7-cyclin H, which forms part of the CAK complex (Devault *et al.*, 1995; Tassan *et al.*, 1995) and is responsible for activating other CDKs; and CDK9-cyclin T, which forms part of the P-TEFb complex, and is involved in the regulation of gene transcription (Zhou *et al.*, 2012). Other CDKs perform various tissue-

specific roles including CDK5 which regulates nerve cell differentiation (Malumbres, 2011).

1.2.1 The cell cycle CDKs

The essential role of the cell-cycle CDKs in driving proliferation has been tested through knockout studies which have also highlighted the high levels of redundancy between the CDKs (Malumbres and Barbacid, 2009). Knockout mice have shown that only CDK1 is required for cell cycle progression. Embryos lacking CDK1 but retaining the other cell cycle CDKs do not progress past the two cell stage (Santamaria *et al.*, 2007) and mice in which the endogenous *CDK1* gene has been replaced with *CDK2* are also embryonic lethal (Satyanarayana *et al.*, 2008). Mice lacking all interphase CDKs (CDK2, 4 and 6), however, still develop to midgestation (Santamaria *et al.*, 2007) and *in vitro* mouse embryonic fibroblasts (MEFs) retaining only CDK1 can still divide (Santamaria *et al.*, 2007). These results show that CDK1 is capable of binding and being activated by each of the cyclins and can phosphorylate a wide range of targets (Santamaria *et al.*, 2007). CDK2 knockout mice are viable, although both male and female mice are sterile (Berthet *et al.*, 2003), while CDK2 knockout fibroblasts become immortal (Ortega *et al.*, 2003). The sterility in CDK2 knockout mice has been associated with the requirement for CDK2 kinase activity for completing prophase 1 during meiosis in gametes (Chauhan *et al.*, 2016).

CDK4 (Rane *et al.*, 1999; Tsutsui *et al.*, 1999) and CDK6 (Malumbres *et al.*, 2004) knockout mice show far more tissue-specific defects suggesting alternative roles in certain tissues between these functionally related CDKs. CDK4 knockout mice express defective endocrine cells, causing most mice to develop diabetes and die at an early age due to defective pancreatic β -cell development, as well as some defects in adipogenesis (Rane *et al.*, 1999). Mice that have had both CDK4 and CDK2 knocked out die during late development due to cardiac defects showing some level of redundancy in this mechanism between the two CDKs (Malumbres, 2011). CDK6 knockout mice develop normally although homeostasis is slightly impaired reducing thymus and spleen sizes as well as the numbers of certain blood cells. Erythropoiesis and T-cell development is deficient, implicating a potential role of CDK6 in regulating differentiation (Grossel and Hinds, 2006; Kohrt *et al.*, 2014). CDK2 and CDK6 double knockout mice show a

combination of fertility and haematological defects observed in the individual knockout mice. Finally, when CDK4 and CDK6 are knocked out together mice die during late stage embryonic development due to severe anaemia. *In vitro* CDK4/CDK6 double knockout cells proliferate normally and still weakly respond to mitogenic signals, suggesting either CDK2 or CDK1 can compensate (Malumbres *et al.*, 2004).

1.3 CDK4/6-cyclin D complexes regulate the G1 phase of the cell cycle

Entry into the G1 phase of the cell cycle is regulated by CDK4 and CDK6-cyclin D complexes. CDK4 was first identified in murine macrophages through its ability to bind D-type cyclins during G1 resulting in retinoblastoma protein (pRB) phosphorylation (Matsushime *et al.*, 1992). Later, CDK6 was identified through its homology with CDK4 and was also found to bind the D-type cyclins from human lysates and could also phosphorylate pRB during G1 (Meyerson and Harlow, 1994).

In yeast the rate of proliferation is controlled by the availability of extracellular nutrients, while in animals proliferation depends on a combination of tissue-specific genetic programming and extracellular protein signals from other cells (Morgan, 2006). D-type cyclin expression in the G1 phase is dependent on external mitogenic stimuli, unlike the other cell cycle cyclins, and these signals must be maintained for continued cyclin D expression and CDK activation. The removal of mitogenic stimuli results in rapid D-type cyclin degradation (Matsushime *et al.*, 1994).

1.3.1 Differential expression of cyclin D isoforms

The D-type cyclins are expressed as three different isoforms, cyclin D1, D2 and D3 which share around 60% sequence identity with each other (Figure 1-3). All three are capable of binding to and activating both CDK4 and CDK6 (Matsushime *et al.*, 1994). The N-terminal region of the D-type cyclins contains a LXCXE motif (single letter amino acid code where X stands for any amino acid) that is responsible for recognition and binding to pRB to direct the CDK activity (Figure 1-3). The C-terminal region of each cyclin D contains a PEST motif which targets the cyclins for ubiquitin-mediated degradation after phosphorylation on Thr286, Thr280 or Thr283 on cyclin D1, D2 or D3 respectively. Between these motifs lies the most highly conserved cyclin box region responsible for CDK binding and activation (Musgrove *et al.*, 2011).

oestrogen receptor activity by binding to the steroid receptor co-activators SRC1 and AIB1 through the LLXXL motif (Zwijsen *et al.*, 1998).

Cyclin D2 has been linked to Megalencephaly (MEG), a developmental disorder characterized by brain overgrowth due to either increased number or size of neurons and glial cells. Cyclin D2 activating mutations cause cyclin D2 stabilisation and accumulation through the AKT pathway (Mirzaa *et al.*, 2014). This phenotype mirrors that of cyclin D2 knockout mice that show mild alterations in gonadal proliferation and abnormal postnatal cerebellar development due to reduced numbers of granule neurones (Sicinski *et al.*, 1996). Cyclin D2 has also been identified as a co-factor in cardiogenesis by enhancing the activity of transcription factor GATA4 (Yamak *et al.*, 2014).

Cyclin D3 knockout mice fail to undergo normal expansion of T-lymphocytes showing that cyclin D3 is required for lymphocyte development (Sicinska *et al.*, 2003). Characteristically, cyclin D has increased expression profiles in T-cell leukemias and related malignancies. Multiple D-type cyclin knockouts result in embryonic death generally because of severe haematological defects suggesting the D-type cyclins are not completely redundant for all cellular processes. Triple knockout MEFs, however, can still proliferate in culture showing that other cyclins can still compensate for cyclin D activities required for cell cycle progression (Kozar *et al.*, 2004).

1.3.2 Passing the restriction point

Most adult cells are quiescent in G0 and will maintain this state for their lifetime (Malumbres, 2011). Mitogenic signals cause cells to re-enter G1 through the expression of D-type cyclins although irreversible entry into the cell cycle, shown by the start of DNA replication, is controlled by a checkpoint at G1/S known as the restriction point (Pardee, 1974). Once this checkpoint is passed cells are committed to division. Failure at any stage will result in cellular apoptosis to maintain fidelity of the subsequent generations.

In animals the restriction point is dependent on the E2F family of transcription factors (Trimarchi and Lees, 2002) which govern gene expression required for DNA synthesis as well as cyclin E and cyclin A expression required for progression to the next stage of the

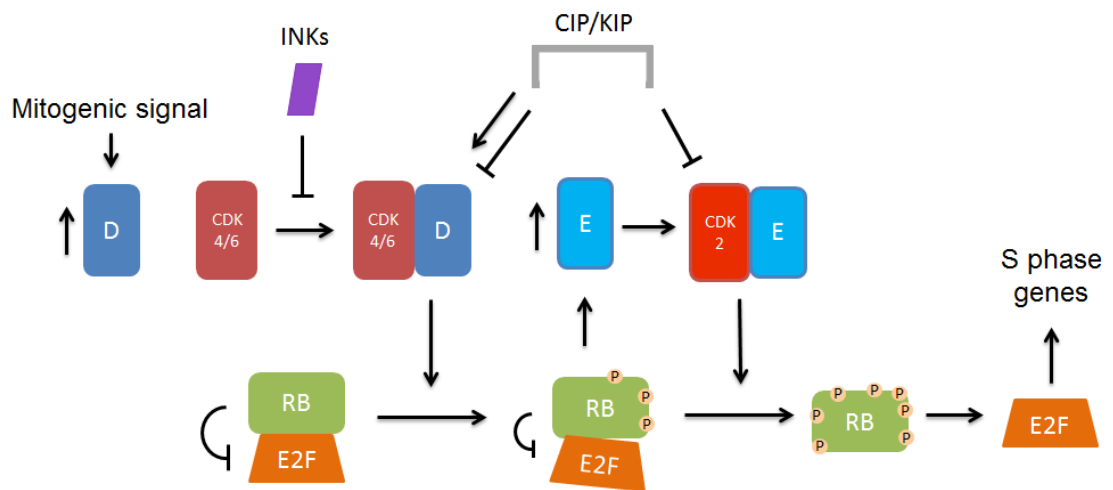


Figure 1-4 The role of CDK4/6-cyclin D

A schematic of the mechanism of CDK4/6-cyclin D action during the G1 phase. Mitogenic signals trigger D-type cyclin (dark blue) expression. The rise in D-type cyclin concentrations form CDK4 or CDK6-cyclin D heterodimers. CDK4/6-cyclin D hypo-phosphorylates the retinoblastoma protein (pRB, green) causing partial inactivation. Partial inactivation results in the start of cyclin E (light blue) expression which forms complexes with CDK2 (red). Active CDK2 then hyper-phosphorylates pRB resulting in complete inactivation and the release of E2F (orange) transcription factors triggering expression of S phase genes. Further regulation of CDK activity is provided by the CKIs; the INKs (purple) and CIP/KIP (grey) family as described in Section 1.3.3.

cell cycle. The activities of the E2F transcription factors are controlled by pocket proteins of the pRB family including pRB and p107 (Giacinti and Giordano, 2006; Dyson, 2016). pRB represses the E2F transcription factors through direct binding to the E2F transcriptional domain as well as through the recruitment of chromatin remodelling factors (Dyson, 2016). Upon receiving a mitogenic signal D-type cyclin levels rise forming the CDK4/6-cyclin D heterodimer, which begins the phosphorylation of pRB (Figure 1-4). pRB is first partially inactivated by monophosphorylation by CDK4 and CDK6 on multiple sites followed by hyperphosphorylation and inactivation by CDK2-cyclin E (Zarkowska and Mittnacht, 1997; Narasimha *et al.*, 2014).

1.3.3 Further regulation by binding partner association

Two different classes of CKI regulate the cell cycle. These are: the Inhibitor of cyclin dependent Kinase 4 (INK) proteins consisting of p16INK4a (p16), p15INK4b (p15), p18INK4c (p18) and p19INK4d (p19) and the CDK-interacting protein (CIP)/ Kinase inhibitor protein (KIP) family comprising of p21CIP1, p27KIP1 and p57KIP2.

The INKs are highly specific inhibitors of CDK4 and CDK6, forming stoichiometric complexes with the CDKs and preventing cyclin binding (Figure 1-4) (Canepa *et al.*,

2007). Initially, p16 was identified as a binding partner of CDK4 that inhibited CDK4 activity (Serrano *et al.*, 1993). Subsequently, p15 (Hannon and Beach, 1994), and p18 and p19 (Hirai *et al.*, 1995) were identified based on their sequence homology. p15 was expressed when cells were exposed to Transforming growth factor-beta (TGF- β), an anti-mitotic signal. The four INKs are comprised of a stack of 4-5 ankyrin repeats and appear to be functionally redundant as all four are capable of inhibiting both CDK4 and CDK6 to arrest cells in G1 (Canepa *et al.*, 2007). p15 and p16 appear to be ubiquitously expressed at fairly constant levels throughout the cell cycle, unless triggered by anti-mitotic signals (Ruas and Peters, 1998). p18 has been observed at higher levels in skeletal muscle (Guan *et al.*, 1994) and myoblasts (Franklin and Xiong, 1996) while p19 transcription is higher in the thymus, peripheral blood leukocytes and testis (Guan *et al.*, 1996). Despite each INK appearing to be equipotent at inhibiting the CDKs, p16 is by far the most commonly mutated or lost in human malignancies suggesting that it has the predominant role in cell cycle inhibition (Sherr, 2012).

The CIP/KIP family are capable of binding to and inhibiting each of the G1 and S phase CDK-cyclin heterodimers (Figure 1-4) (Toyoshima and Hunter, 1994; Lin *et al.*, 1996). p21CIP1 expression is triggered in response to DNA damage via the p53 transduction pathway (Bartek *et al.*, 2007; Karimian *et al.*, 2016) while p27KIP1 accumulation occurs under more general G1 inhibitory conditions such as Transforming growth factor beta

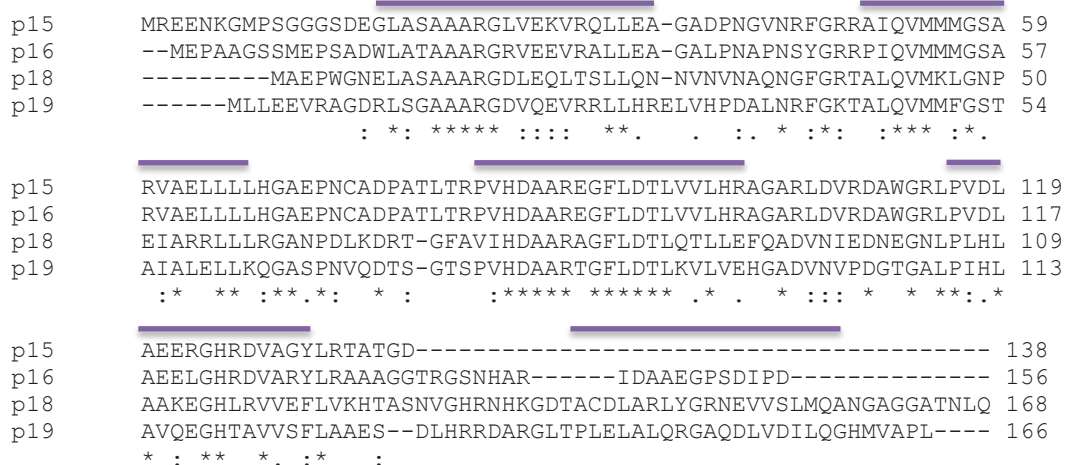


Figure 1-5 INK amino acid sequence alignment and key structural features.

Human p15, p16, p18 and p19 (Uniprot entries P42772, P42771, P42773 and P55273 respectively) were aligned using Clustal Omega (Sievers *et al.*, 2011). Identical residues are marked by stars and conserved residues with a colon (:) or dot (.) respectively. Purple bars represent the ankyrin repeats based on (Brotherton *et al.*, 1998).

(TGF- β) or chemical inhibition (Reed *et al.*, 1994). Progression into the G1 phase of the cell cycle requires p27KIP1 removal to allow CDK2 activity. The loss of p27KIP1 at the G1/S phase transition occurs through a combination of p27KIP1 sequestering by CDK4/6-cyclin D complexes and proteolytic degradation via the ubiquitin-mediated SCF pathway (Sherr and Roberts, 1999).

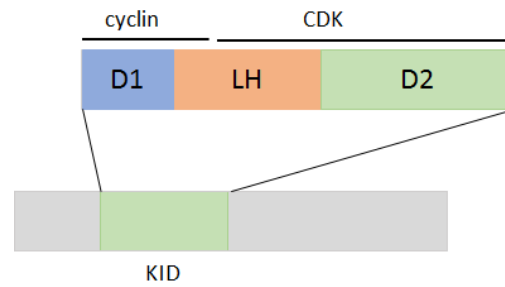
In contradiction to their inhibitory role, p21CIP1 and p27KIP1 have also been described as assembly factors for CDK4 and CDK6 (Sherr and Roberts, 1999). Ternary complexes containing D-type cyclins, CDK4/6 and p27KIP1 have been isolated that are both highly stable and active (LaBaer *et al.*, 1997; Cerqueira *et al.*, 2014). Further evidence for this role is the seemingly weaker affinity of the D-type cyclins for CDK4/6 over the other CDK-cyclin partners (Kato *et al.*, 1994; Matsushime *et al.*, 1994). Part of this assembly role may be through providing a nuclear transport signal for the CDK4/6-cyclin D complexes thereby increasing the rate of uptake to the nucleus for pRB phosphorylation (Sherr and Roberts, 1999). Consistent with this assembly role, mouse embryonic fibroblasts (MEFs) lacking p21CIP1 or p27KIP1 have reduced CDK4/6-cyclin D activity but enhanced CDK2-cyclin E activity (Cheng *et al.*, 1999; Sugimoto *et al.*, 2002).

1.3.4 Roles outside the cell cycle

As mentioned above, the cyclins are also involved in other regulatory events in addition to their CDK activating role. CDKs regulate multiple pathways independent of their kinase activity that include transcription, DNA damage repair, differentiation, metabolism and immune response (Kung and Jura, 2016). CDK6 has been identified together with c-Jun as part of a transcription complex that induces expression of Vascular Endothelial Growth Factor A (VEGF-A) when overexpressed in BCR-ABL-transformed B-cell lymphoma cells (Kollmann *et al.*, 2013). VEGF-A is hormone that binds to the receptors VEGFR1/2 to regulate cell growth and angiogenesis- the stimulation of new blood vessels.

Cyclin D was not found within the complex, and the overexpression of CDK4 did not have the same effect on VEGF-A expression differentiating CDK4 and CDK6 behaviour. In the same study the overexpression of CDK6 also corresponded with increased levels of the CKI p16. CDK6 was identified in a transcriptional complex with cyclin D2 and STAT3 at the p16 promoter sequence seemingly creating a negative feedback loop to inhibit CDK6

A



B

```

p27      MSNVRVSNNGSPSLERMDARQAEHPKPSAC RNLFG PVDHEELTRDLEKHCRDMEEASQRKW 60
p21      -----MSEFAGDVRQNPCGSKAC RRLFG PVDSEQLSRDCDALMAGCIQEARERW 49
          * . : : .***.***** *:*** : . : : : *

p27      NFDFQNHKPLEGKYEQEVEKGSLEPEFYRPPRPPKGACKVPAQESQDVSGSRPAA--PL 118
p21      NFDFVTETPLEGDFAWERVRGLGLPKLYLPT-GPRRGRDELGG-----GRRPGTSPAL 101
          **** ...***. : *:.*. .**::* * : * : : . * **.: *

p27      IGAPANSEDTHLVDPKTDPSDSQTGLAEQCAGIRKRPATDDSSTQNKRANRTEENVSDGS 178
p21      LQGTAE--EDH-----VDLSLSCTLVPRSGE-----QAEGS 130
          : . * : : * ..*:.*::: : : : **

p27      PNAGSVEQTPKKPGLRRRQT----- 198
p21      PGG----PGDSQGRKRRQTSMTDFYHSKRRLIFSKRKP 164
          *.. .. * :****
  
```

Figure 1-6 CIP/KIP amino acid sequence alignment and key structural features.

Human p21CIP1 (p21) and p27KIP1 (p27), (Uniprot entries P38936 and P46527 respectively) were aligned using Clustal Omega (Sievers *et al.*, 2011). Residues that are identical are marked by stars, conserved residues are highlighted with a colon (:) or dot (.) respectively. Dashes represent insertions to align the two sequences. The green bar represents the kinase inhibitory domain, based on (Yoon *et al.*, 2012). The RXL motif (RNLFG and RRLFG in p27 and p21 respectively (Adams *et al.*, 1996)) that binds to the cyclin recruitment site is highlighted in red.

activity at high concentrations. The substitution of CDK6 with a kinase-dead mutant showed this role to be independent of CDK6 kinase activity despite the presence of cyclin D2 (Kollmann *et al.*, 2013). CDK6 has also been described as part of a transcriptional complex with the Androgen Receptor (AR), upregulating AR transcription of Prostate-Specific Antigen (PSA) (Lim *et al.*, 2005). Cyclin D1 binding to the AR has been shown to reverse the effect and inhibit AR transcriptional activity (Reutens *et al.*, 2001).

CDK4 in contrast, has not been reported to have a kinase-independent function in the context of any transcription factor complex. However, CDK4-cyclin D has been observed to phosphorylate (i) SMAD3, causing downregulation of TGF- β expression; (ii) FOXM1, which regulates the expression of cell-cycle regulators and suppresses cellular senescence, and (iii) PPAR γ , which induces adipogenesis with cyclin D1 through repression of MYOD to block myoblast differentiation (Hydbring *et al.*, 2016).

1.4 The CDK structural paradigm

The core kinase fold and the mechanism of kinase activation is highly conserved (Jura *et al.*, 2011; Endicott *et al.*, 2012) and is epitomised by contrasting the structures of monomeric CDK2 (Figure 1-7 A), which adopts an inactive conformation, and CDK2-cyclin A (Figure 1-7 B) which has an active conformation. All CDK-cyclin complexes share the same common features although CDK4 appears to differ slightly from the quintessential mechanism of activation (Day *et al.*, 2009; Takaki *et al.*, 2009). The CDKs contain only the fundamental kinase core which consists of two lobes. The N-terminal lobe (cyan) is comprised predominantly of β -sheets with one α -helix, the C-helix (yellow), while the C-terminal lobe (blue) is composed entirely of α -helices. The ATP and substrate binding site is situated on the interface between the two lobes.

The CDKs are characterised by their requirement for cyclin binding to form the active CDK structure. When unbound the CDK C-helix is in a more open 'out' position (Figure 1-7 A) and the activation loop (red) is disordered preventing both substrate and ATP access to the active site (Debondt *et al.*, 1993). The cyclins are entirely α -helical (Brown *et al.*, 1995). Cyclin binding (Figure 1-7 B green) causes considerable structural changes within the CDK by moving the C-helix position from the more open 'out' position to the more tightly packed 'in' position. The repositioning of the C-helix has quite a profound effect on the internal structure of the CDK causing the rearrangement of key catalytic residues, including the conserved DFG motif, and begins to order the activation loop. Key to this rearrangement is the catalytic aspartic acid residue which becomes orientated to chelate a magnesium ion in the C-helix 'in' conformation. The magnesium ion in turn coordinates with the phosphate groups of ATP, a conserved glutamate from the C-helix and a lysine residue on β 3, positioning the phosphates for subsequent transfer to the substrate (Jeffrey *et al.*, 1995). Ultimately these changes establish two "spines" of conserved residues, termed the catalytic and regulatory spines, that ensure that changes within the catalytic cleft are transmitted throughout the kinase fold (Kornev and Taylor, 2010).

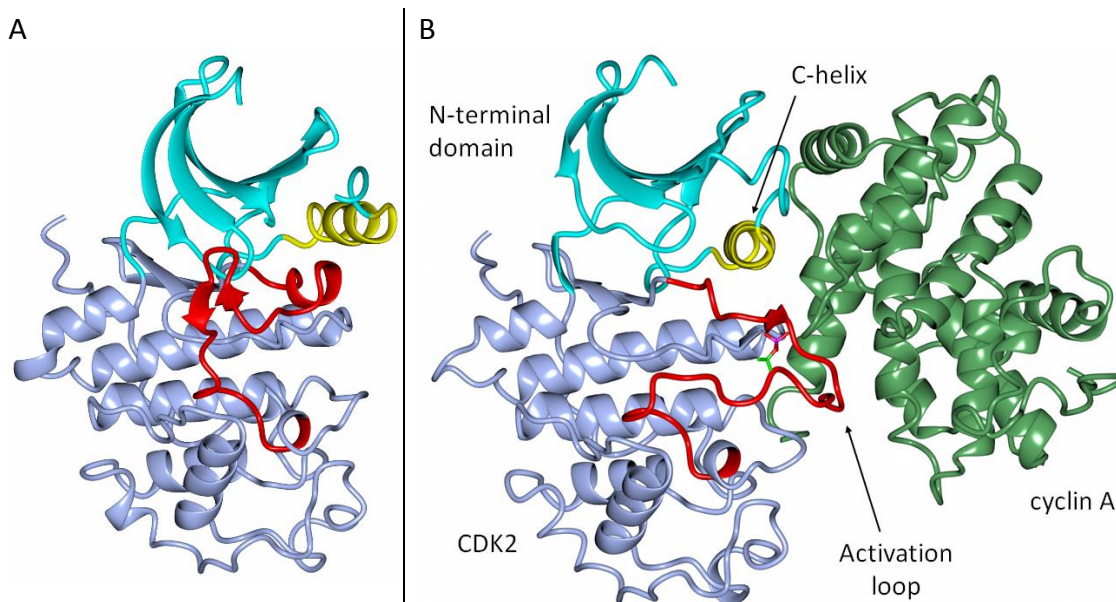


Figure 1-7 Quintessential structures described by CDK2 vs CDK2/cyclin A

The CDKs undergo a conserved mechanism of activation upon cyclin binding. Proteins displayed in ribbon format. (A) Monomeric CDK2 (PDB: 1HCK) shows the C-helix (yellow) in the 'out' position and the activation loop (red) is disordered. (B) CDK2-cyclin A (PDB: 1JST) shows repositioning of the C-helix (yellow) from the 'out' to the 'in' position and ordering of the activation loop (red) upon cyclin (green) binding. The phosphorylated threonine on the activation loop is shown in cylinders with atoms coloured by atom type. In both images the N-terminal domain is highlighted in cyan. Figures created using CCP4MG (Potterton *et al.*, 2002).

For full activation, the CDKs require phosphorylation on a threonine residue on the activation loop, Thr160 on CDK2 (Figure 1-7 B cylinder form), which is performed by CAK (Brown *et al.*, 1999b). Phosphorylation causes substantial rearrangements of the activation loop moving by as much as 7 Å to accommodate substrate binding as well as dramatically enhancing the rate of phosphate transfer (Russo *et al.*, 1996b; Hagopian *et al.*, 2001). The CDKs recognise a peptide consensus sequence S/TPXK/R (where P, K and R correspond to their respective amino acids and X denotes any amino acid) and phosphorylate either the serine or threonine (Brown *et al.*, 1999a). Rearrangement of the activation loop provides additional cyclin contacts further stabilising the complex (Russo *et al.*, 1996b). Together these two mechanisms of activation offer tight control over the activation of the CDKs. This mechanism is described in more detail in Chapter 6.

1.4.1 CDK4-cyclin D breaks the structural paradigm

Structures of other CDK family members have also now been determined and reveal a conserved mechanism of activation. CDK1 is particularly similar to CDK2 (Brown *et al.*, 2015). The structure of CDK1-cyclin B-CKS2 (Figure 1-8 B) resembles that of CDK2-cyclin A, although a slight twist in the subunit orientation in relation to the CDK2-cyclin A structure reduces the interacting surface area between cyclin B and the C-lobe of CDK1. The CDK1 activation loop was only partially ordered and was not visibly phosphorylated. λ -phosphatase treatment subsequent to treatment with CAK revealed that the activation loop in CDK1 retains a higher level of flexibility compared to CDK2-cyclin A, perhaps reflecting the larger range of substrates which the activation loop must accommodate (Brown *et al.*, 2015). The structure of CDK9-cyclin T (Figure 1-8 C), differs again in its CDK-cyclin interface. In this case cyclin T is rotated by 26° away from CDK9 compared to cyclin A bound to CDK2 (Baumli *et al.*, 2008). CDK9-cyclin T shows an even greater reduction in the interface between the cyclin and the CDK C-lobe than observed for CDK1. Despite the smaller interface the phosphorylated activation loop still forms the ordered, active conformation and the DFG motif is aligned for phosphotransfer (Baumli *et al.*, 2008).

The structures of CDK4-cyclin D3 (Takaki *et al.*, 2009) and phosphorylated CDK4-cyclin D1 (Day *et al.*, 2009), however, differ from the quintessential CDK structural paradigm exemplified by CDK2-cyclin A. Both structures show an ostensibly inactive CDK4 conformation even with the cyclin bound (Figure 1-8 D). Cyclin D3 and D1 interact almost exclusively with the N-lobe of CDK4 and more closely resemble the CDK9-cyclin T structure (Baumli *et al.*, 2008) than CDK2-cyclin A (Russo *et al.*, 1996b). The C-terminal lobe of cyclin T is involved in the recognition of regulatory proteins (Gu *et al.*, 2014) whereas to date the C-terminal lobes of cyclins E, A and B are yet to be found to encode a protein interaction site. It has therefore been speculated that this more open conformation observed with CDK4-cyclin D may reflect an ability to interact with other as yet unknown regulatory proteins (Takaki *et al.*, 2009). The most striking part of the CDK4-cyclin D structure was that cyclin binding appeared insufficient to reposition the C-helix from the 'out' to the 'in' position. Despite this lack of activation loop order, phosphorylated CDK4-cyclin D3 was active against pRB *in vitro* suggesting a unique mechanism of substrate-assisted catalysis (Takaki *et al.*, 2009).

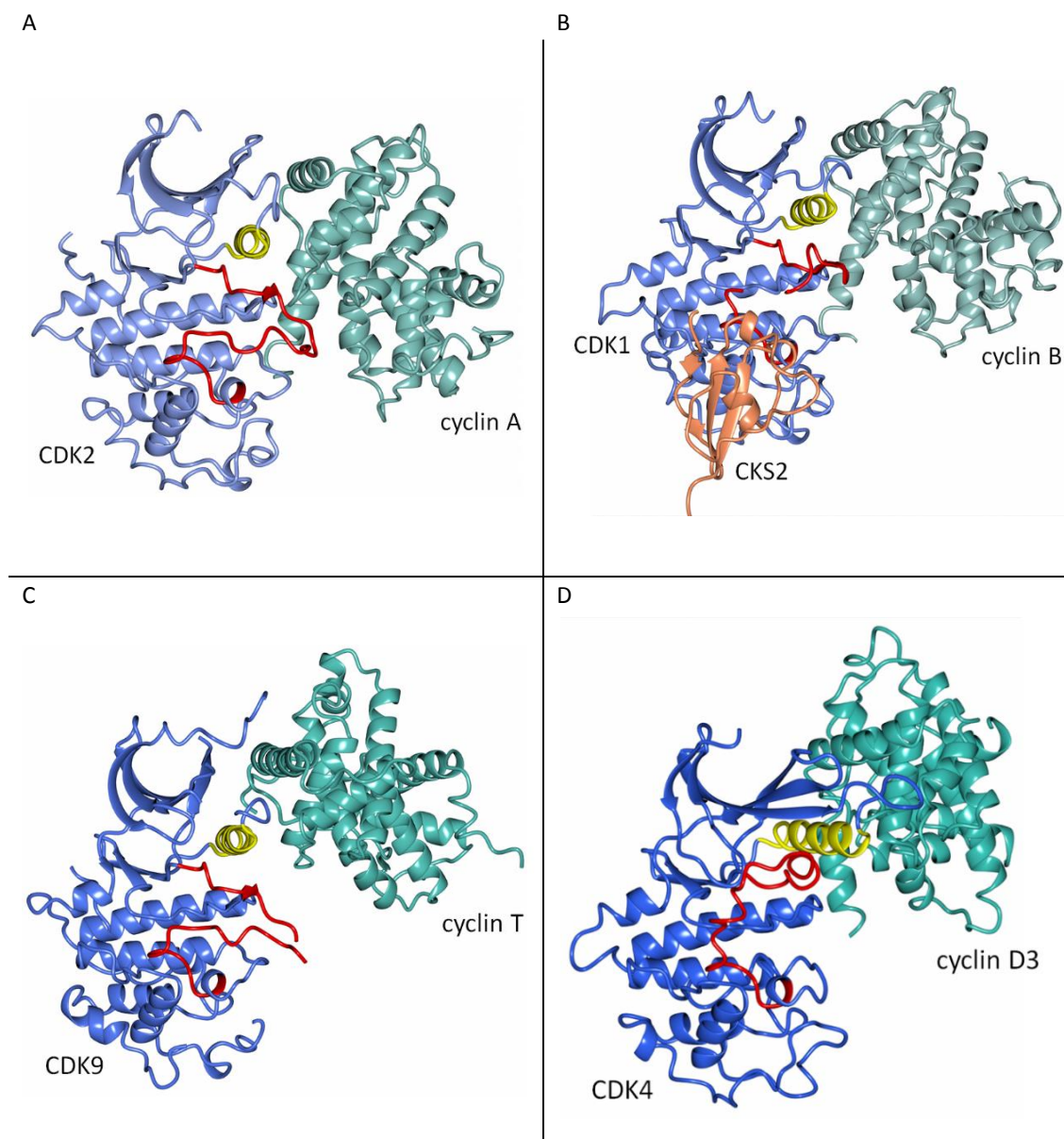


Figure 1-8 Comparison of CDK4/cyclin D3 and CDK9/cyclin T structures

The CDKs undergo a conserved mechanism of activation upon cyclin binding. Proteins displayed in ribbon format. (A) CDK2-cyclin A (PDB: 1JST). (B) CDK1-cyclin B-CKS2 (PDB: 4YC3) CKS2 is displayed in coral. (C) CDK9-cyclin T (cyclin box only) (PDB: 3BLH) (D) CDK4-cyclin D3 (PDB: 3G33). CDKs are in blue and the cyclins are in green and graded from light to dark to reflect the degree of cyclin rotation away from the CDK. The C-helix for each are in yellow and the activation loop red. Figures created using CCP4MG (Potterton *et al.*, 2002).

Structures of monomeric CDK6 show that CDK6 shares the conserved disordered features attributed to the inactive CDK fold (Cho *et al.*, 2012). However, the structure of CDK6 bound to a canonical D-type cyclin has not been determined. Due to the sequence similarity and closely linked activity of CDK6-cyclin D and CDK4-cyclin D it is expected to form a similar ostensibly inactive conformation. Crystal structures of CDK6 in complex with the viral D-type cyclins, however, have been determined (Jeffrey *et al.*, 2000;

Schulze-Gahmen and Kim, 2002). Bound to the viral cyclins CDK6 adopts an active conformation reminiscent of CDK2-cyclin A and makes extensive interactions through both its N and C-terminal lobes. The viral cyclins are capable of ordering the CDK6 activation loop even without phosphorylation on Thr177 and the resulting complex is active (Lu and Schulze-Gahmen, 2006). The viral cyclins are discussed in more detail in Chapter 3.

1.4.2 CDK-cyclin-CKI structures reveal the molecular details of CDK inhibition

The structures of the CKIs p27KIP1 bound to CDK2-cyclin A and the INKs p16, p18 and p19 bound to CDK6 have been determined by X-ray crystallography and reveal the molecular details of CDK inhibition.

p27KIP1 inhibition of the CDK-cyclin complexes

The structure of the CDK2-cyclin A-p27₂₂₋₁₀₆ complex (Figure 1-9) shows how the intrinsically disordered p27KIP1 binds to an extended surface area across both CDK2 and cyclin A and inhibits the CDK-cyclin complex (Russo *et al.*, 1996a). An extended rigid coil (magenta) containing the conserved LFG motif binds a shallow groove in cyclin A (green) formed by the α 1, α 3 and α 4 helices. The LFG sequence is conserved among the CIP/KIP family as well as pocket proteins such as p107 suggesting this site may otherwise contribute to substrate recognition. Followed on from the ridged coil an aliphatic helix (coral, residues 38-49) which contains the RXL motif (Adams *et al.*, 1996), interacts with the α 4 and α 5 helices of the cyclin box and then extends, through a partially disordered region, to the CDK2 (blue) N-terminal domain where the helix ends. p27KIP1 then forms a β -hairpin (purple) followed by a β -sheet (yellow) which packs against the N-terminal β 2 sheet of CDK2 by displacing and partially disordering the β 1 sheet. p27KIP1 then enters the CDK2 catalytic cleft where it forms a 3_{10} helix (red) blocking the ATP binding site thereby inhibiting the CDK catalytic activity. The remaining C-terminal sequence of the p27KIP1 fragment is not visible in the crystal structure but is believed to progress further towards the activation loop of CDK2 to inhibit by preventing substrate binding and possibly phosphorylation by CAK (Russo *et al.*, 1996a).

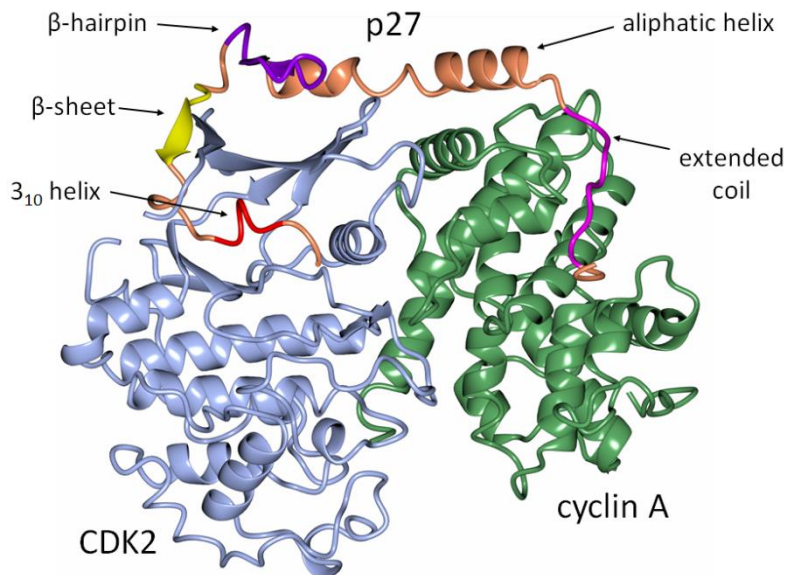


Figure 1-9 The binding and inhibition mechanism of p27 on CDK2-cyclin A

p27KIP1 binds across the CDK-cyclin heterodimer and inhibits CDK activity by entering and blocking the active site. CDK2-cyclin A-p27KIP1 (PDB: 1JSU) Proteins are represented in ribbon form. CDK2 is in blue, cyclin A in green and p27KIP1 in coral. The extended rigid coil is shown in magenta, the aliphatic helix which stretches between the cyclin and CDK is in coral, the β -hairpin in purple and the β -sheet in yellow. The 3_{10} helix which blocks the ATP binding pocket is in red. Figure created using CCP4MG (Potterton *et al.*, 2002).

INK inhibition of CDK4 and CDK6

The mechanism of INK inhibition of CDK4 and CDK6 has been described through X-ray structure determination of CDK6 in complex with p16 (Russo *et al.*, 1998), p19 (Brotherton *et al.*, 1998) and in a ternary complex with p18 and a viral cyclin (Jeffrey *et al.*, 2000). The structure of p16-CDK6 is shown in Figure 1-10 below. The INKs (yellow) bind to the hinge region of CDK6 (blue) between the N and C-terminal lobes in direct competition with the p27KIP1 binding site and explains why the binding of these two CKIs is mutually exclusive (Parry *et al.*, 1999). INK binding rotates the two CDK lobes relative to each other causing a large allosteric distortion of the cyclin binding site which substantially reduces the surface area available for cyclin binding and so weakens the CDK-cyclin interaction (Jeffrey *et al.*, 2000). The INKs also distort the activation loop causing it to fold back and pack against the INK, further inhibiting the CDK by preventing substrate binding and phosphorylation by CAK (Russo *et al.*, 1998). This mechanism of inhibition is described in more detail in Chapter 5.

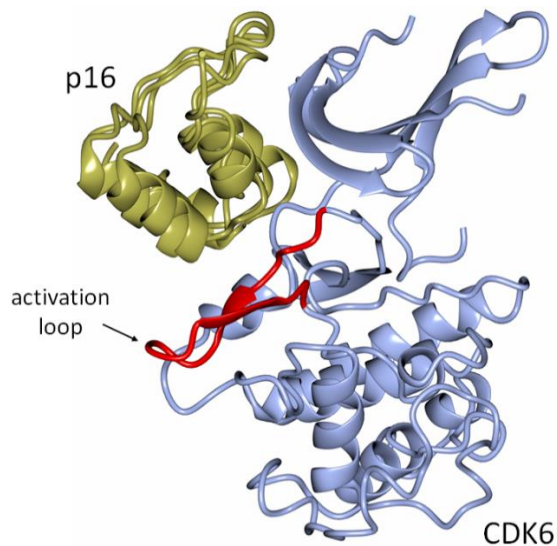


Figure 1-10 Structure of p16 bound to CDK6 showing mechanism of inhibition

The INKs inhibit monomeric CDK4 and CDK6 by interacting with the hinge region between the N and C-lobes of the CDK distorting them in relation to each other. The activation loop packs back against p16. CDK6-p16 (PDB: 1BI7) Proteins are represented in ribbon form. CDK6 is in blue and p16 in gold. The activation loop of CDK6 is in red. Figure created using CCP4MG (Potterton *et al.*, 2002).

1.5 The Hsp90 chaperone system

Protein chaperone systems are involved in the processing and regulation of client proteins. Quintessentially, chaperone complexes, such as heat shock protein 70 (Hsp70), assist with protein folding in the protein crowded environment of the cell (Hartl *et al.*, 2011). The heat shock proteins (HSPs) gained their name as they are upregulated during cellular stress. Large multi-domain proteins may take hours to fold without assistance which leaves them open to unwanted aggregation which could be damaging to the cell. Various disease states such as Parkinson’s and Alzheimer’s have been linked to the decline in chaperone function and are characterised by an increase in aggregated protein species (Hartl *et al.*, 2011). The HSPs assist protein folding through an ATP-dependent mechanism which causes large changes in the chaperone structure. They are also assisted by the binding of multiple co-factors (Pearl and Prodromou, 2006).

Hsp90 is one of the most abundant proteins in the cell making up between 1-2% of the total protein concentration (Stepanova *et al.*, 1996). It is involved in the regulation of around 7% of transcription factors, 30% of ubiquitin ligases and 60% of kinases each of which show a large range of affinities for the chaperone complex (Taipale *et al.*, 2012). Hsp90 lies downstream of Hsp70 and can accept ready folded proteins via

tetratricopeptide repeat (TPR) domain co-chaperones such as HOP, which directly links Hsp70 to Hsp90 (Hartl *et al.*, 2011). Other co-factors such as Cdc37, AHA1 and p23 provide client specificity and recruitment or can further regulate the kinetics of client release by either promoting or inhibiting ATP hydrolysis (Pearl and Prodromou, 2006). Further fine tuning of client or co-chaperone release can be applied through phosphorylation of Hsp90 by casein kinase 2 (CK2) (Olesen *et al.*, 2015) or YES (Xu *et al.*, 2012). Cdc37 is required for the recruitment of kinases to Hsp90 including CDK4 (Stepanova *et al.*, 1996). It has been suggested that Cdc37 selects kinase clients based on their general thermal stabilities rather than a single binding site (Taipale *et al.*, 2012; Keramisanou *et al.*, 2016). The current understanding of the interactions of Cdc37 are described in further detail in Chapter 3.

1.5.1 The Hsp90-Cdc37-client structure and mechanism

The structure of Hsp90 has been determined through a combination of cryo-EM studies and X-ray crystallography of human Hsp90 fragments or homologues from species such as *E. coli*. The structures reveal that Hsp90 forms a dimer connected by a bundle of four α -helices between the C-terminal domains. The crystal structure of the *E. coli* Hsp90 equivalent, HtpG, revealed a more open 'V' shaped conformation with the N-terminal domains separated (Figure 1-11 A) (Shiau *et al.*, 2006) while more recent single particle cryo-EM structures with CDK4 bound show the more closed conformation with the N-terminal domains brought together (Figure 1-11 B) (Verba *et al.*, 2016). The N-terminal domains of Hsp90 contain the ATP binding site while the middle domains have been implicated in client binding (Pearl and Prodromou, 2006). The EM structure (Figure 1-11 B) shows the dimer of Hsp90 (brown and grey) with CDK4 (blue) unhinged between the N and C-terminal lobes and threaded through the middle of the Hsp90 dimer. In this structure Cdc37 (yellow) interacts predominantly with the N terminal lobe of Hsp90 forming a CDK4-Cdc37-Hsp90 complex in a 1:1:2 ratio as has been observed by size exclusion chromatography (SEC) (Vaughan *et al.*, 2006). The molecular clamp-like mechanism which closes around the client is caused by ATP hydrolysis to ADP and results in substantial alterations in the Hsp90 structure allowing for the capture and rearrangement of clients (Pearl and Prodromou, 2006; Krukenberg *et al.*, 2011).

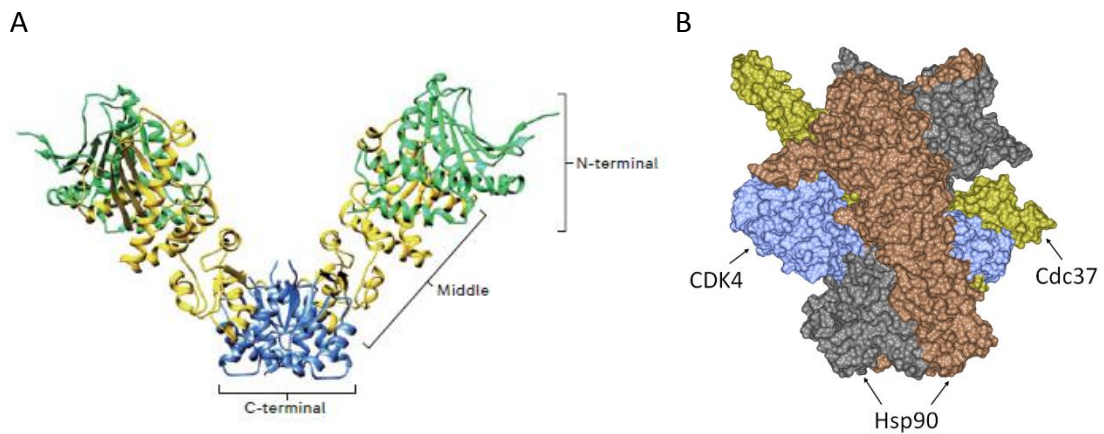


Figure 1-11 An overview of the structure of the CDK4-Cdc37-Hsp90 complex

Hsp90 acts as a molecular clamp involving large ATP-dependent conformational changes from the open 'V' like ligand free structure (A) to the closed ATP-bound structure (B). (A) Image taken from (Saibil, 2013) and shows the Hsp90 dimer in an open conformation displayed in ribbon form. The C-terminal is in blue, the middle terminal in yellow and the N-terminal in green. (B) surface of the cryo-EM model of CDK4-Cdc37-Hsp90 (PDB: 5FWL) The Hsp90 monomers are shown in brown and grey, Cdc37 is shown in yellow and CDK4 in blue. Figure created using CCP4MG (Potterton *et al.*, 2002).

Despite the structural understanding of the Hsp90 complex and the known involvement of multiple co-chaperones, the question as to what Hsp90 actually does to the client remains unclear as clients are often received from Hsp70 in a folded and in some cases already active state (Pearl and Prodromou, 2006). However, protein folding is of a dynamic nature, particularly for many large multi-domain species found in eukaryotes. Unstable proteins may require constant chaperoning throughout their lifetime involving cycles of release and recapture to maintain their folded state (Figure 1-12) (Hartl *et al.*, 2011). Alternatively, Hsp90 may provide a more regulatory role assisting in the rearrangement of client for better access to posttranslational modifying enzymes or client binding partners. Like most chaperone systems Hsp90 may provide a more favourable transition pathway to the active state through an unfolded intermediate (Verba *et al.*, 2016). Conversely Hsp90 binding may serve to protect clients from being dephosphorylated or degraded thereby maintaining an active pool ready for a rapid response when released (Pearl and Prodromou, 2006). The mechanism by which the kinase is removed from this very stable complex is not well understood and has been investigated in this project.

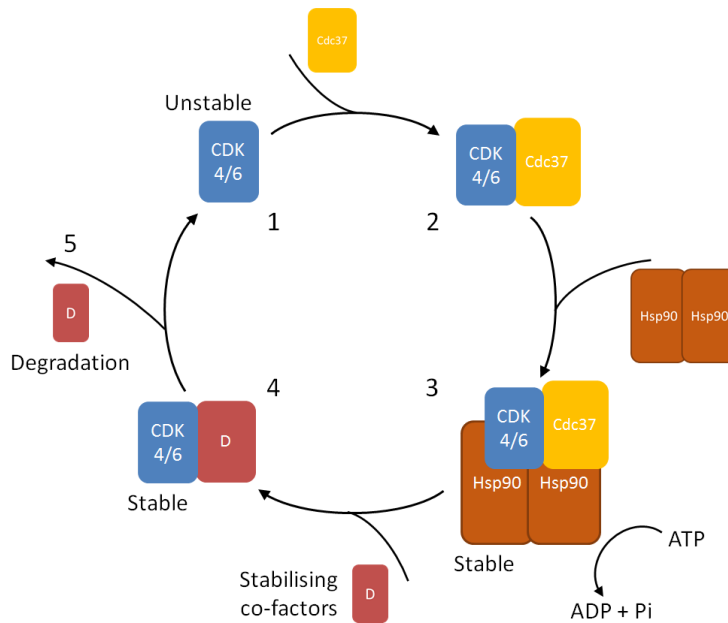


Figure 1-12 Schematic of Hsp90 client regulation

Hsp90 clients, such as CDK4 (1), are believed to be less stable than non-clients. Unstable kinase clients are recognised and recruited by Cdc37 (2) and then subsequently recruited to Hsp90 (3) which undergoes ATP-dependent rearrangement to stabilise the client and sequester it until an appropriate binding partner is found (4). Alternative modifications, such as phosphorylation, may also result in client release from Hsp90. When binding partners are lost, such as through cyclin degradation (5), unstable clients are released.

1.6 CDK deregulation in cancer

Cancer development is a multistep process that evolves through multiple acquired aberrations in a number of cellular mechanisms. These alterations in cellular pathways arise through genetic mutations which can either be inherited or occur through environmental factors such as cigarette smoke or UV radiation (Morgan, 2006). Cancerous cells have escaped the tightly controlled division process and have become able to grow independently and proliferate indefinitely without the need for external growth factors. They are also immune to anti-proliferative signals and the normal routes to cell death. Together with stimulating angiogenesis- blood vessel growth, and metastasis- the ability to spread to new tissues, these traits are often referred to as the hallmarks of cancer (Hanahan and Weinberg, 2011).

The molecular basis of tumorigenesis can vary between tissues due to the different regulatory pathways that control tissue-specific proliferation (Morgan, 2006). Mutations that arise in key tumour suppressors, such as pRB, or mitogenic signalling pathways, such as Ras, can occur in many different tumours and as such are very common in human cancers (Coleman *et al.*, 2004). Due to their prevalence in signalling cascades regulating

growth, proliferation and survival protein kinases are also often upregulated in cancers (Fleuren *et al.*, 2016). The necessity for cancers to overcome the normal quiescent state of adult cells usually results in alterations in the G1/S phase regulators, their targets or their repressors (Malumbres and Barbacid, 2001).

1.6.1 CDK4 and CDK6 dysregulation in cancer

Alterations in CDK4 and CDK6 expression levels are surprisingly less common than defects in their regulation such as by the loss of p16 inhibition or amplification of the D-type cyclins (Figure 1-13, (Asghar *et al.*, 2015) and see www.tumorportal.org). However, CDK4 has been linked to breast cancer progression (Jirawatnotai *et al.*, 2014), some sarcoma cell lines (Khatib *et al.*, 1993) and a mutant form of CDK4 (CDK4^{R24C}), which is incapable of binding to the INKs and therefore is not inhibited by their suppression, has been identified in multiple familial melanoma cases (Malumbres and Barbacid, 2007). CDK6 is overexpressed in a range of leukaemias and lymphomas (Placke *et al.*, 2014) consistent with the haematopoietic tissue specificity observed for CDK6 in the knockout mice. Downregulation of CDK6 in acute myeloid leukaemia led to growth inhibition and differentiation while inhibition of CDK4 had no effect (Antony-Debre and Steidl, 2014). Furthermore, CDK6 has been linked to tumour angiogenesis through its transcription factor role driving expression of the pro-angiogenic factor VEGF-A (Kollmann *et al.*, 2013).

Of the D-type cyclins cyclin D1 is by far the most commonly overexpressed and is amplified in 30-50% of cancers (Casimiro *et al.*, 2014). High levels of expression are particularly observed in breast cancer (Sicinski *et al.*, 1995), pancreatic cancer and melanoma, non-small cell lung cancer and head and neck squamous cell carcinoma (Musgrove *et al.*, 2011). Strikingly *CCND1* chromosomal rearrangements causing increased expression are seen in over 90% of mantle cell lymphoma cases (Bertoni *et al.*, 2006) and perhaps correlate with CDK6 activity as shown by the CDK6 expression phenotype in knockout mice. Although much rarer cyclin D3 amplification has been observed in cancers originating in haematopoietic cell lines (Sicinska *et al.*, 2003) while cyclin D2 amplification has only been observed to be actively overexpressed in 2% of gliomas (Cancer Genome Atlas Research, 2008; Musgrove *et al.*, 2011).

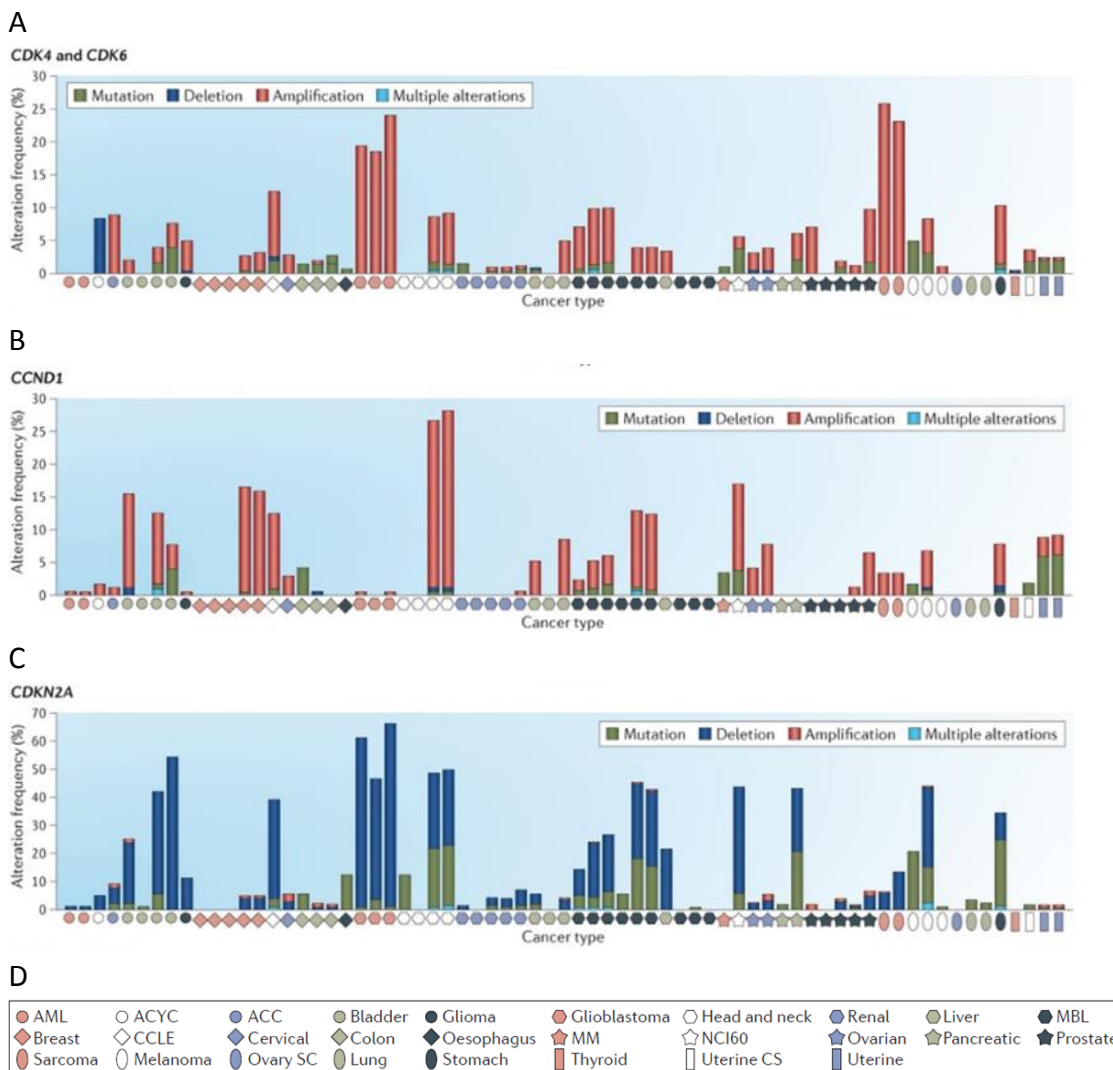


Figure 1-13 Chart of amplifications/ deletions in various cancers

Figure taken from (Asghar *et al.*, 2015). The G1 cell cycle regulators are regularly deregulated in a variety of cancers. CDK4, CDK6 (A) and cyclin D1 (B) are generally amplified (red) while the CKI p16 (C) is commonly deleted (blue) or mutated (green). The frequency of gene alterations is plotted for different cancer types described in symbols along the X-axis. Symbol meanings are described in chart (D).

p16 is by far the most frequently lost CKI reported in cancer cases -approximately 50% of gliomas and mesotheliomas, 40–60% of nasopharyngeal, pancreatic and biliary tract tumours and 20–30% of acute lymphoblastic leukaemias (Vermeulen *et al.*, 2003) and it is commonly mutated in melanoma (Smith-Sorensen and Hovig, 1996). Taken together with the changes to CDK4 expression observed in melanoma, it shows the importance of CDK4 regulation to the proliferation of this particular cancer. p16 and p15 knock out mice are prone to spontaneous tumour development (Malumbres and Barbacid, 2001). However, the loss of p15 is far less common in human cancers and has only been identified in a few rare glial tumours and hematologic neoplasms (Esteller *et al.*, 2001). The loss of p18 in cancer SC appears equally rare and has only been identified in some

Hodgkin lymphomas (Sanchez-Aguilera *et al.*, 2004) and medulloblastomas (Uziel *et al.*, 2005). Notably p18 knock out mice develop pituitary tumours (Malumbres and Barbacid, 2001).

The highest levels of p18 are observed in human skeletal muscle while moderate levels are present in pancreas and heart tissue (Guan *et al.*, 1996). p18 has also been identified as part of the mechanism that regulates myogenic differentiation (Franklin and Xiong, 1996). Finally, p19 mRNA has been observed at high levels in the thymus, peripheral blood leukocytes, and brain while moderate levels are present in the spleen, testis, skeletal muscle, and heart (Hirai *et al.*, 1995). p19 knockout mice, however, only show mild testicular atrophy but remain fertile and are no more susceptible to spontaneous tumour formation than wild-type animals. The testicular atrophy is associated with increased levels of apoptosis (Canepa *et al.*, 2007). As such p19 loss has not been specifically identified in any tumour setting.

The complete loss of CIP/KIP has not been observed in cancer and instead low levels of p27KIP1 seem to enhance tumorigenesis, perhaps through a CDK4/6-cyclin D assembly role. However, p27KIP1 knockout mice are more prone to induced tumours from carcinogenic agents, most likely from the loss of a DNA damage inhibitory response and upregulation of CDK2-cyclin E activity (Sherr and Roberts, 1999).

1.6.2 Hsp90 dysregulation in cancer

The role of Hsp90 in regulating the activity of many oncogenic kinases including B-Raf, ErbB2, Bcr-Abl and CDK4 highlights it as a prime candidate for the development of broad spectrum oncogenic kinase inhibitors capable of treating multiple cancer types (Pearl *et al.*, 2008). Cancers have a greater dependency on chaperone systems as high levels of genetic instability within cancer cells gives rise to higher levels of mutated and dysfunctional proteins which may require greater levels of chaperone activity to effectively regulate them (Whitesell and Lindquist, 2005). As such Hsp90 has been observed to be upregulated in certain cancers including breast cancer (Pick *et al.*, 2007). The inhibition of Hsp90 should therefore have a greater negative effect on these oncogenic kinase- and Hsp90-addicted tumour cells than on normal functioning cells providing a therapeutic window. Initially, it was thought that Hsp90 inhibitors would be too cytotoxic due to many Hsp90 clients being vital for cell survival and proliferation.

However, multiple ATP-competitive inhibitors specific for Hsp90 are currently in clinical trials for the treatment of a number of cancer types, and further development is underway to target co-chaperone and client interactions (Sidera and Patsavoudi, 2014).

Overexpression of the scaffold protein Cdc37 has been shown to be oncogenic and is found in various cancers including prostate cancer and presents frequently with increased CDK4 levels and Hsp90 complex formation (Smith *et al.*, 2015). The upregulation of CDK4 by increased levels of Cdc37 highlights Cdc37 as the rate limiting factor in the Hsp90 chaperone cycle. siRNA knockdown of Cdc37 results in proteasomal degradation of client kinases, as was observed for Hsp90 inhibition (Smith and Workman, 2009), and also highlights Cdc37 as a potential kinase-specific alternative anticancer target to Hsp90. In the same way ATP-competitive inhibitors specific to client kinases have been shown to disrupt the interaction between the kinase and Cdc37-Hsp90 resulting in degradation by the proteasome (Polier *et al.*, 2013). This mechanism of Cdc37 complex disruption has been investigated in Chapter 6.

1.7 Aims of the Thesis

This project aims to provide a better understanding of CDK6-cyclin D structure and regulation through the measurement of protein-protein interactions with various binding partners using a range of biochemical, biophysical and crystallographic studies. Particular focus has been paid to elucidating the role of the Cdc37-Hsp90 chaperone system in CDK4/6 activation and the mechanism by which the client CDKs are regulated by it and subsequently released by CDK binding partners. CDK4 and CDK6 are uniquely poised amongst Hsp90 client kinases due to the plethora of well characterised binding partners. Throughout the interactions involving CDK4 and CDK6 have been compared to better understand the differences between this seemingly cell cycle redundant CDK pair. Improved knowledge of the role of CDK4/6-cyclin D in cell cycle regulatory mechanisms and potential involvement in oncogenic pathways as well as better structural characterisation through crystallographic studies could lead to the identification of alternative cancer treatments.

Chapter 2 first describes the generation of the protein library required to answer these questions followed by how the interactions of CDK4 and CDK6 with Cdc37 has been quantified, predominantly through a fluorescent based assay, in Chapter 3. To better understand the mechanism by which the CDKs are relinquished from the Hsp90 chaperone system the fluorescent assay has been adapted in Chapter 4 and used to compare the regulation by the D-type cyclins and the potential involvement of the CIP/KIP family in this process. Chapter 5 continues the study to investigate the ability of the INKs to regulate CDK activity from the Hsp90 chaperone system and the effect that INK point mutants might have on this mechanism. Finally, in Chapter 6, crystallographic studies have been performed on CDK4/6 specific ATP-competitive inhibitors to better understand the specificity and the effects that they have on kinase regulation by Hsp90.

Chapter 2. Reagent generation

2.1 Introduction

2.1.1 Recombinant protein expression systems

The expression and purification of high quality recombinant eukaryotic proteins in sufficient yields for biochemical, biophysical and crystallographic analysis holds many challenges. For this purpose, a number of different recombinant protein expression systems have been developed including *E. coli* (Baneyx, 1999), yeast (Cregg *et al.*, 2000), insect cells (Beljelarskaya, 2011), mammalian cells (Andersen and Krummen, 2002) or even in plants (Doran, 2000). Each method has merits and disadvantages. In this thesis, recombinant proteins have been expressed using a combination of *E. coli* and insect cell expression systems.

E. coli are widely used for recombinant protein expression due to their rapid growth rates to high densities and low cost of maintenance, and as such have been well-characterised genetically (Baneyx, 1999). The ability of these prokaryotes to take up foreign DNA and their sensitivity to antibiotics have been exploited to selectively introduce exogenous DNA sequences. A large selection of vectors containing a variety of antibiotic resistance genes, promoters and sequences that encode tags to improve protein yields have been designed to this end (Makrides, 1996). A variety of host strains containing alternative chaperones and transcriptional mechanisms to assist with expression and folding of difficult or toxic proteins have also been produced. The main disadvantages of *E. coli* expression is that they lack the posttranslational modifying, disulphide bond forming or secretion mechanisms that their eukaryotic counterparts possess (Makrides, 1996). Thus, some expressed eukaryotic proteins are unstable or inactive.

An alternative heterologous protein expression system to *E. coli* is immortalized insect cells such as those derived from the moth, *Spodoptera frugiperda* (Sf21 and its derivative Sf9). *Spodoptera frugiperda* cells are eukaryotic and as such possess most of the posttranslational modification, chaperone and transportation systems needed for the assembly and activation of eukaryotic proteins (Luckow and Summers, 1988; Trowitzsch *et al.*, 2010; Beljelarskaya, 2011). N-linked glycosylation mechanisms required for the

activation of some proteins however are different to mammalian cells (Luckow and Summers, 1988). Insect cells are readily cultured in suspension and expression can be scaled up with the use of bioreactors if required (Trowitzsch *et al.*, 2010). DNA to express the protein of interest is introduced by infection with recombinant baculoviruses. These viruses are non-pathogenic, cannot replicate in mammalian cells and can introduce far larger DNA sequences than can be taken up by *E. coli* transformation. They are therefore ideal for the transfer and expression of very large proteins or multi-protein complexes (Trowitzsch *et al.*, 2010). The main drawbacks are slower insect cell growth (doubling time of 24 hours compared to 20 minutes for *E. coli*) and the time taken to amplify baculovirus stocks.

The MultiBac™ system (Geneva-Biotech) has been developed by the Berger group at EMBL for expression of eukaryotic protein complexes (Figure 2-1) (Fitzgerald *et al.*, 2006; Trowitzsch *et al.*, 2010). It allows for the modular combination of multiple protein species for expression from the same baculovirus in insect cells. “Acceptor vectors” pACEBac1 and pACEBac2, and “donor vectors” pIDC, pIDK and pIDS, can be combined by an *in vitro* Cre-LoxP recombinase reaction to drive multi-protein expression from the same virus (Figure 2-1, step 2). Co-expression from a single virus greatly simplifies the process of multi-protein expression as multiple viruses do not have to be created and maintained. Each vector contains different antibiotic resistance markers to permit different vector combinations to be selected.

The MultiBac system has also modified the baculovirus sequence to improve protein yields: (i) the *v-cath* gene which codes for a viral protease activated upon cell death has been removed to delay the onset of cell lysis and reduce proteolytic cleavage of overexpressed proteins (Trowitzsch *et al.*, 2010); (ii) the virus is generated as a bacmid in a modified DH10 *E. coli* cell line the success of which can be monitored by blue/white colony formation through lacZ α gene disruption by Tn7 transposition (Figure 2-1, step 5); and (iii) a fluorescent marker (yellow fluorescent protein (YFP)) under the control of a late *polh* promoter has been inserted to permit monitoring of expression of the gene of interest (Figure 2-1, step 7).

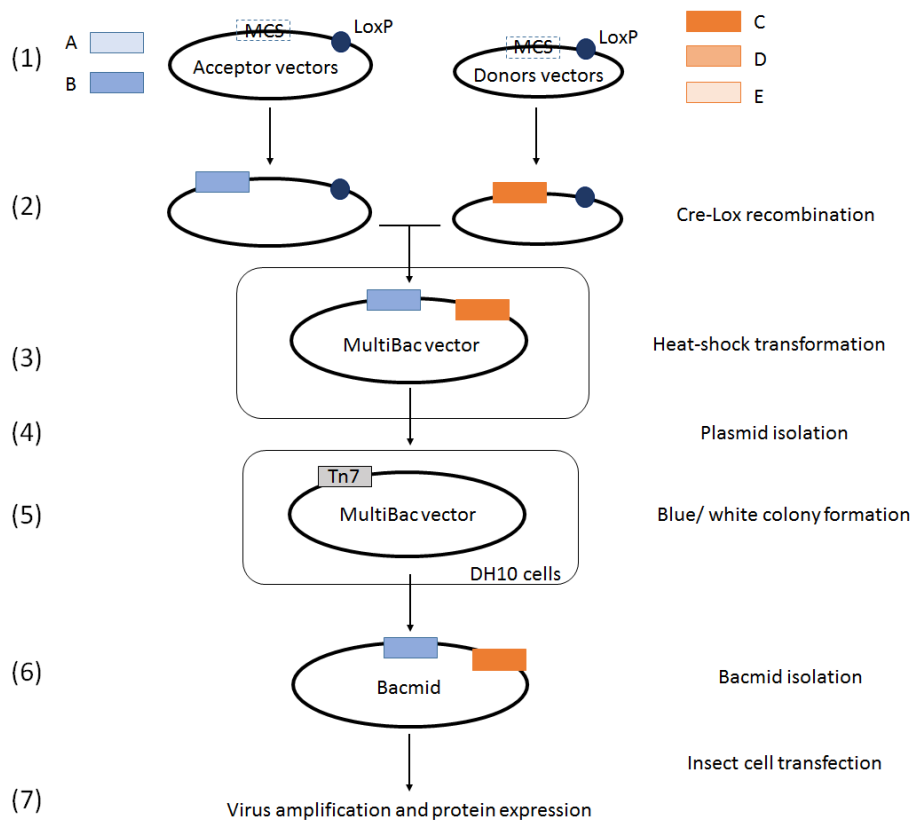


Figure 2-1 Schematic of the MultiBac system

Figure adapted from (Sari *et al.*, 2016) (1). Individual proteins are cloned into acceptor and donor vectors. (2). Vectors are combined by a Cre-LoxP recombinase reaction to produce a multigene expression construct (3). (4). The multigene expression vector is combined with viral DNA to produce a Bacmid (5) in modified DH10 cells. (6). Sf9 insect cells are transfected with the purified Bacmid to express protein complexes (7).

Overall, a low multiplicity of infection (moi) must be maintained to avoid detrimental gene deletion during virus amplification. To ensure this is the case, cell counting is used to determine virus titre: the amount of virus used is determined by that needed to allow one doubling of the insect cells but not more. This activity is reflective of the virus titre as once infected the insect cells no longer divide.

This MultiBac™ system is of particular interest as it would allow multiple combinations of different CDK4 and CDK6 constructs to be combined with different cyclin D species and as well as other binding partners for co-expression such as Cdc37 or p27KIP1.

2.1.2 Tailoring protein expression

As discussed above the majority of eukaryotic proteins are found as parts of larger complexes, where they cooperate to perform cellular functions (Alberts, 1998). When individually expressed many eukaryotic proteins are often expressed in low yields, are

aggregated or insoluble. This behaviour results from a number of protein characteristics: many are multi-domain with individual folds carrying out specific functions and cannot acquire their native structure without the assistance of chaperones. Unstructured regions between domains offer the possibility to remodel proteins in response to signalling events and are frequently subject to post-translational modifications (van der Lee *et al.*, 2014) (Jakob *et al.*, 2014), but in the absence of an appropriate cellular environment, may lack defined structure. Finally, many domains offer surfaces to mediate protein-protein interactions which require a specific binding partner for stability.

To address these concerns several approaches have been taken. Tertiary structure prediction methods, for example HHPred (Soding *et al.*, 2005) that aligns the protein sequence to proteins of known structure deposited in the PDB can be used to identify potential domain boundaries that may delineate a more stable sequence. In the absence of a match, secondary structure prediction (for example CFSSP (Chou and Fasman, 1974) or JPred (Drozdetskiy *et al.*, 2015)) can be used to identify potential boundaries that may define stable constructs. Within a potential fold, the removal of long, unstructured regions without compromising function may aid expression. For all these methods, sequences that book end the conserved core fold may be required to stabilise it necessitating screening several constructs to optimise expression. Techniques such as limited proteolysis and 1D-NMR for example are also useful to define and refine the domain boundaries and identify the percentage of unstructured amino acids. As examples, a number of cyclin structures have been determined following identification of C-terminal stable fragments that encode tandem cyclin box folds that bind and activate the CDK fold (Brown *et al.*, 1995; Honda *et al.*, 2005; Petri *et al.*, 2007).

Finally, mutations can be made to the protein to try and improve solubility and stability (van den Burg and Eijsink, 2002). These mutations, for example cysteine to serine may help to avoid inappropriate disulphide bond formation. Alternatively, the introduction of disulphide bonds or salt bridges to the surface of the protein either intra-molecularly, to stabilise single protein folds, or inter-molecularly to stabilise complex formation may be helpful. Other point mutations which reduce the entropy of the unfolded state, thereby increasing the preference to adopt the folded state, or which improve the hydrophobic packing of the core have also been explored as methods to improve protein

solubility (van den Burg and Eijnsink, 2002). Changing species to study an orthologue can be viewed as an extreme case of protein mutation. Because of insurmountable difficulties attempting to express monomeric human cyclin D1, D2 and D3, two viral D-type cyclins derived from herpesvirus saimiri (Vcyclin) and Kaposi's sarcoma-associated herpes virus (Kcyclin) were used as surrogates in this study.

Co-expression or co-purification with binding partners has also proven successful in some cases, and this approach has been used extensively throughout this thesis to produce proteins for analysis. For example, a cyclin A2 fragment identified by partial proteolysis (Brown *et al.*, 1995) aggregates readily, but forms a monodisperse binary complex when co-purified with CDK2 (Brown *et al.*, 1999a). Determination of the CDK1 structure was aided by the presence of the binding partner CKS1 (Brown *et al.*, 2015). Co-expression with the necessary posttranslational modifiers or chaperone proteins not found in the host cell can also be used to improve solubility and increase yields (Brown *et al.*, 1999b). For example, co-expression of CDK2 with the yeast kinase CDK-activating kinase 1 (CAK1) which phosphorylates CDK2 on a key threonine residue (T160) promoted structural rearrangements and an increase in stability and yield.

Modifications to proteins are also employed to aid with both purification and stability. An example of this approach are affinity tags initially used to separate the desired protein from those of the host after cell lysis. In this thesis, a mixture of polyhistidine (His₆) and glutathione S-transferase (GST) affinity tags have been used for purification and a combination of Avidity (Avi) and FLAG tags used for subsequent biophysical analysis.

The His₆ tag binds to transition metal ions, typically Ni²⁺, immobilised on a nitrilotriacetic acid matrix. High levels of background protein binding is a drawback to its use, exacerbated in our case by kinases having a propensity to bind non-specifically to nickel resin and insect cell media leaching Ni²⁺ from the resin. Non-specific binders can be removed by washing with a low concentration of imidazole (a competing ligand), and high levels of imidazole must be removed from the eluted protein as it causes protein aggregation and affects crystallisation (Terpe, 2003).

The GST tag binds specifically to glutathione which can be coupled to a resin to generate an affinity column and subsequently used as a competing ligand to elute bound proteins

of interest. The GST tag also aids solubility, can help protect against intracellular proteases and can be exploited as an antibody target for subsequent assays. GST however does form dimers in solution, so alternative monomeric tags such as maltose-binding protein (MBP) that can also aid solubility of eukaryotic proteins in *E. coli* may be preferred (Terpe, 2003). Tags can be positioned on either the N or C-termini and cleaved specifically using proteases such as thrombin or the human rhinovirus 3C protease.

Many other affinity tags are available for both purification procedures and subsequent assays, including the Avi and FLAG-tags, allowing the binding of the target proteins to be tailored to the assay at hand. The FLAG tag is a short sequence of eight amino acids which is recognised by monoclonal antibodies making it highly specific for protein detection from cell lysates and for biophysical assays (Terpe, 2003). Bound proteins can then be selectively eluted by competition with FLAG peptide. The Avi-tag consists of a twenty amino acid sequence which contains the recognition site for a biotin ligase (Schatz, 1993). Following biotinylation of the tag, either *in vivo* or *in vitro*, it binds tightly to streptavidin (Kd, 1 fM). The strength of this interaction makes it ideal for immobilising proteins to streptavidin surfaces for biophysical assays, but less useful for protein purification.

2.1.3 Design of truncated CDK6, cyclin D1 and cyclin D3

Prior to the start of this project, structures had been determined for CDK4-cyclin D1 (Day *et al.*, 2009), CDK4-cyclin D3 (Takaki *et al.*, 2009) and for CDK6 bound to a herpes virus saimiri cyclin (Vcyclin, (Schulze-Gahmen and Kim, 2001)). Collectively these structures revealed regions of each protein prone to disorder and provided a starting point from which to design constructs with potentially improved properties for both assays and further structure determination. Though starting from the full-length CDK4 and cyclin D3 sequences only residues 5-295 of CDK4 and 23-254 of cyclin D3 had defined electron density (Takaki *et al.*, 2009). The lack of density for residues 255-292 at the C-terminus of cyclin D3 suggested that this region is highly disordered. This structure contrasts with that of the equivalent sequence (residues 402-432) of cyclin A which in the CDK2-cyclin A structure has an extended interaction with CDK2 (Russo *et al.*, 1996b). However, this region of cyclin D3 is also involved in extensive crystal contacts with the adjacent cyclin

```

                                αN-term
D1  MEHQLLCCEVE-TIRRAYPDANLLN-DRVLRAMLKAEETCAPSVSYFKCVQKEVLPSMRK 58
D3  --MELLCEGTRHAPRAGPDPRLLGDQRVLQSLLRLEERYVPRASYFQCVQREIKPHMRK 58
      :*****      * * * . * * : * * * : * * : * * * * * * * * * * * * *
      α1                α2                α3
D1  IVATWMLEVCEEQKCEEEVFPLAMNYLDRFLSLEPVKKSRLQLLGATCMFVASKMKETIP 118
D3  MLAYWMLEVCEEQRCEEEVFPLAMNYLDRYLSCVPTRKAQLQLLGAVCMLLASKLRETTP 118
      : * * * * * * * * * * * * * * * * * * * * * * * * * * * * * * * * * * *
      α4                α5                α1'
D1  LTAEKLCIYTDNSIRPEELLQMELLLVNKLKWNLAAMTPHDFIEHFLSKMPEAEENKQII 178
D3  LTIEKLCIYTDHAVPRQLRDWEVLVLGKLKWDLAAVIAHDFLAFILHRSLPRDRQALV 178
      * * * * * * * * * * * * * * * * * * * * * * * * * * * * * * * * * * *
      α2'                α3'                α4'
D1  RKHAQTFVALCATDVKFISNPPSMVAAGSVVAAVQGLNLRSPNNFLSYRLTRFLSRVIK 238
D3  KKHAQTFLALCATDYFAMYPPSMIATGSIGAAVQGLGACSM---SGDELTELLAGITG 234
      : * * * * * * * * * * * * * * * * * * * * * * * * * * * * * * * * * * *
      A5'
D1  CDPDCLRACQEQIEALLESSLRQAQQNMDPKAAEE-EEEEEEVDLACTPTDVRDVDI 295
D3  TEVDCLRACQEQIEALLRESLREAAQTSSPAPKAPRGSSSQGPSQTSTPTDVTAIHL 292
      : * * * * * * * * * * * * * * * * * * * * * * * * * * * * * * * * * * *

```

Figure 2-2 Cyclin D1 and D3 secondary structure alignment

Human cyclins D1 and D3 were aligned using Clustal Omega (Sievers *et al.*, 2011) and show an entirely α-helical structure with long unstructured regions at both the N and C-termini. Residues that are identical are marked by stars, conserved residues are highlighted with a colon (:), or dot (.). Human cyclin D1 and D3 sequences taken from Uniprot entries P24385 and P30281 respectively. The secondary structure is taken from the PDB: 2W96 and 3G33 for cyclin D1 and cyclin D3 respectively. α-helices are shown in red with the corresponding helix numbers are displayed above.

D3 molecule suggesting that crystal packing may be influencing the cyclin D3 structure in this region.

To improve the quality of the CDK4-cyclin D1 crystals, Day *et al.* made several truncations to the CDK4 and cyclin D1 sequences. The C-terminal region of cyclin D1 comprised of residues 271-295 that contains a polyglutamate region and a phosphorylation site, and the first (N-terminal) 14 residues that includes the LxCxE motif were removed. Though crystal quality was improved, the final six cyclin D1 residues were still not visible. (Day *et al.*, 2009). Day *et al.* also removed the last 5 residues of CDK4 and mutated an internal flexible loop region, (residues 42-48, consisting of seven glycine residues) with the equivalent GEEG sequence from CDK6.

Structures for CDK6 have been determined using the full-length sequence as well as sequences with minor modifications to the C-terminus to remove either the last 18 or 25 amino acids and so terminate at residue 308 or 301 respectively. For each of the CDK6 structures the initial 10 residues at the N-terminus and residues beyond 301 are rarely visible suggesting that these regions are disordered (Jeffrey *et al.*, 2000; Schulze-Gahmen and Kim, 2002; Lu and Schulze-Gahmen, 2006).

10	20	30	40	50	60
MEKDGLCRAD	QQYECVAEIG	EGAYGKVFKA	RDLKNGGRFV	ALKRVRVQTG	EEGMPLSTIR
70	80	90	100	110	120
EVAVLRHLET	FEHPNVVRLF	DVCTVSRTDR	ETKLTLVFEH	VDQDLTTYLD	KVPEPGVPTĒ
130	140	150	160	170	180
TIKDMMFQLL	RGLDFLHSHR	VVHRDLKPQN	ILVTSSGQIK	LADFGGLARIY	SFQMALTSVV
190	200	210	220	230	240
VTLWYRAPEV	LLQSSYATPV	DLWSVGCIFA	EMFRRKPLFR	GSSDVDQLGK	ILDVIGLPGE
250	260	270	280	290	300
EDWPRDVALP	RQAFHSKSAQ	PIEKFVTDID	ELGKDLLLKC	LTFNPAKRIS	AYSALSHPYF
310	320				
QDLERCKENL	DSHLPPSQNT	SELNTA			

Figure 2-4 CDK6 has short predicted disordered regions at the N and C-termini
XtalPRED was used to predict disordered regions in CDK6 and to predict the effects of truncations (Slabinski *et al.*, 2007). The amino acids within predicted disordered regions are boxed.

A

10	20	30	40	50	60
MEHQLLCCEV	ETIRRAYPDA	NLLNDRVLRA	MLKAEETCAP	SVSYFKCVQK	EVLPSMRKIV
70	80	90	100	110	120
ATWMLEVCEE	QKCEEEVFPL	AMNYLDRFLS	LEPVKKSRLQ	LLGATCMFVA	SKMKETIPLT
130	140	150	160	170	180
AEKLCIYTDN	SIRPEELLQM	ELLLVNKLKW	NLAAMTPHDF	IEHFLSKMPE	AEENKQIIRK
190	200	210	220	230	240
HAQTFVALCA	TDVKFISNPP	SMVAAGSVVA	AVQGLNLRSP	NNFLSYRYLT	RFLSRVIKCD
250	260	270	280	290	
PDCLRACQEQ	IEALLESSLR	QAQQNMDPKA	AEEEEEEEEEE	VDLACTPTDV	RDVDI

B

10	20	30	40	50	60
MELLCCEGTR	HAPFRAGPDP	LLGDQRVLQS	LLRLEERYVP	RASYFQCVQR	EIKPHMRKML
70	80	90	100	110	120
AYWMLEVCEE	QRCEEEVFPL	AMNYLDRYLS	CVPTRKAQLQ	LLGAVCMLLA	SKLRETTPLT
130	140	150	160	170	180
IEKLCIYTDH	AVSPRQLRDW	EVLVLGKLLK	DLAAVIAHDF	LAFILHRLSL	PRDRQALVKK
190	200	210	220	230	240
HAQTFVALCA	TDYTFAMYPP	SMIATGSIGA	AVQGLGACSM	SGDELTELLA	GITGTEVDCL
250	260	270	280	290	
RACQEQIEFAA	LRESLREAAQ	TSSSPAPKAP	RGSSSQGPSQ	TSTPTDVTAI	HL

Figure 2-5 The D-cyclins show an extended disordered region towards the C-terminus
XtalPRED was used to predict disordered regions of (A) cyclin D1 and (B) cyclin D3 and to predict the effects of truncations (Slabinski *et al.*, 2007). The amino acids within predicted disordered regions are boxed.

Considering the available crystal structures and secondary structure predictions, a number of CDK6 and cyclin D1 and cyclin D3 constructs were prepared (Table 2-1). Sequences were sub-cloned into baculovirus transfer vectors for subsequent expression in insect cells.

Full length protein	Truncated constructs		
CDK6		CDK6 ₁₀₋₃₂₆	
(1-326)	CDK6 ₁₋₃₀₁	CDK6 ₁₀₋₃₀₁	
cyclin D1		cyclin D1 ₁₅₋₂₉₅	cyclin D1 ₂₀₋₂₉₅
(1-295)	cyclin D1 ₁₋₂₇₁	cyclin D1 ₁₅₋₂₇₁	cyclin D1 ₂₀₋₂₇₁
	cyclin D1 ₁₋₂₅₅	cyclin D1 ₁₅₋₂₅₅	cyclin D1 ₂₀₋₂₅₅
cyclin D3		cyclin D3 ₂₀₋₂₉₂	
(1-292)	cyclin D3 ₁₋₂₆₀	cyclin D3 ₂₀₋₂₆₀	
	cyclin D3 ₁₋₂₅₅	cyclin D3 ₂₀₋₂₅₅	

Table 2-1 CDK6 and cyclin D truncated constructs

A summary of the CDK6 and cyclin D1 and D3 truncated constructs designed.

2.1.4 Design of constructs to express cyclin-dependent kinase inhibitor p27KIP1

CDK4 and CDK6 are inhibited by members of both the INK and CIP/KIP families of cyclin-dependent kinase inhibitors (CKIs). The four INK proteins are comprised of multiple tandem arrays of ankyrin repeats and have proved to be very amenable to heterologous expression in *E. coli*. In contrast, p21CIP1 and p27KIP1 encode extended unstructured regions and to date structural information for family members has been derived from co-complex structures (Russo *et al.*, 1996a; Duffy *et al.*, 2016). The structure of CDK2-cyclin A-p27KIP1 revealed that p27KIP1 bound across an extended interface interacting with both CDK2 and cyclin A ((Russo *et al.*, 1996a), Figure 1-9). A p27KIP1 construct encoding residues 22-106 was expressed, but only residues 25-93 were visible in the electron density (Russo *et al.*, 1996a). For functional studies, p27KIP1 constructs were designed starting with the published construct from the crystal structure. As well as full-length p27, truncated constructs p27M, encoding residues 1-106, p27S, corresponding to the residues built in the structure (23-106) and p27XS (residues 34-106) which lacks the RXL cyclin binding motif (residues 30-32) were prepared. The equivalent p21CIP1 constructs, p21M (residues 1-87), p21S (residues 9-87) and p21XS (residues 23-87), were also made. Taken together, these constructs can be used to assess the importance of

A

```

                                aliphatic-helix
p27      MSNVRVSNNGSPSLERMDARQAEHPKPSACRNLFGPVDHEELTRDLEKHCRDMEEASQRKW 60
p21      -----MSEPAGDVRQNPCKGSKACRRLLFGPVDSEQLSRDCDALMAGCIQEARERW 49
          * . : : .***.***** *:***: . : : : : *
          β-hairpin      β-sheet      310
p27      NFDFQNHKPLEGKYEWQEVEKGSLPEFYYRPPRPPKGACKVPAQESQDVSGSRPAA--PL 118
p21      NFDFVTETPLEGDFAWERVRGLGLPKLYLPT-GPRRGRDELGG-----GRRPGTSPAL 101
          **** .***. : *:.*. .***:* *:* : : . * ** : *

p27      IGAPANSEDTHLVDPKTDPSDSQTGLAEQCAGIRKRPATDDSSSTQNKRANRTEENVSDGS 178
p21      LQGTAE--EDH-----VDLSLSCTLVPRSGE-----QAEGS 130
          : . * : * . .*: .*: : : : : **

p27      PNAGSVEQTPKKPGLRRRQT----- 198
p21      PGG----PGDSQGRKRRQTSMTDFYHSKRRLLIFSKRKP 164
          *.. .. * :****

```

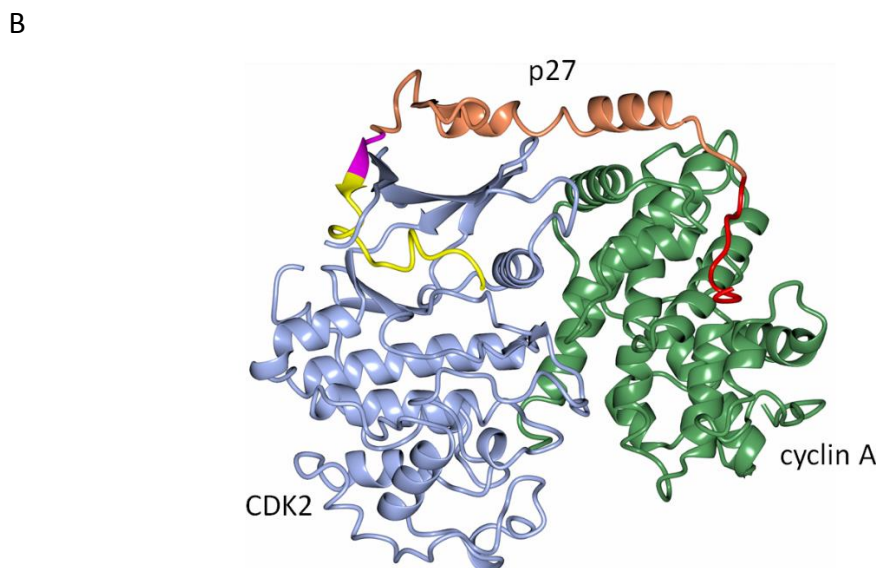


Figure 2-6 p21 and p27 sequence and constructs

(A) Human p21 and p27 (Uniprot entries P38936 and P46527 respectively) were aligned using Clustal Omega (Sievers *et al.*, 2011). The secondary structure when bound to CDK2-cyclin A is taken from the PDB: 1JSU. α -helices are shown in red and β -sheets in blue and key secondary structure elements are labelled above the sequence. Residues that are identical are marked by stars, conserved residues are highlighted with a colon (:) or dot (.). (B) p27 constructs as displayed on the CDK2-cyclin A-p27 structure (PDB: 1JSU). Proteins are displayed in ribbon form. CDK2 is in blue and cyclin A in green. Both p27M and p27S cover the full sequence observed in the crystal structure. p27XS does not include the sequence in red, p27₁₋₇₉ the sequence in yellow and p27₁₋₇₅ additionally the sequence in magenta. Image prepared using CCP4MG (McNicholas *et al.*, 2011).

the cyclin RXL recruitment site and the p21CIP1 and p27KIP RXL motifs to cyclin and CKI function.

p27KIP1 inhibits CDK2 by distorting the N-terminal β -sheet, and inserting a 3₁₀ helix and extended sequence into the catalytic cleft to block ATP and peptide substrate binding respectively. p27KIP1 residues 1-79 (p27₁₋₇₉) was designed to remove the 3₁₀ helix (residues 85-89) and the subsequent residues which would proceed into the substrate

Full length	Truncated constructs		
p27KIP1 (1-198)	p27M (1-106)	p27S (23-106)	p27XS (34-106)
	p27 (1-79)	p27 (1-75)	
p21CIP1 (1-164)	p27M (1-87)	p27S (9-87)	p27XS (23-87)

Table 2-2 Truncated CIP/KIP constructs designed for this study

A summary of p27 truncated constructs used in subsequent experiments. The table gives the construct name and the residue range in brackets.

binding site. A shorter p27KIP1 construct (p27₁₋₇₅) removes the CDK interacting region of the p27 β -strand that forces itself between β -sheets 1 and 2 of CDK2. As a result of this interaction, there is no visible electron density for the CDK2 β -sheet (Russo *et al.*, 1996a). Additionally, tyrosine to glutamic acid mutations were made at residues Tyr88 and both Tyr88 and Tyr89 within the p27M sequence to investigate the effect of phosphorylation on these residues. These CIP/KIP constructs were kindly provided by Dr Martyna Pastok (Postdoc, Endicott lab, NICR) and are summarised in Table 2-2.

2.2 Biophysical methods to characterise proteins

Expressed proteins can be characterised by a variety of techniques to ascertain their purity and integrity. These methods include mass spectrometry (MS), circular dichroism (CD), dynamic light scattering (DLS), analytical size exclusion chromatography (SEC), UV spectroscopy at 280 nm and sodium dodecylsulfate polyacrylamide gel electrophoresis (SDS-PAGE). Non-equilibrium pH-gradient electrophoresis of CDK4-cyclin D3 has revealed that CDK4 is expressed as a mixture of phosphorylated and non-phosphorylated species with around 62% of CDK4 being mono-phosphorylated on Thr172 (Takaki *et al.*, 2009). Day *et al.* removed the last 24 residues on cyclin D1 as it contained a potential phosphorylation site (Day *et al.*, 2009). Constructs have been analysed by a combination of the above techniques to assess their quality and purity for subsequent assays.

2.2.1 Mass spectrometry

Mass spectrometry can be used to accurately determine the mass of proteins. Proteins are first ionised and then accelerated towards a detector by an applied electric field. Mass spectrometric analysis is often coupled with liquid chromatography (LC) to provide sample clean up and separation directly before direct injection onto the mass spectrometer. The most common method of protein ionisation is electrospray (ES). In ES, samples are ejected from a hypodermic needle at high voltage where the water in the micro-droplets rapidly evaporates and imparts its charge onto the protein. ES is a gentle method of protein ionisation which does not cause fragmentation of the protein making it ideal for intact protein mass analysis to identify potential posttranslational modifications or truncations of the protein. Large species such as proteins become multiply charged by the addition of protons imparting them with a mass-to-charge ratio (m/z) sufficient for analysis. By varying the electric field, ions of different m/z can be re-directed towards the detector in order to produce a spectrum of the different charged species in a sample (Mann *et al.*, 2001).

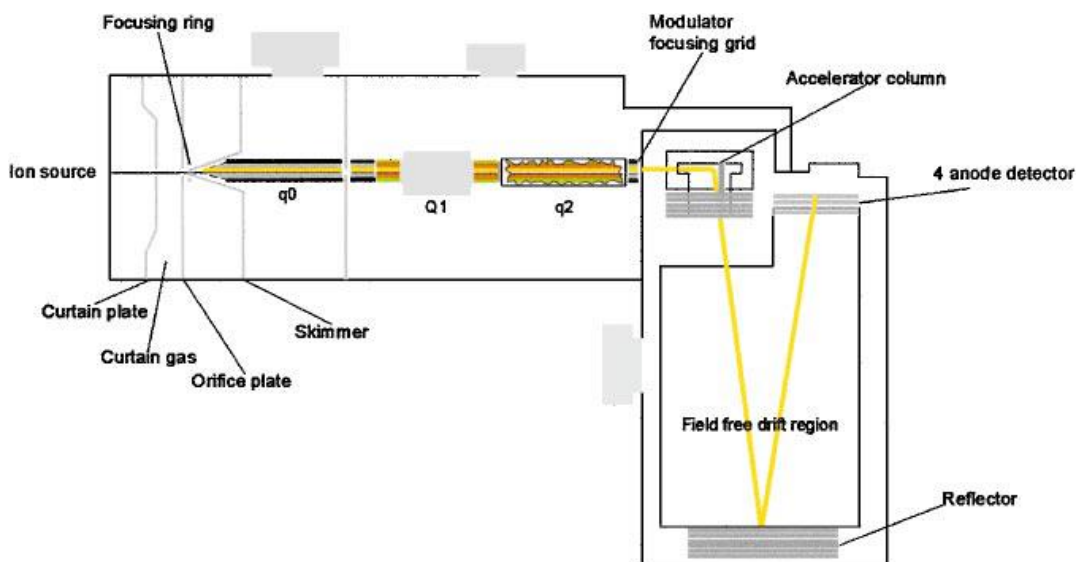


Figure 2-7 Schematic of a quadrupole TOF instrument.

A schematic of a quadrupole TOF instrument. Image taken from (Mann *et al.*, 2001) Ions are produced at the source (left) at atmospheric pressure and are then focussed in the vacuumed quadrupole (q_0) separated in Q1 and dissociated in q_2 . Ions enter the time-of flight analyser through a grid, are pulsed into the reflector and onto the detector.

2.2.2 Differential scanning fluorimetry

Differential scanning fluorimetry (DSF) can be used to analyse protein and protein complex stability (Ericsson *et al.*, 2006). DSF uses a fluorescent dye, such as Sypro Orange to monitor protein unfolding with increasing temperature. The dye binds to hydrophobic regions of the protein which are typically concealed within the protein fold away from the surrounding solvent. As the temperature is increased the protein will begin to denature and unfold exposing the hydrophobic regions and allowing the dye molecules to bind, whereby their fluorescence is increased by the loss of the quenching effect of water. At higher temperatures the protein will begin to aggregate resulting in dye dissociation and the loss of fluorescence. From the initial dye binding curve a melting temperature for the protein (T_m) can be determined as the temperature at which half of the protein is unfolded. The assay can then be used to determine the effect on the melting temperature of the protein from the introduction of compounds or point mutations (Niesen *et al.*, 2007), which may stabilise or destabilise the protein, or from adjusting the buffer conditions (Ericsson *et al.*, 2006).

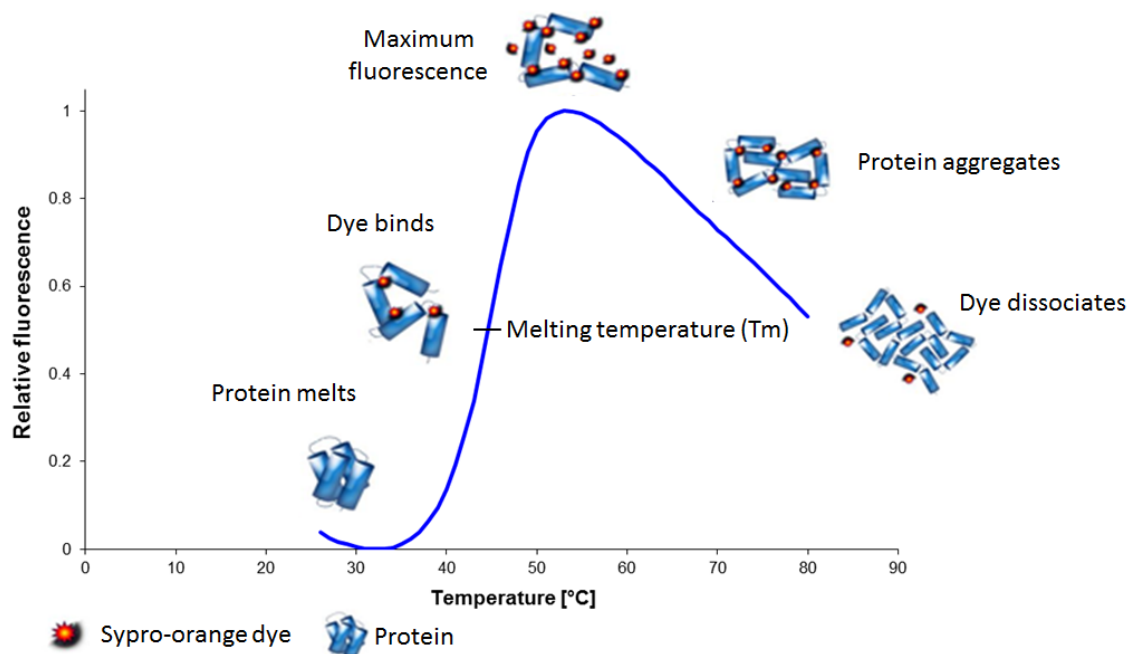


Figure 2-8 Diagram of thermal melt assay

A schematic of a protein thermal melt assay. Figure adapted from (Niesen *et al.*, 2007). As the temperature increases the protein (blue) begins to unfold. Dye (orange) binds to exposed hydrophobic regions until all hydrophobic regions are filled. At higher temperatures, the protein begins to aggregate concealing hydrophobic regions causing a decline in fluorescence.

2.3 Materials and methods

All chemicals listed in the materials and methods were of analytical grade and obtained from Sigma Aldrich unless otherwise stated.

2.3.1 Construct generation

A pGEX-6P1 derivative to co-express full length human CDK2 and *Saccharomyces cerevisiae* CAK1 (the CDK-activating kinase) as GST fusions, and a modified pET21d vector to express a C-terminal His₆-tagged cyclin A2₁₇₃₋₄₃₂ sequence were kindly provided (Brown *et al.*, 1999a). p27KIP1 and p21CIP1 constructs were a gift from Dr Martyna Pastok (Postdoc, Endicott lab, NICR). INK, Vcyclin and Kcyclin sequences were synthesised (IDT, Integrated DNA Technologies) and subsequently sub-cloned into the pGEX6P-1 vector to generate N-terminal GST fusions. Cdc37₁₋₃₄₈, Cdc37₁₋₃₇₈, Cdc37^{S13E}₁₋₃₇₈, Cdc37^{Q247R}₁₋₃₇₈ and Hsp90β₁₋₇₂₄ were all provided as N-terminal His₆ fusion proteins in the pRSETA vector by our collaborator Dr Marc Morgan (Postdoc, Pearl lab, University of Sussex). N-terminal GST fusions of human CDK4 and CDK6 and untagged human cyclin D1 and cyclin D3 sequences were provided in the pVL1392 vector by Dr Martyna Pastok (Postdoc, Endicott lab, NICR).

For subsequent cloning, primers were purchased from Eurofins Genomics, purified using standard desalting methods and re-suspended to 100 μM in nuclease-free water (Ambion). A full list of primers is provided in Appendix A. All PCR reactions were performed using the standard protocol described in Appendix A. Template DNA was removed by DpnI (New England Biolabs) digestion using 5 μl of Buffer 4 and 0.5 μl DpnI per 50 μl PCR reaction product and incubated at 37°C for 1 hour. The Qiagen QIAquick PCR purification kit were used to remove excess primers, template DNA fragments, enzymes and to buffer exchange. DNA concentrations were determined using a Nanodrop Spectrophotometer 2000 (Thermo Scientific).

2.3.2 Cloning

Cloning was performed using a combination of In-Fusion cloning (Clontech) and ligation by T4 DNA ligase (New England Biolabs) of restriction enzyme digested PCR products and vectors.

In-fusion

In-fusion reactions were used to generate full length and truncated CDK6 and cyclin D1 and D3 constructs for the MultiBac™ system as well as sub-cloning of INKs, INK mutants and viral cyclins. 2 µl of 5x In-fusion Enzyme premix was added to 100 ng of purified PCR product and 100 ng of vector, linearized by restriction digest. Reactions were made up to 10 µl using nuclease-free water and incubated at 50 °C for 15 mins before returning to ice. GST-tagged human CDK6 and CDK4 were cloned into the pACEBac1 vector using the 5' BamH1 and 3' EcoR1 restriction sites. Human cyclin D1 and cyclin D3 were cloned into the pDK donor vector at 5' Xho1 and 3' Nhe1 restriction sites. For multi-protein expression, vectors were combined by the Cre-LoxP reaction using Cre recombinase (New England Biolabs). 1 µg of each vector were incubated with 1 unit of Cre recombinase for 1 hour at 37°C.

Ligation

Ligation cloning was used to prepare Avi-tagged constructs of Cdc37, Hsp90, the INKs and INK mutants. 5 µl Buffer 4, 1µl Nco1 (20 U/µl), 1µl Spe1 (10 U/µl), 1 µl DpnI (20 U/µl) (New England Biolabs) were added to 30 µl of PCR-purified PCR product and made up to a total of 50 µl using nuclease-free water and incubated at 37 °C for 90 minutes. Vector stocks of pET3d vectors containing either an N-terminal His₆-3C or His₆-3C-Avi sequence were kindly provided by Dr Richard Heath (Postdoc, Endicott lab, NICR) and were subjected to Nco1 and Spe1 restriction enzyme treatment under conditions described above, followed by the addition of 1 µl of CIP (10 U/µl) (New England Biolabs) and incubated at 37°C for a further 30 minutes. C-terminal Avi-tagged constructs were generated by including the Avi-tag sequence in the PCR primer and then ligation into the N-terminal His₆-3C modified pET3d vector for expression. Constructs containing an Avi-tag at the N-terminus are referred to as N-Avi and those with an Avi-tag at the C-terminus C-Avi. All samples were subsequently purified using a Qiagen QIAquick PCR purification kit. Ligation reactions were performed using 1 µl 1 x T4 ligation buffer, 50 ng of the digested vector, 50 ng of the digested insert and 0.5 µl T4 DNA ligase (400 u/µl) (New England Biolabs) to give a total volume of 10 µl and then incubated at room temperature for 1 hour.

2.3.3 *E. coli* transformation

Construct-containing vectors were transformed into chemically competent *E. coli* Stellar cells (Clonetechn). 2 µl of the In-fusion or ligation reaction was incubated with 30 µl of thawed competent cells on ice for 15 minutes and then heat-shocked at 42 °C for 1 minute before being returned to ice. 400 µl of SOC media was added to the cells which were then incubated at 37 °C, with shaking, for 1 hour. Cells were plated onto antibiotic-containing agar plates and incubated at 37°C overnight. Individual colonies were used to inoculate 10 ml of LB media, containing the appropriate antibiotics, which were then grown overnight while shaking at 37 °C. Cell pellets were harvested by centrifugation at 1876 x g for 10 minutes and the DNA extracted using the standard protocol supplied with the Miniprep kits (Qiagen). DNA concentrations were measured by absorbance at 280 nm determined by Nanodrop 2000 (Thermo Scientific). Sequences were confirmed by sequencing analysis (Eurofins Genomics) and analysed using the ExpASY translate tool (Gasteiger *et al.*, 2003) and sequence alignment by Clustal Omega (Sievers *et al.*, 2011).

Bacmids were produced by transformation of DH10EMBacY cells with 1 µg of either GSTCDK6 containing pACEBac1 or CDK6-cyclin D multigene fusion vector. Colonies were grown on LB agar plates containing ampicillin (50 µg/ml), kanamycin (30 µg/ml), gentamycin (7 µg/ml), tetracyclin (10 µg/ml) X-Gal (100 µg/ml) and IPTG (40 µg/ml) for 16 hours at 37°C to produce the bacmid. White colonies were then selected after a total of 24 hours incubation and the bacmid isolated by isopropanol precipitation of the DNA. The bacmid pellet was washed twice with 70% ethanol, dried, re-suspended in sterilised water in sterile conditions and stored at -20 °C.

2.3.4 Virus production and amplification

Transfections of GST3CCDK6 in pVL1392

The 3C-cleavable GSTCDK6 construct in the pVL1392 transfer vector was prepared (Hallett, 2013). 35 mm dishes were seeded with 2 ml of serum-free Sf900 II media containing 1 x10⁶ Sf9 cells per ml for 1 hour at room temperature. Co-transfection medium was prepared using the FlashBac Ultra system (Oxford Expression Technologies, OET) consisting of 500 ng 3C-cleavable GSTCDK6 transfer vector, 100 ng supplied flashBAC DNA and 5 µl Genejuice transfection reagent and incubated at room temperature for 30 minutes. Excess media and cells were removed from the seeding

dish and the cell monolayer washed with 2 x 1 ml of fresh media. 1ml of co-transfection medium was added and the cells were incubated at 28°C overnight. After 12 hours the co-transfection medium was removed and replaced with 1ml of untreated Sf900 media. The V0 stage virus was harvested in this media after a total of 5 days incubation and then amplified as described below.

Transfection of Bacmids

Bacmid DNA, as prepared from 3 ml of cells, was re-suspended in 20 µl of nuclease-free sterile water to which 200 µl of Sf900 media had been added. 100 µl of a 1 in 10 v/v dilution of Gene Juice™ (Novagen) transfection reagent in media was added to each bacmid DNA sample. 0.5×10^6 Sf9 cells per well were seeded in 6-well plates in a total volume of 3 ml per well. 150 µl of each transfection reagent was added to a well, and again to a duplicate, and incubated for 48-60 hours at 27 °C in the dark. Successful transfections were monitored by the appearance of yellow cells using a fluorescent microscope (see below). YFP expression is under a late promoter and so is not expressed until the virus transfection is well established. Transfections were repeated if no fluorescence was observed after 60 hours. The media from each well was harvested as the V0 virus stock and used for subsequent amplification steps.

Successful transfections determined using fluorescence microscopy

Transfection efficiency was monitored by visualisation of YFP expression within the cells using a fluorescent microscope (Nikon Eclipse TE2000-U) using a green filter. Fluorescent images were overlaid over light microscope images to identify the locations of cells that were fluorescing. The expression of YFP indicated transfection of the bacmid containing both YFP and the gene of interest into the insect cells. However, expression tests were still required to determine the levels of soluble expression of the protein of interest.

Virus amplification

V0 virus was amplified twice to V1 then V2 by infection of 50 ml Sf9 cells at 0.5×10^6 cells per ml with 0.5ml of the previous generation of viral stock. Cultures were incubated at 27°C with shaking (120 rpm) and the number of cells per ml counted each day to monitor when cellular division stops and therefore every cell was infected. If necessary cells were diluted back down to 0.5×10^6 cells per ml to maintain cell numbers. The virus was

harvested 24 hours after arrest of cell proliferation, typically 72 hours after infection, by centrifugation at 2095 x g for 15 minutes. The V2 generation was used for protein expression. Cell pellets were used for expression tests.

Small scale optimization of expression

The optimum amount of each virus to use for expression was determined, 30 ml cultures of 1.0×10^6 cell per ml of Sf9 cells were infected with varying volumes of V2 viral stock, typically 10 μ l, 50 μ l or 100 μ l of virus and incubated at 27 °C with shaking (120 rpm) for a total of 72 hours. After 24 and 48 hours, cells were counted to identify when they had doubled once and then stopped dividing and therefore the optimum virus concentration had been achieved. Small scale expression tests were repeated using different concentrations of virus until the optimum viral stock volume was determined. Cells were harvested by centrifugation at 646 x g for 15 minutes and frozen at -20°C and were also used for expression tests. At each 24 hour time point the YFP levels were determined by excitation at 488 nm and then measuring the emission at 530 nm to determine when a constant reading had been reached. The expression profiles of YFP and the recombinant construct generally correspond with each other as they were under the same promoter. Typically, the maximum expression was observed after 72 hours. This timescale was therefore used for subsequent protein expression.

2.3.5 Expression tests

The cell pellets from the virus amplification steps were lysed using 6 ml of lysis buffer, (50 mM HEPES pH 7.5, 150 mM NaCl, 2 mM DTT, 1% Tween20), to which 200 μ l of 10 mg/ml RNase A, 2 mg/ml DNase I, 1 M MgCl₂ and 1 complete EDTA-free protease inhibitor cocktail tablet (Roche) was added. The cell lysate was subsequently incubated at room temperature for 30 minutes with rotation, and then the supernatant harvested by centrifugation at 6500 x g for 30 minutes. 100 μ l of Glutathione-Sepharose resin was added to the supernatant and incubated for 1 hour at room temperature, or overnight at 4 °C, with rotation. The Glutathione-Sepharose beads were harvested by centrifugation at 1610 x g for 15 minutes and washed 3 times by adding 200 μ l of lysis buffer without Tween20. After the final wash 10 μ l SDS loading dye was added to the pellet, boiled and analysed by SDS-PAGE as described in Appendix A.

2.3.6 Protein expression in *E. coli*

CDK2-cyclin A2, Cdc37, Hsp90, viral cyclins and CKI constructs were expressed in *E. coli* BL21 Star (DE3) cells (Invitrogen). 10 ml LB media starter cultures containing ampicillin (50 µg/ml) were grown overnight at 37 °C. Overnight cultures were then used to inoculate 1L of 2YT media (Cdc37, Hsp90, viral cyclins and CKI constructs), or LB media (CDK2 and cyclin A2), supplemented with ampicillin (50 µg/ml). (See Appendix A for media details). CDK2 and cyclin A2 were incubated at 37 °C with shaking (120 rpm) until an optical density at 600 nm (OD₆₀₀) of 0.8-0.9 or 0.6-0.7 respectively. For all other protein expression, cultures were incubated at 30 °C with shaking (120 rpm) until an OD₆₀₀ of 0.6 was achieved. The temperature was then reduced to 18 °C for 30 minutes before the cultures were induced with 80 µM, 100 µM or 500 µM IPTG for CDK2, cyclin A2 and all other proteins respectively. Cultures were incubated for 16-20 hours, or 24 hours for CDK2 to allow for complete phosphorylation, before being harvested by centrifugation, (JLA 8.1000 rotor at 6238 x g for 20 minutes), re-suspended in 25 ml of HBS buffer (10mM HEPES pH7.5, 150mM NaCl, 0.5mM TCEP, 0.5mM EDTA). Cell pellets were stored at -20 °C. Prior to column chromatography, *E. coli* cell pellets were thawed in cold water and 200 µl of 1 M MgCl₂, 10 mg/ml RNAse A, 2 mg/ml DNAse I; 400µl of 25mg/ml lysozyme and 1 cOmplete protease inhibitor tablet (Roche) were added to each 30 ml pellet. Cells were lysed on ice by sonication using a Sonics vibra-cell sonicator at 30% amplitude cycles of 15 seconds on and 45 seconds off. Cycles were repeated for a total of 3 minutes 30 seconds or until the lysate became fluid. Cell debris was removed by centrifugation using JA 25.50 rotor at 48384 x g for 1hour (Beckman Coulter Avanti, JA 25.5) and the supernatant filtered through 0.45 µm filters to remove larger debris.

2.3.7 Protein expression in Insect cells

Full-length human CDK4 and CDK6 with an N-terminal glutathione-S-transferase (GST)-tag and 3C protease recognition site in the pVL1392 vector were initially expressed in 500 ml Sf9 insect cell cultures of 1.5 x10⁶ cells per ml infected with 1% v/v of their respective baculovirus. CDK-cyclin D complexes were produced through co-expression by inoculating the cultures with two baculoviruses expressing either the CDK or the cyclin D. After adoption of the MultiBac™ baculovirus expression system monomeric CDK4 and CDK6, and CDK4 and CDK6 in complex with their respective cyclin D1 and cyclin D3 partners were routinely expressed from 500 ml Sf9 insect cell cultures of 1.0 x10⁶

cells per ml infected with 400 μ l of their respective baculovirus per litre of cell culture. Infected cultures were incubated at 27°C with shaking (120 rpm) for 72 hours and then harvested by centrifugation, (Beckman Coulter Avanti JLA 8.1000 rotor, at 6238 x g for 20 minutes). Cell pellets were re-suspended in 25 ml of mHBS buffer and stored at -20°C. Insect cell expressed proteins were purified as described above.

2.4 Protein purification by column chromatography

2.4.1 *Glutathione-affinity chromatography*

For GST-tagged proteins the supernatant was incubated with 3 ml of glutathione-sepharose resin (GE Healthcare) slurry at 50:50 glutathione resin to mHBS buffer for 2 hours at 4 °C with rotation. The suspension was loaded onto gravity columns and washed with 50 ml of mHBS buffer and 1 column volume of mHBS buffer containing 1 M NaCl followed by a further column volume of mHBS buffer. GST-fusion proteins were eluted in 1 ml fractions using mHBS buffer containing 20 mM reduced glutathione, pH 8.0. Protein concentrations were measured using a Nanodrop and then pooled. The GST tag was removed by incubation with 1:50 wt/wt 3C protease at 4°C overnight. The thrombin-cleavable GST-CDK6 construct was incubated with 35 units of thrombin and 12.5 μ l of 1M CaCl₂ at 4°C for 16 hours.

2.4.2 *Ni-NTA chelate chromatography*

The supernatants of His₆-tagged proteins were purified using 5 ml Ni-NTA His-Trap columns (GE Healthcare). Samples were washed with 5 column volumes (CV) of imidazole buffer A (10 mM HEPES pH 7.5, 300 mM NaCl, 0.5 mM TCEP and 50 mM imidazole) before the protein of interest was eluted using an imidazole gradient from 50 mM to 500 mM using imidazole buffer B (10 mM HEPES pH 7.5, 300 mM NaCl, 0.5 mM TCEP and 500 mM imidazole). Protein elution was monitored by measuring absorbance at 280 nm and fractions containing the desired protein were pooled. The His₆ affinity tag was removed by incubation with 1:50 wt/wt 3C protease at 4°C overnight.

2.4.3 *Size exclusion chromatography*

All proteins were subjected to size exclusion chromatography (SEC) post cleavage to remove further impurities. Individual proteins were concentrated to between 2-5 ml and loaded onto a Superdex 75 (26/60) (GE Healthcare) column pre-equilibrated in mHBS.

Protein complexes over 60 kDa were separated on a Superdex 200 (26/60) (GE Healthcare). 4 ml fractions were collected and those containing proteins as judged by absorbance at 280 nm were analysed by SDS-PAGE (see Appendix A). All complexes containing CDK4 or CDK6 were purified at 4 °C. The fractions containing the desired proteins were pooled and concentrated in VivaSpin filter concentrators (Sartorius), by centrifugation at 5,000 rpm (Beckman Coulter Allegra 25R, TA-10-250) and at 4°C, using either 10 kDa, 30 kDa or 50 kDa molecular weight cut-offs depending on the protein/protein complex size.

2.4.4 Subtractive affinity purification

Many of the proteins co-eluted with GST from the SEC column. To remove unwanted GST, pooled fractions containing the desired proteins were re-applied to a gravity flow column containing 3 mls of clean glutathione-Sepharose. This step was repeated a minimum of 3 times or until no residual GST remained in the unbound fraction, as analysed by SDS-PAGE.

For His₆-tagged proteins, reverse Ni-affinity purification was performed using a clean 5 ml Ni-NTA His-Trap column (GE Healthcare). Protein samples were loaded by syringe and the unbound fraction collected. This process was again repeated 3 times.

2.4.5 Biotinylation

After purification, Avi-tagged constructs were biotinylated *in vitro* using BirA, provided by Dr Richard Heath (Postdoc, Endicott lab, NICR). 80 µM of each Avi-tagged construct was diluted two-fold using a 2 X concentrated biotinylation buffer of 0.5 M bicine pH 8.3, 100 mM ATP, 100 mM MgOAc and 500 µM *d*-biotin. To this mixture, 10 µg of BirA was added and incubated for 1 hour at 30 °C. The resulting biotinylated constructs were buffer exchanged back to mHBS using a Superdex 75 10/60, pre-equilibrated with mHBS. This step was necessary to remove residual ATP and biotin which could interfere with subsequent experiments.

2.4.6 Mass Spectrometry

LC-MS and analysis was performed by Dr Claire Jennings (Postdoc, Endicott lab, NICR) on samples provided. HPLC was performed using a PepSwift monolithic PS-DVB 200µM

x 50 mm column (Thermo Scientific) at 60 °C. 2 µl samples of 10 µM were loaded onto the column at 3 µl/ minute and run at 1 µl/ minute using a buffer gradient from 95 % buffer A (0.05% formic acid) to 90% buffer B (60% acetonitrile, 20% isopropanol and 0.08% formic acid). HPLC eluate was loaded onto a MaXis 4G+ MicroTOF (Bruker) operated in positive mode under the following conditions: capillary voltage: 1800 V; drying gas: 3.0 L/min; drying temperature: 150°C; Spectra rate: 1.0 Hz. Data analysed using the Compass Data Analysis 4.0 SP5 software.

2.4.7 Differential scanning fluorimetry

A standard buffer screen was prepared by Dr Claire Jennings (Postdoc, Endicott lab, NICR) based on a NMR buffer screen. 9 µl of each condition was dispensed into 96 wells of a 384 well plate with 2 µl of 30 µM CDK6 or CDK6-cyclin D3 to give a final concentration of 4 µM. 4 µl of a 37.5 X Sypro orange stock (Thermofisher Scientific) was then dispensed into each well to give a final concentration of 10 X in the 15 µl well. The plate was incubated for 1 hour at 4 °C and then scanned using an RT-PCR instrument (ViiA7, Applied Biosystems). The fluorescent emission signal from dye at 570 nm was measured after excitation at 470 nm. The temperature was increased by 3 °C per minute from 25 °C to 95 °C and measurements were taken at 1 °C intervals. Analysis was performed using the Boltzmann equation in GraphPad Prism 6.0.

2.5 Examples of protein purification from recombinant *E. coli* cells

The expression of recombinant proteins in *E. coli* generally yielded high levels of protein after purification ranging from 3-5 mg/L for Cdc37 and Hsp90 constructs up to 80 mg/L for some of the INKs. However, two p16INK4a point mutants, p16^{D108N} and p16^{M53I} yielded less than 1 mg/L. Multiple litres of *E. coli* culture had to be purified to give sufficient yields for subsequent biophysical assays. The low expression level for these point mutants likely reflects a lowered stability, possibly from alterations in the protein fold or surface entropy, and may be a contributing factor to the reduction in function observed *in vivo*. Addition of the 15 amino acid Avi-tag to the N-terminus of p16^{M53I} (as described in Section 2.3.2) resulted in no observable soluble expression and instead pushed the protein into the insoluble fraction of the cell pellet. Interestingly, the related p16 mutant p16^{M53E} remained one of the highest expressing proteins, even with the N-terminal Avi tag, with expression levels equivalent to the wild-type.

For soluble expression of Avi-tagged p16^{M53I}, the Avi-tag sequence was introduced into the GST-p16^{M53I} sequence in the pGEX-6P1 vector through PCR. Extended primers were used for the PCR, both primers were 5' phosphorylated and contained the C-terminal half of the Avi-tag sequence followed by the start of the p16^{M53I} sequence while the reverse primer coded for the C-terminus of GST containing the 3C protease site followed by the N-terminal half of the Avi-tag sequence (Appendix A). The standard PCR reaction scheme described in Appendix A was modified by extending the elongation time to 180 seconds. PCR products were subsequently treated with DpnI to remove the template

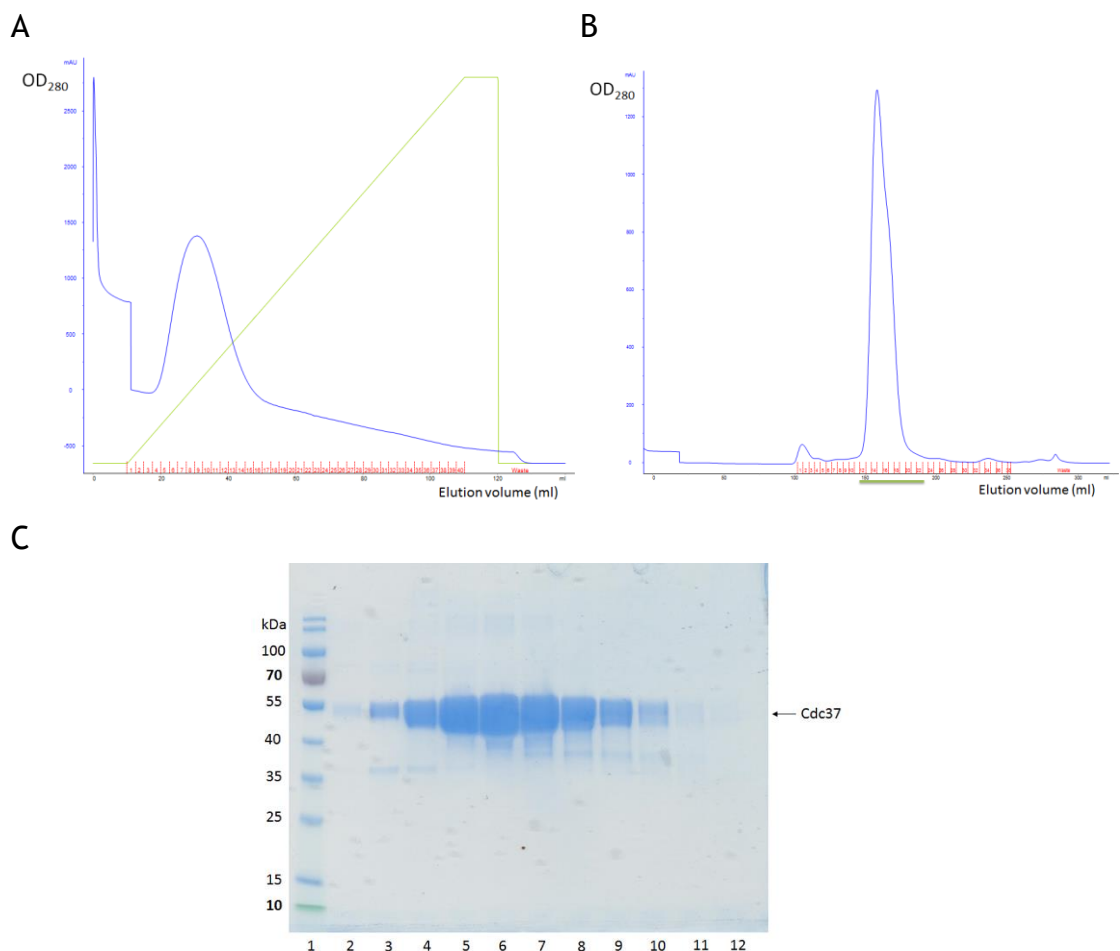


Figure 2-9 Example purification of a Cdc37 construct

Purification of a C-Avi-tagged Cdc37 construct is shown as an example purification of a His₆-tagged protein by sequential Ni-NTA affinity and size-exclusion chromatography (SEC). (A) Chromatogram of the C-Avi Cdc37 nickel affinity column purification. Absorbance at 280 nm shown in blue, gradient of buffer B from 50 mM to 300 mM imidazole to shown in green. (B) Chromatogram for the size-exclusion chromatography (SEC) purification step using a Superdex 75 26/60 column. Absorbance at 280 nm is shown in blue (C) Corresponding SDS-PAGE of fractions following SEC purification. Lane 1 PageRuler protein ladder, Lanes 2-12 correspond to fractions 12-22 of the SEC run (green bar). Proteins were visualised by staining with InstantBlue.

DNA and the vector was fused by ligation as described in Section 2.3.2. The substitution of the His₆-tag for the GST-tag allowed for the purification of low yields of GST-3C-Avi-p16^{M53I} which remained in solution after cleavage of the GST-tag.

Other Avi-tagged constructs to express Cdc37, Hsp90 and the viral cyclins did not show such marked variation in expression levels from their non-Avi-tag containing predecessors and positioning of the tag on either the N or the C-terminus did not affect expression. A typical purification profile of one of the Cdc37 constructs is shown in Figure 2-9 as an example of these *E. coli* expressed species.

Truncations of p21CIP1 and p27KIP1 also showed marked variations in expression levels with, in general, the longer full-length species being expressed in far lower yields than the truncated variants. Full-length p21CIP1 in particular was always found in the insoluble fraction after cell lysis. Full-length p27KIP1 could be expressed in *E. coli* but with low yields (circa 2 mg/L) compared to the truncated variants and it was prone to aggregation when concentrated.

The poor expression levels of these full-length species is likely due to their naturally highly disordered structure which could make them prone to aggregation. The p27M fragment for example (Figure 2-10) had 92 residues removed from the C-terminus and

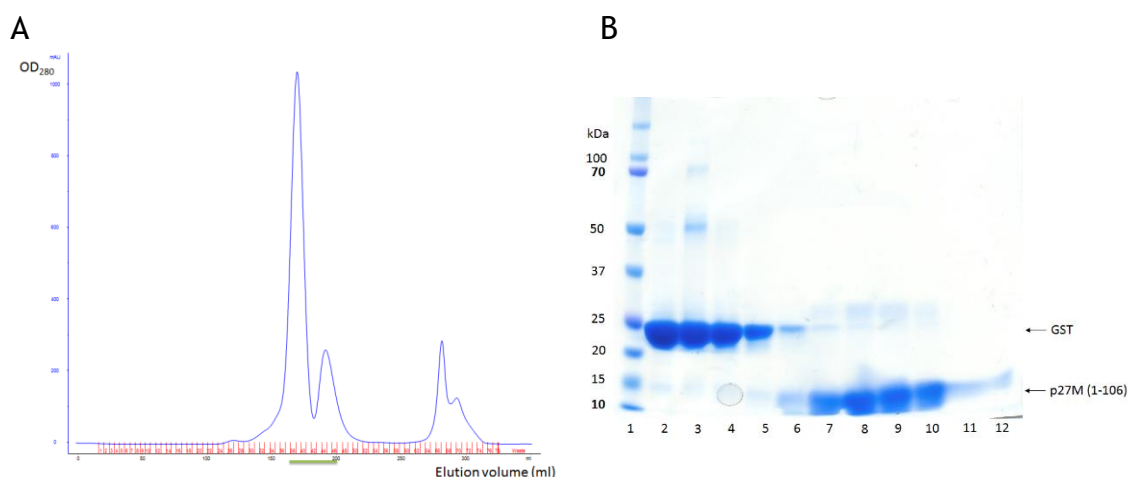


Figure 2-10 Example of p27M purification

Purification of a GST-tagged p27M construct is shown as an example purification of a GST-tagged protein from *E. coli*. (A). Chromatogram for the size-exclusion chromatography (SEC) purification step using a Superdex 75 26/60 column. Absorbance at 280 nm is shown in blue. (B). Corresponding SDS-PAGE of fractions following SEC purification. Lane 1 DuelColour protein ladder, Lanes 2-10 correspond to fractions 38-46 (green bar) of the SEC run and lane 11-12 correspond to fractions 67 and 70 respectively. Proteins were visualised by staining with InstantBlue.

as such produced yields of circa 15-20 mg/L and could be comfortably concentrated to over 5 mg/ml without signs of precipitation or aggregation.

2.6 CDK6-cyclin D3 expression in insect cells

Insect cell expression of the CDKs has greatly improved throughout the project. The original CDK6 construct was obtained as a kind gift from Professor Ernest Laue (University of Cambridge) as a recombinant baculovirus expressing full-length CDK6 with an N-terminal GST tag. This virus produced good yields of GSTCDK6 of *circa* 3 mg/L of Sf9 cell culture. However, problems arose with cleavage of the GST-tag. This original construct contained a thrombin cleavage site between the GST and CDK6. Complete cleavage of the tag was not achieved after overnight incubation (Lane 5, Figure 2-11)

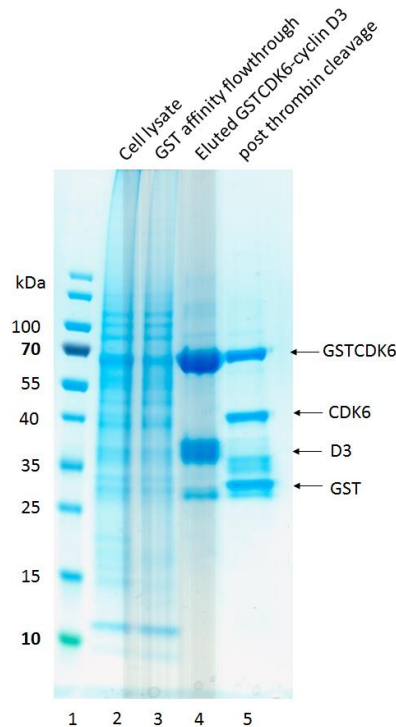


Figure 2-11 Thrombin cleavage of the GST tag is incomplete and is accompanied by cyclin D3 degradation

SDS-PAGE of CDK6-cyclin D3 at various stages of the purification protocol. In this example, the thrombin cleavable GSTCDK6 construct has been expressed. Lane 1 PageRuler protein ladder, Lane 2 Lysate after centrifugation, Lane 3 Flowthrough from GST column, Lane 4 GSTCDK6-cyclin D3 eluted from the glutathione resin, Lane 5 GSTCDK6-cyclin D3 complex after overnight incubation with thrombin. In lane 5 GST migrates as two bands, the upper band derives from the recombinant GST-fusion protein (apparent after thrombin treatment), the lower band is the endogenous insect cell GST (present in lane 4). Cyclin D migrates as two bands in lane 4 suggesting some proteolytic digestion in the insect cells. However, after thrombin treatment, both cyclin D3 bands migrate as smaller species indicative of thrombin cleavage. Proteins were visualised by staining with InstantBlue.

and was still not observed when the incubation period was extended to 24 hours. Further complications arose when co-expressed with cyclin D3 as clear degradation of the cyclin was observed after incubation with thrombin to cleave the GST tag (Figure 2-11 Lane 5).

To better understand why cyclin D3 degradation was occurring the amino acid sequence of cyclin D3 was investigated for potential thrombin cleavage sites (Hallett, 2013). Thrombin preferentially cleaves at Gly-Arg-/Gly but will also cleave at sites consisting of A-B-Pro-Arg-/X-Y, where A and B are hydrophobic amino acids and X and Y are non-acidic amino acids (Chang, 1985). Although no exact match to a preferred thrombin cleavage site was found in cyclin D3, a potential site of sequence YVPRAS at residues 38-43 was identified that would cleave 41 amino acids from the cyclin D3 N-terminus to yield a fragment 4.7 kDa smaller in size (Figure 2-2). To prevent cyclin D3 degradation

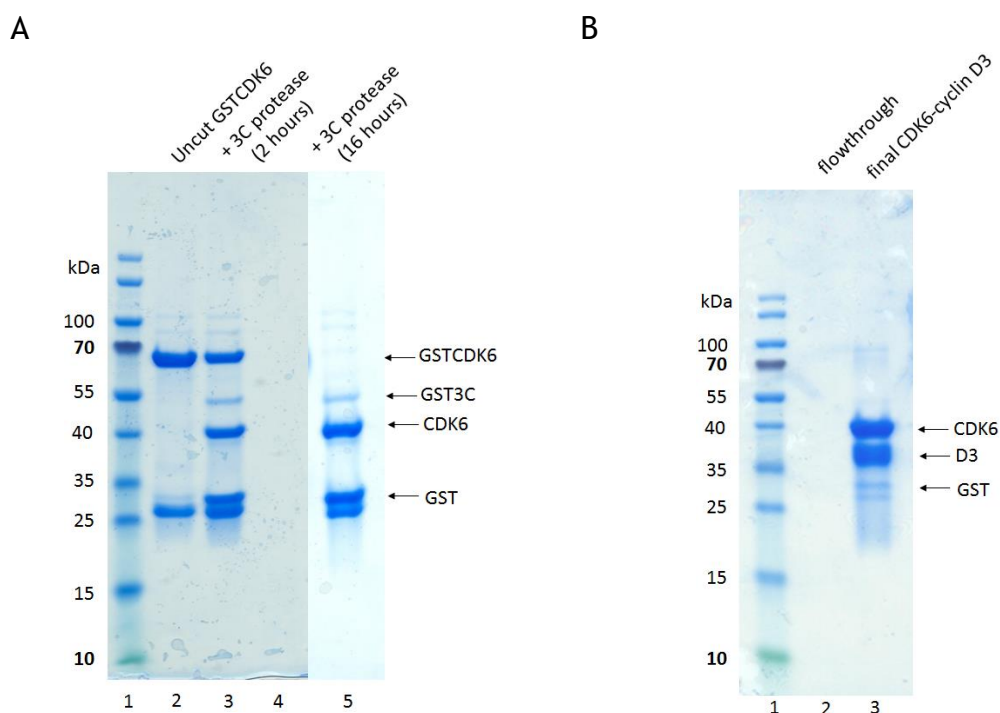


Figure 2-12 3C protease completely cleaves the GST tag from GST3CCDK6 without degrading cyclin D3

(A) SDS-PAGE to monitor 3C protease cleavage of GST3CCDK6. Lane 1, PageRuler protein ladder; Lane 2, Uncut GST3CCDK6 eluted from the glutathione resin; Lane 3, GST3CCDK6 after incubation with 3C protease for 2 hours at 4 °C; Lane 4, blank; Lane 5, (separate gel) GST3CCDK6 after incubation with 3C protease for 16 hours at 4 °C. (B) SDS PAGE of 3C protease cleavage test of the GST3CCDK6-cyclin D3 complex. Lane 1, PageRuler protein ladder; Lane 2, concentrator flow through; Lane 3, CDK6-cyclin D3 after GST cleavage and purification by size-exclusion chromatography. Proteins were visualised by staining with InstantBlue.

and improve the completeness of GST cleavage the thrombin cleavage site was replaced by the more specific 3C protease cleavage site and transferred to the pVL1392 vector (Hallett, 2013). Successful transfection of the 3C cleavable construct into Sf9 cells was achieved using the protocol outlined in Section 2.3.4. CDK6 expression from this new virus was lower than the previous version only yielding *circa* 2mg/L of Sf9 cell culture. However, initial 3C cleavage tests, performed at 4°C using 1:50 wt/wt of GSTCDK6 to 3C protease, showed that complete cleavage of the GST tag could be achieved with overnight incubation, as observed by SDS-PAGE (Figure 2-12 A; Lane 5). Complete GST cleavage had not been possible with the thrombin cleavable version. In addition, Figure 2-12 B shows that cyclin D3 degradation was not observed when the CDK6-cyclin D3 complex was incubated with 3C protease.

2.6.1 Conversion to the MultiBac™ system for complex expression

Further developments in multi-protein complex expression using the MultiBac™ baculovirus system were investigated. It was hoped that the modular design of the system would make the production of new truncated CDK and cyclin D complex variations much faster and easier. The ability to express multiple genes from a single virus would also allow for the more reliable expression of higher order CDK complexes, such as ternary complexes containing p27KIP1, without the need for the production of each individual virus for co-transfection.

Full-length CDK4 and CDK6 constructs with a 3C-cleavable GST tag as well as the truncated variants described in Section 2.1.3 were cloned into the pACEBac1 acceptor vector, while the untagged human cyclin D1 and cyclin D3 and their truncated variants were cloned into the donor vector pDK. Cloning was carried out using the primers described in Appendix A and as described in Section 2.3.2. PCR products of each of the truncated CDK6, cyclin D1 and cyclin D3 constructs were successful (Figure 2-13) as shown by the strong PCR product band around 900 bp. From the constructs available, construct combinations of CDK6₁₋₃₀₁-cyclin D1₁₅₋₂₇₁ and CDK6₁₋₃₀₁-cyclin D3₁₋₂₆₀ were chosen as the constructs that most closely resembled the CDK6 and cyclin D1 sequences previously used in successful structure determination (Schulze-Gahmen and Kim, 2002; Day *et al.*, 2009) and based on the observable region in the cyclin D3 structure (Takaki *et al.*, 2009). The constructs CDK6₁₀₋₃₀₁-cyclin D1₂₀₋₂₅₅ and CDK6₁₀₋₃₀₁-cyclin D3₂₀₋₂₅₅ were

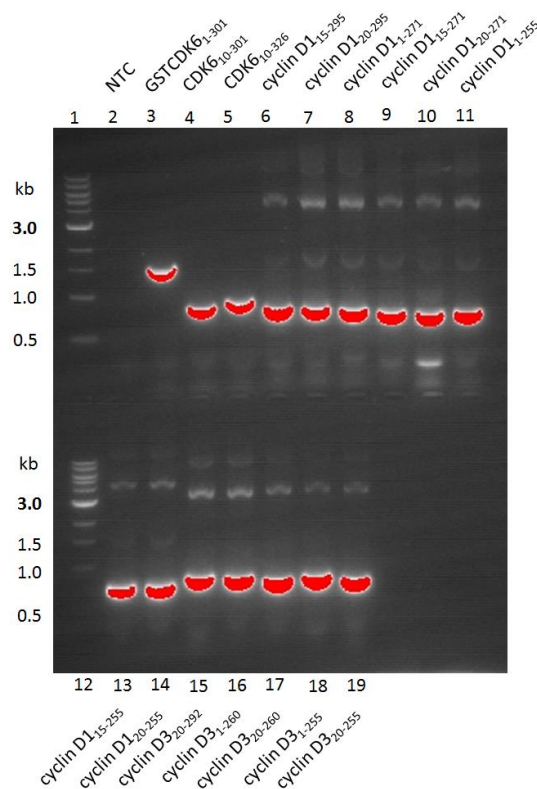


Figure 2-13 PCR amplification of DNA sequences to express truncated constructs of CDK6 and cyclin D

The truncated CDK6, cyclin D1 and D3 construct PCR products were analysed by 1% agarose gel electrophoresis. 8 μ l aliquots of each PCR reaction were used. Lane 1, 1 kb DNA ladder; Lane 2, no template control; Lane 3, GSTCDK6₁₋₃₀₁; Lane 4, CDK6₁₀₋₃₀₁; Lane 5, CDK6₁₀₋₃₂₆; Lane 6, cyclin D1₁₅₋₂₉₅; Lane 7, cyclin D1₂₀₋₂₉₅; Lane 8, cyclin D1₁₋₂₇₁; Lane 9, cyclin D1₁₅₋₂₇₁; Lane 10, cyclin D1₂₀₋₂₇₁; Lane 11, cyclin D1₁₋₂₅₅; Lane 12, 1 kb DNA ladder; Lane 13, cyclin D1₁₅₋₂₅₅; Lane 14, cyclin D1₂₀₋₂₅₅; Lane 15, cyclin D3₂₀₋₂₉₂; Lane 16, cyclin D3₁₋₂₆₀; Lane 17, cyclin D3₂₀₋₂₆₀; Lane 18, cyclin D3₁₋₂₅₅; Lane 19, cyclin D3₂₀₋₂₅₅.

also combined and rationalised as the shortest fragments designed with the maximum amount of disordered sequence removed from each protein, as predicted by XtalPRED.

The Cre-LoxP reaction, as described in Section 2.3.4, allows different acceptor and donor vectors each containing one of the desired constructs to be quickly and easily combined in a variety of combinations without the need for further cloning. Successful incorporation of each component vector was verified by a combination of DNA sequencing (Eurofins), PCR reaction or restriction enzyme digestion. Figure 2-14 shows the successful combination of the truncated CDK6 and cyclin D constructs as determined by PCR. The PCR was performed using the PCR primers for each of the individual components of the Cre-combined vectors. The PCR products visible at around 1 kb from each set of primers correlate with the sequence size expected for the CDK6 and cyclin constructs.

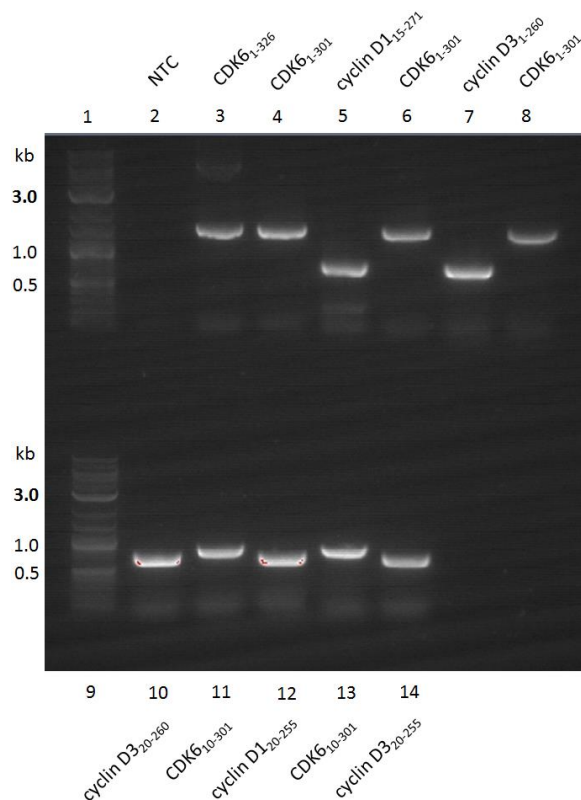


Figure 2-14 Successful Cre-LoxP reactions to generate transfer vectors to co-express various CDK6 and cyclin D proteins were confirmed by PCR

Lane 1, 1 kb DNA ladder; Lane 2, no template control; Lane 3, CDK6₁₋₃₂₆ control; Lane 4, CDK6₁₋₃₀₁; Lane 5, cyclin D₁₅₋₂₇₁; Lane 6, CDK6₁₋₃₀₁; Lane 7, cyclin D₃₁₋₂₆₀; Lane 8, CDK6₁₋₃₀₁; Lane 9, 1 kb DNA ladder; Lane 10, cyclin D₂₀₋₂₆₀; Lane 11, CDK6₁₀₋₃₀₁; Lane 12, cyclin D₁₂₀₋₂₅₅; Lane 13, CDK6₁₀₋₃₀₁; Lane 14, cyclin D₂₀₋₂₅₅.

Sequence verified vectors were transfected into Sf9 cells as described in Section 2.3.4 and fluorescence microscopy was used to visualise successfully transfected insect cells (Figure 2-15). The majority of the cells were rounded and healthy suggesting that non-fluorescent cells had not been transfected. The proportion of fluorescent cells greatly increased between 48 and 60 hours as YFP expression levels increased towards the later stages of infection. Wells showing the highest numbers of fluorescent cells and therefore the best transfection rates were harvested (P0) and amplified for expression.

Starting from P0 viruses, P1 and P2 stocks were successfully generated using the protocol described in Section 2.3.4. Subsequent testing for expression revealed that GSTCDK4 and GSTCDK6 could both be expressed in significant quantities using the MultiBac™ system. A large overexpressed GSTCDK4 band can be observed at *circa* 60 kDa (Figure 2-16 lane 2) whilst a band of GSTCDK6 at *circa* 65 kDa is detectable in lane 4. Expression tests of baculoviruses that co-expressed CDK4 and CDK6 with the cognate

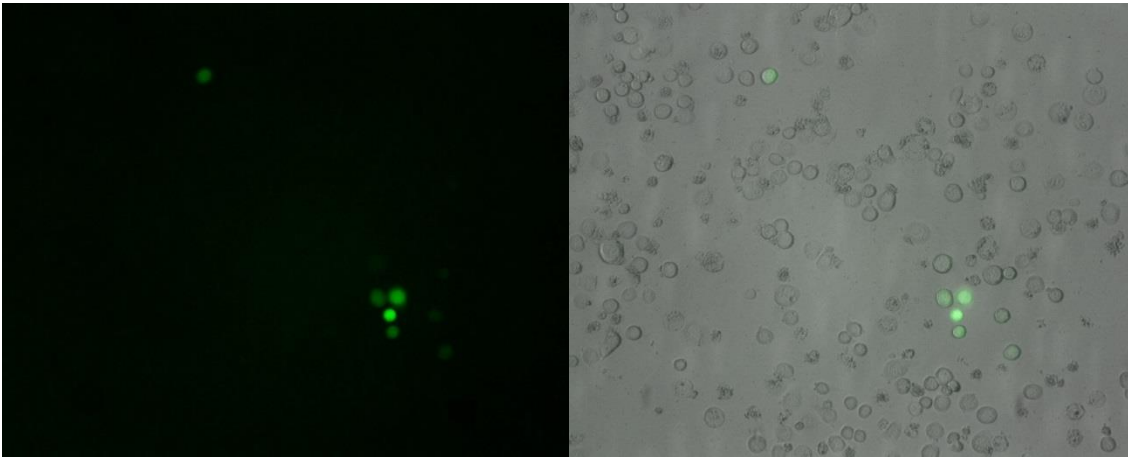


Figure 2-15 Successful transfections were identified by YFP expression levels

Successful transfections were monitored by the expression of YFP. Image was taken on a Nikon Eclipse TE2000-U microscope using the green filter. (A) Fluorescence microscope image showing YFP expression from a GSTCDK6 containing bacmid transfection. (B) Overlay of fluorescent image onto light microscope image shows the individual cells expressing YFP.

cyclins D1 and D3 showed that significant yields of stoichiometric complexes could be obtained (Figure 2-16). Further expression tests using the MultiBac™ system revealed that far lower volumes of virus were needed to cause complete proliferation arrest.

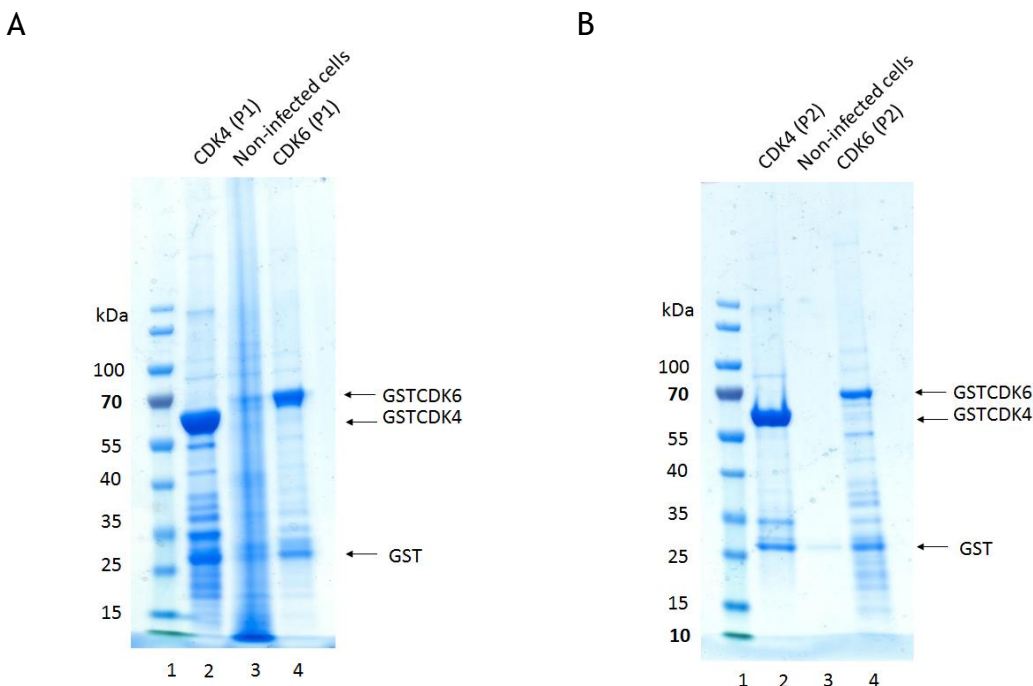


Figure 2-16 GSTCDK4 and GSTCDK6 expression from the MultiBac system

(A) SDS-PAGE of GST pull-downs performed on P1 and (B) P2 virus amplification cell pellets of GSTCDK4 and GSTCDK6 using the MultiBac™ system. (A) Lane 1, PageRuler protein ladder; Lane 2, GST pull-down of GSTCDK4 from P1 amplification; Lane 3, non-infected cells; Lane 4, GST pull-down of GSTCDK6 from P1 amplification. (B) Lane 1, PageRuler protein ladder; Lane 2, GST pull-down of GSTCDK4 from P2 amplification; Lane 3, non-infected cells; Lane 4, GST pull-down of GSTCDK6 from P2 amplification. Proteins were visualised by staining with InstantBlue.

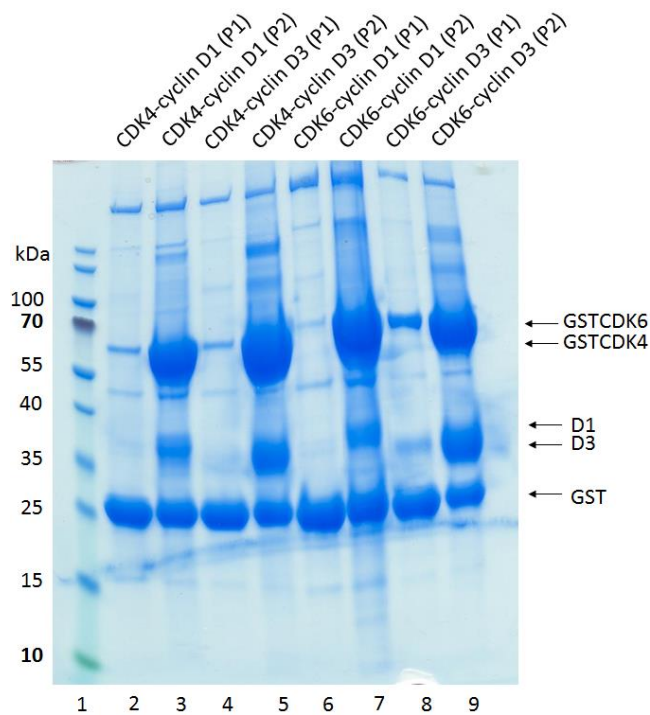


Figure 2-17 GSTCDK4 and GSTCDK6 co-expression with the D-type cyclins using the MultiBac™ system

Samples provided and SDS-PAGE performed by Dr Martyna Pastok (Postdoc, Endicott lab, NICR). GST pull-downs performed on the Sf9 cell pellets from 30 ml virus amplification steps. Lane 1, PageRuler protein ladder; Lane 2, CDK4-cyclin D1 (P1 virus); Lane 3 CDK4-cyclin D1 (P2 virus); Lane 4, CDK4-cyclin D3 (P1 virus); Lane 5, CDK4-cyclin D3 (P2 virus); Lane 6, CDK6-cyclin D1 (P1 virus); Lane 7, CDK6-cyclin D1 (P2 virus); Lane 8, CDK6-cyclin D3 (P1 virus); Lane 9 CDK6-cyclin D3 (P2 virus). Proteins were visualised by staining with InstantBlue.

Expression was optimal at 72 hours, as determined by when the maximum YFP levels were reached. Expression tests were repeated for the multigene CDK6-cyclin D3 expressing vector and showed good expression of both CDK6 and cyclin D3 (Figure 2-17).

However, expression tests of the variously truncated CDK4, CDK6, cyclin D1 and cyclin D3 constructs from viral amplification steps P1 and P2 showed no obvious bands consistent with overexpression of proteins of the expected molecular weights (Figure 2-18). Despite attempts to improve the stringency of the washing steps for the P2 virus pull-downs (Figure 2-18 B), high background contamination remained. It would appear that these transfections were not successful. Neither the expression tests nor the transfections have been repeated. Detecting low but useful levels of recombinant protein expression would be helped by improvements to the pull-down protocol washing steps to further reduce background.

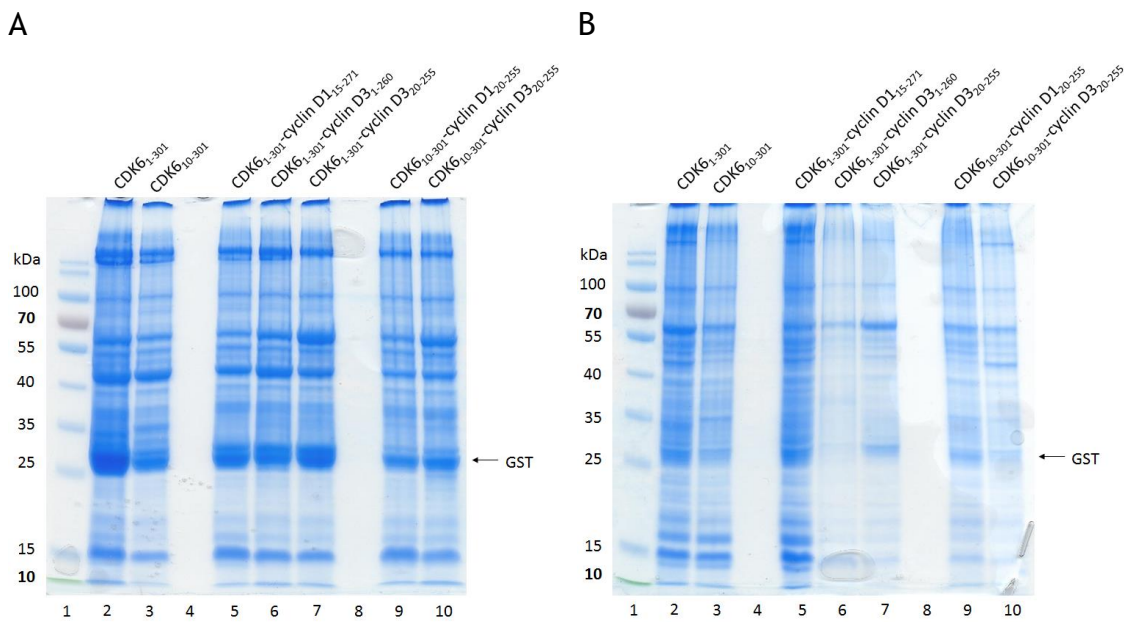


Figure 2-18 Truncated CDK6-cyclin D constructs proved challenging to express

(A) SDS-PAGE of truncated CDK6-cyclin D constructs from P1 viral amplification cell pellets. Lane 1, PageRuler protein ladder; Lane 2, CDK6₁₋₃₀₁; Lane 3, CDK6₁₀₋₃₀₁; Lane 4, blank; Lane 5, CDK6₁₋₃₀₁-cyclin D₁₁₅₋₂₇₁; Lane 6, CDK6₁₋₃₀₁-cyclin D₃₁₋₂₆₀; Lane 7, CDK6₁₋₃₀₁-cyclin D₃₂₀₋₂₅₅; Lane 8, blank; Lane 9, CDK6₁₀₋₃₀₁-cyclin D₁₂₀₋₂₅₅; Lane 10, CDK6₁₀₋₃₀₁-cyclin D₃₂₀₋₂₅₅. (B) SDS-PAGE of truncated CDK6-cyclin D constructs from P2 viral amplification cell pellets. Lane 1, PageRuler protein ladder; Lane 2, CDK6₁₋₃₀₁; Lane 3, CDK6₁₀₋₃₀₁; Lane 4, blank; Lane 5, CDK6₁₋₃₀₁-cyclin D₁₁₅₋₂₇₁; Lane 6, CDK6₁₋₃₀₁-cyclin D₃₁₋₂₆₀; Lane 7, CDK6₁₋₃₀₁-cyclin D₃₂₀₋₂₅₅; Lane 8, blank; Lane 9, CDK6₁₀₋₃₀₁-cyclin D₁₂₀₋₂₅₅; Lane 10, CDK6₁₀₋₃₀₁-cyclin D₃₂₀₋₂₅₅. Proteins were visualised by staining with InstantBlue.

Of the successful transfections, the expression of CDK4 and CDK6 and cyclin D containing complexes from a single virus greatly improved the efficiency and reliability of these complex expressions. Typical yields of these complexes were around 3-5 mg/L of Sf9 cells using just 400 µl/L of virus. An example of a purification of CDK6-cyclin D3 using the method described in Section 2.4.1 is presented in Figure 2-19.

Purification of CDK6 alone and in complex with cyclin D3 typically produced higher yields than those containing CDK4, with final yields nearer 4 mg/L of Sf9 cells compared to 3 mg/L respectively. In contrast, the expression levels are reversed for the cyclin D1-containing complexes whereby CDK6-cyclin D1 complexes also appeared less stable during SEC than the CDK4 containing counterparts.

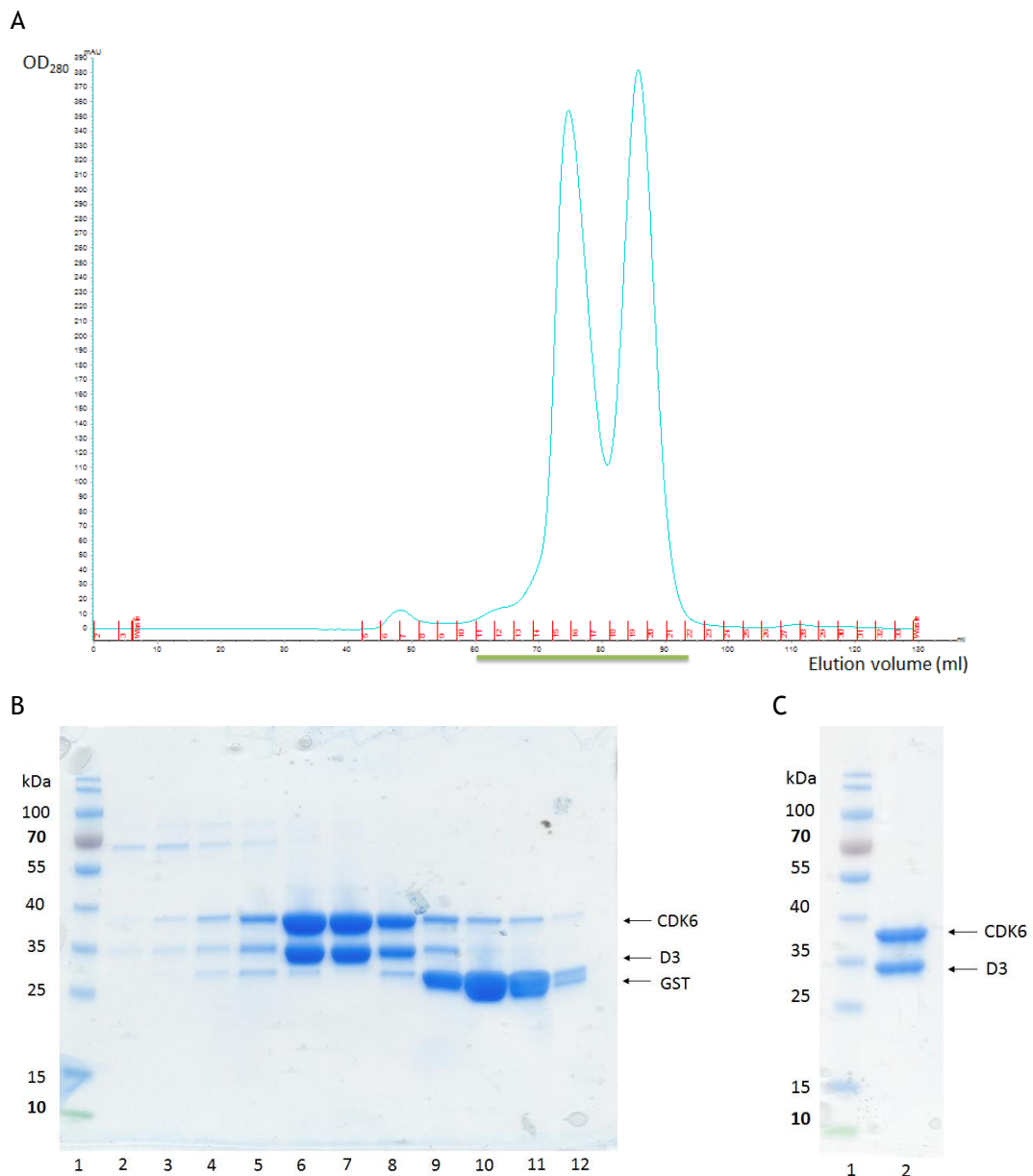


Figure 2-19 CDK6-cyclin D3 expression using the MultiBac™ system

Example of a CDK6-cyclin D3 co-purification from Sf9 cells expressed with the MultiBac™ system. (A) Chromatogram from a CDK6-cyclin D3 size-exclusion chromatography (SEC) purification step using a Superdex 200 16/60 column. Absorbance at 280 nm is plotted against elution volume in ml. (B) SDS-PAGE corresponding to peak fractions from the SEC purification. Lane 1, PageRuler protein ladder; Lanes 2-12 correspond to fractions 11-21 from the SEC run (green bar). (C) Final CDK6-cyclin D3 complex after GST removal. Lane 1, PageRuler protein ladder; Lane 2, CDK6-cyclin D3. Proteins were visualised by staining with InstantBlue.

2.6.2 Building larger complexes

A number of CDK4/6 binding partners, apart from cyclin D, can be stably expressed in *E. coli*. To investigate their interactions through biophysical or crystallographic methods, the expression products from *E. coli* and insect cells have to be combined. CDK4/6-Cdc37 and CDK4/6-INK mutant complexes were produced for crystallographic studies by

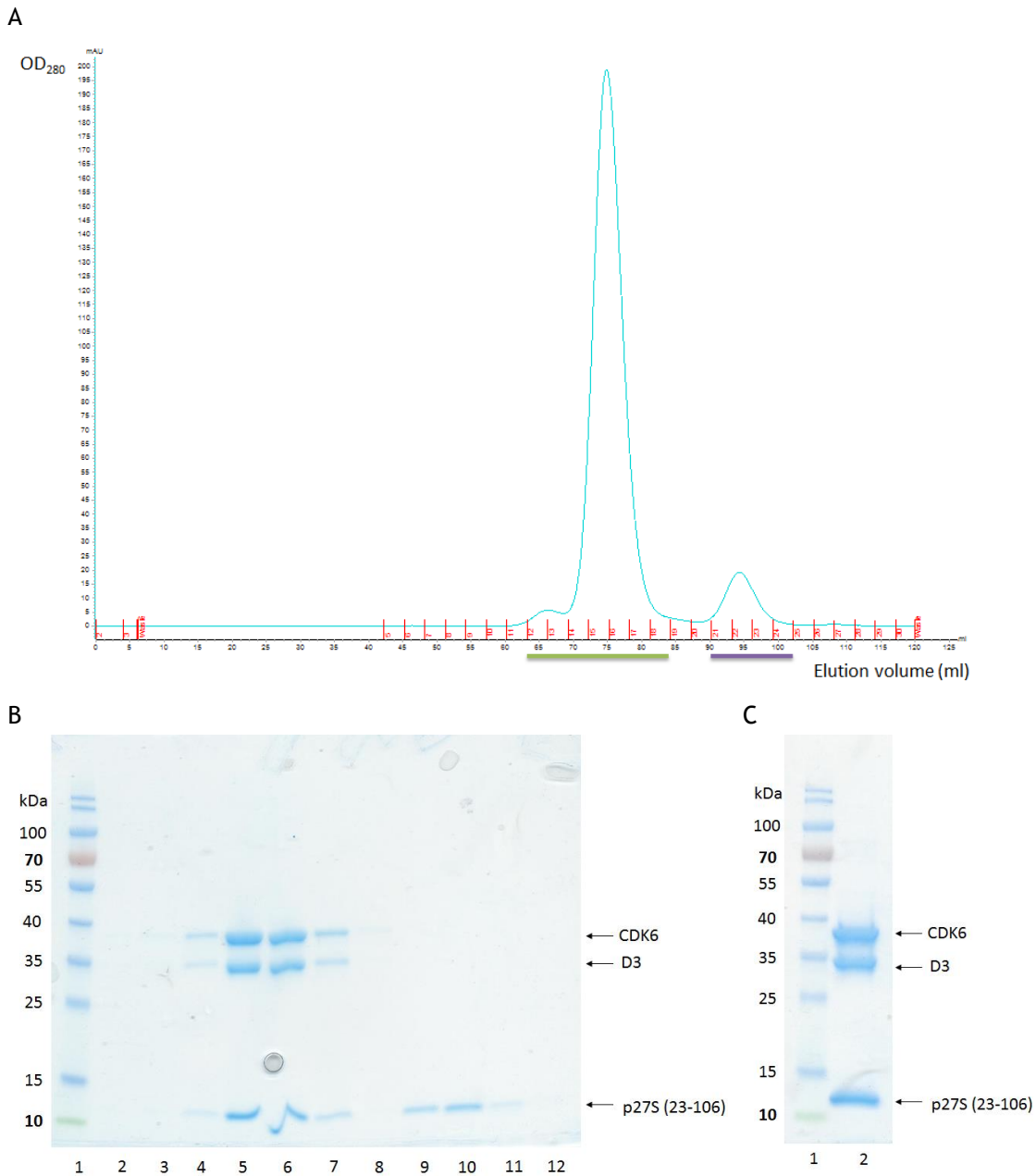


Figure 2-20 Formation of ternary CDK6-cyclin D3-p27S complexes

Ternary CDK6-cyclin D-p27KIP1 complexes were generated by mixing purified CDK6-cyclin D with a 2-fold molar excess of p27KIP1 and separating the ternary complex from excess p27KIP1 by size-exclusion chromatography (A) Chromatogram from a CDK6-cyclin D3-p27S size-exclusion chromatography (SEC) purification step using a Superdex 200 16/60 column. Absorbance at 280 nm is plotted against elution volume in ml. (B) SDS-PAGE corresponding to peak fractions from the SEC purification. Lane 1, PageRuler protein ladder; Lanes 2-8 correspond to fractions 12-18 (green bar); Lanes 9-12 correspond to fractions 21-24 (purple bar) from the SEC run (green bar). (C) Final CDK6-cyclin D3-p27S complex after concentrating. Lane 1, PageRuler protein ladder; Lane 2, CDK6-cyclin D3-p27S. Proteins were visualised by staining with InstantBlue.

individual expression and purification of each component before complex formation. Baculoviruses to co-express CDK4/6-Cdc37 were prepared by Dr Martyna Pastok (Postdoc, Endicott lab, NICR). However, they did not produce as high a yield of complex

as could be generated by expressing the proteins individually. The binding partner, being more abundantly and easily expressed in each case, was added in a 2-fold molar excess to the CDK and the mixture was then re-applied to a size exclusion column after incubation for 1 hour at 4 °C. The larger complex eluted earlier from the column.

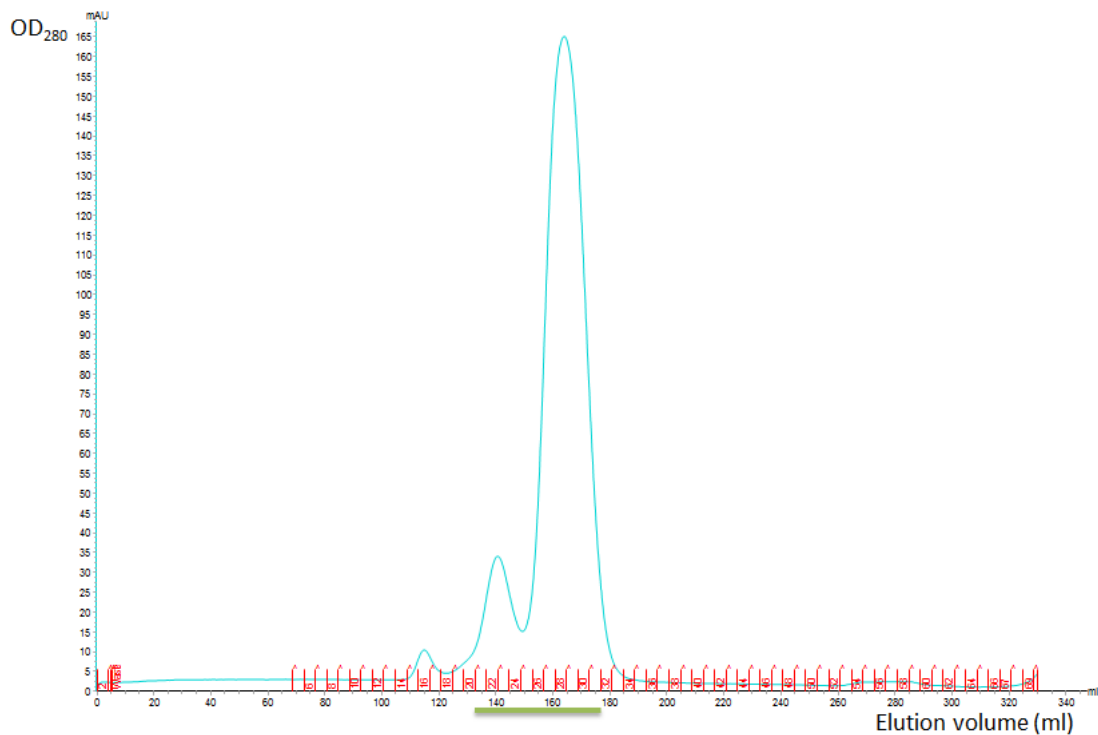
Co-expression of CDK4(6)-cyclin D complexes permitted the formation of larger ternary complexes containing the CKIs p21CIP1 and p27KIP1. As described above the CDK-cyclin D complexes and the p21CIP1 or p27KIP1 constructs were purified separately before being mixed and subsequently subjected to SEC. However, due to the poor stability of the CDK6-cyclin D1 complex on the SEC column, p27KIP1 was added immediately after CDK6-cyclin D1 elution from the glutathione resin. It was hoped that early addition of p27KIP1 would minimise the amount of cyclin D1 lost by dissociation during SEC thereby maximising the yield of the ternary complex. An example of stoichiometric CDK6-cyclin D3-p27S ternary complex formation is shown below in Figure 2-20.

Recently a selection of baculoviruses which allowed for the co-expression of ternary CDK-cyclin D-p27KIP1 complexes from a single virus were produced by Dr Martyna Pastok (Postdoc, Endicott lab, NICR). These viruses should improve the efficiency of ternary complex expression and purification. However, as the library was not yet comprehensive, complexes produced from these viruses were not used for the comparison of CDK4 and CDK6 containing ternary complexes in subsequent biophysical assays.

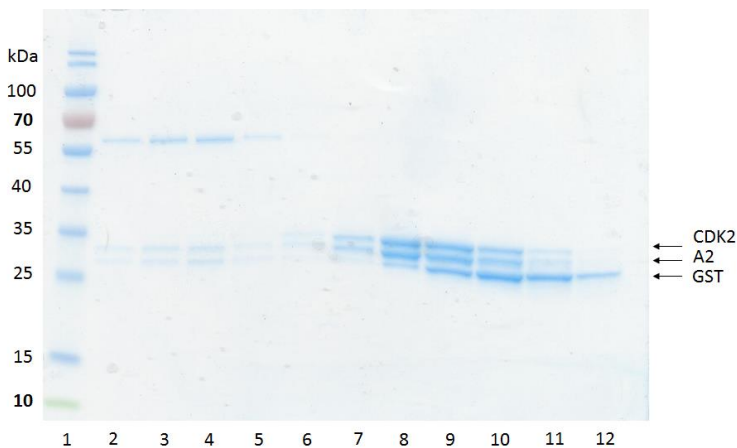
2.6.3 Purification of CDK2-cyclin A2

The expression and purification protocol to generate human CDK2-cyclin A2 was well established (Brown *et al.*, 1999b). CDK2 was co-expressed with *S. cerevisiae* CAK1 to yield phosphorylated CDK2 that can be subsequently activated by cyclin binding. Human cyclin A was expressed in *E. coli* but has limited solubility in solution when purified without a binding partner. Therefore, the *E. coli* lysates containing cyclin A and CDK2 were mixed post sonication to form the complex *in situ*. The CDK2-cyclin A2 complex was then subsequently purified exploiting the GST-tag on the CDK2. An example purification of phosphorylated CDK2-cyclin A2 is shown in Figure 2-21.

A



B



C

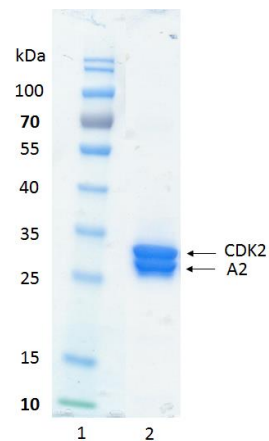


Figure 2-21 Purification of CDK2-cyclin A2. CDK2 is co-expressed with *S. cerevisiae* CAK1 to generate CDK2 phosphorylated on Thr160.

Example of a CDK2-cyclin A2 co-purification from *E. coli*. (A) Chromatogram from a CDK2-cyclin A2 size-exclusion chromatography (SEC) purification step using a Superdex 75 26/60 column. Absorbance at 280 nm is plotted against elution volume in ml. (B) SDS-PAGE corresponding to peak fractions from the SEC purification. Lane 1, PageRuler protein ladder; Lanes 2-12 correspond to fractions 21-31 from the SEC run (green bar). (C) Final CDK2-cyclin A2 complex after GST removal. Lane 1, PageRuler protein ladder; Lane 2, CDK2-cyclin A2. Proteins were visualised by staining with InstantBlue.

2.7 Quality control (QC) of protein samples

Protein expression using a combination of *E. coli* and insect cell expression systems have resulted in significant yields of a variety of protein species. These expression systems, particularly insect cells, are however capable of introducing a variety of posttranslational modifications, such as phosphorylation or methylation, to the expressed proteins. Post-translational modifications, such as phosphorylation, are used to modify the function of proteins. Identifying modifications on purified proteins is vital for fully understanding subsequent protein-protein interactions as they can greatly alter the structure and therefore interactions of a protein. Variation between protein purifications may result in significant differences in biophysical measurements leading to large errors or non-reproducible results. In addition, the host cells contain multiple proteases which can unwantedly cleave disordered regions. Levels of these harmful proteases are particularly high in stressed cells such as when they are harvested and lysed making it essential to keep them cold and to extract the recombinant protein from the lysate as soon as possible.

There are many techniques to assess the integrity of protein samples. Here SDS-PAGE stained with either InstantBlue or the more sensitive silver stain and Liquid Chromatography Mass Spectrometry (LC-MS) have been used to assess sample purity. LC-MS also allows for the identification of posttranslational modifications or the proteolytic cleavage of the protein. CDK4 has previously been shown to be partially phosphorylated (Takaki *et al.*, 2009) and so the phosphorylation status of these new CDK6 constructs needs to be confirmed. Alternative methods such as Circular dichroism (CD) and Multi-angle light scattering (MALS) can also be used to routinely check the quality of protein batches by determining the fold, oligomerization state and homogeneity of the sample. Kinase assays, such as the ADP-Glo assay, can be used as another marker of protein quality and phosphorylation state between batches by determining the activity of the CDKs. Finally, here Differential Scanning Fluorimetry (DSF) has also been used to perform a thermal melt buffer screen to optimise buffer conditions.

2.7.1 SDS-PAGE and silver staining to assess protein complexes for use in homogeneous time-resolved fluorescence assays

All expressed proteins were analysed by SDS-PAGE throughout purification and at the final stages before freezing. Figure 2-22 shows the purity of a selection of GSTCDK, GSTCDK-cyclin D and GSTCDK-cyclin-p27M complexes. Most importantly for their use in subsequent biophysical assays no contaminating GST band can be observed at *circa* 26 kDa and an inspection of the relative intensities of each band suggests good stoichiometric complex formation. Faint higher molecular weight bands, potentially relating to the presence of a chaperone, were often seen with CDK4 (lane 2) although this was not usually the case for CDK6. The difference in the amounts of co-purifying chaperone proteins likely relates to the differing stabilities of CDK4 and CDK6, with CDK4 being less stable and therefore more prone to association with chaperones.

2.7.2 Characterisation of CDK6-cyclin complexes by mass spectrometry

LC-MS analysis of CDK6-cyclin D3 and N-Avi p16INK4a was carried out by Dr Claire Jennings (Postdoc, Endicott lab, NICR). The CDK6-cyclin D3 complex was separated before injection into the mass spectrometer therefore no mass at the expected molecular complex weight of 69835.5 Da was observed (Figure 2-23). A mass of 37349.6

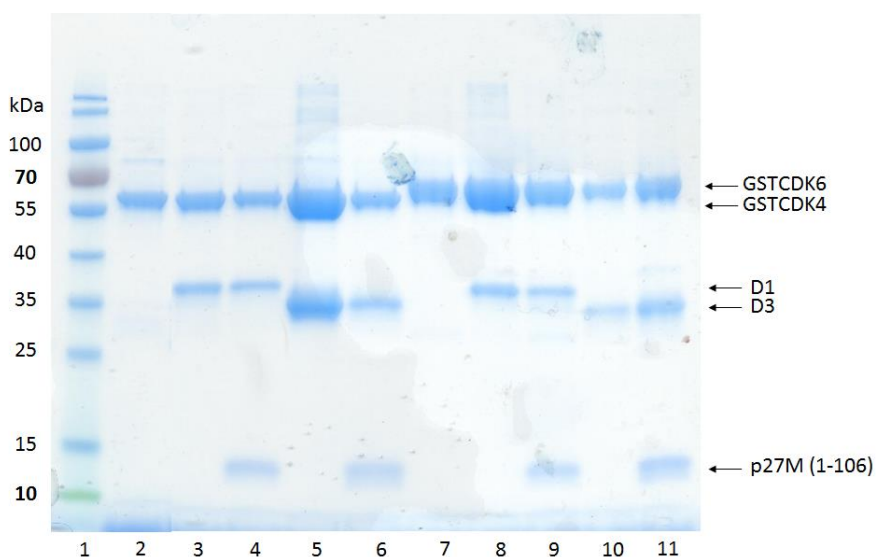


Figure 2-22 SDS-PAGE analysis of purified proteins

Purified proteins were examined by SDS-PAGE to check for contaminants, in particular GST. Lane 1, PageRuler protein ladder; Lane 2, GSTCDK4; Lane 3, GSTCDK4-cyclin D1; Lane 4, GSTCDK4-cyclin D1-p27M; Lane 5, GSTCDK4-cyclin D3; Lane 6, GSTCDK4-cyclin D3-p27M; Lane 7, GSTCDK6; Lane 8, GSTCDK6-cyclin D1; Lane 9, GSTCDK6-cyclin D1-p27M; Lane 10, GSTCDK6-cyclin D3; Lane 11, GSTCDK6-cyclin D3-p27M. Proteins were visualised by staining with InstantBlue.

Da was detected, 0.2 Da below the 37349.8 Da expected mass of CDK6 (Figure 2-23 A). In contrast to previous analysis of CDK4 expressed in Sf9 cells, that showed that *circa* 60% of CDK4 was mono-phosphorylated (Takaki *et al.*, 2009), no post-translational modifications were present on CDK6. It can be hypothesized that the difference in extent of phosphorylation between CDK4 and CDK6 may result from a number of factors. As CDK4 is less stable it may be more prone to non-specific phosphorylation, insect cell CAK1 may more efficiently recognise human CDK4 rather than CDK6 as a substrate, or alternatively phosphorylated CDK6 may be a better substrate for insect cell phosphatases.

A species with a mass of 32530.5 Da was also observed from this CDK6-cyclin D3 sample and is likely to derive from cyclin D3 which has an expected mass of 32503.7 Da (Figure 2-23 B). This observed mass is 26.8 Da higher than the expected mass suggesting that cyclin D3 may have undergone post-translational modification. Potential modifications

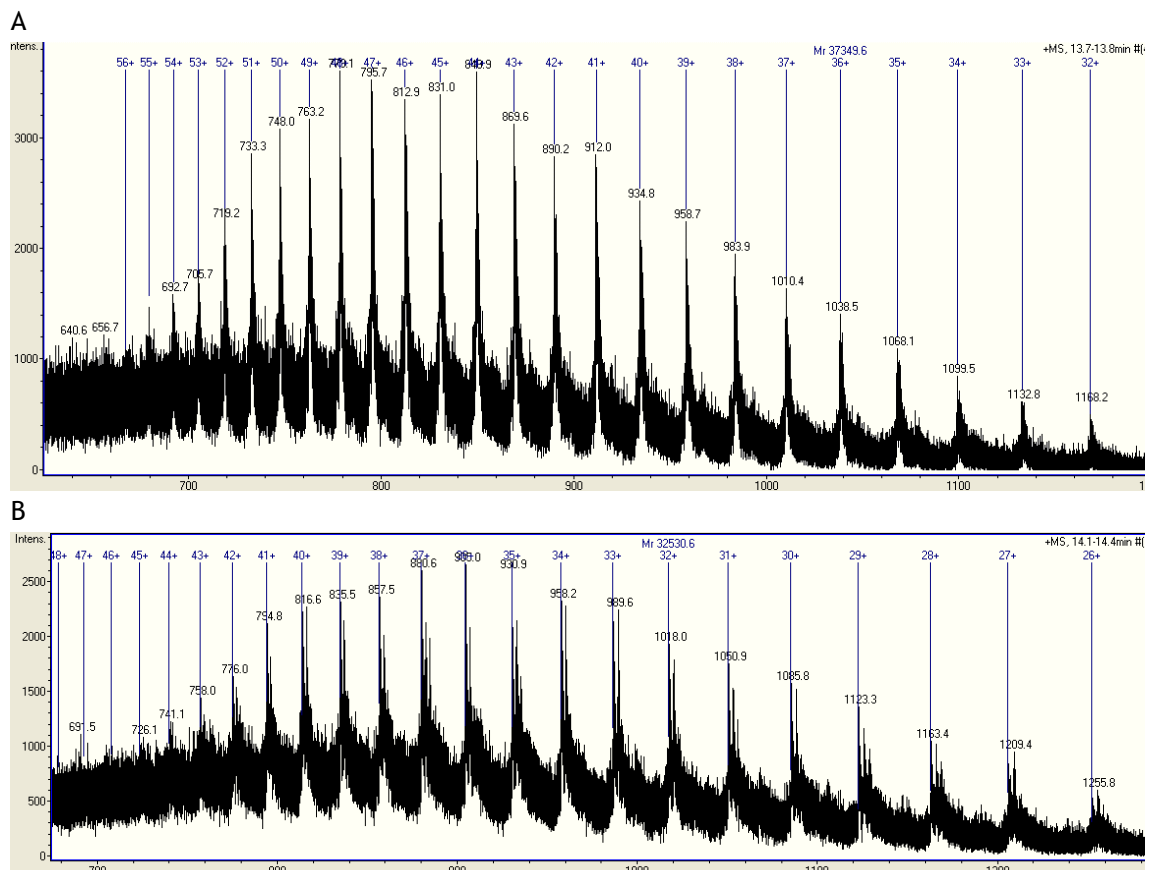


Figure 2-23 Analysis of CDK6-cyclin D3 by mass spectrometry.

Mass spectrometry of CDK6-cyclin D3 was performed and analysed by Dr Claire Jennings (Postdoc, Endicott lab, NICR) on samples provided. Analysis of CDK6-cyclin D3 reveals dominant mass species at 37349.6 Da corresponding to CDK6 (A) which was not post-translationally modified and 32530.5 Da corresponding to cyclin D3 (B).

presenting with a similar change in mass include formylation (+28.0 Da), ethylation (+28.1 Da) or similarly two methylations (2 x 14.0 Da).

Accurate quantitative assessment of phosphorylation levels can be difficult, particularly for sub-stoichiometric populations. The negatively-charged phosphates are susceptible to loss during ionisation and phosphate addition can be masked by concomitant losses. To account for these losses and to identify the phosphorylated population the results should have been compared to equivalent phosphatase treated samples to determine the true native state. Alternative methods for determining phosphorylation including phosphospecific antibodies, which specifically target the phosphorylated form of a protein, can also be used to identify phosphorylation either by western blot or used for the enrichment of phosphorylated samples for mass spectrometry (McLachlin and Chait, 2001). Although CDK6-cyclin D3 was examined for potential posttranslational modifications this was not done routinely for the CDKs or the proteins investigated due to limited access to mass spectrometry equipment.

2.7.3 Thermal melt buffer screen to optimise buffer conditions

DSF, described in Section 2.2.2, can be used to assess buffer conditions by measuring the stability of a protein in a range of different buffers. CDK6 and CDK6-cyclin D3 were tested against a standard set of 96 buffer conditions (Appendix A). The melting temperatures (T_m) derived from the corresponding melting curves were used to identify potential buffer components that would aid protein stability during purification.

CDK6 showed improvements in stability in sodium cacodylate and sodium phosphate buffers (Table 2-3) as well as a clear preference for 150 mM NaCl. Examples of some melting curves for CDK6 are shown in Figure 2-24. Perhaps unsurprisingly, due to both samples containing the same protein, CDK6-cyclin D3 also showed improvements in stability in 150 mM NaCl and sodium cacodylate and sodium phosphate buffers. However, unlike monomeric CDK6, a range of other buffers including Tris, HEPES and MOPS also gave increases in T_m (Table 2-4). The melting curves of CDK6-cyclin D3 (Figure 2-25) often present with two distinct unfolding events caused by the different stabilities of each protein component. In these cases the melting temperature (T_m) was determined as the midpoint from the final maximum fluorescent signal. The largest

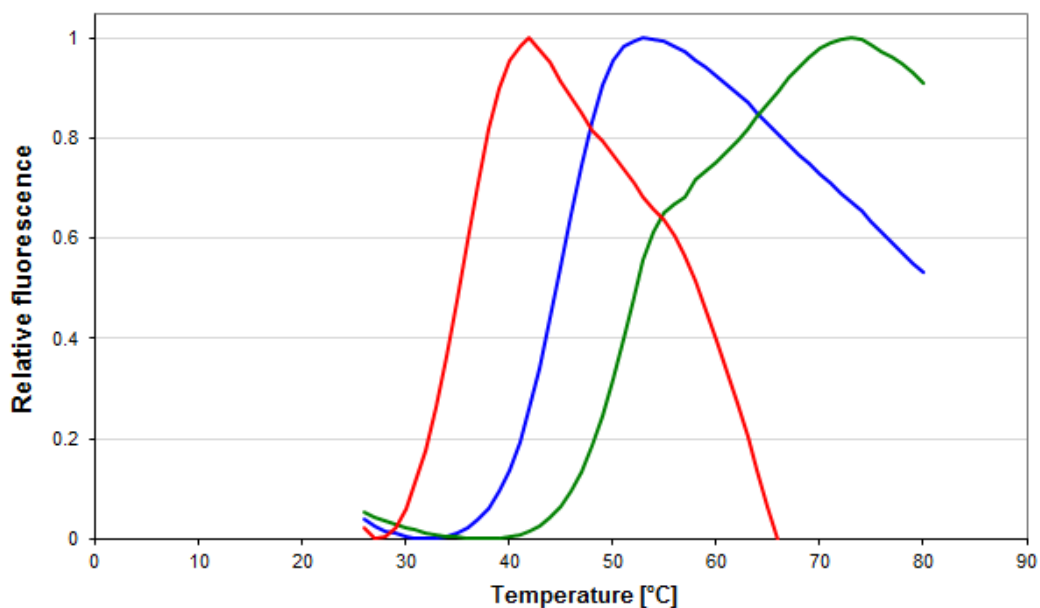


Figure 2-24 Differential scanning fluorimetry to assess CDK6 stability in different buffers

A thermal melt screen was performed in a predesigned buffer screen to assess buffer conditions which could help to improve protein stability. Melting curves showing improved and weakened thermostability of CDK6 compared to water. The melting curve of CDK6 in water is shown in blue ($T_m = 44.59\text{ }^\circ\text{C}$), improved stability of CDK6 in Na Phosphate pH 7.0, 150mM NaCl, 10% Glycerol in green ($T_m = 52.48\text{ }^\circ\text{C}$) and reduced stability of CDK6 in Bis-Tris pH 6.0, 2 mM CHAPS, 150 mM NaCl in red ($T_m = 35.04\text{ }^\circ\text{C}$). Graphs plotted in Excel.

difference between these two unfolding events was the pH ranges within which each was found to be most stable. CDK6 had a very narrow range between pH 6.5 and 7.0, perhaps caused by an overwhelming binding preference for the cacodylate and

Buffer Description	T_m ($^\circ\text{C}$)	ΔT_m	R squared
Na Cacodylate pH 6.5, 150mM NaCl, 10% Glycerol	52.84	8.25	0.9989
Na Phosphate pH 7.0, 150mM NaCl, 10% Glycerol	52.48	7.89	0.9903
Na Cacodylate pH 6.5, 150mM NaCl, 0.5M TMAO	52.36	7.77	0.9996
Na Cacodylate pH 6.5, 150 mM NaCl, 200mM Sucrose	51.79	7.2	0.9954
Na Phosphate pH 7.0, 150mM NaCl, 0.5M TMAO	50.99	6.4	0.9813
Na Cacodylate pH 6.5, 150mM NH_4SO_4	50.17	5.58	0.9987
Na Phosphate pH 7.0, 150 mM NaCl, 200mM Sucrose	50.15	5.56	0.9982
Na Cacodylate pH 6.5, 500mM NaCl	50.13	5.54	0.9992
150mM NaCl, 0.5M TMAO	50.11	5.52	0.9999
Tris pH 8.0, 150mM NaCl, 0.5M TMAO	49.82	5.23	0.9993

Table 2-3 Buffer compositions that stabilised CDK6.

The compositions of the 10 buffer conditions from the buffer screen that gave the largest gain in thermal stability for CDK6 alone.

phosphate species, while CDK6-cyclin D3 had a larger stable pH range of between 6.5 and 8.0.

The presence of cyclin D3 gave a significant improvement to the stability of CDK6 increasing the T_m by 6.3 °C from 44.6 °C to 50.9 °C in water (compare the blue curves in Figure 2-24 and Figure 2-25) highlighting the importance of binding partners for the stability of some proteins. This difference in stability was also reflected in the range of melting temperatures measured for monomeric CDK6 in different buffers that ranged from 34.62 °C to 52.84 °C, a range of 18.22 °C. In the presence of cyclin D3 a much narrower spread of 13.7 °C was observed (42.56 °C to 56.26 °C). Interestingly, for both monomeric CDK6 and in complex with cyclin D3 the lowest T_m was measured in the buffer containing Bis-Tris pH 6.0 and 150mM $MgCl_2$ suggesting either or both reagents have a particularly destabilising effect on the complex. Other commonly used stabilisation agents such as 10% glycerol and 0.5 M TMAO were also found to stabilise CDK6 and the CDK6-cyclin D3 complex.

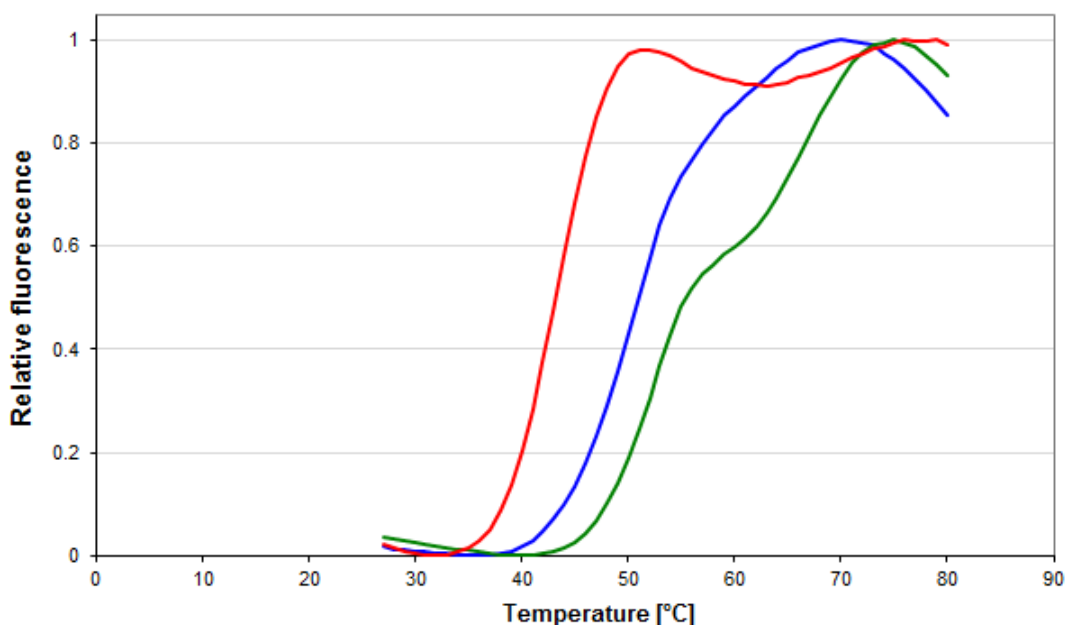


Figure 2-25 CDK6-cyclin D3 has two distinct melting events

The thermal melt screen was repeated to assess buffer conditions which could help to improve stability of the CDK6-cyclin D3 complex. Melting curves for CDK6-cyclin D3 in water is shown in blue ($T_m = 50.92$ °C), CDK6-cyclin D3 in 500 mM NaCl which gave the largest gain in thermal stability is shown in green ($T_m = 56.26$ °C) and CDK6-cyclin D3 in MES pH 6.5, 2 mM CHAPS and 150 mM NaCl which decreased thermal stability is shown in red. ($T_m = 42.95$ °C).

Buffer Description	T _m (°C)	ΔT _m	R square
500mM NaCl	56.26	5.34	0.9888
150mM NaCl, 0.5M TMAO	54.96	4.04	0.9917
Tris pH 8.0, 150mM NaCl, 0.5M TMAO	54.67	3.75	0.9845
Na Cacodylate pH 6.5, 150mM NaCl, 0.5M TMAO	54.46	3.54	0.9889
Na Phosphate pH 7.0, 150mM NaCl, 0.5M TMAO	54.21	3.29	0.9809
Tris pH 8.0, 150mM KCl	53.54	2.62	0.9808
150mM MgCl ₂	53.37	2.45	0.9739
HEPES pH 7.5, 150mM NaCl, 0.5M TMAO	53.17	2.25	0.9996
150mM NaCl	52.85	1.93	0.9927
MOPS pH 7.0, 150mM NaCl, 0.5M TMAO	52.84	1.92	0.9951

Table 2-4 Buffer compositions that stabilised CDK6-cyclin D3

The compositions of the 10 buffer conditions from the buffer screen that gave the largest gain in thermal stability for the CDK6-cyclin D3 complex.

The range of buffer conditions that improve both CDK6 and CDK6-cyclin D3 stability made it difficult to produce an overall set of buffer conditions which would ideally stabilise CDK6 and related complexes. The preferred sodium chloride concentration of 150 mM was already used for the purification buffer and the range of preferred pH values for the CDK6-cyclin D3 complex of 6.5 to 8.0 also includes pH 7.5, the buffer pH.

It was decided that the multiple small polar tetrahedral molecules, such as TMAO, phosphate, cacodylate and NH₄SO₄, that were seen to stabilise both samples should not be added to the purification buffer. High concentrations of these components, particularly phosphates and sulfates, are known to adversely affect protein crystallisation as they readily crystallise and are a distraction in crystallisation trials. Cacodylate is also harmful. 10% glycerol, which was observed to stabilise CDK6, was adopted into the purification buffer for a short time however it caused problems during purification and would have negatively affected subsequent biophysical assays and so was not continued. However, it would be appropriate to consider adding it as a component to the buffer to stabilise CDK6 prior to crystallisation trials. The final mHBS buffer conditions used for all subsequent purifications is shown in Appendix A.

2.8 Discussion

Great improvements have been made to improve the yield and quality of various CDK4 and CDK6 complexes. The use of the MultiBac™ system allowed for the rapid and relatively straight forward production of baculoviruses which can co-express CDK4 and CDK6 alone and in complex with cyclin D1 and cyclin D3 from a single virus. Co-expression from a single virus improved the yields and reliability of expression of these complex. The modular nature of the MultiBac™ system was used to produce a variety of CDK6 and cyclin D truncates based on the removal of predicted flexible regions at the N and C-termini to create more stable constructs for subsequent biophysical, biochemical and crystallographic studies. Unfortunately, expression tests suggest that the initial virus production was unsuccessful.

The quality of CDK6 complex purifications were greatly improved by the replacement of the thrombin cleavage site with a 3C protease alternative. DSF analysis of these complexes revealed a range of potential stabilising conditions for which the mHBS buffer, described in Appendix A, does best to satisfy the range of complexes produced. Further improvements to protein stability suggested by the assay using phosphate buffers or the addition of 10% glycerol were decided against because of potential effects on subsequent crystallisation trials and biophysical assays.

Alternative complexes to those expressed using the MultiBac™ can be produced by mixing the proteins after purification from *E. coli* and insect cell expression systems. The identity and integrity of some of these species have been examined by SDS-PAGE and mass spectrometry. The routine use of additional validation techniques on protein samples would have greatly improved the extent and confidence of the results from subsequent biophysical experiments. Mass spectrometry analysis of the CDK6-cyclin D3 complex has revealed that CDK6 was unmodified while cyclin D3 appears to have undergone a posttranslational modification corresponding to either formylation, ethylation or two methylations. Further analysis by a technique such as (LC)/MS/MS is required to identify the location and exact identity of this modification. A full list of proteins prepared for the subsequent biophysical, biochemical and structural studies described in the following chapters is provided in Appendix A.

Chapter 3. The CDK-Cdc37 interaction

3.1 Introduction

3.1.1 Hsp90 regulates a large proportion of the protein kinome

Hsp90 is one of the most abundant proteins in the cell making up around 1% of the total soluble protein (Stepanova *et al.*, 1996; Jorgensen *et al.*, 2002; Ghaemmaghami *et al.*, 2003). Hsp90 is responsible for the activation of a wide range of clients making up around 7% of transcription factors, 30% of ubiquitin ligases and 60% of kinases from multiple families across the kinome (Figure 3-1) (Taipale *et al.*, 2012). The scaffold protein Cdc37 is required for recognition and recruitment of kinases to Hsp90 (Cutforth and Rubin, 1994; Gerber *et al.*, 1995). Cdc37 was first identified in mammals as a subunit of Hsp90 where it was also found to bind tightly to CDK4, less efficiently to CDK6 and CDK7 but not to its homologues CDK1, CDK2, CDK3 and CDK5 (Dai *et al.*, 1996). Binding of the CDK to its cognate cyclin and to Cdc37 was also shown to be mutually exclusive (Dai *et al.*, 1996; Stepanova *et al.*, 1996; Lamphere *et al.*, 1997). Both Cdc37 and cyclin

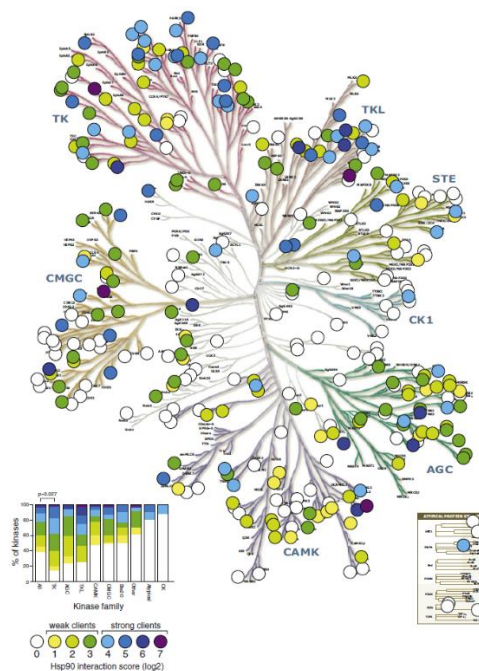


Figure 3-1 Hsp90 dependency varies considerably across the kinome

Figure taken from (Taipale *et al.*, 2012). Kinases throughout multiple families are clients of Hsp90. Clients show a wide range of affinities even within closely related families. The dependency on Hsp90 for most members of the human kinome are shown by coloured dots representing the interaction strength to the chaperone. Kinases are graded from white = no interaction, to yellow = weak client, to purple = strong client.

D1 are expressed at the same time in proliferating cells, where around 30% of CDK4 from extracts was found to be associated with Cdc37, but CDK6 association in comparison was very weak (Stepanova *et al.*, 1996). The relative distribution of these complexes within cells at a given time will arise from a combination of affinity, protein concentrations and location.

3.1.2 Kinase sequence features that identify a Cdc37 client

Despite the knowledge of this interaction for some time, until recently, the molecular details of the interaction between Cdc37 and its client kinases were lacking. In particular, the flexible nature of Cdc37 has hindered crystallisation attempts. However, studies to characterise client kinase and Cdc37 mutants that affected the interaction identified several important sequence features (Figure 3-2). The GXGXXG motif towards the N-terminus of many kinases, which is required for stabilising ATP binding, has been linked to the interaction of Cdc37 with CDK4 (green sequence in Figure 3-2). Mutation of Gly15 and Gly18 to alanine prevented the interaction (Zhao *et al.*, 2004), although the isolated motif was not found to interact on its own (Terasawa *et al.*, 2006). However, many kinases including non-clients possess this sequence making it inconclusive as to where the distinction between client and non-client arises.

Another important factor is that phosphorylation of the activation loop appears to reduce the interaction with Cdc37 ((Terasawa *et al.*, 2006), Figure 3-2, marked). Several studies have shown that this loop, that connects the α C-helix and β 4 strand in the N lobe (Figure 3-2, gold), is required for the interaction of ErbB2 (Xu *et al.*, 2005) and CDK4 (Terasawa *et al.*, 2006) with Cdc37. C-terminal truncations back to Pro69 on CDK4 located in the middle of the α C-helix to β 4 loop (Zhao *et al.*, 2004) and chimeras, made by splicing the N-lobe of CDK4 onto the C-lobe of CDK2 at the same location were able to bind Cdc37 (Terasawa *et al.*, 2006). Taken together, these results highlight the importance of the kinase N-terminal lobe for the Cdc37 interaction. Alternative chimeras of other kinases have produced more intermediate results and suggest that the integrity of both lobes are needed for the interaction. Inserting a loop between α D and α E (red in Figure 3-2) can turn a non-client into a client (Taipale *et al.*, 2012).

A

10	20	30	40	50	60
MATSRYEPVA	EIGV GAYG TV	YKARDPHSGH	FV ALKSV RVP	NGGGGGGGLP	ISTVREVALL
70	80	90	100	110	120
RRLE A FEHPN	VVR L MDVCAT	SRTDREIKVT	LVFEHVDQDL	RTYLD KAPPP	GI PAETIKDL
130	140	150	160	170	180
MRQFLRGLDF	LHANCIVHRD	LKPENILVTS	GGTVKLADFG	LARIYSYQMA	LTPVVVTLWY
190	200	210	220	230	240
RAPEVLLQST	YATPVD M SV	GCIFAEMFRR	KPLFCGNSEA	DQLGKIFDLI	GLPPEDDWPR
250	260	270	280	290	300
DVSLPRGAFF	PRGP RPVQSV	VPEMEESGAQ	LLLEMLTFNP	HKRISAFRAL	QHSYLHKDEG

NPE

B

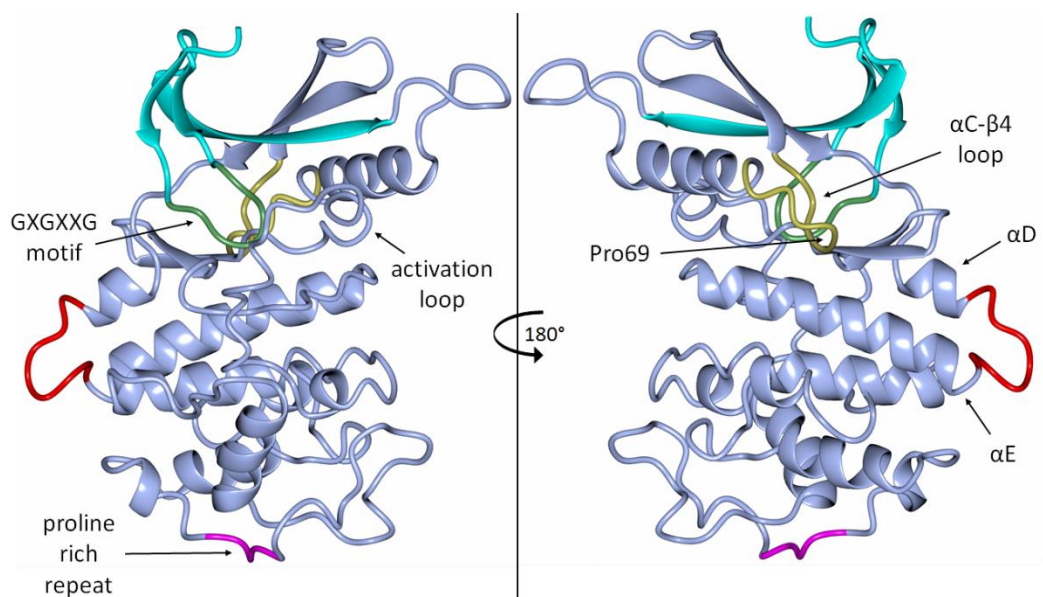


Figure 3-2 Regions of CDK4 identified for Cdc37 interactions

Multiple regions of CDK4 have been reported to interact with Cdc37 and Hsp90. These regions lie mainly on extended loops and have been highlighted on the CDK4 sequence (A) and a ribbon model of CDK4 (B). The GXGXXG motif is green, the α C- β 4 loop is gold (Proline 69 lies at the tip of this loop), the loop between α D and α E is red and the proline rich repeat in purple. Also, marked with arrows are the activation loop and the α D and α E helices. (B) prepared using CCP4MG (McNicholas *et al.*, 2011).

The α C- β 4 loop has also been linked with the interaction of kinases to Hsp90 and again it appears to recognise surface features rather than the specific amino acid sequence. Clients display an overall positive or neutral charge around this loop (Xu *et al.*, 2005; Citri *et al.*, 2006; Gould *et al.*, 2009). However, these features cannot be the sole driver of the interaction, as they would predict that CDK2 would be a client and ERK5 a non-client (Citri *et al.*, 2006) which is not the case.

A conserved PXXP motif in the C-terminal tail of protein kinase C (PKC) has also been linked to Hsp90 binding to this alternative client kinase (Gould *et al.*, 2009). Mutations in this region reduce Hsp90 binding, however, the interaction is not believed to be directly to the sequence itself but to the surrounding regions which are affected by mutations on this helix (Gould *et al.*, 2009). This study identified these regions as the Gly-rich P-loop, the β 1-3 strands, the α C- β 4 loop and the α D-helix. Deuterium exchange experiments on v-Src confirmed the involvement of these sequences in a second kinase client (Boczek *et al.*, 2015). This study found that the degree of exposure of Hsp90 binding sites determines client strength and hypothesized that displacement and partial unfolding were significant changes accompanying client kinase binding to Hsp90.

As no specific sequence can be identified, an alternative hypothesis is that it is the propensity of the kinase to unfold between the N- and C-lobes that makes them a Hsp90 client (Verba *et al.*, 2016). This characteristic is reflected in the observation that replacing the flexible seven glycine repeat loop sequence of CDK4 with the more rigid sequence present in CDK6, weakens the ability of CDK4 to bind Cdc37/Hsp90 (Verba *et al.*, 2016). As a group, Hsp90 clients are also less well expressed and fewer structures of them have been determined suggesting they have a propensity for disorder (Taipale *et al.*, 2012). For example, a modest difference has been found in the number of glycine residues present in the α C helix of client kinases as compared to non-clients (Taipale *et al.*, 2012). Recent NMR studies of the Cdc37 N-terminal domain suggest that it acts not just as an adapter of the client fold but also to selectively recruit kinases to the Cdc37-Hsp90 system (Keramisanou *et al.*, 2016). The interaction of the N-terminus of Cdc37 is hypothesized to challenge the conformational stability of clients by locally unfolding them, and as such acts as an allosteric activator. Non-clients are proposed to interact through the formation of far weaker and therefore transient interactions.

3.1.3 Cdc37 sequence features that identify a client kinase

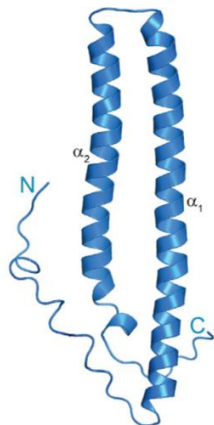
The structure of Cdc37 has been divided into three regions, the N-terminal region (Figure 3-3 B), the mid-section and the C-terminal lobe (Figure 3-3 D). The N-terminal region (residues 1-126) is responsible for the interaction with clients and when the first 30 amino acids are removed, no interaction is observed (Shao *et al.*, 2003). Further dissection of the sequence requirements shows that mutations to residues 2, 3, 4 or 7

dramatically inhibit kinase binding whereas similar mutations on residues 5, 6 or 8 have no effect (Figure 3-3 A in red). Interestingly, mutations at Trp7 also affected the ability of Cdc37 to interact with Hsp90 (Shao *et al.*, 2003; Vaughan *et al.*, 2006). Recent NMR studies have shown that the N-terminal domain of Cdc37 consists of a two helical bundle, that forms a U shape, connected by a hydrophobic core that generates an extended hydrophobic patch where kinase clients can bind ((Keramisanou *et al.*, 2016), Figure 3-3 B). Earlier studies had predicted an extended coiled coil structure for this region (Roe *et al.*, 2004).

A

10	20	30	40	50	60
MVDYSVWDHI	EVSDDEDETH	PNIDTASLFR	WRHQARVERM	EQFQKEKEEL	DRGCRECKRK
70	80	90	100	110	120
VAECQRKLKE	LEVAEGGKAE	LERLQAEAQQ	LRKEERSWEQ	KLEEMRKEKEK	SMPWNVDTLS
130	140	150	160	170	180
KDGFSSM ^{VN}	TKPEKTEED ^S	E ^V REQKHKT	FVEKYEQIK	HFGMLRRWDD	SQKYLSDNVH
190	200	210	220	230	240
LVCEETANYL	VIWCIDLEVE	EKCALMEQVA	HQTIVMQFIL	ELAKSLKVDP	RACFRQFFTK
250	260	270	280	290	300
IKTADRQYME	GFNDELEAFK	ERVRGRAKLR	IEKAMKEYEE	EERKKRLGPG	GLDPVEVYES
310	320	330	340	350	360
LPEELQKCFD	VKDVQMLQDA	ISKMDPTDAK	YHMQRCDISG	LWVPNSKASE	AKEGEEAGPG
370					
DPLLEAVPKT	GDEKDVSV				

B



C



D

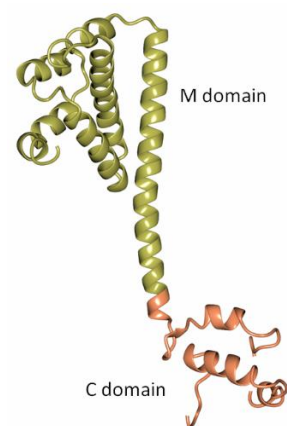


Figure 3-3 Cdc37 structural features

Cdc37 consists of three main domains. (A) The amino acid sequence of Cdc37. Key residues identified for interactions with client kinases and Hsp90 are highlighted in red. The sequence is colour coded by domain as described in (C). (B) Image taken from (Keramisanou *et al.*, 2016). The structure of the N-terminal region of Cdc37 solved by NMR, displayed in ribbon form, forms a U-shaped two helical bundle. (C) Diagram of the domain structure of Cdc37. The residues that mark the boundaries of these regions are displayed above the diagram. (D) The crystal structure of part of the mid and C-terminal domains of Cdc37 displayed in ribbon form (PDB: 1US7). Throughout the N-terminal domain is blue, the middle domain yellow and the C-terminal domain orange.

The structure of Cdc37 (residues 148-315) bound to the N-terminal region of Hsp90 has been determined and the interaction between Cdc37 to Hsp90 measured to have a dissociation constant of 1.46 μM (Figure 3-4 B). The mid-section of Cdc37 (residues 128-282), in particular Ser127-Gly163, is responsible for the interaction with Hsp90 ((Shao *et al.*, 2003), Figure 3-4 A). The Cdc37 C-terminal lobe is entirely helical consisting of a bundle of six helices (residues 148-245) and three more helices between residues 292-347 (Figure 3-4 A). These two bundles are connected by a long helix (residues 246-286).

In the Cdc37-Hsp90 complex structure (Figure 3-4), helices 2, 3 and 5 of the six helical bundle of Cdc37 pack against Hsp90 residues 100-121. Cdc37 Arg167 protrudes into the ATP binding pocket of Hsp90 to displace a nucleophilic water from a key Glu33 residue and so prevent ATPase activity, although ATP and inhibitors can still bind. This interaction prevents the 'lid' section of Hsp90 from closing over ATP. In addition, the Cdc37 dimer sits between the two Hsp90 molecules in the asymmetric unit and holds them open to together prevent Hsp90 activity (Roe *et al.*, 2004).

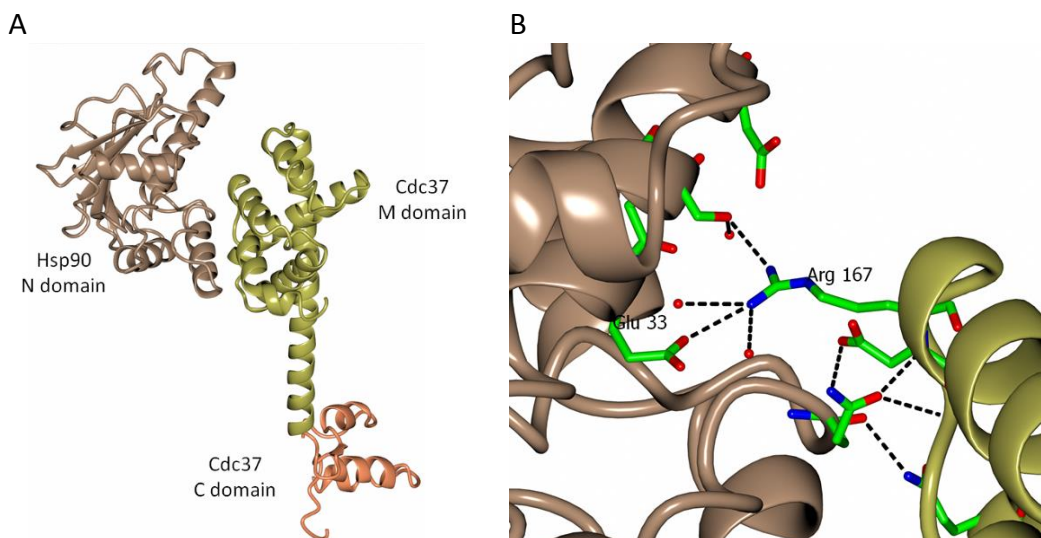


Figure 3-4 Hsp90 interactions with CDC37

The crystal structure of the Mid and C-terminal domain of Cdc37 have been determined bound to the N-terminal domain of Hsp90 where it blocks Hsp90 kinase activity. (A) The N-terminal domain of Hsp90 (brown) interacts with the bundle of six helices in the Mid terminal domain of Cdc37 (yellow). A helical bundle towards the C-terminal domain of Cdc37 is in orange. (B) Cdc37 binding blocks Hsp90 kinase activity through the interaction of Arg167 on Cdc37 with Glu33 of Hsp90 and the surrounding water network. Proteins are displayed in ribbon form with key interacting residues displayed as cylinders and colour coded by atom type. Hydrogen bonds are shown by dashed lines. Images created from PDB: 1US7 using CCP4MG (McNicholas *et al.*, 2011).

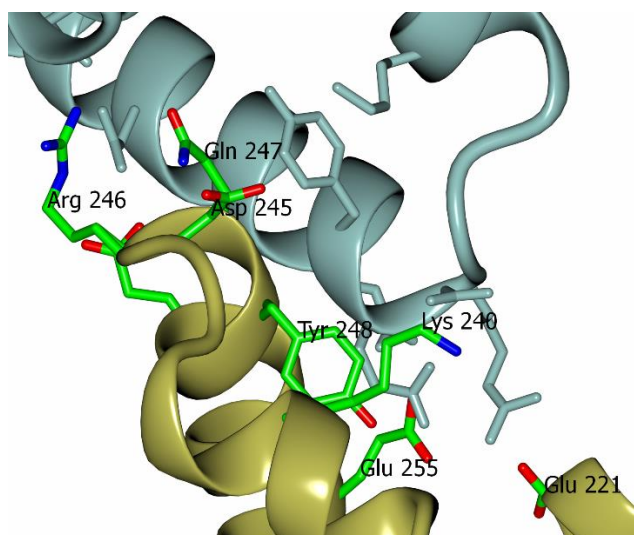


Figure 3-5 Cdc37 dimer interactions in crystal structure

Cdc37 forms dimer like interactions with a symmetry related Cdc37 molecule in the crystal structure. (PDB: 1US7). This interaction involves a range of close packing and hydrogen bonding interactions. Image created using CCP4MG (McNicholas *et al.*, 2011).

The crystal structure of the Hsp90-Cdc37 complex also revealed a Cdc37 homodimer structure mediated by the crystal lattice packing (Figure 3-5). There are close packing interactions between Gln247 and Tyr248, reinforced by ionic interactions between Lys240 and Asp245, from the symmetry-related Cdc37 molecule. Asp294 from each Cdc37 and hydrogen bonds between Arg246 and Glu250 with Glu221 and Glu255 from each symmetry pair complete the interface (Roe *et al.*, 2004). There has been some debate as to whether Cdc37 exists as a dimer or a monomer as both forms have been identified (Stepanova *et al.*, 1996; Vaughan *et al.*, 2006). However, the comparatively weak dimerisation interaction compared to that of the Cdc37-client kinase interaction suggests a Cdc37 dimer is unlikely to exist in cells (Krukenberg *et al.*, 2011).

3.1.4 Molecular details of the interaction of Cdc37-Hsp90 with a client kinase

The large and flexible nature of the Cdc37-Hsp90 complex has made it refractory to crystallographic studies. However, two single particle cryo-EM structures have been determined of CDK4-Cdc37-Hsp90. The first structure was to 19 Å resolution and revealed a dimer of Hsp90 bound to one Cdc37 and one CDK4 molecule creating a structure that was around 140-150 Å long and 85-95 Å wide (Figure 3-6), (Vaughan *et al.*, 2006)). This complex stoichiometry of 2:1:1 was confirmed by mass spectrometric analysis. The N-termini of Hsp90 formed a more rounded end to which the density for

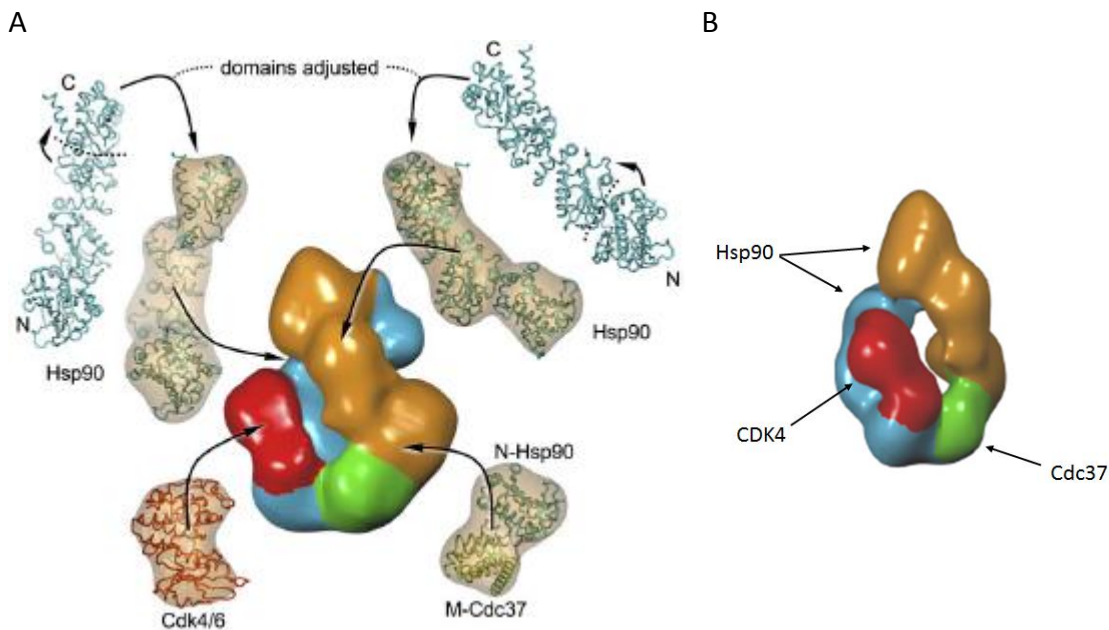


Figure 3-6 The CDK4-Cdc37-Hsp90 complex

Images adapted from (Vaughan *et al.*, 2006). The structure of the CDK4-Cdc37-Hsp90 complex was initially solved by cryo-EM to a resolution to 19 Å. (A) The EM envelope with previously determined crystal structure fragments overlaid. The complex formed a 1:1:2 structure with one CDK4 (red) one Cdc37 (green) and a dimer of Hsp90 (blue and orange). CDK4 was modelled onto the N-terminal domain of one of the Hsp90 molecules. (B) The CDK4-Cdc37-Hsp90 EM envelope from an alternative angle shows an oval channel through the middle of the Hsp90 dimer.

CDK4 and the middle domain of Cdc37 was assigned on opposing Hsp90 molecules (Figure 3-6). The binding of the kinase to one edge of the Hsp90 dimer and not through middle of the complex was deemed unusual. The N-termini of Cdc37 however could not be built although it was assumed they were buried in the Hsp90 N-terminal lobe as they were resistant to dephosphorylation at Ser13 from *in vitro* experiments. The specific interactions between CDK4 and Cdc37 could not be elaborated (Vaughan *et al.*, 2006).

More recently a far higher resolution map ranging in resolution between 3.5-6 Å has been determined for the same complex ((Verba *et al.*, 2016), Figure 3-7). The higher resolution structure has allowed for more specific interactions between subunits to be identified. While both structures have a similar overall shape and position the C-terminal lobe of CDK4 on the M-domain of Hsp90 they differ substantially in the position of the CDK4 N-terminal lobe (Figure 3-7). The residues that usually form β 4- β 5 and residues 87-94 of CDK4 are threaded through the Hsp90 dimer to separate the kinase N and C-terminal lobes. This observation is in direct conflict with the previous low resolution structure which clearly shows an empty channel running through the Hsp90 dimer ((Vaughan *et al.*, 2006), Figure 3-6 B).

The structure of Cdc37 also differs considerably between the two structures. Only the M-domain of Cdc37 was modelled into the lower resolution envelope while for the higher resolution structure Cdc37 was observed to be split round Hsp90 with the Cdc37 M/C-domain (residues 148-260) separated from the N-terminal domain (residues 1-147) by a β -sheet constructed from residues 120-129. This β -sheet interacts with the M domain of Hsp90 which contrasts with the earlier structure where Cdc37 interacts entirely with the N-terminal domain of Hsp90 (Verba *et al.*, 2016). Unfortunately, the N-terminal lobe of CDK4 was too poorly resolved to accurately interpret the molecular interactions with the adjacent M/C-domains of Cdc37, in keeping with the high disorder predicted for this region in both structures. The Cdc37 N-terminal sequence was found to adopt an unusual coiled coil motif, the base of which, encoded by residues 20-24, interacts with the CDK4 C-lobe by mimicking the interactions of the now displaced α C- β 4 loop (Figure 3-7 F). Cdc37 and Hsp90 are bound together by an extensive array of ionic interactions which would explain the sensitivity of the complex to salt (Verba *et al.*, 2016).

While certain aspects of these two structures appear conflicting the differences may simply arise from the two structures being in alternative Hsp90 conformations. The lower resolution Vaughan *et al.* structure is described as being in the 'open' conformation while the Verba *et al.* structure in the 'closed'. Capturing the complex at different phases of the chaperone cycle, a potential side-effect of the purification procedures or the image selection criteria during analysis, may account for the altered locations of CDK4 and Cdc37. Additional differences, observed for Cdc37, mostly arise due to the higher resolution of the Verba *et al.* structure which allowed further detail to be observed and aided in more accurate domain fitting.

Casein kinase 2 (CK2) phosphorylates Cdc37 exclusively on Ser13 (Liu and Landgraf, 2015). Ser13 is phosphorylated in the higher resolution EM structure and forms salt bridges with Arg36 and His33 of Cdc37, and Lys406 of Hsp90, that help to stabilise the complex (Verba *et al.*, 2016). The functional consequences of phosphorylation on this residue are hotly debated. Some experiments have suggested that Ser13 phosphorylation is essential for client binding and that mutants that cannot be phosphorylated no longer bind to kinases, although they are still capable of binding to Hsp90 (Miyata and Nishida, 2004). Protein phosphatase 5 (PP5) dephosphorylates Cdc37

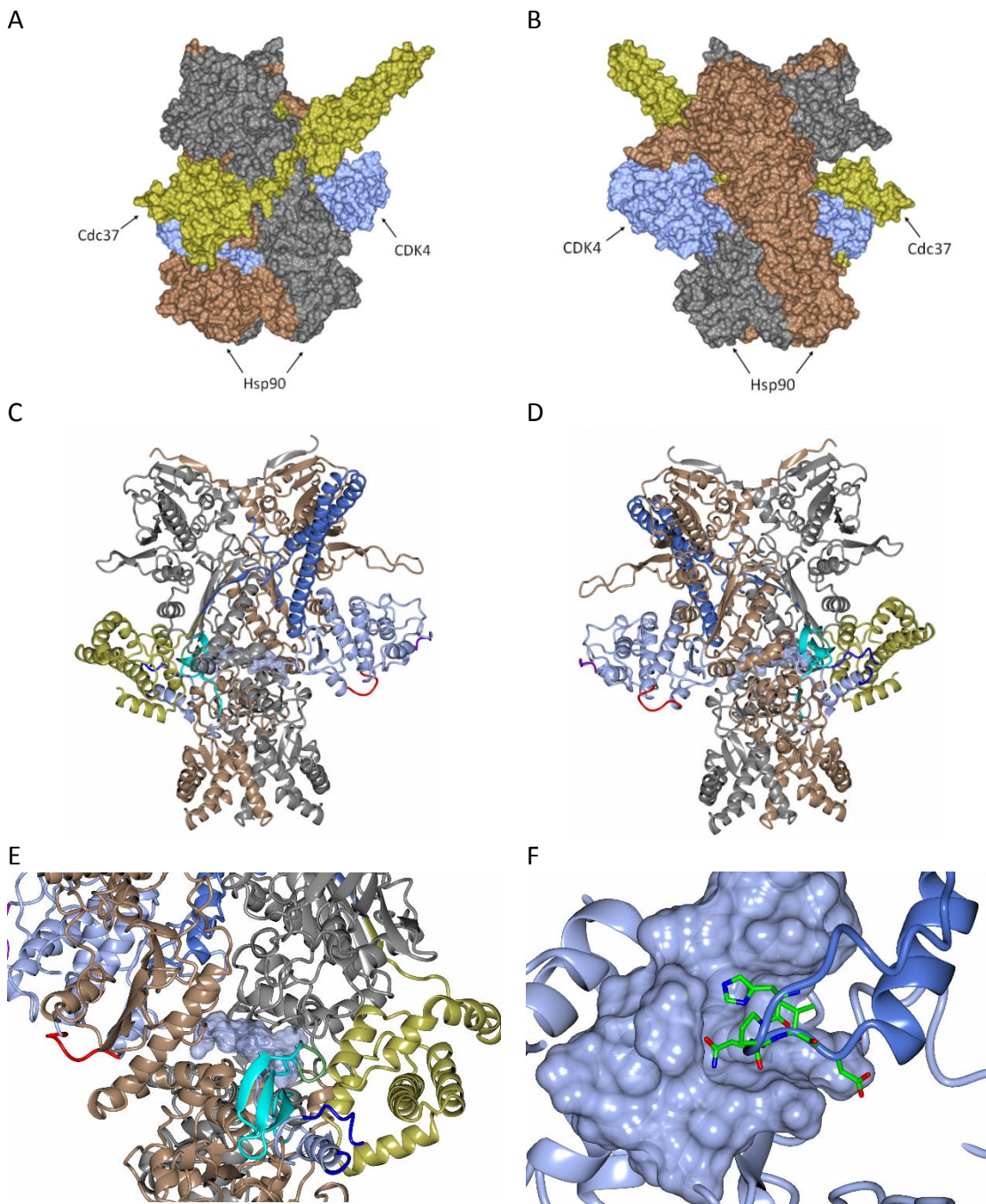


Figure 3-7 High resolution cryo-EM structure of CDK4-Cdc37-Hsp90

The recent higher resolution cryo-EM structure of CDK4-Cdc37-Hsp90 (PDB: 5FWL) reveals more information of key interactions and shows considerable distortion and separation of the CDK4 N and C-lobes through the Hsp90 dimer. (A) and (B) surface view of the CDK4 (blue) Cdc37 (yellow) and Hsp90 (grey and brown) complex from two angles 180 ° apart. (C) and (D) ribbon form view of the CDK4-Cdc37-Hsp90 complex. Hsp90 in brown and grey, CDK4 in ice blue with potential Cdc37 and Hsp90 interacting regions described in Figure 3-2 coloured accordingly. Cdc37 is coloured per Figure 3-3. (E) Close up of the extended $\beta 5$ sheet of CDK4 drawn through the middle of the Hsp90 dimer. Colours are consistent with (C) and (D). The extended $\beta 5$ sheet of CDK4 (residues 87-94) are shown in surface form. (F) Interaction of the base of the Cdc37 N-terminal domain coiled-coil (dark blue) mimics the interactions of the displaced CDK4 αC - $\beta 4$ loop with the C-lobe of CDK4 (ice blue, displayed as a surface). Interacting residues of Cdc37 are displayed as cylinders and coloured by atom type. Figures created using CCP4MG (McNicholas *et al.*, 2011).

and has been shown to be required for kinase release suggesting its importance in complex stability (Oberoi *et al.*, 2016). The general consensus is that Ser13 phosphorylation, or a phosphomimetic, increases kinase-Cdc37-Hsp90 complex recognition and formation but does not directly affect Cdc37 affinity for the kinase (Pearl, 2005; Boczek *et al.*, 2015; Keramisanou *et al.*, 2016). Client kinase release from Cdc37 can also be triggered by phosphorylation of Cdc37 on Tyr298 by the Src family kinase YES (Xu *et al.*, 2012).

CK2 also phosphorylates Hsp90 on Ser226 and Ser255 (Olesen *et al.*, 2015). One study suggested that phosphorylation by CK2 primes the Hsp90 complex for dissociation as it weakens the complex in the presence of ADP but not ATP (Olesen *et al.*, 2015). Other phosphorylation events play alternative roles in complex regulation including phosphorylation of Hsp90 Tyr197 which dissociates Cdc37 from Hsp90 immune complexes, and phosphorylation of Tyr313 that stimulates association with Aha1 (Xu *et al.*, 2012). As mentioned above, Tyr298 phosphorylation by YES triggers Cdc37 client kinase release, while phosphorylation of Hsp90 on Tyr627, also by YES dissociates CDK4. The latter modification also dissociates Aha1 and PP5 from Hsp90 (Oberoi *et al.*, 2016).

Interestingly, both Vaughan *et al.* and Verba *et al.* reported that CDK4-Cdc37-Hsp90 complex formation *in vitro* is inefficient, and in both instances the complex was purified directly from insect cells. This observation suggests a requirement for some form of modification or cooperation with a chaperone *in vivo* (Verba *et al.*, 2016). However, the presence of the co-chaperone Hsp70 has been shown to have no influence on the activity of Hsp90 (Boczek *et al.*, 2015). It should be noted that Cdc37 purified from recombinant *E. coli* is non-phosphorylated (Liu and Landgraf, 2015), whereas Cdc37 expressed in insect or mammalian cells is predominantly phosphorylated (Vaughan *et al.*, 2006; Liu and Landgraf, 2015). The extent to which phosphorylation and the presence of accessory proteins contribute to client kinase-Cdc37-Hsp90 complex formation awaits the reconstitution of the pathway using purified components.

Despite these structural insights, the question as to what Hsp90 actually does to the client is unclear. One hypothesis is that Hsp90 acts in a regulatory mechanism to assist in rearrangement of kinases so that they can be phosphorylated and activated. Hsp90 would prevent client kinases from being dephosphorylated and therefore would help to

maintain an active pool ready for a rapid response (Pearl, 2005; Pearl and Prodromou, 2006). An alternative hypothesis is that Hsp90 may assist in complex formation by binding to unstable kinases in the cytoplasm before they associate with a partner protein and are transported to the nucleus. An example would be Hsp90 binding to CDK4 before it associates with cyclin D (Dai *et al.*, 1996; Stepanova *et al.*, 1996). However, not all kinase clients of Hsp90 require a binding partner for activation (Pearl and Prodromou, 2006).

The most recent hypothesis, proposed subsequent to the determination of the higher resolution CDK4-Cdc37-Hsp90 structure, is that like most chaperone systems, Hsp90 may provide a more favourable transition pathway to the active state through an unfolded state (Verba *et al.*, 2016). This mechanism of activation would accommodate diverse kinase sequences and would also allow the addition of posttranslational modifications. Extensive rearrangements to the kinase fold would be possible so that clients could be more easily tuned to changes in environmental conditions at the protein level rather than relying on transcription to modulate activity (Pearl and Prodromou, 2006). CDK4 and CDK6 provide an excellent model system with which to study the mechanism by which kinases exit the Hsp90 chaperone system due to the availability of multiple widely characterised binding partners including the CKIs and D-type cyclins.

3.2 Biophysical methods to measure protein-protein interactions

Many biophysical and biochemical techniques have been developed to measure protein-protein interactions. Straightforward methods such as simple pull-downs, that use an attached affinity tag to identify interacting partners, or size exclusion chromatography, which can separate complexes from individual components based on their size and shape are semi-quantitative at best and can fail to detect biologically relevant, low affinity ($K_d > 1 \mu\text{M}$) interactions. In this project, surface plasmon resonance (SPR), isothermal titration calorimetry (ITC), microscale thermophoresis (MST) and fluorescence-based methods (homogenous time-resolved fluorescence (HTRF)) have been used to gain a greater understanding of the interactions between CDK4 and CDK6 and the Cdc37-Hsp90 chaperone system. Each of these methods are described in more detail below. These techniques can yield quantitative details about a molecular interaction, but measure different parameters and have different advantages and

disadvantages. Some protein reagents used in biophysical assays were obtained from Dr Martyna Pastok (Postdoc, Endicott lab, NICR) and have been noted in the appropriate figure legends.

3.2.1 Homogenous Time Resolved Fluorescence (HTRF)

Homogenous time resolved fluorescence (HTRF) is ideal for measuring protein-protein or protein-peptide interactions and is, theoretically at least, the most sensitive analytical technique ((Mathis, 1993), Figure 3-8). The fluorescent signal measured in HTRF is dependent on the distance and orientation of two fluorophores to each other based on Förster's theory of non-radiative energy transfer (Förster, 1948). The Förster's resonance energy transfer (FRET) signal is a short-range energy transfer, the efficiency of which drops off rapidly by $1/d^6$, where d is the distance between fluorophores (Mathis, 1993). To this end the rare earth metal cryptates and allophycocyanin fluorophore pairs have been developed to optimise the range of energy transfer to up to 90 Å (Bazin *et al.*, 2001), which is roughly the distance between a protein pair and an attached labelled antibody. As well as direct binding measurements, HTRF can be used to determine the enzymatic or inhibition kinetics of a reaction (Jia *et al.*, 2006).

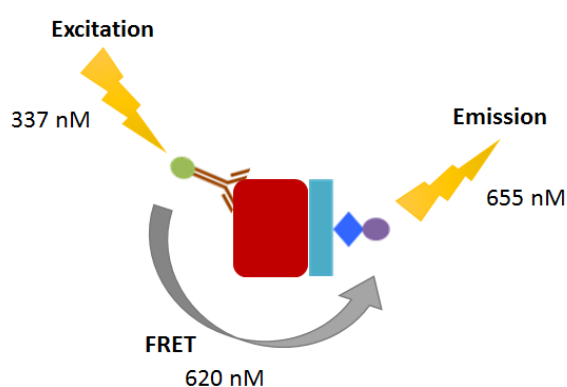


Figure 3-8 Schematic of an HTRF experiment

Homogenous time-resolved fluorescence occurs through a non-radiative energy transfer, FRET. Rare earth metal (green) labelled antibodies recognise a target protein (red) which is interacting with a binding partner (light blue). The binding partner is in turn tagged by streptavidin (dark blue) with a dye molecule (purple) attached. Upon excitation of the rare-earth metal, at 337 nM, a FRET energy transfer, at 620 nM, is established to excite the nearby dye molecule which fluoresces at 655 nM. The efficiency of the FRET signal is dependent on the rare-earth metal and dye molecule being brought close in space by the protein interaction.

The use of cryptates around the metal ion improves the excitation wavelength while cross-linking of the allophycocyanins has produced the dye XL665 which possesses greatly increased stability and quantum yields than its predecessors (Bazin *et al.*, 2001). The distance, timescale and wavelengths of the fluorophores can be adjusted by varying the chelating groups around the metal ion or the dye. Most importantly for HTRF it is vital that the donor and acceptor pair emit at different wavelengths so that their contribution to the emission signal can be distinguished. Rare earth metal cryptate donors, such as Eu^{3+} cryptates, have a long-lived fluorescent half-life and therefore give rise to a long-lived acceptor fluorescent signal (Mathis, 1993). This is important for the clear distinction of the fluorescent signal obtained from complex formation from the contributions of unbound fluorophores. Unbound fluorophores which are just near in space to the excited donor would otherwise lead to high background fluorescence and therefore poor sensitivity (Bazin *et al.*, 2001).

The emission from unbound fluorophores decays much more rapidly than their bound counterparts. The inclusion of a 10-100 μs delay between excitation and the emission measurement allows the short lived emission signal to be removed and allows real time correction of the signal (Mathis, 1999). Further correction to the signal can be applied by taking the ratio of acceptor signal emission to donor metal ion emission. This has the effect of removing any background absorbance effects of the media so that the final ratio obtained should relate entirely to that of the biological interaction (Mathis, 1995).

To determine how tightly the CDKs bound to their binding partners, GST-tagged CDK which binds a Terbium (Tb)-labelled anti-GST antibody (Life Technologies) were both held at fixed concentrations while the Avi-tagged binding partner and streptavidin labelled dye (SAXL665) (Cisbio) were titrated against them (Figure 3-9). Competent binding partners will form a complex thereby bringing the two tags into close proximity. Excitement of the terbium with light at a wavelength of 337 nm results in emission of a Förster resonance energy transfer signal at 620 nm which in turn excites the dye molecule. After a short pause of 60 μs , 300 measurements of the emission signal at 655 nm are taken over a 340 μs period and integrated. From this titration series a binding curve can be plotted of the 655/620 ratio from which a dissociation constant (K_d), the concentration at which half the CDK molecules are bound, for the interaction can be determined.



Figure 3-9 The HTRF assay format for determining CDK interactions with Cdc37.

To measure the interaction of CDK4 and CDK6 with Cdc37 GST-tagged CDK6(4) (orange/red) is incubated with biotinylated Cdc37 (light blue) to form the GSTCDK6-Cdc37 complex. The complex is then incubated with the Tb labelled anti-GST antibody (green/brown) and streptavidin tagged XL665 dye (dark blue/purple). The resulting Tb and XL665 labelled complex should produce a FRET signal resulting in a measurable emission signal upon excitation.

The GST affinity tag was initially chosen for this assay as CDK4 and CDK6, as well as many other proteins of interest, were already expressed with a GST tag using well established protocols that produced high yields of soluble protein. The assay was therefore quick to establish and was readily adaptable for the exploration of multiple interactions. Each of the GST tagged constructs were linked with a 3C protease cleavage site (amino acid sequence LEVLFQGP) which provides some flexibility for antibody binding and hopefully minimises the effect of the antibody presence on the interaction being measured. GST had also previously been successfully used by other members of the lab for alternative HTRF assays which provided the starting point for assay development and the Tb-labelled anti-GST antibody. Due to the expense of labelled antibodies an anti-GST antibody was chosen to allow the exploration of the largest number of targets without having to order multiple labelled antibodies or extensive re-cloning.

A major caveat of GST is that it forms a dimer in solution which can be hard to separate from target proteins, leaving contamination which can affect the signal, and could also lead to artificially enhanced interactions through target proteins being brought together by GST dimerization. Alternatively, the large size of GST may negatively influence protein-protein interactions through steric effects. Dimerization of GST may give rise to aberrant fluorophore signals caused by either multiple antibodies binding to the GST dimer or multiple dye molecules being excited by one antibody which has been brought near in space by GST dimerization. Unfortunately, it is not known whether the antibody binds to only one GST molecule or the GST dimer. The potential for multiple combinations of binding partners and fluorophores could give rise to non-linear binding

responses whereby the binding of the first may hinder or enhance the addition of the second. K_d values determined by the HTRF assay may be affected by these processes and have therefore been described as apparent affinity (K_{d-app}) under these conditions. The hill equation from binding curves analysis was closely monitored to determine whether interactions were cooperative or non-cooperative. While most interactions were non-cooperative, suggesting GST dimerization may not ubiquitously affect measurements, several interactions measured showed some degree of cooperative binding and are described further in the main text. Data did not fit reanalysis for two site binding, therefore, these effects may instead be caused by the aggregation of certain proteins or from limitations in analysis due to incomplete binding curves.

The assay format is highly adaptable and the interaction with many different CDK binding partners can be measured by repositioning the Avi-tag onto alternative proteins. For example, the Avi-tag was moved from Cdc37 to Hsp90 to allow the interaction strength between the CDKs and Hsp90, via Cdc37, to be measured (Figure 3-10). The GST-tag has also been added to other proteins, such as CDK2, to measure comparative interactions. Alternative donor and acceptor fluorophores, such as Europium or GFP, as well as antibodies which bind to different affinity tags, such as the FLAG tag, are also available but have not been explored in this work. This variability allows fine-tuning of the acceptor and emission spectra for different wavelengths and the distances between the fluorophores. Repositioning of the tags onto either end of each binding partner may also help to improve the signal, depending on the nature of the interaction, by bringing

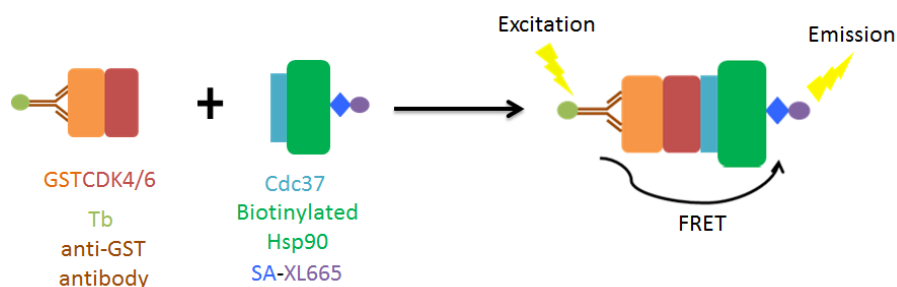


Figure 3-10 The Avi-tag can be repositioned to measure alternative interactions

The assay can be adapted to measure interactions with alternative binding partners such as Hsp90. GST-tagged CDK6 (orange/red) is incubated with biotinylated Cdc37-Hsp90 complex (light blue/green) to form the GSTCDK6-Cdc37-Hsp90 complex. The complex is then incubated with the Tb labelled anti-GST antibody (green/brown) and streptavidin tagged XL665 dye (dark blue/purple). The resulting Tb and XL665 labelled complex should produce a FRET signal resulting in a measurable emission signal upon excitation.

the fluorophores closer together. For the subsequent experiments CDKs N-terminally tagged with GST (GSTCDK) and Avi-tagged binding partners in conjunction with the streptavidin labelled XL665 dye have been used throughout.

3.2.2 Surface plasmon resonance

Surface plasmon resonance (SPR) was first used as a technique to measure the interactions of biomolecules in 1983 by measuring the binding of antibodies to one side of a gold metal surface (Liedberg *et al.*, 1983). The first commercial instrument however was not available until 1990 whereby the gold surfaces had been adapted with a range of carboxymethylated dextran, streptavidin, chelated nickel and hydrophobic surfaces to allow a range of proteins to be bound to it and their interactions with binding partners measured (McDonnell, 2001). SPR can be a label-free technique which allows proteins in solution (termed the analyte) to bind to an immobilised protein (termed the ligand or bait) on the gold surface, the interaction of which can be observed in real time. Because the interaction is observed in real time both the kinetics of the interaction (the on and off rates) as well as the binding at equilibrium can be measured, so that a dissociation constant can be determined knowing either the kinetic or thermodynamic parameters of the interaction.

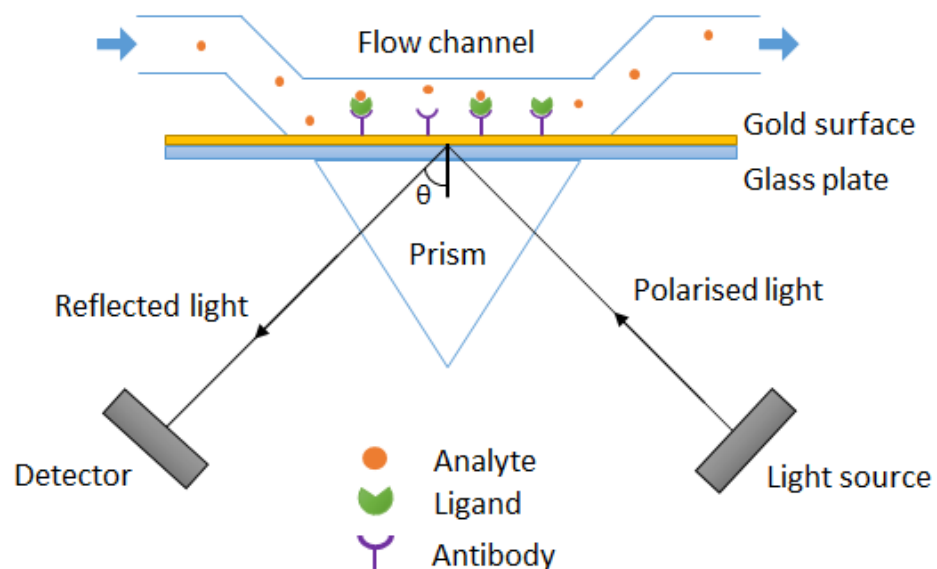


Figure 3-11 Diagram of SPR set-up

SPR can be used to measure protein binding events in real time. A protein of interest (ligand) is attached to a gold surface, such as through an anti-GST antibody, then a binding partner (analyte) is flowed across the surface. The additional mass of analyte binding to the ligand changes the refractive properties of the gold surface which is detected by a reduction in polarised light reflected from the surface at a given angle.

Surface plasmon resonance is the result of long range Coulombic interactions between valence electrons in metals which yield collective plasma oscillations (Pitarke *et al.*, 2007). In short, the presence of a mass at one position of a metal surface affects the resonance properties of the electrons across the entire surface. This change in electron resonance is reflected in the refractive index of the surface which can be measured by the decrease in intensity, at a given angle, of a beam of polarised light reflected from the surface. Changes in refractive index of a surface are directly proportional to the changes in absorbed mass (Malmqvist, 1993).

Modern SPR instruments can measure a range of masses from chemical compounds to cells, and affinities from picomolar to millimolar. This sensitivity to small molecular weights and weak interactions has opened its use for drug discovery. Additional methods of immobilising proteins to surfaces are now available including hydrophobic dextran surfaces, immobilized biotin/avidin or covalent amine, thiol or aldehyde group chemistry (Malmqvist, 1993). SPR also has the advantage of being capable of being performed over a wide range of temperatures, pHs and buffer conditions including cell lysates (McDonnell, 2001). Analysis of the results is relatively straightforward as absorption to the ligand is first order, as the concentration bound to the surface is constant, and the association rate constant can be determined from a series of absorption experiments at different analyte concentrations. The dissociation rate (k_{off}) can be determined from the logarithmic decrease in analyte after the flow of analyte addition is stopped. This method can lead to very long dissociation times of very tight binders due to the associated slow off rates. The accuracy of the binding measurement is increased by the use of double referencing which compares the sample measurement to that of a control surface and removes the measurement as determined from a buffer only run. This approach has the effect of removing any contribution to the signal caused by non-specific binding or from the buffer itself (McDonnell, 2001).

3.2.3 Microscale Thermophoresis

Microscale thermophoresis (MST) uses the change in the movement of a fluorescently labelled molecule in the presence of different concentrations of binding partner when a small temperature gradient is applied to the sample. Thermophoresis describes the motion of molecules in temperature fields which is dependent on properties such as the

size, charge, conformation and solvation shell of a molecule. The technique is therefore suitable for the measurement of interactions with almost any binding partner including ions, compounds or proteins. Additional advantages are that MST is very quick -a binding curve can be collected in just a few minutes, and the use of fluorescent labels makes it very sensitive -only low nanomolar concentrations of sample are needed for each measurement (Jerabek-Willemsen *et al.*, 2011). Figure 3-12 outlines a typical MST experiment. Firstly, an infrared (IR) laser heats the sample by just a few degrees kelvin in a tens of micrometer radius to create a localised temperature field. After an initial temperature jump, thermophoresis occurs which can be described with a linear drift response that is limited by the rate of diffusion. The final fluorescence signal after thermophoresis is measured and compared to the initial fluorescent state. When the laser is turned off, the fluorescence signal increases again due to back diffusion of the

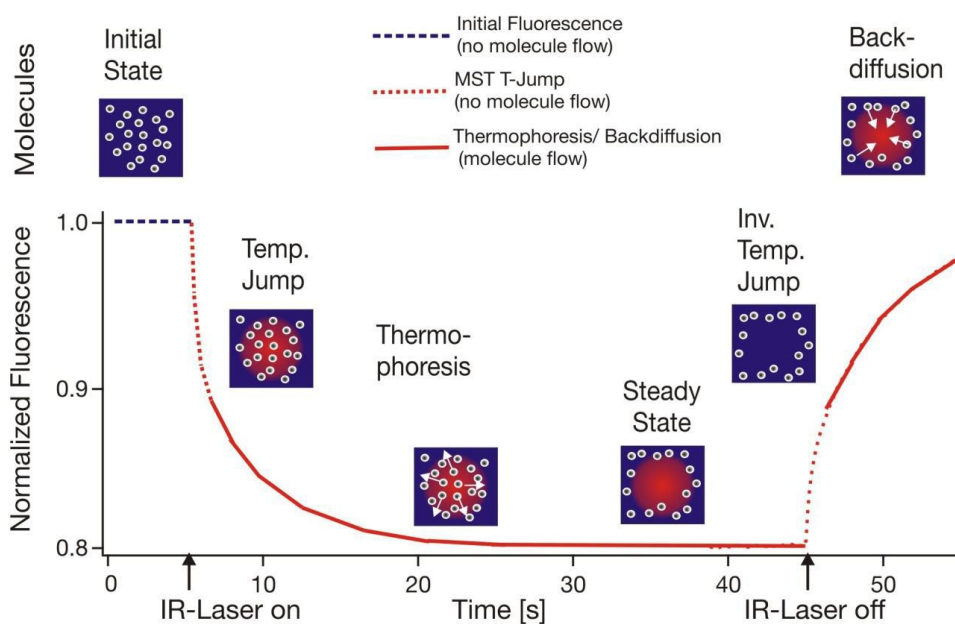


Figure 3-12 Diagram of typical MST experiment

Figure taken from (Jerabek-Willemsen *et al.*, 2011). MST can determine protein-protein and protein-ligand interactions through changes in the diffusion of a fluorescent protein upon heating. A fluorescently labelled protein is heated by an infra-red (IR) laser which heats a small area of the sample solution. After an initial lag stage, where the solution is heated, a temperature gradient is established causing the fluorescent molecules to diffuse to form a new equilibrium state. This is measured by a change in fluorescence. Once the IR laser is switched off the temperature returns to ambient and the fluorescent molecules revert to their original steady state through back-diffusion. The affinity of a binding partner can be determined through repeating the experiment with a range of concentrations of the binding partner and measuring the effect the binding partner has on the thermophoresis of the fluorescently labelled protein.

fluorescent molecule. A titration approach by repeating this process in the presence of increasing binding partner concentration can then be used to measure affinities, enzymatic activation or modifications by the determination of the bound and unbound fractions (Jerabek-Willemsen *et al.*, 2011).

In MST experiments reproducibility of the initial fluorescent signal is very important and this signal is highly dependent on the integrity of the protein sample. Aggregation or oligomerisation can result in changes in back diffusion yielding uneven thermophoresis curves. Interactions with the capillary surfaces can also influence the fluorescent signal but can be overcome by adding detergents to the buffer or using treated capillaries to prevent binding (Jerabek-Willemsen *et al.*, 2011).

MST can be used to analyse samples from blood serum or cell lysates (Wienken *et al.*, 2010), in competitive mode to identify drug binding sites based on known interactions (Mao *et al.*, 2015), and label-free exploiting the inherent UV fluorescence of proteins. In this thesis, CDK4 was labelled using a N-hydroxysuccinimide (NHS) ester dye that reacts with the primary amines of lysine side chains or the N-terminus. The random nature of this attachment should minimise possible local effects on binding behaviour. However, there is no guarantee that the labels will not still influence binding (Seidel *et al.*, 2013).

3.3 Materials and methods

All chemicals were of analytical grade and obtained from Sigma Aldrich unless otherwise stated.

3.3.1 Protein production

CDK4 and CDK6 were expressed as N-terminal GST fusions in Sf9 insect cells (Section 2.3.7). Cdc37 and Hsp90 constructs were expressed from recombinant *E. coli* (Section 2.3.6). Proteins were subsequently purified using standard protocols outlined in Section 2.4.

3.3.2 Biotinylation of Avi-tagged constructs

Avi-tagged proteins (Cdc37, Cdc37^{S13E} and Hsp90 β) were biotinylated *in vitro* using BirA (kindly provided by Dr Richard Heath; Postdoc, Endicott lab, NICR). 40 μ M of each Avi-tagged protein was incubated with 10 μ g BirA in biotinylation buffer (50 mM Bicine pH

8.3, 10 mM ATP, 10 mM MgOAc, 50 μ M *d*-biotin) at 30°C for 60 minutes. Following biotinylation, proteins were buffer-exchanged into mHBS (10 mM HEPES, pH 7.5, 150 mM NaCl, 0.5 mM TECEP and 0.5 mM EDTA) using a Superdex 75 10/60 column, pre-equilibrated with mHBS, to remove residual ATP and biotin which could interfere with subsequent experiments. The extent of protein biotinylation was monitored by pull downs using High Capacity NeutrAvidin® Agarose Resin (Thermo Scientific Pierce).

3.3.3 Streptavidin pull-downs

50 μ l of 5 μ M of protein was incubated with 10 μ l NeutrAvidin® Agarose Resin (Thermo Scientific Pierce) for 60 minutes at 4 °C in mHBS. Resin was pelleted using a table top microcentrifuge at 3381 x g for 2 mins at 4 °C and the supernatant removed. Pellets were washed 3 times by adding 200 μ l ice-cold mHBS buffer and repeating the pelleting step described above between each addition. After the final wash, 10 μ l of SDS loading dye was added to the pellet which was boiled and analysed by SDS-PAGE. Proteins were visualised by InstantBlue staining.

3.3.4 Microscale thermophoresis

MST measurements were carried out using the Monolith NT. 115 Nano-Blue/Red instrument (Nanotemper). CDK4 was chemically tagged with the amine coupling fluorescent dye NT-647 NHS using the Nanotemper protein labelling kit red and following the protocol provided. Samples were centrifuged at 10000 x g at 4 °C (Beckman Coulter Allegra X22R) before use. A twofold 16 point serial dilution series of untagged Cdc37₁₋₃₄₈ was prepared from a 30 μ M stock and titrated against fixed concentrations of NT-647 NHS-labelled CDK4 at 83.3 nM in a total volume of 20 μ L at 22 °C. Samples were diluted using MST buffer (10 mM HEPES pH 7.5, 150 mM NaCl, 0.5 mM TCEP, 0.5 mM EDTA, 0.05% Triton-X-100). Measurements were taken using an LED power of 40% (645 nm) and thermophoresis energy of 20% (1475 nM) and the emission at 680 nm was recorded. K_d values were determined by the MST analytical software using the law of mass action described in Equation 3-1 where A is the concentration of labelled CDK4, B is the concentration of Cdc37, [AB] is the concentration of complex and FB is the fraction bound.

$$FB = \frac{[A] + [B] + Kd - \sqrt{([A] + [B] + Kd)^2 - 4[AB]}}{2[B]}$$

Equation 3-1 The law of mass action

The MST analysis software uses the law of mass action to calculate K_d values based on the concentrations of components used.

3.3.5 Optimisation of the HTRF direct binding mode assay

The HTRF assay protocol was greatly optimised throughout the project and went through many iterations to achieve a suitably large and reliable fluorescent signal and to ensure the maximum level of accuracy from the assay within and between runs. An early parameter that was optimised was temperature. First experiments were carried out at room temperature but subsequently all results included in this thesis, except where noted, were collected at 4 °C. Further optimisation could be divided into optimisation of (i) the reagents, and (ii) the reaction conditions. The main optimisation steps are outlined below.

Optimisation of reagents:

- (i) Biotinylation of Avi-tagged proteins: The *in vitro* biotinylation protocol was reviewed to maximise the extent of biotinylation. The aim was to completely biotinylate the Avi-tagged proteins while minimising the incubation time at 30°C, where protein instability and degradation may occur. Biotinylation of multiple Cdc37 constructs; N-Avi-Cdc37₃₀₋₃₄₈, N-Avi-Cdc37_{30-Fl}, C-Avi-Cdc37_{Fl}, C-Avi-Cdc37_{30-Fl}, N-Avi-Cdc37_{Fl} and N-Avi-Cdc37₁₋₃₄₈ was carried out using the biotinylation protocol described in Section 3.3.2 and 10 µl samples of each construct were taken at time points of 0, 30, 60, 120 and 300 minutes. The relative biotinylation levels at each time point were determined by streptavidin pull-down as described in Section 3.3.3.
- (ii) Avi-tag location: Although the N-terminus of Cdc37 is known to be required for kinase binding, the exact interactions were unclear. Alternative positioning of the Avi-tag on either the N- or the C-terminus of Cdc37 was therefore investigated for potential impact on CDK binding. Secondly, due to the distance restraints imposed by the FRET, alternative Avi-tag positioning was also studied to determine impact on the size of the fluorescence ratio obtained. Experiments were carried out as described in 3.4.2, except that incubations were carried out at room temperature rather than 4 °C.

Optimisation of reaction conditions:

Early experiments set out to optimise the concentration of GST-tagged constructs. Five different concentrations (100 nM, 50 nM, 25 nM, 10 nM and 5 nM) were assayed. Subsequently, assays were repeated to identify the highest concentration of Avi-tagged Cdc37 that could be measured accurately, by varying the Avi-tagged Cdc37 concentration from 0 to 1500 nM. In these experiments the concentration of GSTCDK4 or GSTCDK6 was 10 nM and the concentration of the dye was held at 1/8th the concentration of the Cdc37. The final reaction parameter to be optimised was the incubation time of the reaction prior to addition of the detection reagents and measurement of the fluorescent signal. Alternative incubation times were investigated by repeated measurements over an extended period from 45 minutes to 24 hours to identify when the maximum signal was measured. The reactions were carried out at 4 °C and all other reaction parameters were as described in 3.3.6.

3.3.6 HTRF direct binding mode assay

HTRF assays were performed in 384 well black assay plates. Samples were centrifuged at 10000 x g at 4 °C (Beckman Coulter Allegra X22R) before use. For direct binding measurements the biotinylated protein of interest was titrated, over 11 serial dilution points and an additional buffer blank point, against 5 fixed concentrations of either GSTCDK4 or GSTCDK6 (100 nM, 50 nM, 25 nM, 10 nM and 5 nM) in duplicate. Avi-tagged construct concentrations were chosen based on estimated K_d values for each interaction from literature values and preliminary results. GSTCDK and the binding protein of interest were prepared in HTRF buffer A (50 mM HEPES pH 7.5, 100 mM NaCl, 1 mM DTT and 0.1 mg/ml BSA) and incubated together for 60 minutes at 4°C. 5 nM Tb labelled anti-GST antibody (Life Technologies) and SAXL665 (Cisbio), at 1/8th the concentration of the biotinylated protein, were prepared in HTRF buffer B (50 mM HEPES pH 7.5, 100 mM NaCl and 0.1 mg/ml BSA) and added to each well. The plate was incubated for a further 120 minutes at 4°C before being scanned using the PHERAstar FS (BMG LABTECH). Samples were excited using a wavelength of 337 nm and emission spectra measured at 620 nm and 665 nm. K_{d-app} values were determined from binding curves of the fluorescence 620/665 nm ratio (from which the buffer only measurement containing no GSTCDK was subtracted) against the GSTCDK concentration. Curves were plotted and analysed using GraphPad Prism 6.0.

3.4 Results

3.4.1 Optimisation of the HTRF protocol

The HTRF assay was initially performed at room temperature, however, this met with limited success. Although a fluorescent binding signal could be observed for the CDK-Cdc37 interaction it was small, unreliable and often could not be reproduced. The issue of reproducibility was hypothesized to arise from a combination of poor CDK stability at room temperature, resulting in degradation or aggregation, weak binding of CDK6 to Cdc37 and GST contamination of the GSTCDKs. Prior to HTRF assay, several steps were taken to address issues of reagent stability. As CDK4 had been shown to be particularly susceptible to changes in temperature during purification, both CDKs were purified at 4 °C. GST contamination would result in fluorophore loss through non-specific binding of the terbium labelled anti-GST antibody to GST. To address this pitfall, GSTCDK4 and GSTCDK6 purification protocols were modified to include a more stringent cut-off of the peak fractions to ensure no GST contamination was carried through (Figure 2-22). The larger signal obtained at 4 °C also allowed the concentrations of GSTCDK4 and GSTCDK6 in the direct binding assay to be dramatically lowered, allowing for more accurate K_d determination.

Figure 3-13 B shows that a more than tenfold increase in fluorescent signal was observed for the CDK6-Cdc37 interaction when the HTRF experiment was carried out at 4 °C. It

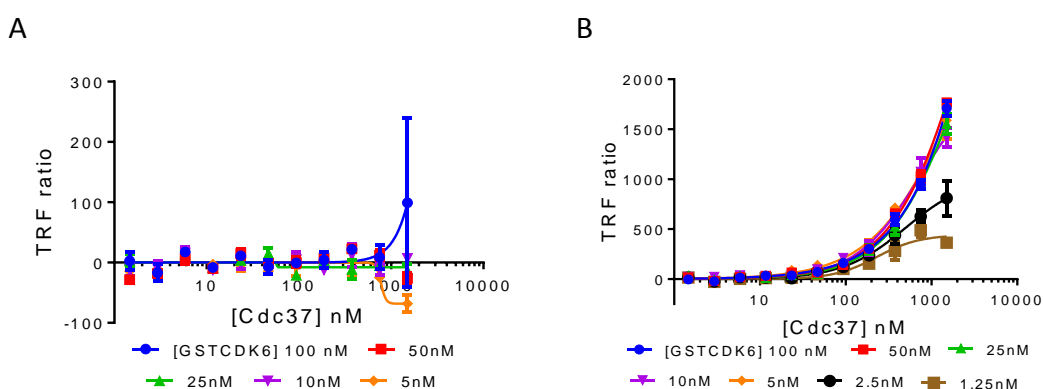


Figure 3-13 Performing the HTRF assay at 4 °C greatly enhances the size and reliability of the fluorescent signal obtained

Examples of the interaction between C-Avi Cdc37 over several concentrations of GSTCDK6 performed at room temperature (A) and 4 °C (B). GSTCDK6 concentrations (nM) at which each of the curves were measured are provided in the panels. The errors represent the standard deviation. Graphs produced using GraphPad Prism.

was not always possible to fit complete binding curves for the CDK6 interaction. However, a sufficient signal was measured to permit direct comparison with CDK4. Because of these experiments, all subsequent HTRF experiments presented in this work were performed at 4 °C.

Similar experiments were carried out to optimise the assay conditions to measure the reconstitution of a CDK-Cdc37-Hsp90 complex (Figure 3-14). Again, only a weak signal could be observed between N-Avi Hsp90 and GSTCDK4, bridged by unlabelled Cdc37, at room temperature (Figure 3-14 A), and no interaction was observed between CDK6 and Hsp90 (Figure 3-14 B). The assay was therefore performed at 4°C, again in the hope of improving protein integrity and complex stability and therefore the size of the signal. The concentrations of GST-tagged CDK4 or CDK6 were also significantly lowered to single digit nanomolar. With these changes to the assay format, formation of a ternary GSTCDK-Cdc37-N-Avi Hsp90 complex could be measured.

The initial protocol for the HTRF assay used a short incubation time of 45 minutes between addition of the detection reagents and measurement of the fluorescent signal. Alternative incubation times were investigated by repeated measurements over an extended period in order to identify when the maximum signal from complex formation was obtained. This may be particularly important for the formation of large complexes containing Hsp90, the kinetics of which may be slow at 4 °C. Time courses performed

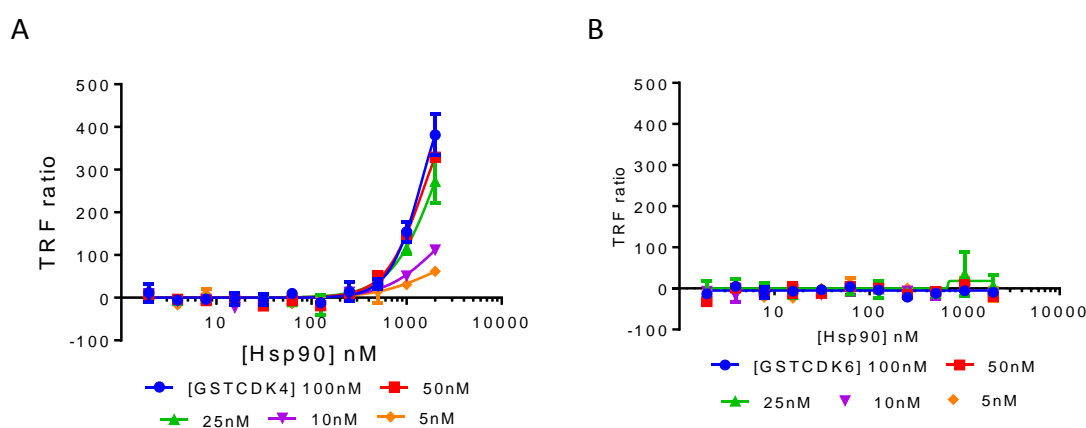


Figure 3-14 The N-Avi Hsp90 interaction is weak at high temperatures

Examples of the interaction between N-Avi Hsp90 interaction performed at room temperature with several concentrations of GSTCDK4 (A) and GSTCDK6 (B). The concentration of GSTCDK4 or GSTCDK6 in each assay is indicated by the colour key in each panel. The errors represent the standard deviation. Graphs plotted using GraphPad Prism.

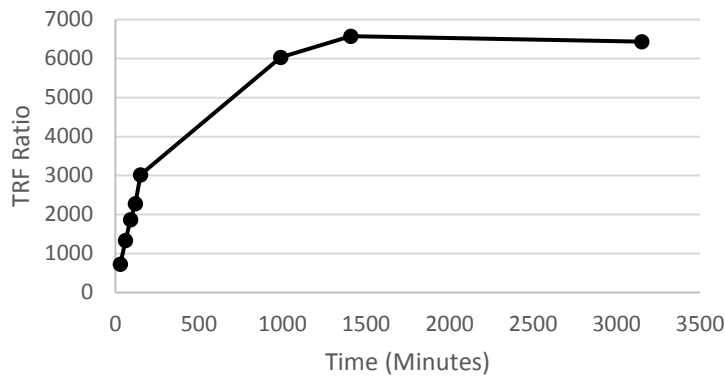


Figure 3-15 The change in fluorescent signal was assessed over time

Average maximum fluorescent signal of CDK6-Cdc37 at 4 °C over a time course of 30, 60, 90, 120, 150, 990, 1410 and 3150 minutes. In this experiment the GSTCDK6 concentration was 10 nM and that of Cdc37, 1500 nM.

signal increased considerably with time. The time course for the CDK6-Cdc37 interaction (Figure 3-15) shows the fluorescent signal increased from a TRF ratio of *circa* 1000 at the original time point of 45 minutes to a maximum of *circa* 6500 after 24 hours, presumably from increased complex formation. From these time course experiments an incubation time of 2 hours was chosen as the time point at which the CDK4-Cdc37-Hsp90 complex reached its maximum, although the maximum signal was not achieved for the CDK6-Cdc37 complex until 24 hours. Longer incubation times were decided against due to both practicality and the potential loss in protein and dye quality over time, as suggested by the gradual decline in signal between 24 and 52.5 hours.

3.4.2 Optimisation of reagents

Biotinylation

All samples show partial biotinylation at time point 0 (Figure 3-16, gel A lanes 2-7) as each Cdc37 construct was pulled out by the streptavidin beads. This background biotinylation is likely performed by the *E. coli* expression system which contains a low level of biotin ligase activity. The extent of biotinylation *in cell* can be increased by co-expression of the BirA enzyme, however this method was not explored as it requires the addition of high quantities of *d*-biotin to the growth media. The extent of biotinylation was measured at 0, 30, 60, 120 and 300 minutes (Figure 3-16). The maximum level of biotinylation was observed after 60 minutes (Figure 3-16, gel B lanes 3-8) as shown by the most intense bands, roughly double that at 30 minutes (Figure 3-16, gel A lanes 8-12). Unfortunately, the samples for the 120 minute time point (gel C lanes 2-7) were

accidentally over boiled before SDS-PAGE analysis and so are not available for interpretation. What is clear is the relative decrease in biotinylated protein after 300 minutes (Figure 3-16, gel c lanes 8-12) in comparison to those taken at the 60 minute

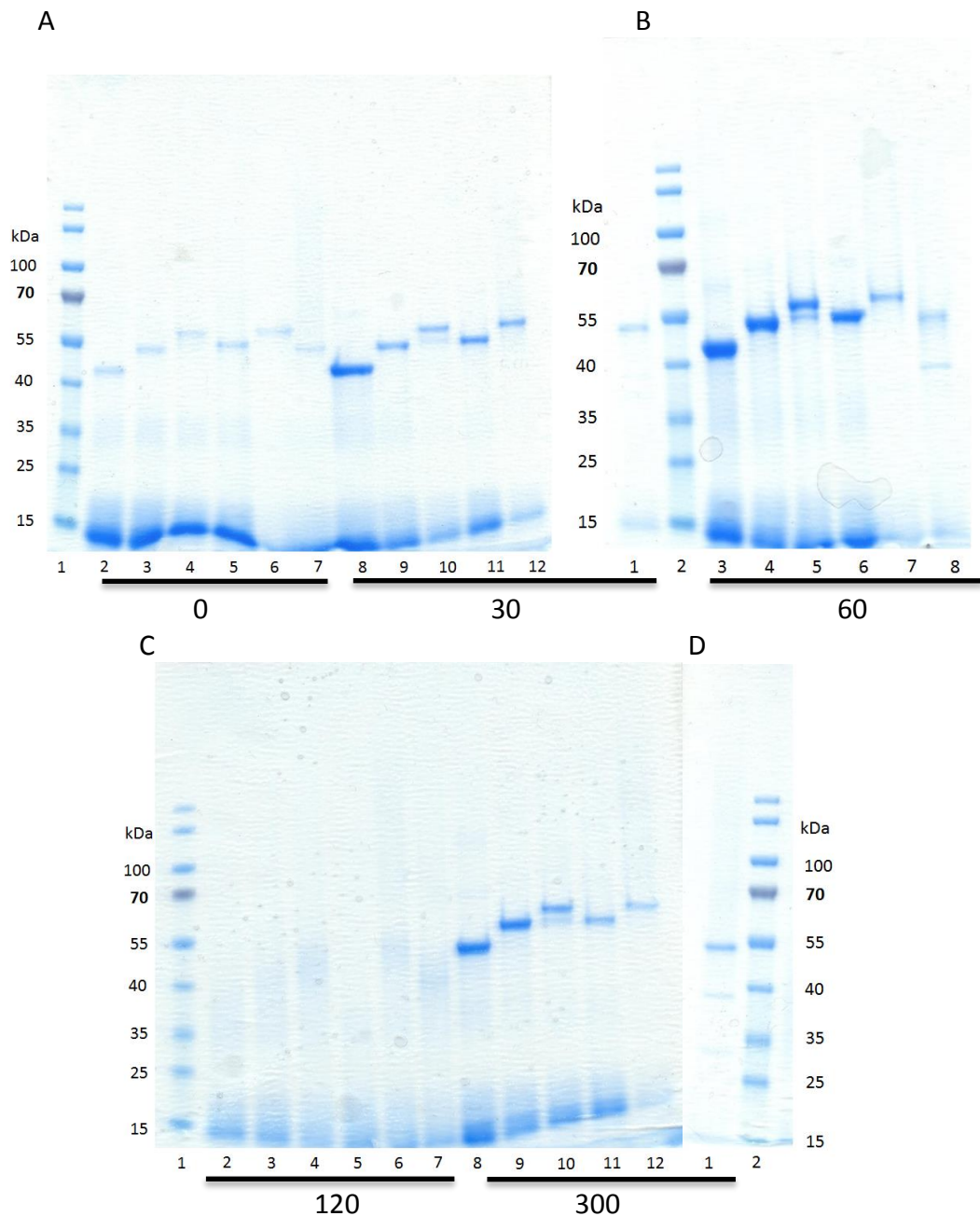


Figure 3-16 Biotinylation levels assessed by streptavidin pull-downs

The extent of biotinylation of a collection of Cdc37 constructs was determined at multiple time points during an *in vitro* biotinylation reaction by streptavidin pull-downs. Bars show the repeated set of Cdc37 constructs measured at each time point. The number associated with each bar corresponds to the length of incubation in minutes. Sets of Cdc37 constructs are laid out as; N-avi-Cdc37₃₀₋₃₄₈, N-avi-Cdc37_{30-FI}, C-avi-Cdc37_{FI}, C-avi-Cdc37_{30-FI}, N-avi-Cdc37_{FI} and N-avi-Cdc37₁₋₃₄₈, in respective lanes. The protein size marker used throughout is PageRuler protein ladder and proteins were visualised using InstantBlue.

time point. The decrease in biotinylated protein after 300 minutes is likely due to protein degradation caused by the extended incubation at 30 °C.

From these experiments an incubation time of 60 minutes was selected for subsequent *in vitro* biotinylation reactions. Although initial optimisation was carried out on a range of constructs subsequent assays were performed using full-length Cdc37 unless specifically stated.

Avi-tag positioning

Initial streptavidin pull-downs revealed that both N and C Avi-tagged Cdc37 still bound to CDK4 and CDK6. This observation was subsequently verified when they were subjected to the HTRF assay as described in Section 3.3.6. Fluorescent ratio signals obtained for each terminally tagged construct were almost equivalent. Due to the equivalent signal the full-length C-terminally tagged Cdc37 construct was chosen for all subsequent HTRF experiments because of the larger protein yields obtained.

Similar optimisation experiments were not carried out to explore the effect on signal of moving the Avi-tag to either end of Hsp90. In this case, the Avi-tag was only positioned on the N-terminus on Hsp90. This decision was based on the single particle cryo-EM structure at the time which showed CDK4 to be positioned at the N-terminus of Hsp90. As such, the N-terminus of Hsp90 was closest in space to CDK4 and therefore best positioned to give the largest signal. Due to the size of Hsp90, (*circa* 150 Å), it was possible that positioning tags at these extremes of the molecule would be too far away for FRET. An N-terminal luciferase tag had been placed on Hsp90 by Taipale et al. (Taipale *et al.*, 2012) and was still able to bind CDK4 and CDK6, as well as a range of other kinases, so the far smaller Avi-tag was not expected to interfere with the interaction.

Optimisation of the reaction conditions

A concentration of 100 mM NaCl was primarily used to maintain CDK4 and CDK6 stability. It is also around physiological concentrations and so should more closely mimic interaction conditions found in the cell. While a more accurate determination of biological K_d values could be measured through the inclusion of other cations and co-factors, such as potassium, magnesium or ATP, they were not included to keep assay conditions to a minimum and facilitate the optimisation process by. Early experiments

set out to optimise the concentration of GST-tagged CDK constructs. Of the five different concentrations that were assayed (100 nM, 50 nM, 25 nM, 10 nM and 5 nM, (Figure 3-17), a concentration of 10 nM was found to be the lowest concentration which still gave well defined binding curves. Examples of binding curves presented in this work were performed using 10 nM GSTCDK unless otherwise stated. In order to measure relatively weak interactions, higher concentrations of titrating ligand are required. The next optimisation step set out to determine the highest concentration of Avi-tagged Cdc37 that could be accurately measured. Throughout, the concentration of the dye was held at 1/8th the concentration of the Cdc37.

Although there is no theoretical limit to how weak an interaction can be measured using HTRF, practical issues have shown that higher dye concentrations can lead to larger signal variation and it has been noted that higher concentrations of dye can lead to a quenching of the fluorescent signal (Jia *et al.*, 2006). We observed that increasing the Avi-tagged Cdc37 above 1.5 μ M and therefore the dye above 187.5 nM (1/8th the Cdc37 concentration) lead to increased variation and a drop in observed signal (Results not shown). Possible reasons for this arise from the Hook effect, caused by a mismatch in fluorophore concentrations compared to the interacting proteins resulting in a drop of fluorescent signal being measured despite more protein-protein interactions being

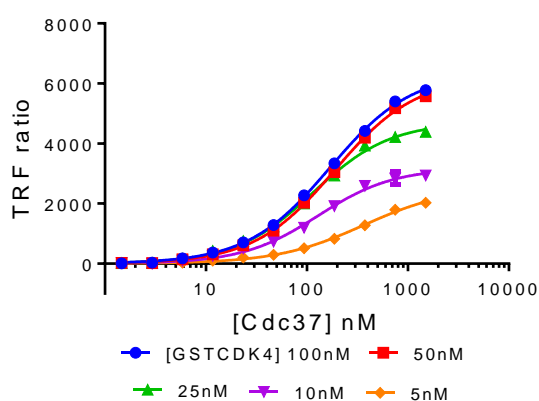


Figure 3-17 Concentration dependent conditions

An example of the interaction between C-Avi Cdc37 over several concentrations of GSTCDK4 performed at 4 °C. GSTCDK4 concentrations (nM) at which each of the curves were measured are provided in the panel. The errors represent the standard deviation. Graphs produced using GraphPad Prism.

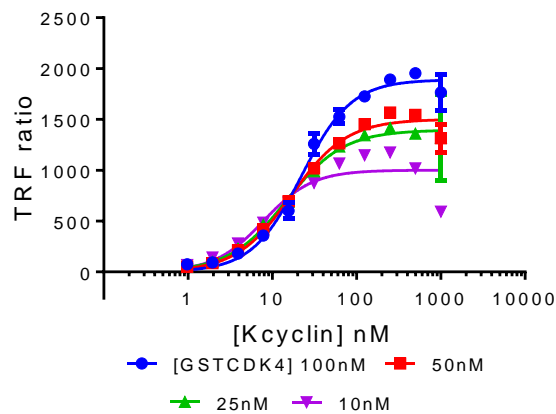


Figure 3-18 Potential Hook effect

An example of the interaction between C-Avi Kcyclin over several concentrations of GSTCDK4 performed at 4 °C to demonstrate the hook effect. At C-Avi Kcyclin concentrations of around 100 nM the fluorescent signal begins to plateau however after around 250 nM the fluorescent signal begins to decline. This is most obvious for the 10 nM GSTCDK4 curve (purple). GSTCDK4 concentrations (nM) at which each of the curves were measured are provided in the panels. The errors represent the standard deviation. Graphs produced using GraphPad Prism.

made, or quenching of the dye by hydrophobic interactions with the proteins or protein aggregates at higher concentrations. The concentration of dye and therefore Cdc37 used in the assay were capped at 187.5 nM and 1.5 μ M respectively for the majority of direct binding experiments. Figure 3-18 demonstrates the hook effect using the interaction between GSTCDK4 and C-Avi Kcyclin as an example.

3.5 Determining Cdc37 affinity for CDK4 and CDK6

As described in Section 3.1.1 the recruitment of kinases to the Hsp90 chaperone system is dependent on the co-chaperone Cdc37. A greater understanding of this key interaction would help us to better understand the regulation of kinases by the Hsp90 chaperone system. Preliminary experiments using pull-downs and SEC suggested an interaction between Cdc37 and CDKs 4 and 6. However, SEC results were inconclusive as the complexes could not be clearly separated from the individual components. Alternative more quantitative techniques have therefore been used to measure the Cdc37 interaction with the CDKs.

Here HTRF has been used, as described in Section 3.3.6, to measure the direct interaction of a dilution series of full-length C-Avi Cdc37 against fixed concentrations of full-length GST-CDK4 (Figure 3-19 A) or GST-CDK6 (Figure 3-19 B). K_{d-app} values for these

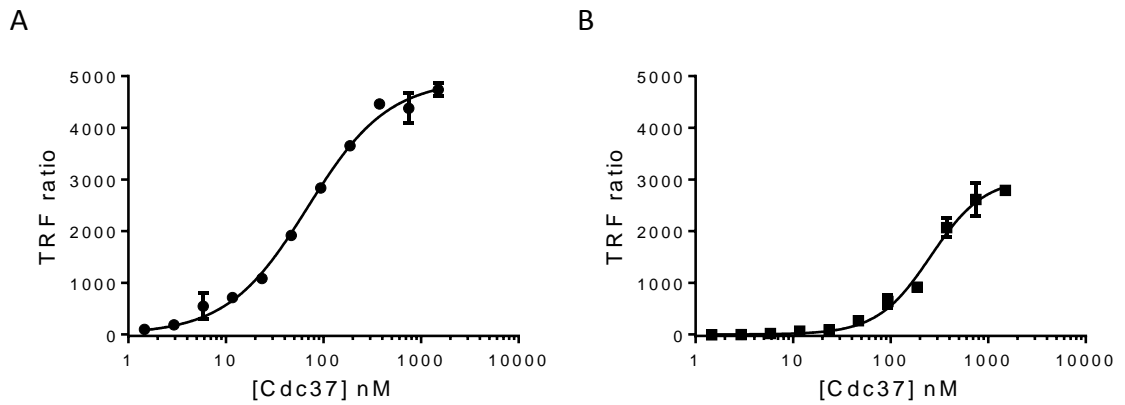


Figure 3-19 CDK4 binds tighter than CDK6 to Cdc37

Binding curve of the C-Avi Cdc37 interaction with GSTCDK4 (A) and GSTCDK6 (B) determined by Homogenous Time Resolved Fluorescence (HTRF) assay. The concentration of GSTCDK4 and GSTCDK6 used in these assays was 10 nM. HTRF measurements were carried out in duplicate a total of 7 and 6 times for CDK4 and CDK6 respectively using two independently expressed and purified C-Avi Cdc37 samples. The error bars represent the standard deviation. Binding curves produced using GraphPad Prism.

interactions were determined from the binding curves to be 92 +/- 29 nM and >500 nM for CDK4 and CDK6 respectively. Hill slope evaluation from analysis gave 1.08 +/- 0.10 and 1.42 +/- 0.32 for CDK4 and CDK6 respectively suggesting cooperative effects with CDK6, although accurate analysis is hindered by incomplete saturation of CDK6 binding curves. This difference is reflective of previous studies that have suggested CDK4 to be a stronger client of Cdc37 than CDK6 (Stepanova *et al.*, 1996; Taipale *et al.*, 2012). The K_{d-app} for CDK6 could not be more accurately determined as it fell at the upper limit of detection for the assay. However, the values are consistent with an affinity of 200 nM for the interaction between $Braf^{V600E}$, a strong kinase client, and Cdc37 determined by our collaborators using the alternative technique of ITC (Polier *et al.*, 2013).

The HTRF assay was repeated using GST (Figure 3-20 A) and GSTCDK2 (Figure 3-20 B) which are not clients of Cdc37-Hsp90. As CDK2 is not a Cdc37 client, as expected, no detectable association with Cdc37 was observed. At higher Cdc37 concentrations, some small changes in fluorescence were observed with GST although these were far smaller than the observed interactions with CDK4 and CDK6.

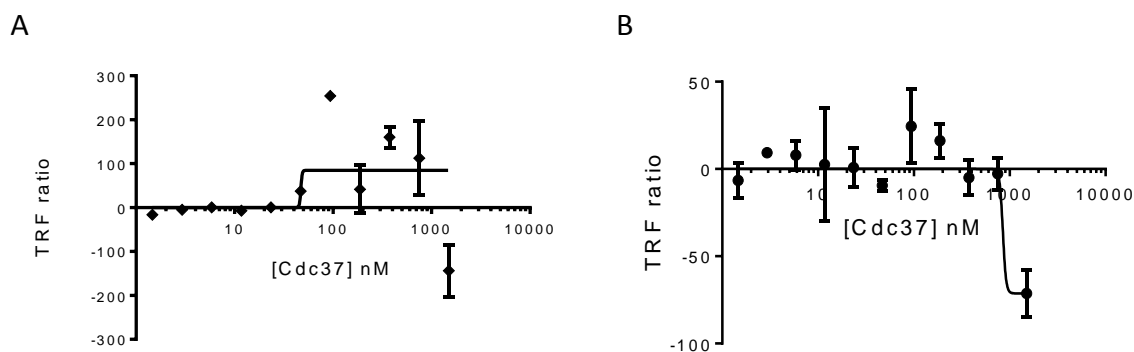


Figure 3-20 Cdc37 does not interact with GST or CDK2

Cdc37 does not bind to glutathione-S-transferase (GST) (A) or GSTCDK2 (B). The GST and GSTCDK2 concentrations were 25 nM and measurements were carried out only once in duplicate. In both panels the error bars indicate standard deviation. Graphs produced using GraphPad Prism.

3.5.1 Cdc37 interactions confirmed by MST

Several orthogonal techniques including ITC, MST and SPR were explored to confirm the K_d measurements determined by HTRF. Although tested, ITC required too much of the CDK proteins than were available at the time and so was not taken further. Equally SPR has recently been trialled but insufficient time remained to optimise the conditions. The interaction between CDK4 and Cdc37₁₋₃₄₈ was measured by MST. However, the interaction between CDK6 and Cdc37 did not appear to be directly amenable to MST and would have required considerable further optimisation.

MST has the advantage that there is no need to tag the reagents and so these can be removed to reduce potential steric clashes that could affect the interaction. It was of concern that the presence of a GST tag, antibody or streptavidin-bound dye detection reagents may influence the HTRF K_d determination. CDK4 was successfully amine coupled to the fluorescent dye NT-647 NHS and the MST assay was carried out as described in Section 3.3.4. A K_d of 477 +/- 42.7 nM was determined using the integrated analysis software from three repeat experiments (Figure 3-21). The maximum unbound fluorescent signal was 876 and the maximum bound fluorescent signal was 827 which left an amplitude between them of 48.4. Due to instrument setup the MST experiments were carried out at room temperature. The K_{d-app} for this interaction at room temperature as determined by HTRF was 190 +/- 43 nM. These values are reasonably similar and consistent with the interaction between Cdc37 and Braf^{V600E} as measured by ITC (Polier *et al.*, 2013). It should be noted that at different laser energy setting (20% instead of 40%) the K_d value determined for this interaction was different

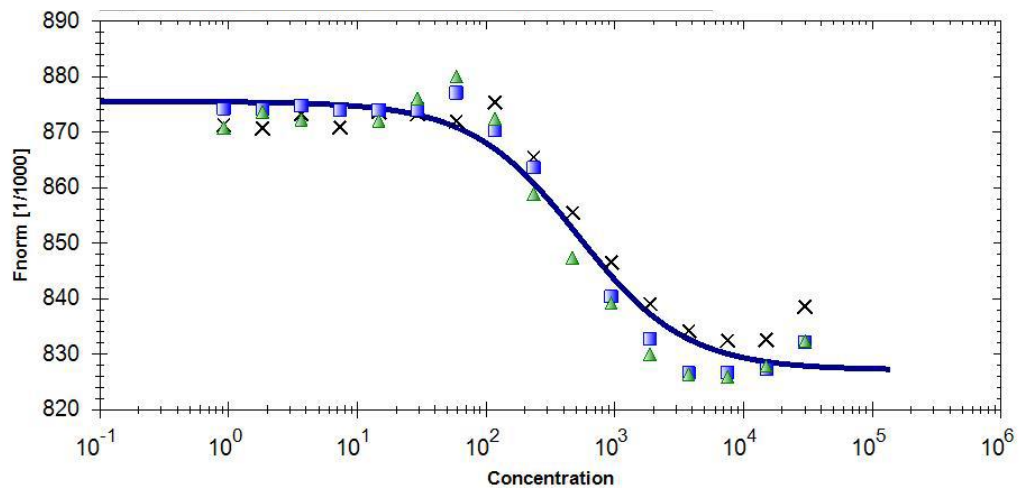


Figure 3-21 MST confirms CDK4/Cdc37₁₋₃₄₈ interaction strength

Plot of the change in fluorescence upon thermophoresis with increasing Cdc37₃₄₈ concentration. The three repeat measurements are shown with blue squares, green triangles and black crosses. The best fit binding curve for K_d determination is shown in blue. MST measurements were carried out a total of 3 times performed on different days.

(321 +/- 40.7 nM). Ideally this experiment would need to be repeated at a range of settings to get a more accurate average using this technique. GST-tagged CDK4 and CDK6 were also chemically labelled with the NT-647 NHS dye to allow for direct comparison with the HTRF assay. However, these constructs were not amenable to MST and did not produce a stable signal, potentially caused by the dimerisation of the GST.

3.5.2 Cdc37^{S13E} does not show an enhanced interaction with the CDKs

The phosphorylation of Ser13 on Cdc37 has been shown to be important for stabilising the CDK4-Cdc37-Hsp90 complex (Verba *et al.*, 2016) and to influence the interaction of Cdc37 with client kinases (Miyata and Nishida, 2004). To investigate the effects of phosphorylation at this site on CDK4 and CDK6 binding, a Ser13 phosphomimetic mutant (C-Avi Cdc37^{S13E}) was used in the HTRF assay. No significant changes in interaction were observed for either CDK4 (Figure 3-22 A) or CDK6 (Figure 3-22 B).

The K_{d-apps} for the interaction of wild-type Cdc37 and Cdc37^{S13E} were 92 +/- 29 nM and 56 +/- 20 nM respectively with CDK4, and >500 nM and >950 nM respectively with CDK6. Hill slope evaluation from analysis gave 1.23 +/- 0.02 and 0.99 +/- 0.01 for CDK4 and CDK6 respectively suggesting cooperative effects with CDK4. The enhancement in interaction with CDK4 is modest particularly considering the variation in signal observed between readings. The phosphomimetic appeared to have little effect with CDK6 eliciting an almost twofold weaker interaction than the wild-type.

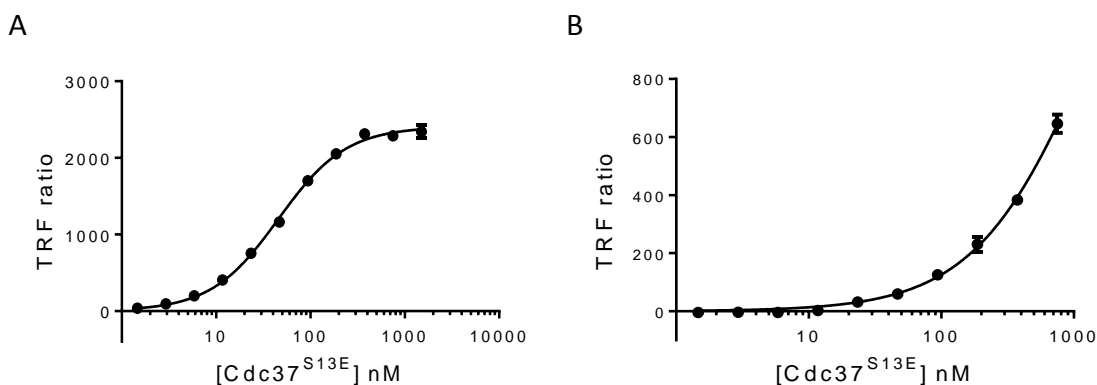


Figure 3-22 Interactions with Cdc37^{S13E} are comparable to wild-type

Binding curve of C-Avi Cdc37 S13E with GSTCDK4 (A) and GSTCDK6 (B). The GSTCDK concentrations were 10 nM and measurements were carried out in duplicate. HTRF measurements were carried out in duplicate a total of 3 times for both CDKs performed on different days. In both panels the error bars indicate standard deviation. Binding curves produced using GraphPad Prism.

However, large variations in K_{d-app} determination between repeats occur for this interaction (+/-234 nM) due to the inaccuracies of predicting a K_{d-app} value from incomplete binding curves at the highest concentration ranges. Taken together these results suggest that this limited phosphomimic on Ser13 does not enhance the interaction between Cdc37 and client kinases, however, alternative phosphomimics or the phosphorylated species were not explored.

It was hoped that an enhancement in the binding strength of the Cdc37^{S13E} construct for CDK6 would help to improve the accuracy of the K_d determination by bringing the binding curve further into the Cdc37 concentration range so that saturation could be achieved. This would have allowed for a more accurate direct comparison of binding strengths between CDK4 and CDK6. A summary of the K_d values determined between Cdc37 and CDK4 or CDK6 is provided in Table 3-1.

Binding partner	Technique	Temperature	CDK4 (nM)	CDK6 (nM)
Cdc37	HTRF	4°C	92 +/- 29	>500
Cdc37 ^{S13E}	HTRF	4°C	56 +/- 20	>950
Cdc37 ₃₄₈	MST	RT	477 +/- 42.7	ND
	HTRF	RT	190 +/- 43	ND

Table 3-1 Table of Cdc37 affinities

Summary of K_d values determined for Cdc37 to CDK4 and CDK6 by different techniques.

3.6 Formation of a CDK-Cdc37-Hsp90 complex *in vitro*

Once the interaction with the co-chaperone Cdc37 had been established by HTRF, an attempt was made to measure the interaction with Hsp90. Initial attempts to introduce untagged Hsp90 into the GSTCDK-C-Avi Cdc37 system resulted in quenching of the fluorescent signal, potentially due to steric interference between Hsp90 and the Avi-tag on Cdc37. The Avi-tag was therefore moved to the N-terminus of Hsp90 based on the single particle cryo-EM structure at the time which showed CDK4 to be positioned at the N-terminus of Hsp90 (Vaughan *et al.*, 2006). This position of the Avi-tag would locate it closest in space to CDK4 and therefore hopefully maximise the FRET signal and emission.

Firstly, attempts were made to confirm the dependency of CDK4 on Cdc37 for the interaction with Hsp90. As described in Section 3.1.1, kinases require Cdc37 to recruit them to Hsp90, and without Cdc37 no binding should occur. The HTRF assay was carried out with Hsp90 in direct binding mode, as described in Section 3.3.6, using a twofold serial dilution of N-Avi Hsp90 from 3 μM combined with a twofold serial dilution of untagged Cdc37 from 1.5 μM . These concentrations were defined by the the 2:1:1 (Hsp90:Cdc37:CDK4) stoichiometry of the complex. Each Hsp90-Cdc37 concentration was titrated against fixed concentrations of 5 nM, 4 nM, 3 nM, 2 nM and 1 nM of the GSTCDKs. No signal was observed in the absence of Cdc37 (Results not shown).

HTRF was then used to measure the interaction of N-Avi Hsp90 via Cdc37 with GSTCDK4 (Figure 3-23 A) and GSTCDK6 (Figure 3-23 B) using the protocol described in Section 3.3.6. From these binding curves $K_{d\text{-app}}$ values of 519 \pm 1.25 nM and 927 nM ($n = 1$) were determined using GSTCDK4 and GSTCDK6 concentrations, each of 5 nM, however the interaction with CDK6 was not reproducible with other Hsp90 samples. Both estimates are near the upper concentration limit of this assay. Hill slope evaluation from analysis showed non-cooperative interactions with either CDK4 and CDK6. The $K_{d\text{-app}}$ of CDK6 to Hsp90 is similar to that observed for direct binding of CDK6 to Cdc37 while that for CDK4 is weaker (>500 nM vs 927 nM and 92 nM vs 519 nM respectively). However, CDK4 is again shown to be a stronger client than CDK6. Previous studies have reported the direct interaction between Cdc37 and Hsp90 to be 1.1 μM (Olesen *et al.*, 2015) which is not dissimilar to the values measured in these

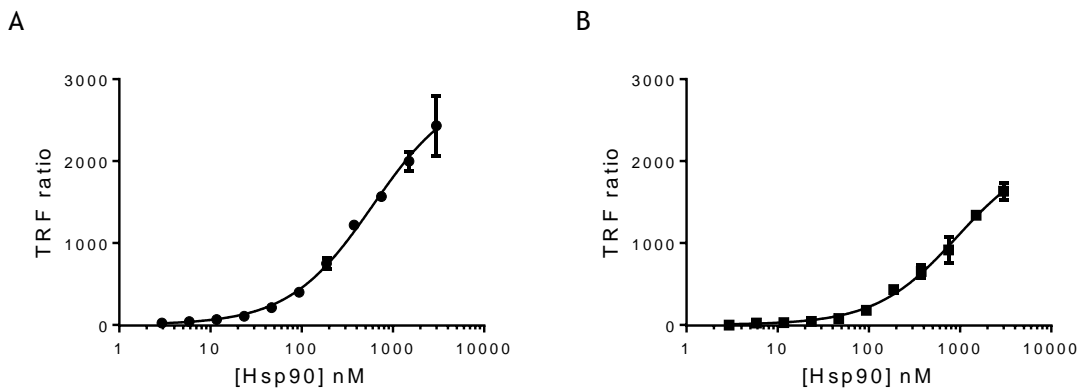


Figure 3-23 GST-CDK-Cdc37-N-Avi Hsp90 complex formation measured by HTRF

Binding curve of the N-Avi Hsp90 interaction with GST-CDK4 (A) and GSTCDK6 (B). The GSTCDK concentration was 5 nM and N-Avi Hsp90 and untagged Cdc37 were titrated in a twofold dilution series from 3 μ M and 1.5 μ M respectively. HTRF measurements were carried out in duplicate a total of 2 times for CDK4, performed on different days, but only once with CDK6. The error bars indicate standard deviation. Binding curves produced using GraphPad Prism.

experiments. These results would suggest that the main driver of client kinase recruitment to the Hsp90 pathway is the interaction of the kinase with Cdc37.

3.6.1 The Q247R mutant did not enhance CDK interactions with Hsp90

A Cdc37 mutant (Cdc37^{Q247R}) was provided by our collaborators. They have shown that it enhances Hsp90 complex stability (Personal communication with Dr Marc Morgan; Postdoc, Pearl lab, University of Sussex). Gln247 is part of the Cdc37 dimerisation interface in the crystal structure of the Cdc37 C-terminal lobe with the Hsp90 N-terminal lobe ((Roe *et al.*, 2004), Figure 3-5) and therefore potential stabilisation of the Hsp90 complex may arise from destabilisation of the Cdc37 dimer. The assay described above was repeated using GSTCDK4 and N-Avi Hsp90 in the presence Cdc37^{Q247R} (Figure 3-24). A modest twofold increase in affinity for the Cdc37^{Q247R} mutant for CDK4 over the wild-type Cdc37 was observed (Kd values of 212 +/- 10.5 nM (n = 2) and 519 +/- 1.25 nM respectively) suggesting some stabilisation of the Hsp90 complex. Hillslope evaluation from analysis suggested potential cooperative effects (1.46 +/- 0.10) unlike the wild-type Cdc37. This mutant may therefore be more prone to aggregation.

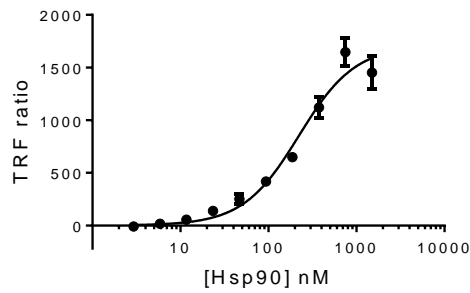


Figure 3-24 The Cdc37^{Q247R} mutant does not dramatically affect the GSTCDK4-N-Avi Hsp90 interaction

Binding curves of the N-Avi Hsp90 interaction with several concentrations of GSTCDK4 via Cdc37^{Q247R}. 5 nM GSTCDK4 was used. HTRF measurements were carried out in duplicate a total of 2 times performed on different days. The error bars represent the standard deviation. Graphs plotted using GraphPad Prism.

Cdc37^{S13E} and Cdc37^{Q247R} were not investigated in more depth due to poor reproducibility of the assay with Hsp90. The CDK4-Cdc37-Hsp90 complex was optimised for use in the HTRF competition mode, described in Section 4.2.4. However, the results were not reproducible and the use of Hsp90 in the competition assay was discontinued. The problems with reproducibility are likely caused by the complexity of the system being measured with multiple proteins potentially forming interactions and dimerising as well as simply the malleability of Hsp90 itself. A summary of the K_{d-app} values determined between Hsp90 and CDK4 or CDK6 is provided in Table 3-2.

Binding partner	Technique	Temperature	CDK4 (nM)	CDK6 (nM)
Hsp90	HTRF	4°C	519 +/- 1.25	927
Cdc37 ^{Q247R}	HTRF	4°C	212 +/- 10.5	ND

Table 3-2 Table of Hsp90 affinities

Summary of K_{d-app} values determined for Hsp90 to CDK4 and CDK6 by different techniques.

3.7 Discussion

The interaction of Cdc37 with CDK4 and CDK6 have been measured through a variety of techniques. While initial pull-downs and SEC experiments were inconclusive, the interaction was analysed quantitatively by HTRF and by MST. The K_d values determined by experiments reported in this Chapter are compiled in Table 3-3. Following considerable optimisation of the HTRF assay protocol, the interaction between Cdc37 and CDK4 has been determined to be 92 ± 29 nM, whereas CDK6 bound significantly weaker with a K_{d-app} of >500 nM. This trend is consistent with previously reported values (Stepanova *et al.*, 1996; Taipale *et al.*, 2012) and suggests that CDK4 would bind preferentially to Cdc37 and be sequestered by the Hsp90 chaperone system. This may reflect either the less stable nature of CDK4 within cells or a greater need for CDK4 regulation to insure appropriate association with binding partners.

The orthogonal technique of MST was also used to measure the interaction between CDK4 and Cdc37. The K_d determined for this interaction from this experiment was 321 nM ± 40.7 nM which lies in the same range as the equivalent K_{d-app} determined by HTRF at room temperature (190 ± 43 nM). Both these values are consistent with the previously published value for the interaction of Cdc37 with an alternative strong kinase client Braf^{V600E} (Vaughan *et al.*, 2006). K_{d-app} values were also determined for the Cdc37-dependent interaction of CDK4 and CDK6 with Hsp90 as 602 nM and 927 nM respectively, although the interaction with CDK6 could not be reproduced. The more similar binding strength of both CDKs for Hsp90 and the far weaker interaction observed for CDK4 suggests that it is this initial tight interaction with Cdc37 that determines the dependency of the client kinases for the Hsp90 chaperone system, and that subsequent binding to Hsp90 is predominantly determined by the Cdc37 interaction with Hsp90.

In direct binding assays the mutation of Ser13 to a glutamate did not appear to alter the interaction between Cdc37 with either CDK4 or CDK6. The K_d values were determined as 56 ± 20 nM and >950 nM respectively. Phosphorylation of Ser13 has been proposed to be a pre-requisite for the interaction of Cdc37 with kinases (Miyata and Nishida, 2004). However, the recent EM structure of a CDK4-Cdc37-Hsp90 complex shows that there is no direct interaction between CDK4 and the phosphorylated Ser13 residue on

Binding partner	Technique	Temperature	CDK4 (nM)	CDK6 (nM)
Cdc37	HTRF	4°C	92 +/- 29	>500
Cdc37 ^{S13E}	HTRF	4°C	56 +/- 20	>950
Hsp90	HTRF	4°C	519 +/- 1.25	927
Cdc37 ^{Q247R}	HTRF	4°C	212 +/- 10.5	ND
Cdc37 ₃₄₈	MST	RT	477 +/- 42.7	ND
	HTRF	RT	190 +/- 43	ND

Table 3-3 Table of CDK4 and CDK6 affinities

Summary of K_d values determined for Cdc37 and Hsp90 to CDK4 and CDK6 by different techniques.

Cdc37. Instead this phosphate group assists in stabilising the Cdc37-Hsp90 fold. Based on this observation, it would be interesting to repeat the Hsp90 experiments with the Cdc37 phosphomimetic mutant as it would be predicted to enhance the stability of the CDK4-Cdc37-Hsp90 complex.

Despite the recent high resolution structure it is difficult to make predictions for further CDK4 residues that could be mutated to affect the interaction between CDK4 and Cdc37 as the interface described between them is limited. Of the interfaces that are visible, interactions with Cdc37 mimic interactions between the N and C kinase lobes and interactions with Hsp90 are predominantly through interactions with extensive regions of the kinase β 4 sheet of the N-terminal lobe. Mutations in these regions would likely lead to a highly unstable CDK4 construct. The main region of Cdc37 in this structure that interacts with CDK4 comprises residues 20-24. Deletion of this region has already been shown to prevent interactions with kinases (Shao *et al.*, 2003). These studies identified Cdc37 residues 2, 3, 4, and 7 as important for kinase recognition. However, in this structure these residues are packed against Hsp90 and do not contribute to the Cdc37-kinase interface. Therefore, instead of further examination of the CDK-Cdc37 interaction, the HTRF assay has been adapted in an attempt to better understand the mechanism through which CDKs are extracted from the Cdc37-Hsp90 chaperone system.

Chapter 4. CDK regulation by the Hsp90 chaperone system

4.1 Introduction

Despite the structural insights provided by the recent cryo-EM structure of the CDK-Cdc37-Hsp90 complex, and crystal structures of sub-domains, the mechanism of Hsp90 action and subsequent client release is still unknown. One hypothesis is that Hsp90 is a more traditional chaperone that can promote and accommodate extensive rearrangements of the kinase fold to support a more favourable transition pathway for phosphorylation events or client binding partner interactions (Taipale *et al.*, 2012; Verba *et al.*, 2016). An alternative model is that Hsp90 may act in a more regulatory role whereby unstable kinases are requisitioned and protected from degradation or dephosphorylation until required, thereby maintaining an active pool ready for a rapid response (Pearl and Prodromou, 2006). It should be noted, that the two hypotheses are not mutually exclusive and share many mechanistic aspects. We have explored the Cdc37-Hsp90 chaperone system in this role whereby CDK4 is sequestered away until released by an appropriate binding partner.

4.1.1 Viral cyclins are surrogates for canonical D-type cyclins

The canonical D-type cyclins, D1, D2 and D3, are not suitable reagents for probing the mechanism of client handoff from the Cdc37-Hsp90 chaperone system as they are unstable as monomeric proteins. They cannot be expressed alone in heterologous expression systems and are frequently found in the insoluble fraction- a state that can be avoided by co-expression with either CDK4 or CDK6. The viral D-type cyclins were therefore explored as surrogates as they can be readily expressed in *E. coli*.

Vcyclin and Kcyclin are cyclins of Herpesvirus saimiri and Kaposi's sarcoma virus respectively. The viral sequences were identified as cyclin homologues as they share 22% sequence identity and 46% similarity to the human cyclin D1 (Figure 4-1) and at 29 kDa are similar in size to a typical cyclin (Jung *et al.*, 1994; Li *et al.*, 1997). Both viral cyclins have been linked to cancer progression. Monkeys infected with Herpesvirus saimiri are prone to lymphomas and leukemias (Jung *et al.*, 1994), and Kaposi's sarcoma virus is associated with increased levels of body cavity lymphomas and lymphoproliferative disorders (Swanton *et al.*, 1997; Kaldis, 2005).

A

```

D1  MEHQLLCCEVETIRRAYPDANLLNDRVLRAMLKAEETCAPSVSYFKCVQKEVLPMSRKIV 60
V   -----MADSPNRLNRAKIDSTTMKDPVRLNNLKLRELLLPKFTSLWEIQTEVTVDNRTIL 55
K   -----MATA-NNPPSGLLDPTLCEDRIFYNILEIEPRFLTSDSVFGTFQQSLTSHMRKLL 54
      :.  :  .  *  .  :*  .  *:  .  .  :  :  .*  .:  *:::

D1  ATWMLEVCEEQKCEEEVFPLAMNYLDRFLSLEPVKKSRLQLLGATCMFVASKMKETIPLT 120
V   LTWMHLLCESFELDKSVFPLSVSILDRYLCKKQGTKKTLQKIGAACVLIIGSKIRTVKPMT 115
K   GTWMFSVCQEYNLEPNVVALALNLLDRLLLIKQVSKEHFQKTGSACLLVASKLRSLTPIS 114
      ***  *:  .  :  :  .*  *::  ***  *  :  .*  :*  *::*:  .:  *:::  *:

D1  AEKLCIYTDNSIRPEELLQMELLLVNKLKWNLAAMTPHDFIEHFLSKMPEAEENKQIIRK 180
V   VSKLTYLSCDCFTNLELINQEKDILEALKWDTEAVLATDFLIPLCNAL---KIPEDLWPQ 172
K   TSSLCYAAADFSRQELIDQEKELLEKLAWRTEAVLATDVTSFLLLKLLGGSQHLDFWHH 174
      ...*  :  ::  **::  *  ::  *  *  *:  *.  :  :  .  ::  :

D1  H---AQTFVALCATDVKFISNPPSMVAAGSVVAAVQGLNLRSPNNFLSYRRLTRFLSRVI 237
V   LYEAASTTICKALIQPNIALLSPGLICAGLLTTIETDNTNCR-PW---TCYLEDLSSIL 228
K   E---VNTLITKALVDPKGTGSLPASIISAAGCALLVPANVIPQDTHS---GGVVPQLASIL 228
      ..*  :  .  :  :  .::.*..  :  :  *  ::

D1  KCDPDCLRACQEQIEALLES-SLRQAQQNMDPKAAEEEEEEEEVLDLACTPTDVRDVDI 295
V   NFSTNTVRTVKDQVSEAFSLYDLEIL----- 254
K   GCDVSVLQAAVEQILTSVSDFDLRILDSY----- 257
      .  .  :::  :*  .  .  .*

```

B

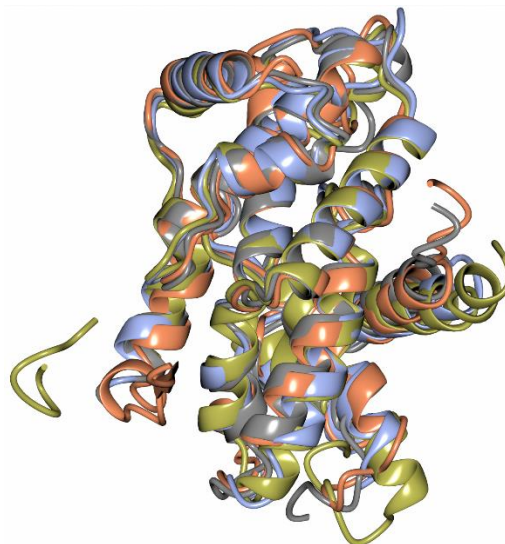


Figure 4-1 The viral cyclins share high structural homology canonical cyclins

(A) Sequence alignment of cyclin D1 with the viral cyclins Vcyclin and Kcyclin. Conserved residues are marked with an ‘*’ and similar residues are marked with a ‘.’. Sequence alignment performed with ClustalOmega (Sievers *et al.*, 2011). (B) Structural alignment of cyclins D1 and D3 with the viral cyclins Vcyclin and Kcyclin to show structural homology. All cyclins are displayed as ribbons. Cyclin D1 and D3 are extracted from the PDB entries 2W96 and 3G33 and drawn in gold and blue respectively. Vcyclin is taken from the structure (2EUF) and is shown in coral and Kcyclin from the structure (1G3N) and is shown in grey. Image produced using CCP4MG (McNicholas *et al.*, 2011).

Vcyclin and Kcyclin have since been well characterised as D-type cyclin homologues found predominantly in complexes with CDK6 (Swanton *et al.*, 1997; Laman *et al.*, 2001) but also weakly associated with CDK4 (Li *et al.*, 1997; Mann *et al.*, 1999; Schulze-Gahmen and Kim, 2002) and to some extent CDK5 (GoddenKent *et al.*, 1997) and CDK2 (Kaldis *et*

al., 2001). However, the viral cyclins appear only to activate CDK6, as shown by immunodepletion assays (Jarviluoma *et al.*, 2004). Once activated, CDK6 bound to viral cyclins can phosphorylate a much broader range of substrates more efficiently than when bound to canonical D-type cyclins. These novel substrates include histone H1, Thr187 of p27KIP1 and CDK2-cyclin E DNA replication targets. Collectively these new activities promote progression into the S-phase of the cell cycle (Mann *et al.*, 1999; Laman *et al.*, 2001; Kaldis, 2005).

The viral cyclins are also resistant to both p27KIP1 and INK inhibition making them completely invulnerable to G1 arrest (Swanton *et al.*, 1997; Jarviluoma *et al.*, 2004). Resistance to p27KIP1 arises from both an altered binding surface on the cyclin where the RXL motif of p27KIP1 binds (Schulze-Gahmen *et al.*, 1999) as well p27KIP1 downregulation. This activity results from the ability of CDK6-Vcyclin to phosphorylate p27KIP1 on Thr187 targeting it for degradation by SCF-Skp2 ubiquitin pathway (Grimmler *et al.*, 2007).

Both p16 and p18 form ternary complexes with CDK6 and Kcyclin which retain some activity. The structure of a ternary p18-CDK6-Kcyclin complex shows p18 distorts the kinase catalytic cleft leading to the misalignment of ATP binding residues, disordering of the activation loop and a reduction in the surface area for the Kcyclin interaction that would prevent canonical cyclin binding (Jeffrey *et al.*, 2000). CDK6-Kcyclin complexes however have been shown to be resistant to INK inhibition when phosphorylated on CDK6 Thr177 suggesting that reordering and stabilisation of the activation loop promotes a more rigid CDK6-Kcyclin structure (Kaldis *et al.*, 2001; Schulze-Gahmen and Kim, 2002). Although Thr177 phosphorylation gives CDK6-Kcyclin complexes resistance to p16 inhibition, unlike the canonical D-type cyclins, viral cyclin activation of CDK6 does not require Thr177 phosphorylation and is capable of phosphorylating downstream targets without it both *in vitro* and *in vivo* (Kaldis, 2005). This activity was identified through a CDK6^{T177A} mutant, which cannot be phosphorylated, and which showed activity in the presence of Kcyclin but not cyclin D1 (Kaldis *et al.*, 2001).

Multiple structures of CDK6-Vcyclin complexes have been determined and reveal that despite their low sequence homology, the viral cyclin adopts a typical all α -helical cyclin fold (Figure 4-1 B). Compared to other cyclins, Vcyclin also has an additional N-terminal

helix and a C-terminal loop which may contribute to the observed altered substrate specificity (Schulze-Gahmen *et al.*, 1999). In these structures the Vcyclin causes CDK6 to adopt the quintessentially active CDK conformation, as described by the phosphorylated CDK2-cyclin A structure, whereby the CDK C-helix is shifted to the 'in' position and the activation segment is ordered (Figure 4-2 A). The ordering of the activation loop arises through an increased interaction surface between the viral cyclin and the CDK activation loop that is 20% larger than that of CDK2-cyclin A (Figure 4-2 B). The extended interaction surface comprises an extensive network of Van der Waals interactions which would clash with the known CDK2 structure and may help to explain the viral cyclin specificity (Schulze-Gahmen and Kim, 2002). However, the orientation of the viral cyclins in relation to the kinase and the interaction entirely with the kinase N-terminal lobe (Schulze-Gahmen *et al.*, 1999) is reminiscent of the CDK4-cyclin D binding model ((Takaki *et al.*, 2009), Figure 4-2 C).

Whether the difference in activation loop conformation observed between CDK6-Vcyclin and CDK4-cyclin D structures is due to an inherent difference in the binding mode of CDK6 or a characteristic of the viral cyclins is not known. To resolve the question will require either a structure of CDK4 bound to a viral cyclin or CDK6 bound to a canonical cyclin partner.

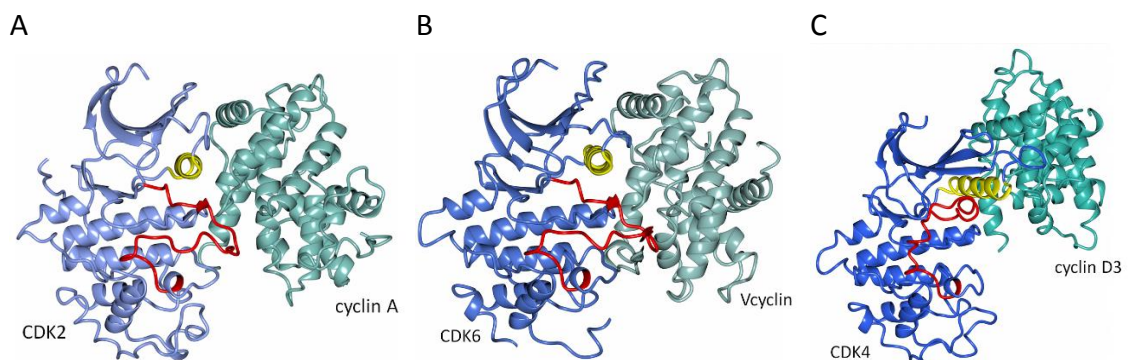


Figure 4-2 Comparison of CDK2-cyclin A to CDK6-Vcyclin and CDK4-cyclin D3

Structural comparison of CDK cyclin complexes. CDK2-cyclin A (A) (PDB: 1JST) shows the classical cyclin to CDK interaction whereby cyclin binding causes repositioning of the C-helix and assists in ordering the activation loop. CDK6-Vcyclin (B) (PDB: 2EUF) also shows the active conformation with a larger cyclin interface with the CDK. In contrast CDK4-cyclin D3 (C) (PDB: 3G33) has a small interface between the CDK and cyclin and remains in an inactive conformation. All proteins are rendered in ribbon representation and are coloured with the CDK in blue, cyclin in green, C-helix in yellow and activation loop in red. Figures created using CCP4MG (McNicholas *et al.*, 2011).

4.1.2 The CIP-KIP family as assembly factors

The cell cycle regulators p21CIP1 and p27KIP1 are a family of intrinsically disordered proteins that are capable of binding and inhibiting all cell cycle CDK-cyclin complexes (Mitrea *et al.*, 2012). However, CDK4-cyclin D complexes containing either p21CIP1 (Zhang *et al.*, 1994) or p27KIP1 (Blain *et al.*, 1997; Larrea *et al.*, 2008; Ou *et al.*, 2011) have been found to be active and still capable of phosphorylating pRb both *in vitro* and *in vivo*. The comparatively weak interaction between CDK4 and canonical cyclins has led to the suggestion that p21CIP1 and p27KIP1 may therefore be required for effective complex formation and indeed p21CIP1 and p27KIP1 have been shown to promote CDK4-cyclin D complex formation that is associated with an increase in kinase activity both *in vitro* and *in vivo* (LaBaer *et al.*, 1997; Cheng *et al.*, 1999). In cell lysates CDK4-cyclin D is almost always associated with the constitutively expressed p27KIP1, whereas CDK6-cyclin D complexes are rarely so (Blain, 2008), while at low concentrations of cyclin D the majority of CDK4 is found in inactive pools with either the INKs or Cdc37-Hsp90 (Dai *et al.*, 1996).

The importance of p21CIP1 and p27KIP1 for CDK4-cyclin D assembly *in vivo* has been shown in studies using mouse embryonic fibroblasts (MEFs) derived from knockout mice whereby cells lacking both p21CIP1 and p27KIP1 failed to assemble CDK4 complexes with cyclin D (Cheng *et al.*, 1999). As a result less cyclin D-associated migration of CDK4 to the nucleus was observed. Overexpression had the opposite effect increasing CDK4-cyclin D levels and reversing the effects caused by knockdown. Unfortunately, CDK6 and cyclin D3 expression in these cells was too low to detect for comparison (Cheng *et al.*, 1999; Sugimoto *et al.*, 2002). Interestingly no halt or adverse effects on the cell cycle were observed suggesting either enough residual CDK4 activity remained or that other CDKs could compensate for the loss (Cheng *et al.*, 1999; Sugimoto *et al.*, 2002).

The structure of CDK2-cyclin A-p27KIP1 shows that the main inhibitory role of p27KIP1 comes from protrusion into the CDK ATP binding pocket thereby preventing ATP binding and hence kinase activity (Figure 4-3 B). The sequence C-terminal to the residues that bind into the ATP binding pocket are not visible, but are hypothesized to head further towards the activation loop as when bound they inhibit CDK2 phosphorylation by CAK (Russo *et al.*, 1996a). The structure shows the N-terminal residues of p27KIP1 (residues 25-50) bind to the cyclin through a coil region and a large α -helix which interacts with α -

with and inhibit each of the cell cycle regulating CDK-cyclin complexes (Yoon *et al.*, 2012). Differences in the interacting residues between CDK2 and CDK4 may limit the hydrophobic interactions to p27KIP1 and reduce binding (Ou *et al.*, 2011).

However, it is hard to see how the binding of such a potent inhibitor is compatible with CDK4-cyclin D activity. An answer to this conundrum came from NMR studies by Grimmier *et al.* which showed that phosphorylation on residues Tyr88 or Tyr89 of p27KIP1, located on the 3_{10} helix, resulted in the ejection of the p27KIP1 sequence from the CDK catalytic cleft. As a result partial catalytic activity was restored, and the post-translational modifications did not affect the overall affinity of p27KIP1 for the tested CDK-cyclin complexes. In the case of CDK2-cyclin E, phosphorylation of Tyr88 also resulted in subsequent intra-molecular phosphorylation of p27KIP1 on Thr187 by CDK2, targeting the p27KIP1 for degradation via the SCF-Skp2 pathway (Grimmier *et al.*, 2007). Phosphorylation of Tyr88 and Tyr89 also tracks with the expression profiles of tyrosine kinases, including Abl and Lyn, which are most active just after G_0 when the activities of CDK4 and CDK6 begin to rise (Blain, 2008). Differences between CDK2-cyclin A and CDK4-cyclin D surface features suggest Tyr88 is more exposed when bound to CDK4 priming it for phosphorylation (Ou *et al.*, 2011). However only 5-10% of CDK4-cyclin D-p27KIP1 complexes are phosphorylated on Tyr88 or Tyr89 in cells which leaves only a small active pool -although seemingly still enough to hyper-phosphorylate pRB (Blain, 2008).

The increased CDK4/6 activity accompanying increased p21CIP1 and p27KIP1 expression may instead be caused by enhanced localisation of CDK4-cyclin D to the nucleus as D-type cyclins lack a nuclear import signal of their own (Cheng *et al.*, 1999). Once in the nucleus, these complexes phosphorylate pocket proteins (LaBaer *et al.*, 1997; Blain, 2008). Alternatively, p27KIP1 interactions may prevent cyclin D1 phosphorylation at Thr286 thereby stabilising it against degradation (LaBaer *et al.*, 1997). The potential role of p21CIP1-p27KIP1 as assembly factors was explored in the context of the Hsp90 chaperone system as a mechanism by which the CIP/KIP proteins could assist D-types cyclins to extract the CDKs from the CDK-Cdc37-Hsp90 complex.

4.1.3 HTRF in competition mode

To investigate the mechanism of client handoff from the Hsp90 chaperone system, the HTRF direct binding assay, described in Section 3.3.6 was adapted to run in competition mode. In competition mode the concentrations of CDK, C-Avi Cdc37, Tb-labelled antibody and SAXL665 remain constant while a dilution series of a potential competitor is introduced (Figure 4-4). The fluorescent signal should therefore remain constant across all conditions unless the CDK-Cdc37 complex is disrupted by the competitor which resulting in a loss in fluorescent signal.

This assay uses the short-range FRET signal to determine the proportion of C-Avi Cdc37 to that of a CDK potential binding partner as exchange of the GSTCDK would result in a drop in fluorescence from the loss of the FRET pair. By poisoning the concentration of C-Avi Cdc37 at the determined CDK-Cdc37 K_d , the contribution of the Cdc37 component can be removed so that the disruption in fluorescent signal is directly related to the concentration of competitor. The fluorescent signal, at a given competitor concentration, is compared to that of an experimentally determined maximum signal, where no competitor is present, and a minimum signal, where no GSTCDK is present, so that the percentage inhibition can be calculated using Equation 4-1. Percentage inhibition was then plotted against competitor concentration using GraphPad Prism.

Due to problems with reproducibility, Hsp90 has not been used in the competition assay. Instead the interaction of Cdc37 has been used as a surrogate for the Cdc37-Hsp90 complex as the initial binding to Cdc37 is required for client kinase binding to Hsp90. This assay format has been used to investigate and compare the abilities of a range of

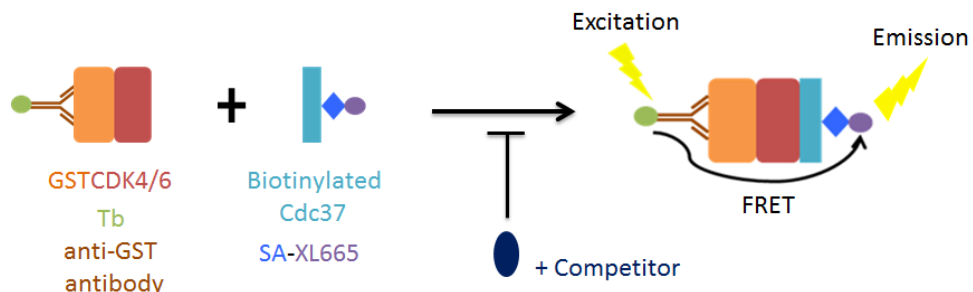


Figure 4-4 Diagram of the HTRF assay in competition mode

The CDK binding partners act as competitors for CDK4(6) and prevent formation of the CDK-Cdc37 complex, resulting in a loss of signal.

$$\% \textit{Inhibition} = \left(\frac{(TRF_{Max} - TRF_{Com})}{(TRF_{Max} - TRF_{Min})} \right) * 100$$

Equation 4-1 % inhibition calculation for competition mode HTRF assays

The percentage inhibition at each competitor concentration was determined. TRF_{max} = the TRF ratio determined from the average of the maximum signal control wells. TRF_{Min} = the TRF ratio determined from the average of the minimum signal control wells. TRF_{Com} = the TRF ratio determined from the average of the signal from wells containing a particular competitor concentration.

CDK binding partners, including the D-type viral cyclins, CIP/KIP proteins, INKs and small molecule ATP-competitive inhibitors, to compete with Cdc37 for binding to CDK4 and CDK6. These experiments aim to develop a better understanding of how these CDK binding partners can compete with the Hsp90 chaperone complex to regulate CDK activity.

4.2 Materials and Methods

All chemicals listed in the materials and methods were of analytical grade and obtained from Sigma Aldrich unless otherwise stated.

4.2.1 Protein production

CDK4 and CDK6 were expressed as N-terminal GST fusions in Sf9 insect cells, either alone or co-expressed with untagged cyclin D1 or cyclin D3 to prepare CDK-cyclin complexes, as described in Section 2.3.6. Kcyclin, Vcyclin, p21CIP1 and p27KIP1 constructs were expressed as N-terminal GST fusions in BL21STAR (DE3) *E. coli*, as described in Section 2.3.7. Cdc37 constructs were also expressed from the BL21STAR (DE3) strain, but were alternatively tagged with an N-terminal His₆ sequence. Proteins were purified as described in Section 2.4.

4.2.2 Biotinylation of Avi-tagged constructs

Avi-tagged Cdc37, Kcyclin and Vcyclin were biotinylated *in vitro* per the protocol outlined in Section 2.4.5

4.2.3 HTRF in direct binding mode

All direct binding HTRF assays were carried out as described in Section 3.3.6

4.2.4 HTRF in Competition mode

Competition mode optimisation

To determine optimum detection reagent concentrations, a matrix of Tb-labelled anti-GST antibody (5, 3, 1, 0.5 and 0.3 nM) and SAXL665 dye (50, 37.5, 18.75 and 9.38 nM for CDK4 and 250, 125, 62.5 and 31.25 nM for CDK6) was assayed against a fixed concentration of either 10 nM GSTCDK4 or GSTCDK6 and either 150 nM or 500 nM C-Avi Cdc37 for CDK4 and CDK6 respectively. The C-Avi Cdc37 concentrations were selected as the K_d values of Cdc37 for CDK4 and CDK6 determined by direct binding assays. Protein components were diluted using HTRF buffer A (50 mM HEPES pH 7.5, 100 mM NaCl, 1 mM DTT and 0.1 mg/ml BSA) while detection reagents were diluted in HTRF buffer B (50 mM HEPES pH 7.5, 100 mM NaCl and 0.1 mg/ml BSA). Incubation times and plate reading were performed as described in Section 3.3.6 for the direct binding mode assay. TRF and signal to noise (S-N) ratios were plotted for each combination of Tb-labelled-anti-GST antibody and dye combination using GraphPad Prism.

For subsequent optimisation of GSTCDK component concentrations GSTCDK4 and GSTCDK6 were titrated as twofold serial dilutions from 25 nM and 50 nM against 150 nM and 1000 nM C-Avi Cdc37 respectively. Protein components were diluted using HTRF buffer A (described above). After 60 minutes incubation at 4 °C, 0.5 nM Tb-labelled anti-GST antibody and 18.75 nM SAXL665 or 3 nM Terbium-labelled anti-GST antibody and 250 nM SAXL665, as determined by the previous experiment, were added to CDK4 or CDK6 respectively. Detection reagents were diluted in HTRF buffer B (described above) and incubation times, plate reading and data analysis were performed as described for the direct binding mode assay in Section 3.3.6. The TRF ratio was plotted against GSTCDK concentration using GraphPad Prism.

Competition mode

Competition mode was used to compare the ability of CDK binding partners to compete with full-length Cdc37. 8 nM GSTCDK4 and 150 nM C-Avi Cdc37, or 6 nM GSTCDK6 and 500 nM C-Avi Cdc37, as determined above, were added to each well with a twofold serial dilution of the competitor protein, set up in duplicate. Concentrations of the competitor protein varied depending on their suspected K_d values from the literature and preliminary results. All protein dilutions were made using HTRF buffer A (50 mM HEPES

pH 7.5, 100 mM NaCl, 1 mM DTT and 0.1 mg/ml BSA). Following incubation for 60 minutes at 4°C, 0.5 nM Tb-labelled anti-GST antibody and 18.75 nM SAXL665 (for CDK4 measurements) or 3 nM Tb-labelled anti-GST antibody and 62.5 nM of SAXL665 (for CDK6 measurements), as determined from the previous experiment described above, were added to each well. Concentrations of detection reagents were prepared using HTRF buffer B (50 mM HEPES pH 7.5, 100 mM NaCl and 0.1 mg/ml BSA). The plate was incubated for a further 120 minutes at 4°C before being scanned using the PHERAstar FS (BMG LABTECH) as described in Section 3.3.6. Percentage inhibition at a given competitor concentration was determined using Equation 4-1 and plotted against competitor concentration, using GraphPad Prism 6.

4.2.5 Competitive pull-downs

Competitive pull-downs for the comparison of Cdc37 and Cdc37-Hsp90 binding to CDK4 or CDK6 in the presence of cyclin D1 or cyclin D3, shown in Section 1.4.3, were performed by Dr Martyna Pastok (Postdoc, Endicott lab, NICR). 90 nmol of N-terminally FLAG-tagged Cdc37 or Cdc37-Hsp90 complex were incubated for 60 minutes at 4 °C with 30 µl Anti-FLAG M2 Affinity Agarose Gel (Sigma Aldrich) in 20 mM Tris pH 7.5, 150 mM NaCl, 5 mM Na₂MoO₄, 0.5 mM EDTA, 0.5 mM TCEP and 0.5% Igepal. A 3-fold molar excess of CDK-cyclin D complexes, purified from insect cells, was added and incubated for a further 60 minutes at 4 °C. Each pull-down was washed 3 times using 200 µl of pull-down buffer, the resin pelleted using a table top microcentrifuge at 8000 x g for 3 mins and the supernatant removed after each incubation period. Pull-downs were boiled in 10 µl SDS loading dye prior to separation by SDS-PAGE. Proteins were visualised by InstantBlue staining.

4.3 Results

4.3.1 Competition mode optimisation

The HTRF assay was adapted from measuring the direct binding of CDKs to their partners to a competition mode whereby we could evaluate the ability of binding partners to compete with Cdc37 for the CDKs. Firstly, the concentrations of detection reagents were optimised by comparing the TRF ratios from a matrix of detection reagent concentrations to ensure the maximum signal with minimum background noise. For CDK4 the combination of 0.5 nM Tb-labelled anti-GST antibody and 18.75 nM SAXL665

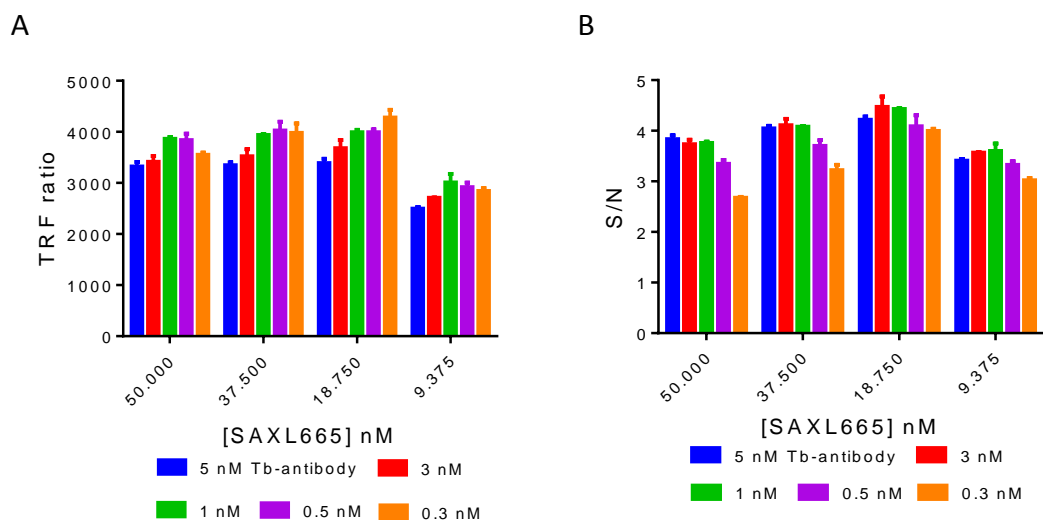


Figure 4-5 Optimisation of detection reagents for the GSTCDK4-C-Avi Cdc37 interaction

Detection reagent concentrations were optimised using a matrix of Tb-antibody and SAXL665 concentrations. Plot of (A) the fluorescent signal and (B) the signal to noise ratio obtained from a matrix of Tb- labelled anti-GST antibody and streptavidin-labelled dye with GSTCDK4-C-Avi Cdc37. Streptavidin bound dye concentration is displayed on the x-axis. In each panel the Tb-labelled anti-GST concentration of 5 nM is shown in blue, 3 nM in red, 1 nM in green, 0.5 nM in purple, and 0.3 nM in orange. The error bars represent the standard deviation of the measurements. Graphs were plotted using GraphPad Prism.

gave one of the strongest signals, at *circa* 4000 (Figure 4-5 A), while maintaining a high signal to noise ratio, (of *circa* 4, Figure 4-5 B). However, it should be noted that there was little difference between each of the sets of conditions except for at the lowest concentrations of dye, which produced a smaller signal, and antibody, which resulted in a lower S-N ratio.

The same set of experiments were carried out to optimise the reagent concentrations for the competition assay with GSTCDK6. Despite a lower TRF signal (*circa* 1750), it was still sufficient to allow for a loss in signal to be robustly detected. The final reagent concentrations for GSTCDK6 were 3 nM Tb-labelled anti-GST antibody and 62.5 nM SAXL665. These concentrations were used for all subsequent competition experiments described here.

Finally, having optimised the fluorophore concentrations, the concentration of the GSTCDK component was optimised. Twofold serial dilutions of GSTCDK4 or GSTCDK6, from 25 nM or 50 nM respectively, were titrated against fixed concentrations of C-Avi Cdc37. From the resulting plots of TRF ratio against GSTCDK concentration the concentration that gave the largest fluorescent signal while still in the initial linear range

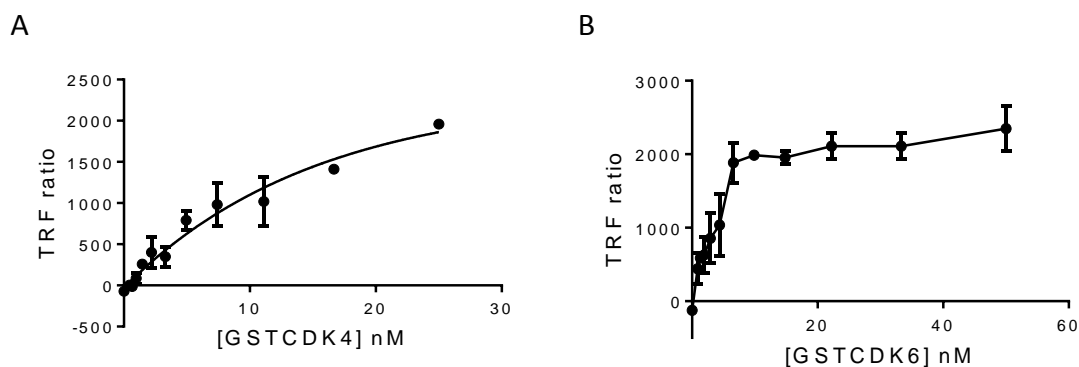


Figure 4-6 Optimisation of the GSTCDK concentrations for use in the HTRF assay in competition mode

The concentrations of GSTCDK were optimised for use in the HTRF competition assay. Fluorescent signal was plotted against increasing GSTCDK concentrations. Plot of fluorescent signal with increasing GSTCDK4 (A) or GSTCDK6 (B) concentration. Graphs were plotted using GraphPad Prism. The error bars represent the standard deviation of the measurements.

for each was determined. For CDK6, the peak of the initial linear range was clearly defined as 6 nM (Figure 4-6 B), shown by the clear plateau in TRF ratio above this concentration. This region was far less distinct for CDK4 (Figure 4-6 A). However, a concentration of 8 nM GSTCDK4 was selected after which the signal began to level off. These concentrations were used for all subsequent HTRF competition assays outlined in this work.

In summary, these modifications to the assay resulted in a dramatic improvement in the lower limit of detection as well as a reduction in the concentrations of proteins and detection reagents required (Table 4-1).

Assay component	Initial conditions (nM)	Revised conditions (nM)
GSTCDK4	625	8
C-Avi Cdc37	250	150
Tb-anti GST-antibody	7	0.5
SA-XL665	31.25	18.75

Table 4-1 Optimisation of the competition assay at 4 °C has greatly reduced the concentrations of reagents required

Changes in conditions for the HTRF assay in competition mode.

4.3.2 The viral cyclins bind tightly to CDK4 and CDK6.

The ability of the D-type cyclins to displace the CDKs from the Cdc37-Hsp90 complex was interrogated with the HTRF assay by using the CDK-Cdc37 interaction as a surrogate for the CDK-Cdc37-Hsp90 complex. As the canonical D-type cyclins are insoluble when expressed alone, the viral cyclins, Vcyclin and Kcyclin were used as surrogates. Full-length viral cyclins were used for all experiments.

Preliminary pull-downs and SEC experiments showed that the viral cyclins bound to both CDK4 and CDK6. The HTRF assay was used in direct binding mode, as described in Section 3.3.6 to quantify these interactions. For these experiments serial dilutions of C-terminal Avi-tagged viral cyclins were prepared starting at 500 nM and titrated against fixed concentrations of GSTCDK4 and GSTCDK6. Vcyclin bound very tightly to CDK4 (Figure 4-7 A) and CDK6 (Figure 4-7 B) at 24.7 ± 5.7 nM and 11.8 ± 2.9 nM respectively. Hillslope evaluation from binding curves gave 1.34 ± 0.11 and 1.81 ± 0.36 for CDK4 and CDK6 respectively suggesting cooperative effects with both CDKs. Vcyclin binding analysis however was severely affected by hook effects. The difference in binding between CDK4 and CDK6 was surprisingly small and much tighter than expected for CDK4. However, the K_{d-app} for CDK6 lies close to the limit of detection (10 nM) and as such may not be accurately determined. This high affinity interaction coupled with high level of expression associated with viral proteins would result in rapid association and activation of the CDKs. These experiments also suffered greatly from signal drop off at high Vcyclin concentrations. This phenomenon is most commonly caused by the Hook effect, whereby insufficient detection reagents are present, and may signify some carry

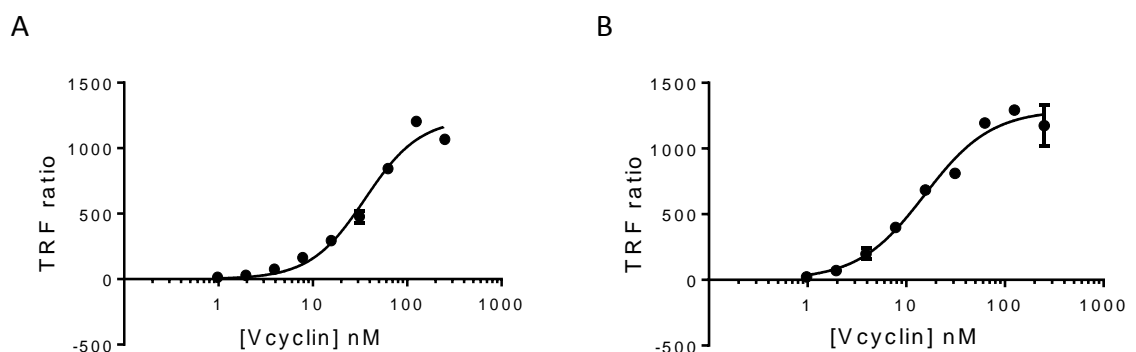


Figure 4-7 Vcyclin binds very tightly to CDK4 and CDK6

Binding curves for the interaction of C-Avi Vcyclin with GSTCDK4 (A) and GSTCDK6 (B). Binding curves produced using GraphPad Prism. HTRF measurements were carried out in duplicate a total of 3 times for both CDKs performed on different days. The error bars represent the standard deviation of the measurements.

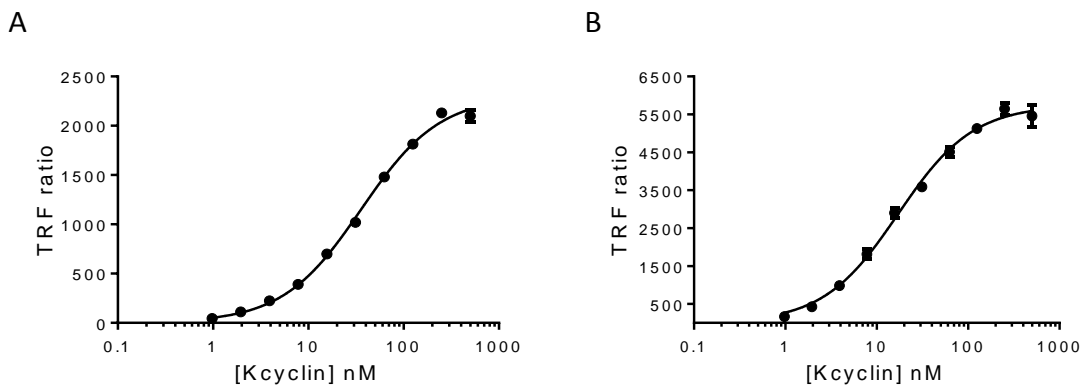


Figure 4-8 Kcyclin binds very tightly to CDK4 and CDK6

Binding curves for the interaction of the C-Avi Kcyclin interaction with GSTCDK4 (A) and GSTCDK6 (B). Binding curves produced using GraphPad Prism. HTRF measurements were carried out in duplicate a total of 3 times for both CDKs performed on different days. The error bars represent the standard deviation of the measurements.

through of excess biotin from the biotinylation reaction. The topmost concentrations have therefore been removed from the binding curves.

The interaction of Kcyclin with CDK4 (Figure 4-8 A) and GSTCDK6 (Figure 4-8 B) was also determined by HTRF. K_{d-app} values determined for these interactions were 31.3 ± 9.9 nM and 13.0 ± 4.4 nM for CDK4 and CDK6 respectively. Hill slope evaluation from analysis gave 1.07 ± 0.10 and 1.66 ± 0.34 for CDK4 and CDK6 respectively suggesting cooperative effects only with CDK6. These values are almost identical to those determined with Vcyclin and show a slight preference for viral cyclin binding to CDK6. The interactions with Kcyclin did not suffer from the same drop in fluorescent signal as observed for Vcyclin.

As a control, potential background interactions of the viral cyclins to GST were investigated by HTRF as some non-specific interactions had been observed during preliminary pull-down experiments. For these experiments the same dilution series of the viral cyclins were titrated against 10 nM of GST as the bait. Some low level non-specific binding is present for both viral cyclins with GST although the interaction is much weaker for Kcyclin (Figure 4-9 A). The interaction with Vcyclin (Figure 4-9 A) was more readily detectable and the fluorescent signal began to rise considerably after 100 nM. However, these signals produced from non-specific interactions are much smaller than the respective CDK binding curves. They are indicative of an interaction of much reduced affinity and as such the overall signal was not adjusted to take this contribution into

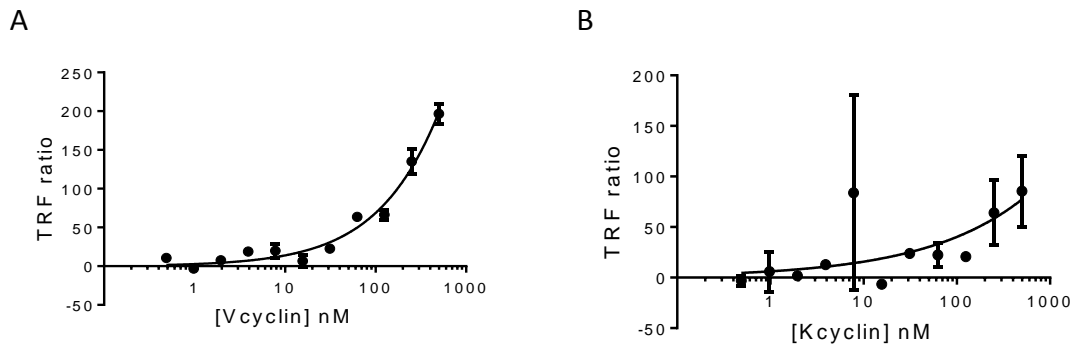


Figure 4-9 Assessment of the non-specific binding between Vcyclin and GST

Negative controls to assess the background (non-specific) binding of C-Avi Vcyclin (A) or C-Avi Kcyclin (B) to GST. Binding curves produced using GraphPad Prism. Measurements were carried out only once in duplicate. The error bars represent the standard deviation of the measurements.

account. The interaction of Vcyclin with GST may partly explain the loss of fluorescence observed at higher Vcyclin concentrations due to an increase in non-specific binding.

The tight binding of the viral cyclins to both CDK4 and CDK6 is somewhat unexpected. Previous studies have shown the viral cyclins to either only interact with CDK6 (Jung *et al.*, 1994; GoddenKent *et al.*, 1997) or to have much higher affinity for CDK6 than CDK4 (Li *et al.*, 1997; Mann *et al.*, 1999; Jarviluoma *et al.*, 2004). However, these studies have all extracted the complexes from cells which may possess alternative mechanisms that affect cyclin binding to CDK4. It is also possible, due to its vicinity to the lower limit of detection, that the interaction between CDK6 and Vcyclin is much tighter than determined.

4.4 Trends in D-type cyclin binding to CDKs

4.4.1 The viral cyclins differ in their ability to displace the CDKs from Cdc37

The direct binding assays showed that both viral cyclins were capable of binding tightly to CDK4 and CDK6. Next their ability to compete with Cdc37 was explored. For these experiments the HTRF assay was used in competition mode as described in Section 4.2.4. Here untagged Vcyclin and Kcyclin were titrated in a twofold dilution from 500 nM against the GSTCDK4-C-Avi Cdc37 and GSTCDK6-C-Avi Cdc37 complexes.

The inhibition curves for both viral cyclins with CDK6 (Figure 4-10 B) show rapid disruption of the Cdc37-containing complex shown by the sharp rise to 100% inhibition at low viral cyclin concentrations. This rapid disruption reflects what would be expected

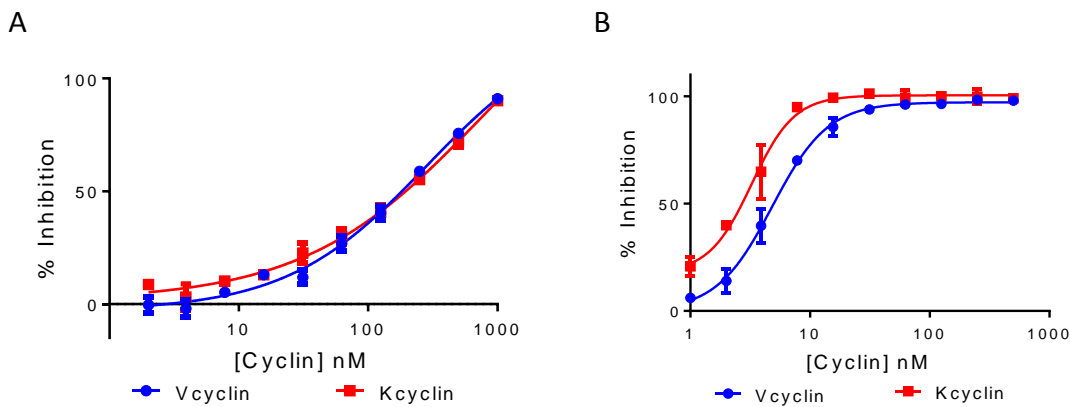


Figure 4-10 The viral cyclins strongly compete with Cdc37 for CDK6 but not CDK4

(A) Inhibition curves showing disruption of the GSTCDK4-C-Avi Cdc37 complex by HTRF. Vcyclin inhibition is shown in blue. Kcyclin inhibition is shown in red. (B) Inhibition curves showing the disruption of the GSTCDK6-C-Avi Cdc37 complex by HTRF. Measurements with both viral cyclins were carried out in duplicate a total of 3 and 5 times with CDK4 and CDK6 respectively performed using two independently expressed and purified samples. Kcyclin and Vcyclin used for one repeat produced by Dr Martyna Pastok (Postdoc, Endicott lab, NICR). Vcyclin inhibition is shown in blue. Kcyclin inhibition is shown in red.

for a tight binding protein as determined by the direct binding assays. The K_d values for the inhibition curves with CDK6 cannot accurately be determined as they are beyond the lower limit of detection of the system (6 nM), which is the concentration of

GSTCDK6. These curves suggest that the interaction of the viral cyclins with CDK6 are even tighter than those determined by the direct binding assay. It is therefore likely that the viral cyclins would readily displace CDK6 from Cdc37 and the Hsp90 complex at low concentrations. The inhibition curves with CDK4 (Figure 4-10 A) do not have a profile expected from the direct binding results, which showed the viral cyclins to bind almost as tightly to CDK4 as to CDK6. Instead they show the viral cyclins to be only weak competitors of Cdc37 for binding to CDK4.

4.4.2 Assessment of the ability of Cdc37 to displace viral cyclins from their CDK partners

As demonstrated above, the viral cyclins vary in their ability to displace Cdc37 from a CDK-Cdc37 complex. The next set of experiments aimed to determine whether the reverse reaction is also the case, i.e. does Cdc37 displace viral cyclins from their CDK partners, and if so does the Cdc37 activity correspond to that we might predict: The viral cyclins have a greater ability to compete CDK6 from Cdc37 in the competition assay (Figure 4-10).

Both of the viral cyclins were bound to CDK4 and CDK6 *in vitro* and the complexes were purified by SEC. As expected from the previous competition assay results, a clear preference of the viral cyclins for CDK6 over CDK4 was observed for both Vcyclin and Kcyclin. This result shows that there is no disruption of the CDK6-Kcyclin complex by Cdc37 in the concentration range used. This trend of incredibly tight binding also correlates with the direct binding assay which showed that the viral cyclins bound with 10 nM affinity or less to CDK6 (Figure 4-7, Figure 4-8). CDK4 showed a very different behaviour and readily redistributed to Cdc37 from the viral cyclins (Figure 4-11 A and C). However, it should be noted that this observation is not what might have been expected,

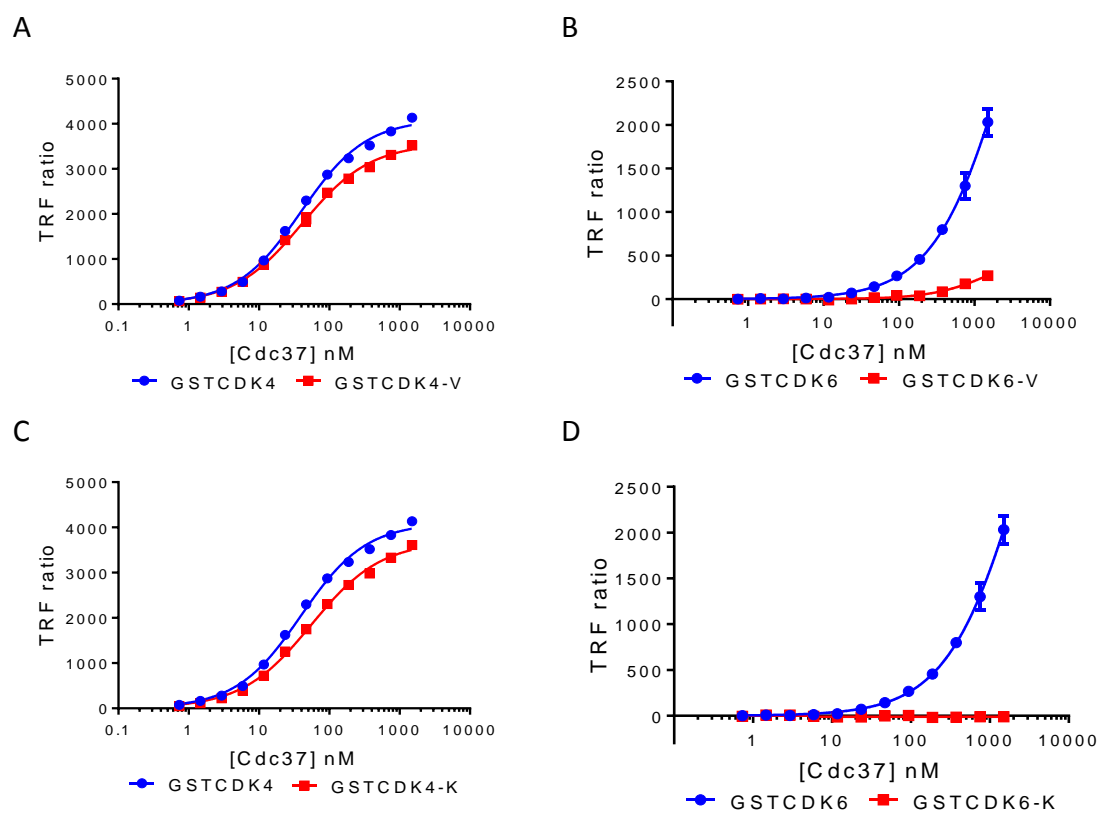


Figure 4-11 Viral cyclin containing CDK6 complexes are resistant to Cdc37 displacement whereas those containing CDK4 are not

(A) Binding curve for the interaction of C-Avi Cdc37 with GSTCDK4 or GSTCDK4-Vcyclin. GSTCDK4 binding curve shown in blue, GSTCDK4-Vcyclin binding curve shown in red. (B) Binding curve of the C-Avi Cdc37 interaction with GSTCDK6 or GSTCDK6-Vcyclin. GSTCDK6 binding curve shown in blue, GSTCDK6-Vcyclin binding curve shown in red. (C) Binding curve of the C-Avi Cdc37 interaction with GSTCDK4 or GSTCDK4-Kcyclin. GSTCDK4 binding curve shown in blue, GSTCDK4-Kcyclin binding curve shown in red. (D) Binding curve of the C-Avi Cdc37 interaction with GSTCDK6 or GSTCDK6-Kcyclin. GSTCDK6 binding curve shown in blue. GSTCDK6-Kcyclin binding curve shown in red. Graphs plotted using GraphPad Prism. Measurements performed only once in duplicate. The error bars represent the standard deviation of the measurements.

given that Kds of *circa* 30 nM were measured for the direct interaction between CDK4 and each of the viral cyclins, and that the experiment was only performed once.

These findings instead correlate with the weak displacement of CDK4 from Cdc37 by the viral cyclins observed in the competition assay (Figure 4-10). They also agree with the literature which suggests that the viral cyclins preferentially bind and activate CDK6 (Jung *et al.*, 1994; GoddenKent *et al.*, 1997; Li *et al.*, 1997; Mann *et al.*, 1999; Jarviluoma *et al.*, 2004). Taken together these findings show that the viral cyclins would preferentially displace CDK6 from the Hsp90 chaperone complex over CDK4.

4.4.3 D-type cyclins vary in their affinities for CDK4 and CDK6

The observed difference between the viral cyclins' abilities to displace CDK4 and CDK6 from Cdc37 may simply be a property of the viral cyclins and as such may not reflect the interaction between CDK4 and CDK6 with Cdc37. We therefore wanted to compare the displacement profiles of the viral cyclins to the canonical D-type cyclins. As mentioned previously, the canonical D-type cyclins are insoluble as monomers and therefore we were unable to directly repeat the competition experiment above. Instead, we again approached the question from the other direction and investigated the ability of C-Avi Cdc37 to disrupt co-purified CDK-canonical cyclin complexes. For this set of experiments, the direct binding assay format was used as described in Section 3.3.6. However, C-Avi Cdc37 was titrated against pre-purified full-length GSTCDK-cyclin D complexes. In this experiment a shift towards the right, at higher Cdc37 concentrations, would signify a stronger interaction of the cyclin with the CDK. This assay format is not quantitative for the cyclin interaction as the canonical D-type cyclins are not poised at their K_d concentrations. However, it does permit comparison of the ability of each of the D-type cyclins to resist competition by Cdc37 and to reveal if there are any differences between CDK4 and CDK6.

First, CDK-cyclin D1 complexes were interrogated for their ability to resist displacement by Cdc37. As previously observed, there is a considerably tighter interaction between C-Avi Cdc37 and GSTCDK4 (Figure 4-12 A) than between C-Avi Cdc37 and GSTCDK6 (Figure 4-12 B). Interestingly however when Cdc37 was introduced in the presence of cyclin D1 (red curves) the binding curves were almost indistinguishable from those without the cyclin present (blue curves). The similar increase in fluorescent signal, from the

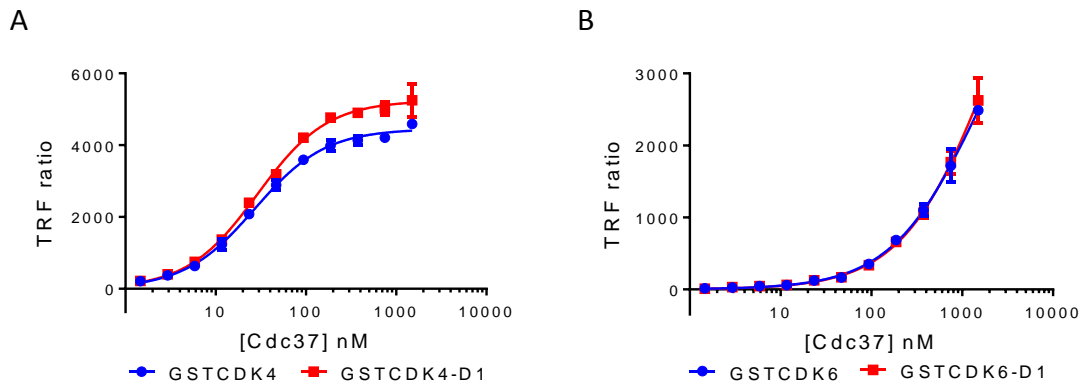


Figure 4-12 Cyclin D1 is readily displaced from CDK4 and CDK6 by Cdc37

(A) Binding curve of the C-Avi Cdc37 interaction with GSTCDK4 or GSTCDK4-cyclin D1. GSTCDK4 binding curve shown in blue. GSTCDK4-cyclin D1 binding curve shown in red. (B) Binding curve of the C-Avi Cdc37 interaction with GSTCDK6 or GSTCDK6-cyclin D1. GSTCDK6 binding curve shown in blue. GSTCDK6-cyclin D1 binding curve shown in red. HTRF measurements were carried out in duplicate a total of 5 and 4 times for CDK4 and CDK6 respectively using two independently expressed and purified GSTCDK and GSTCDK-cyclin D1 samples. Error bars represent the standard deviation of the measurements. Graphs plotted using GraphPad Prism.

formation of the GSTCDK-C-Avi Cdc37 complex, shows that cyclin D1 was readily displaced by Cdc37 from both CDK4 and CDK6 and suggests weaker binding of cyclin D1 to the CDKs compared to Cdc37. The poor ability of cyclin D1 to compete Cdc37 for CDK binding suggests that they would struggle to displace the CDKs from the Hsp90 complex in a cellular context unless high concentrations of cyclin D1 were achieved.

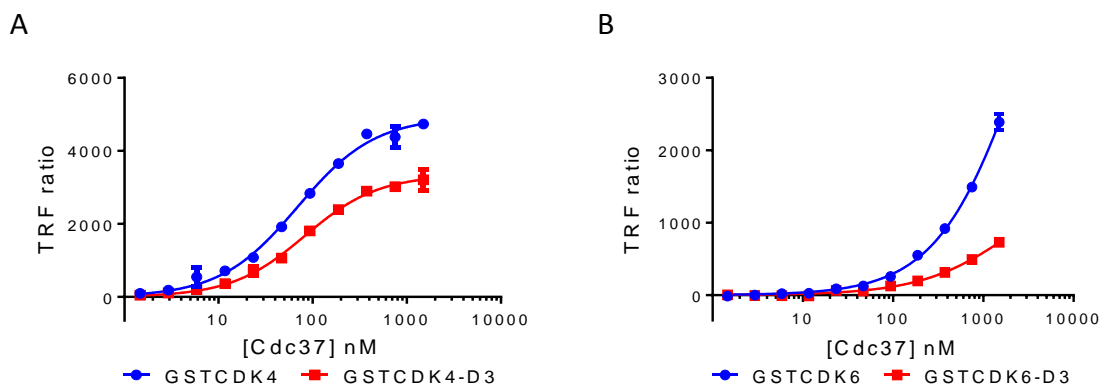


Figure 4-13 The CDK6-cyclin D3 complex is more stable to Cdc37 disruption

(A) Binding curve of the C-Avi Cdc37 interaction with GSTCDK4 or GSTCDK4-cyclin D3. GSTCDK4 binding curve shown in blue. GSTCDK4-cyclin D3 binding curve shown in red. (B) Binding curve of the C-Avi Cdc37 interaction with GSTCDK6 or GSTCDK6-cyclin D3. GSTCDK6 binding curve shown in blue. GSTCDK6-cyclin D3 binding curve shown in red. HTRF measurements were carried out in duplicate a total of 8 times for both CDKs using two independently expressed and purified GSTCDK and GSTCDK-cyclin D3 samples. Error bars represent the standard deviation of the measurements. Graphs plotted using GraphPad Prism.

The HTRF experiment was repeated with GSTCDK-cyclin D3 complexes. This time cyclin D3 formed a complex with CDK6 which was resistant to disruption by Cdc37. This behaviour is revealed by the reduction of fluorescence in the presence of cyclin D3 (Figure 4-13 B red curve) compared to in its absence (Figure 4-13 B blue curve) and distinguishes cyclin D3 from cyclin D1. CDK4, on the other hand, was again readily displaced from cyclin D3 by Cdc37 resulting in a broadly similar binding curve to that observed with cyclin D1 (Figure 4-13 A). The ability of cyclin D3 bound to CDK6 to resist disruption by Cdc37 suggests cyclin D3 binds more tightly to CDK6 than cyclin D1 and that it would be more able to displace CDK6 from a Cdc37-Hsp90 complex.

HTRF experiments involving Hsp90 have proven unreliable and hard to reproduce. Competitive pull-downs, as described in Section 4.2.4, have therefore been performed by Dr Martyna Pastok (Postdoc, Endicott lab, NICR) to determine the interactions between Cdc37, and CDK or CDK-cyclin complexes. Figure 4-14 shows that when FLAG-Cdc37 is now bound to beads, cyclin D1 is again readily displaced from both CDK4 and CDK6 (Figure 4-14), while only CDK4 is displaced from cyclin D3 (Figure 4-14 A). These

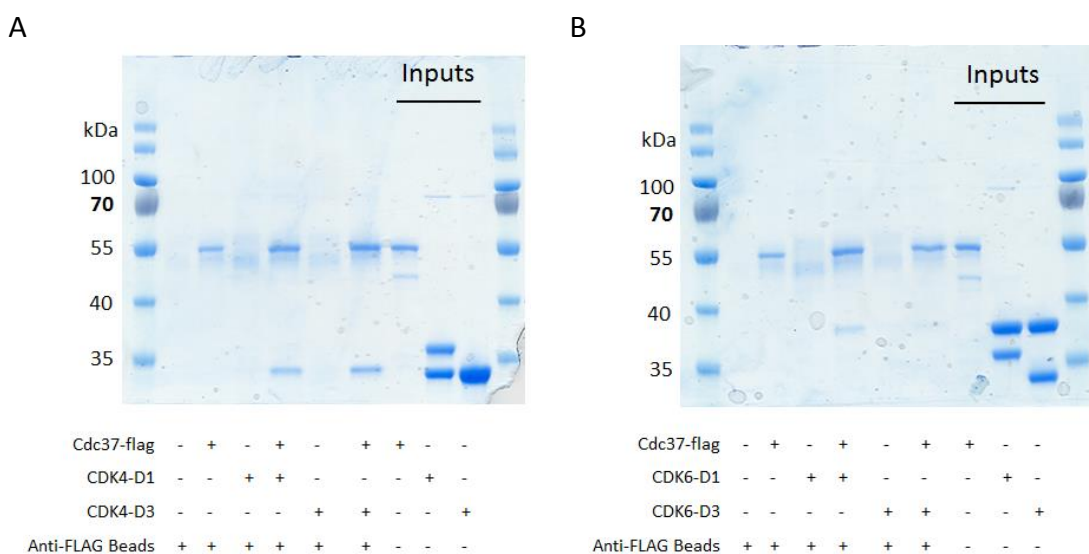


Figure 4-14 Cyclin D1 and D3 can be distinguished by their displacement from CDK4 and CDK6 by CDC37

FLAG-Cdc37 pull-downs. Samples prepared and pull-down performed by Dr Martyna Pastok (Postdoc, Endicott lab, NICR). (A) Incubation of CDK4-cyclin D1 and CDK4-cyclin D3 with Cdc37-FLAG charged anti-FLAG beads. CDK4 readily redistributes into a complex with CDK4 and cyclin D1 or D3 is not present in the pull down. (B) Incubation of CDK6-cyclin D1 and CDK6-cyclin D3 with Cdc37-FLAG charged anti-FLAG beads. CDK6 readily redistributes from CDK6-cyclin D1 into a complex with Cdc37, but not when bound to cyclin D3. The constituent components of each pull-down are displayed below the gels.

pull-downs are not quantitative and do not distinguish if the redistribution is due to a stronger interaction of Cdc37, or a weaker interaction of cyclin D3 with CDK4 as opposed to CDK6. They do, however, confirm that the interaction between Cdc37 and CDK client is mutually exclusive with CDK-cyclin association.

4.5 p27KIP1 can act as an assembly factor

The direct binding assays to measure the activity of Cdc37 towards CDK4-cyclin D complexes show that CDK4 is not readily displaced from a Cdc37-Hsp90 chaperone complex by D-type cyclins. In all experiments so far CDK4 has been observed to readily redistribute into a complex with Cdc37, while CDK6 preferentially complexes with the viral cyclins and to some extent cyclin D3. Therefore, the potential role of p21CIP1 and p27KIP1 as an accessory factor to assist in CDK4-cyclin D complex formation was explored as a mechanism by which D-type cyclins could compete with the Hsp90 chaperone complex for CDK4.

4.5.1 p27KIP1 and p21CIP1 stabilise CDK-cyclin complexes to disruption by Cdc37

When C-Avi Cdc37 was titrated against 10 nM of co-purified CDK-cyclin D1-p27M complexes, dramatic reductions in the ability of Cdc37 to displace the CDKs were observed for both CDK4 (Figure 4-15 A) and CDK6 (Figure 4-15 B). In the presence of p27M (green curves) almost no fluorescent signal was detected demonstrating that the Avi-tagged Cdc37 was not binding to CDK4 or CDK6 in appreciable amounts. In contrast, when CDK-cyclin D1 complexes were incubated with Cdc37 (red curves) significant cyclin D displacement by Cdc37 was observed.

The experiment was repeated starting from CDK-cyclin D3-p27M complexes and they too were highly resistant to disruption by C-Avi Cdc37. For both CDK4 (Figure 4-16 A) and CDK6 (Figure 4-16 B) almost no increase in fluorescence in the presence of p27M (green curves) was observed. To confirm that this stabilisation effect was not a property only of p27KIP1 and was shared with p21CIP1, the p21M fragment was also co-purified with CDK4-cyclin D3 and included in the assay (Figure 4-16 A purple line). p21M was just as effective as p27M at stabilising CDK4-cyclin D3 and no increase in fluorescence was observed.

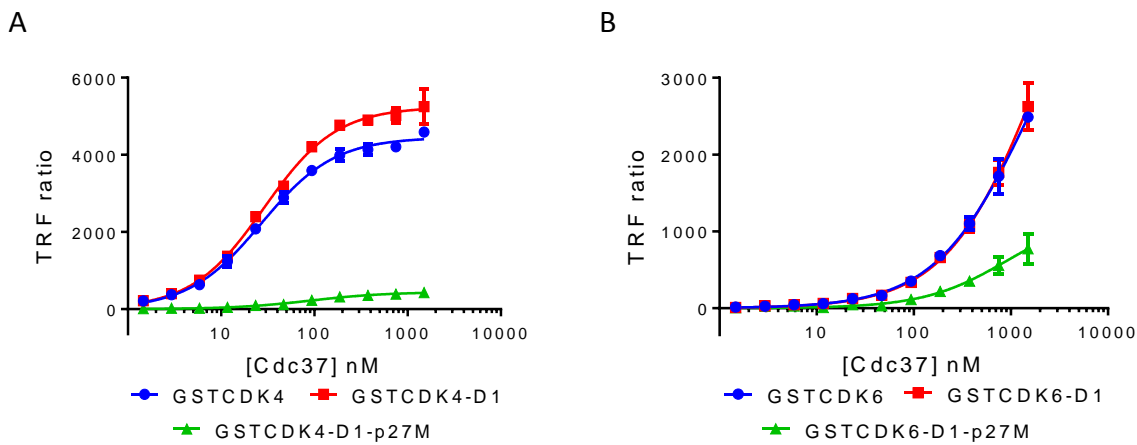


Figure 4-15 p27 stabilised CDK4-cyclin D1 and CDK6-cyclin D1 complexes against Cdc37

(A) Binding curve of the C-Avi Cdc37 interaction with GSTCDK4, GSTCDK4-cyclin D1 or GSTCDK4-cyclin D1-p27KIP1M. GSTCDK4 binding curve shown in blue. GSTCDK4-cyclin D1 binding curve shown in red. GSTCDK4-cyclin D1-p27KIP1M binding curve shown in green. (B) Binding curve of the C-Avi Cdc37 interaction with GSTCDK6, GSTCDK6-cyclin D1 or GSTCDK6-cyclin D1-p27KIP1M. GSTCDK6 binding curve shown in blue. GSTCDK6-cyclin D1 binding curve shown in red. GSTCDK4-cyclin D1-p27KIP1M binding curve shown in green. HTRF measurements were carried out in duplicate a total of 4 times for both CDKs using two independently expressed and purified GSTCDK-cyclin D1-p27KIP1M samples. The error bars represent the standard deviation of the measurements. Graphs plotted using GraphPad Prism.

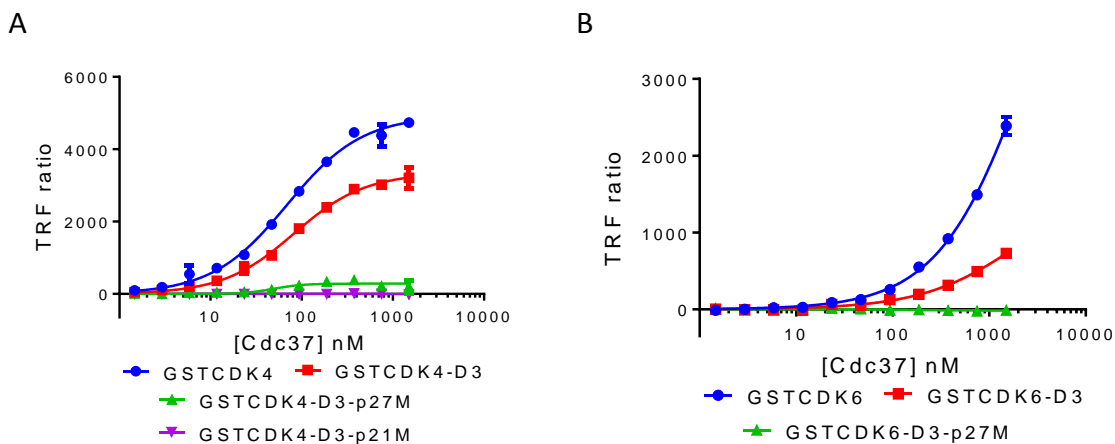


Figure 4-16 p27KIP1 and p21CIP1 stabilise CDK4-cyclin D3 and CDK6-cyclin D3 complexes against Cdc37

(A) Binding curve of the C-Avi Cdc37 interaction with GSTCDK4, GSTCDK4-cyclin D3, GSTCDK4-cyclin D3-p27KIP1M or GSTCDK4-cyclin D3-p21CIP1M. GSTCDK4 binding curve shown in blue. GSTCDK4-cyclin D3 binding curve shown in red. GSTCDK4-cyclin D3-p27KIP1M binding curve shown in green. GSTCDK4-cyclin D3-p21CIP1M binding curve shown in purple. (B) Binding curve of the C-Avi Cdc37 interaction with GSTCDK6, GSTCDK6-cyclin D3 or GSTCDK6-cyclin D3-p27KIP1M. GSTCDK6 binding curve shown in blue. GSTCDK6-cyclin D3 binding curve shown in red. GSTCDK6-cyclin D3-p27KIP1M binding curve shown in green. HTRF measurements were carried out in duplicate a total of 8 times for both CDKs using two independently expressed and purified GSTCDK-cyclin D3-p27KIP1M samples. Measurements for p21CIP1M were only performed once in duplicate. The error bars represent the standard deviation of the measurements. Graphs plotted using GraphPad Prism.

The increase in stability of CDK-cyclin D complexes when challenged with Cdc37 in the presence of p21CIP1 or p27KIP1 suggests that these binding partners could assist in CDK-cyclin D complex formation helping to partition these complexes away from Cdc37-Hsp90. The increased stability observed for the CDK6-cyclin D3 in the presence of Cdc37 suggests that this complex is more likely to form independently of p21CIP1 and p27KIP1. However, the instability of CDK4-cyclin D complexes suggests higher levels of cyclin D1 or D3 or the presence of p21CIP1 or p27KIP1 would be needed before CDK4 is displaced from the Cdc37-Hsp90 chaperone system.

4.5.2 p27M is not sufficient to prevent Cdc37 binding

To check that the prevention of Cdc37 binding was not simply caused by the presence of p27KIP1 perturbing the interaction of the CDK with Cdc37, the C-Avi Cdc37 titration was repeated against a CDK4-p27M complex in the absence of D-type cyclins. Here p27M was included in the assay at a twofold molar excess of CDK4. Figure 4-17 shows that no inhibition was observed following the addition of p27M in the absence of cyclin D (red curve). The binding curve overlaps with the CDK4 control without p27M present (blue curve). This result shows that p27M alone is not sufficient to prevent the interaction of Cdc37 with CDK4 at the concentrations used in the above experiments and that the inhibition of the Cdc37 interaction is therefore cyclin D dependent.

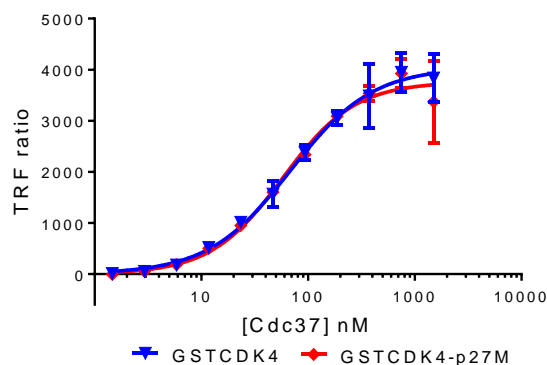


Figure 4-17 p27M is not sufficient to prevent CDK4-Cdc37 complex formation

Binding curve of the C-Avi Cdc37 interaction with GSTCDK4 and GSTCDK4-p27M. GSTCDK4 binding curve shown in blue. GSTCDK4-p27M binding curve shown in red. HTRF measurements were carried out in duplicate a total of 2 times performed on different days. The error bars represent the standard deviation of the measurements. Graphs plotted using GraphPad Prism.

4.5.3 Viral cyclin containing complexes are not affected by p27KIP1

For comparison with the canonical D-type cyclins, the Cdc37 binding assay in the presence of p27M was repeated with the viral cyclins. The viral cyclins lack the RXL binding site which interacts with the CIP/KIP proteins and so their presence was not expected to impact Cdc37 disruption of the CDK-viral cyclin complexes. As both viral cyclins already nearly prevented Cdc37 binding to CDK6-viral cyclin complexes we did not expect to be able to observe a further reduction in signal upon p27M addition. p27M

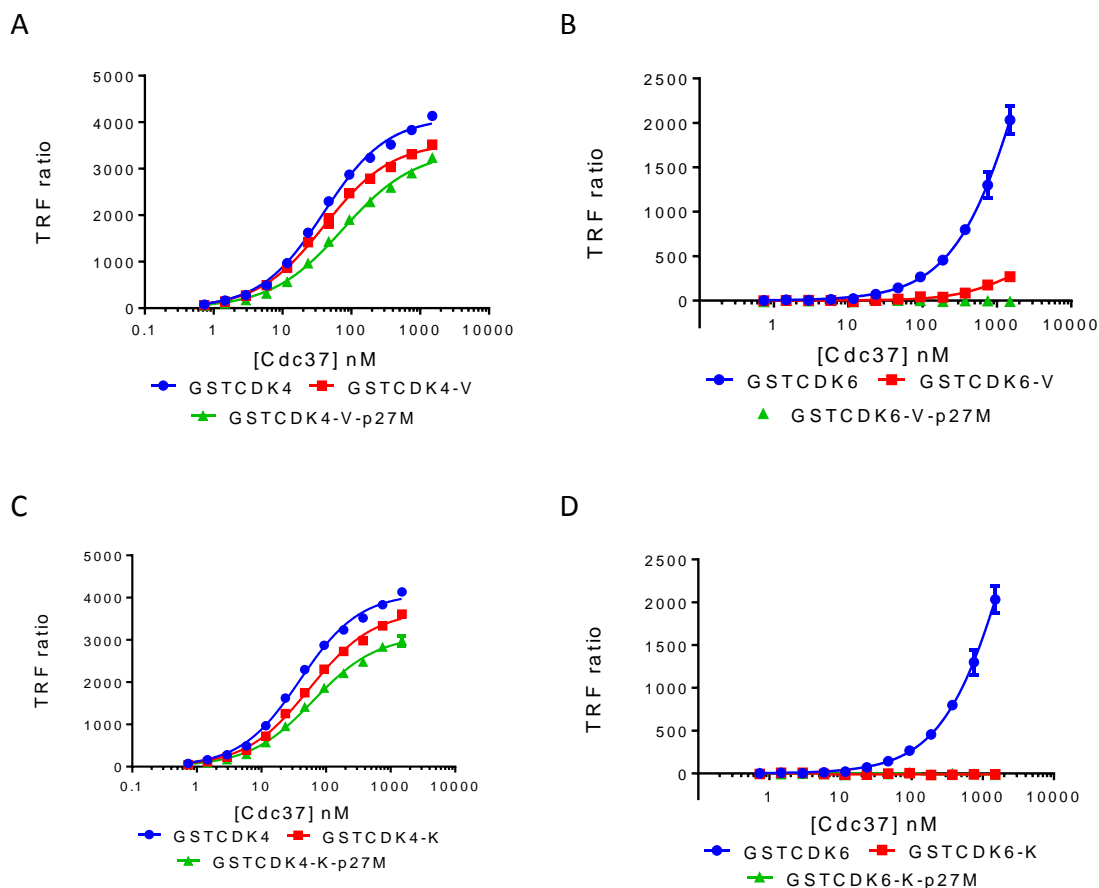


Figure 4-18 p27M addition does not stabilise viral cyclin complexes against Cdc37

(A) Binding curve of the C-Avi Cdc37 interaction with GSTCDK4, GSTCDK4-Vcyclin, GSTCDK4-Vcyclin-p27M. GSTCDK4 binding curve shown in blue. GSTCDK4-Vcyclin binding curve shown in red. GSTCDK4-Vcyclin-p27M binding curve shown in green. (B) Binding curve of the C-Avi Cdc37 interaction with GSTCDK6, GSTCDK6-Vcyclin or GSTCDK6-Vcyclin-p27M. GSTCDK6 binding curve shown in blue. GSTCDK6-Vcyclin binding curve shown in red. GSTCDK4-Vcyclin-p27M binding curve shown in green. (C) Binding curve of the C-Avi Cdc37 interaction with GSTCDK4, GSTCDK4-Kcyclin, GSTCDK4-Kcyclin-p27M. GSTCDK4 binding curve shown in blue. GSTCDK4-Kcyclin binding curve shown in red. GSTCDK4-Kcyclin-p27M binding curve shown in green. (D) Binding curve of the C-Avi Cdc37 interaction with GSTCDK6, GSTCDK6-Kcyclin or GSTCDK6-Kcyclin-p27M. GSTCDK6 binding curve shown in blue. GSTCDK6-Kcyclin binding curve shown in red. GSTCDK6-Kcyclin-p27M binding curve shown in green. Measurements were performed only once in duplicate. The error bars represent the standard deviation of the measurements. Graphs plotted using GraphPad Prism.

was added at a twofold molar excess of the GSTCDK-viral cyclin complexes. For all four complexes tested no substantial stabilisation against Cdc37 was observed, as shown by the similar binding curves in the presence of p27M (green curves) as without (red curves) (Figure 4-18). For CDK4 (Figure 4-18 A and C) the minor reduction in observed signal is likely attributed to inaccuracies in the concentration as the binding does not show a shift towards higher Cdc37 concentrations as would be expected from inhibition of the Cdc37 interaction. These results are preliminary and further verification is required.

Overall these results show that CDK4 and CDK6 can be distinguished by D-type cyclins and that the inability of the D-type cyclins to resist Cdc37 displacement suggests a requirement for an additional assembly factor, an activity that has previously been ascribed to p21CIP1 or p27KIP1. We hypothesise that the stabilisation against Cdc37 displacement caused by CIP/KIP addition would assist CDK4 and CDK6 to re-distribute from Cdc37 complexes into stable complexes containing D-type cyclins.

4.6 Analysis of the p27KIP1 interactions involved in Cdc37 displacement

To better understand the molecular interactions made by p27KIP1 that stabilise the CDK-cyclin D-p27KIP1 complex to disruption by Cdc37, several further truncations and point mutants were made in the p27KIP1 sequence. Phosphomimetic mutations were introduced at residues Tyr88 and Tyr89, by changing both tyrosine residues to glutamate. Tyr88 and Tyr99 phosphorylation is reported to be required to relieve CDK4 or CDK6 from inhibition by p27KIP1 (Grimmler *et al.*, 2007). Further truncations were also made to the C-terminal sequence where it binds and blocks the kinase ATP binding site between the N and C lobes.

4.6.1 p21CIP1/p27KIP1 fragments weakly disrupt CDK-Cdc37 complexes

Direct binding measurements of p21CIP1 and p27KIP1 to CDK4 and CDK6 have not been possible as Avi-tagged constructs were not available. Their highly-disordered nature has also made biophysical assays such as SPR difficult due to non-specific interactions with the surface. To determine their affinity for CDK4 and CDK6 without D-type cyclins present, p21CIP1 and p27KIP1 truncates have been assayed using the HTRF competition format described in Section 4.1.1. Here twofold serial dilutions of a selection of constructs were made, either starting at 10 μ M (for constructs p21M₁₋₈₇, p27M₁₋₁₀₆ and

p27FL₁₋₁₉₇) or 20 μ M, (for constructs p21S₉₋₈₇ and p27S₂₃₋₁₀₆). Comparison with full-length p21 was not been possible as it could not be stably expressed.

Inhibition curves were determined for each construct with both CDK4 (Figure 4-19 A) and CDK6 (Figure 4-19 B). Each CIP/KIP fragment could disrupt the CDK-Cdc37 complex, however their effectiveness varied between fragments and was relatively weak compared to other binding partners tested. There was also considerable variation in K_{d-app} values obtained for some fragments between the repeats, perhaps reflecting the disordered nature of these proteins giving rise to aggregation of some constructs. The most effective displacement was observed using p27FL with K_{d-app} values determined as 67.4 +/- 26.7 nM and 65.4 +/- 21.2 nM for CDK4 and CDK6 respectively. Similar values were obtained for p21M of 158 +/- 89 nM and 90.62 +/- 35.2 nM for CDK4 and CDK6 respectively. The weakest interaction was observed for p27M with CDK6 (3589 +/- 1715 nM) although this also gave the largest variation. In contrast the K_{d-app} determined for p27M with CDK4 was 688 +/- 218 nM for CDK4 which was more consistent with the short

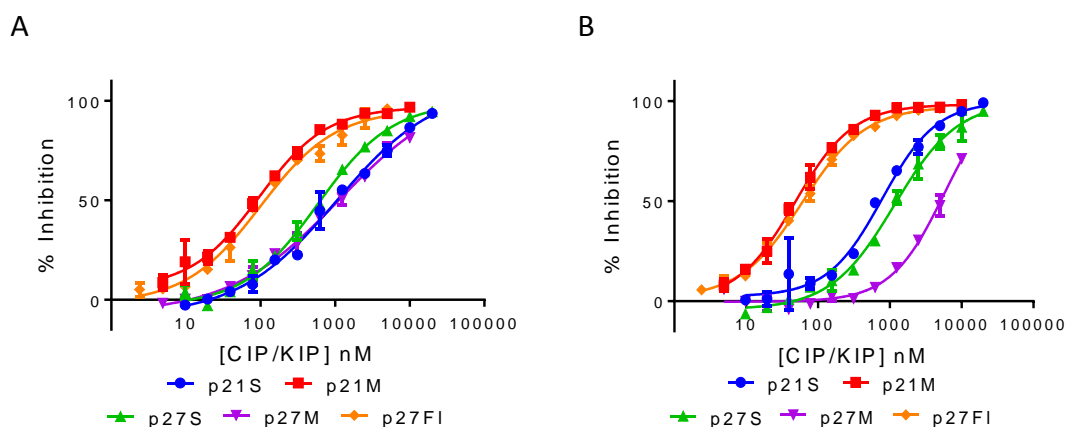


Figure 4-19 p21CIP1 and p27KIP1 fragments can weakly disrupt CDK-Cdc37 complexes
 (A) Inhibition curves showing the disruption of the GSTCDK4-C-Avi Cdc37 complex by p21CIP1 and p27KIP1 constructs using HTRF. p21S inhibition is shown in blue. p21M inhibition is shown in red. p27S inhibition is shown in green. p27M inhibition is shown in purple. p27FL inhibition is shown in orange. (B) Inhibition curves showing the disruption of the GSTCDK6-C-Avi Cdc37 complex by p21 and p27 constructs using HTRF. p21S inhibition is shown in blue. p21M inhibition is shown in red. p27S inhibition is shown in green. p27M inhibition is shown in purple. p27FL inhibition is shown in orange. Measurements with each p21CIP1/p27KIP1 construct were carried out in duplicate a total of 3 times with both CDKs, performed on different days, except for p27M which was carried out 4 times using two independently expressed and purified p27M samples. p27S used in one repeat produced by Dr Martyna Pastok (Postdoc, Endicott lab, NICR). The error bars represent the standard deviation of the measurements. Graphs plotted using GraphPad Prism.

fragments p21S (1058 +/- 313nM and 722.6 +/- 41.5 nM) and p27S (461 +/- 288 nM and 1912 +/- 543 nM) to CDK4 and CDK6 respectively. Evaluation of the hillslopes from these competition assays suggested no cooperative effects with the CDKs. The trends of interaction strength across all but one of the fragments were consistent for CDK4, with p27FL and p21M showing around a 10-fold tighter interaction than the shorter, while the p27M and p27S fragments were both weak towards CDK6.

These shorter fragments were designed based on the p27KIP1 structure that was visible in the CDK2-cyclin A-p27KIP1 crystal structure (Russo *et al.*, 1996a). The weakened ability to displace suggests that part of the sequence outside of this visible region also assists in displacing the CDKs from Cdc37. The binding strength of the p27M and p27S constructs varied greatly between the two CDKs. These fragments bind approximately 4-5 times more tightly to CDK4, than to CDK6. This difference in affinity may arise from a difference in the interactions of p21CIP1 and p27KIP1 with CDK4 and CDK6, as in general the interactions between p27KIP1 truncates and CDK6 are weaker. These results show that at high concentrations p21CIP1 and p27KIP1 can disrupt the CDK-Cdc37 complex in the absence of the D-type cyclins.

4.6.2 The RXL binding motif is not required for p27 stabilisation of CDK-cyclin D complexes

To investigate further the weak ability observed for CIP/KIP fragments to displace the CDKs from Cdc37, we first performed the direct binding assay as described in Section 4.5 with the p27XS construct. This construct encodes p27KIP1 residues 34-106 and lacks the RXL motif in the coil region which is required for cyclin binding. Therefore, the interaction with the CDK-cyclin complex is more dependent on contacts with the CDK subunit. Here p27XS was added in a twofold molar excess of GSTCDK-cyclin D3. Figure 4-20 shows that p27XS (purple) was as capable as the p27M construct (green) at stabilising CDK-cyclin D3 constructs against Cdc37, although this effect is most marked for CDK4. The RXL motif on p27KIP1 is therefore not required to stabilise the CDK-cyclin D3 complexes against Cdc37. However, this effect was stronger than expected when compared to the competition assay and would also suggest that the ability of p27KIP1 to displace Cdc37 from the CDKs is independent of a potential assembly role with the D-type cyclins.

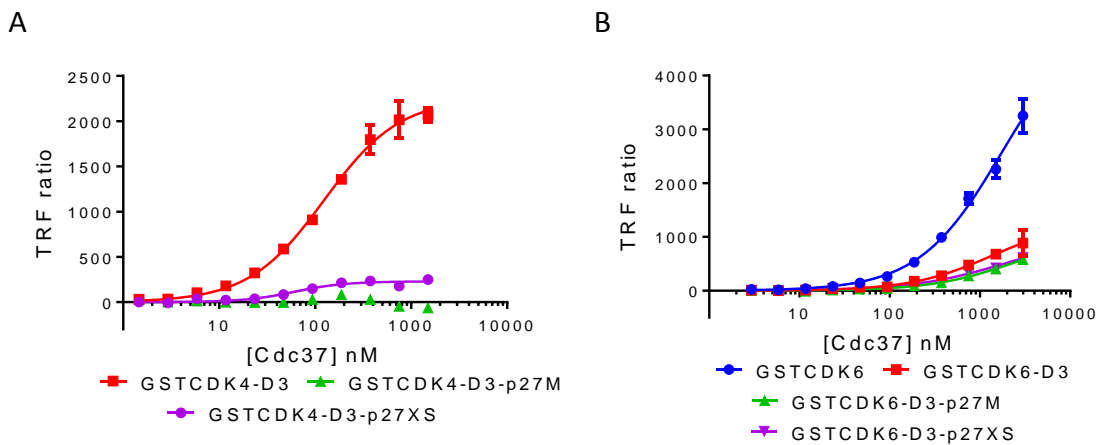


Figure 4-20 The RXL binding site is not required for complex stabilisation

(A) Binding curves of the C-Avi Cdc37 interaction with GSTCDK4-cyclin D3, GSTCDK4-cyclin D3-p27KIP1M or GSTCDK4-cyclin D3-p27KIP1XS. GSTCDK4-cyclin D3 binding curve shown in blue. GSTCDK4-cyclin D3-p27KIP1M binding curve shown in green. GSTCDK4-cyclin D3-p27KIP1XS binding curve shown in red. (B) Binding curves of the C-Avi Cdc37 interaction with GSTCDK6, GSTCDK6-cyclin D3, GSTCDK6-cyclin D3-p27KIP1M or GSTCDK6-cyclin D3-p27KIP1XS. GSTCDK6 binding curve is shown in blue. GSTCDK6-cyclin D3 binding curve shown in red. GSTCDK6-cyclin D3-p27KIP1M binding curve shown in green. GSTCDK6-cyclin D3-p27KIP1XS binding curve shown in purple. Measurements with p27XS were carried out in duplicate a total of 3 and 4 times with CDK4 and CDK6 respectively performed on different days. The error bars represent the standard deviation of the measurements. Graphs plotted using GraphPad Prism.

4.6.3 Phosphomimetic mutants do not decrease p27KIP1 stabilisation

The loss of the inhibitory effect of p27KIP1 and the reactivation of kinase activity has been shown to be dependent on the phosphorylation of residues p27KIP1 Tyr88 and Tyr89 which leads to ejection of p27KIP1 from the ATP binding pocket (Grimmler *et al.*, 2007). For p27KIP1 to act as an assembly factor, complexes containing these phosphorylated residues would need to remain resistant to Cdc37 disruption if the ternary complex formed was to be active. For these experiments the p27^{Y88E} and p27^{Y88E/Y89E} phosphomimetic mutants were used as the polar environment created by the glutamic acid sidechain more resembles a phosphorylated residue.

The experiment performed above for the p27XS construct, (Section 4.6.2), was repeated adding a twofold molar excess of either the p27^{Y88E} or p27^{Y88E/Y89E} double mutant. These results were compared to complexes containing the equivalent wild-type p27M construct and CDK-cyclin D3 with no p27KIP1 present. No difference was observed between the phosphomimetic mutants (Figure 4-21 orange/black curves) and the wild-

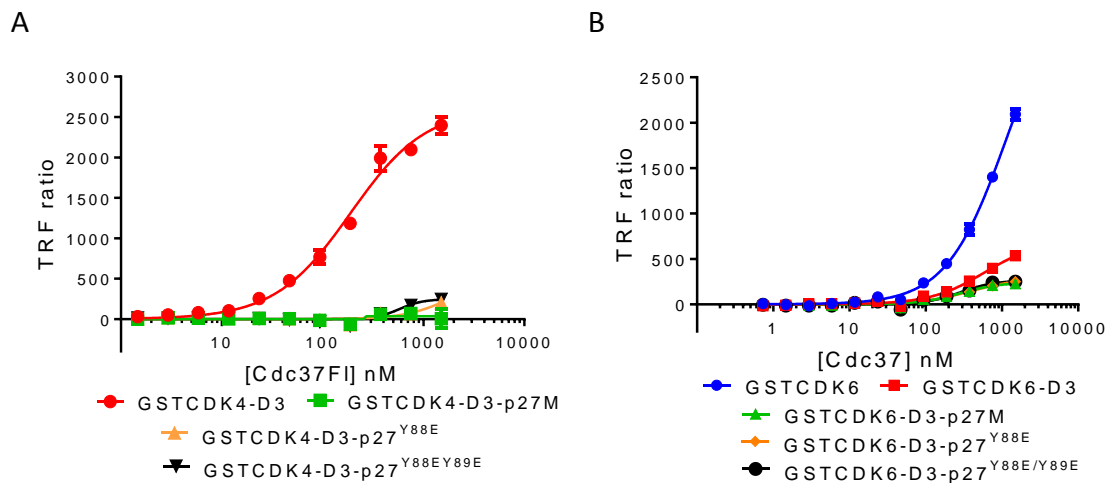


Figure 4-21 p27KIP1 phosphomimetic mutants can still stabilise CDK-cyclin D3 complexes against Cdc37

(A) Binding curves of the C-Avi Cdc37 interaction with GSTCDK4-cyclin D3, GSTCDK4-cyclin D3-p27M, GSTCDK4-cyclin D3-p27Y88E or GSTCDK4-cyclin D3-p27Y88E/Y89E. GSTCDK4-cyclin D3 binding curve shown in blue. GSTCDK4-cyclin D3-p27M binding curve is shown in red. GSTCDK4-cyclin D3-p27Y88E binding curve shown in green. GSTCDK4-cyclin D3-p27Y88E/Y89E binding curve shown in purple. (B) Binding curves of the C-Avi Cdc37 interaction with GSTCDK6, GSTCDK6-cyclin D3, GSTCDK6-cyclin D3-p27M, GSTCDK6-cyclin D3-p27Y88E or GSTCDK6-cyclin D3-p27Y88E/Y89E. GSTCDK6 binding curve is shown in blue. GSTCDK6-cyclin D3 binding curve shown in red. GSTCDK6-cyclin D3-p27M binding curve is shown in green. GSTCDK6-cyclin D3-p27Y88E binding curve shown in orange. GSTCDK4-cyclin D3-p27Y88E/Y89E binding curve shown in black. Measurements with p27Y88E were carried out a total of 3 and 2 times in duplicate with CDK4 and CDK6 respectively and with p27Y88E/Y89E a total of 4 times in duplicate with both CDKs. Measurements performed on different days. The error bars represent the standard deviation of the measurements. Graphs plotted using GraphPad Prism.

type p27M construct (Figure 4-21 green). These results show that these phosphomimetic mutants are still capable of stabilising CDK4-cyclin D3 and CDK6-cyclin D3 against Cdc37. This result would therefore suggest that a p27KIP1 phosphorylated on Tyr88 or Tyr89 would still be able to stabilise the CDK-cyclin D complexes and prevent their redistribution into complexes with Cdc37-Hsp90.

4.6.4 Extended p27KIP1 C-terminal truncations weaken the stabilisation effects of p27KIP1

Previous experiments described in Section 4.6.2 using the p27XS construct have shown that the interaction between p27KIP1 and cyclin D is not required for stabilisation of a CDK-cyclin-p27KIP1 complex to decrease its redistribution into complexes with Cdc37. Further truncations were then made to the C-terminus of p27KIP1 that binds the CDK to investigate the effect of this region on CDK-cyclin D stabilisation against disruption by

Cdc37. Two p27KIP1 constructs were tested; p27₁₋₇₉ and p27₁₋₇₅. The p27₁₋₇₉ construct removes the 3₁₀ helix which binds into the ATP binding pocket between the N and C lobes of the kinase and would confirm the observations made with the phosphomimetic mutants, which should have been ejected from this site (Figure 4-3). The p27₁₋₇₅ construct does not include the sequence that forms the β -sheet that binds against β 1 of the N-terminal lobe of the CDK above the ATP-binding pocket. A twofold molar excess over CDK-cyclin D3 of these constructs was used.

The results with CDK6-cyclin D3 are unclear as the addition of cyclin D3 (Figure 4-22 B red curve) already greatly reduces the ability of Cdc37 to interact with CDK6. However, as cyclin D3 shows only a small reduction in stability against Cdc37 with CDK4 an effect is more pronounced (Figure 4-22 A). Here p27₁₋₇₉ (yellow line) forms a stable complex that is resistant to Cdc37 disruption equal to that of p27M (green line). This observation correlates with the phosphomimetic mutants which show ejection of this region from the ATP binding site did not adversely affect stabilisation against Cdc37. However,

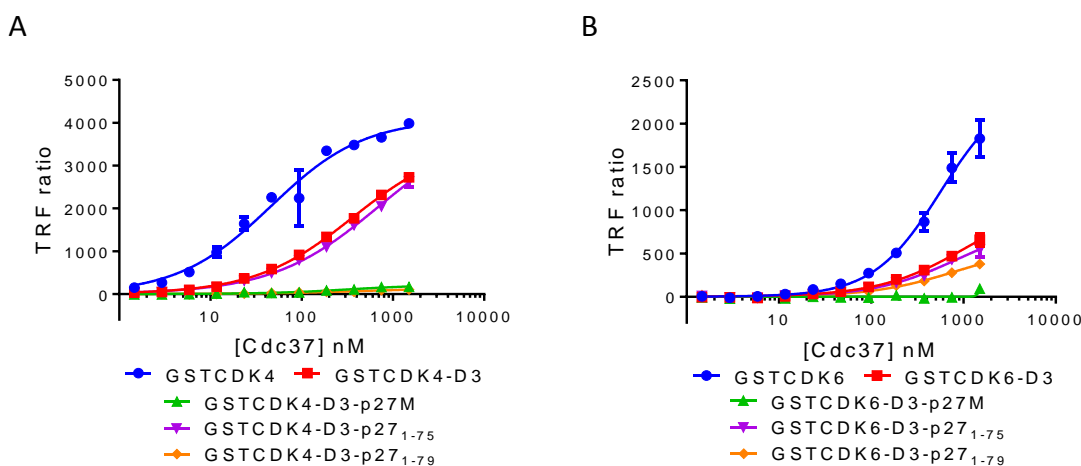


Figure 4-22 p27₁₋₇₅ does not stabilise GSTCDK4-cyclin D3 against Cdc37

(A) Binding curves of the C-Avi Cdc37 interaction with GSTCDK4, GSTCDK4-cyclin D3, GSTCDK4-cyclin D3-p27KIP1M, GSTCDK4-cyclin D3-p27₁₋₇₅ or GSTCDK4-cyclin D3-p27₁₋₇₉. GSTCDK4 binding curve shown in blue. GSTCDK4-cyclin D3 binding curve shown in red. GSTCDK4-cyclin D3-p27KIP1M binding curve is shown in green. GSTCDK4-cyclin D3-p27₁₋₇₅ binding curve shown in purple. GSTCDK4-cyclin D3-p27₁₋₇₉ binding curve shown in orange. (B) Binding curves of the C-Avi Cdc37 interaction with GSTCDK6, GSTCDK6-cyclin D3, GSTCDK6-cyclin D3-p27KIP1M, GSTCDK6-cyclin D3-p27₁₋₇₅ or GSTCDK6-cyclin D3-p27₁₋₇₉. GSTCDK6 binding curve shown in blue. GSTCDK6-cyclin D3 binding curve shown in red. GSTCDK6-cyclin D3-p27KIP1M binding curve is shown in green. GSTCDK6-cyclin D3-p27₁₋₇₅ binding curve shown in purple. GSTCDK6-cyclin D3-p27₁₋₇₉ binding curve shown in orange. Measurements with both p27KIP1 constructs were carried out in duplicate a total of 2 times with both CDKs performed on different days Error bars represent the standard deviation of the measurements. Graphs plotted using GraphPad Prism.

p27₁₋₇₅ (purple line) can no longer stabilise CDK4-cyclin D3 against Cdc37. The CDK4-cyclin D3-p27₁₋₇₅ complex is readily disrupted and its activity towards Cdc37 resembles that of CDK4-cyclin D3 with no p27KIP1 present (red curve). This result suggests that p27KIP1 residues 76-79 that are removed by this truncation are important in stabilising the kinase N-terminal lobe against displacement by Cdc37. These results are preliminary and further verification is required.

4.7 Discussion

HTRF has been used to investigate the mechanism by which client kinases are displaced from the Cdc37-Hsp90 chaperone complex by the D-type cyclins and the role that the CKIs p21CIP1 and p27KIP1 might play in assisting complex assembly. Preliminary experiments using SEC and pull-downs to assess competitive interactions were inconclusive and the presence of multiple species could not be distinguished from ternary complex formation. A modified HTRF assay has been used to quantify these interactions which has been greatly optimised allowing single digit nanomolar interactions of binding partners to be measured for both CDK4 and CDK6.

The direct binding assays showed tight interactions of both viral cyclin surrogates to CDK4 and CDK6 of *circa* 30 nM and 15 nM respectively. Binding of this affinity was unexpected for CDK4 as previous findings had shown the viral cyclins to bind preferentially to CDK6 (Li *et al.*, 1997; Jarviluoma *et al.*, 2004). However, previous studies have used CDK-cyclin complexes extracted from cells which may have additional components aiding complex formation and activation, and we are unaware of any studies that have measured the affinity *in vitro* directly. It is also possible that the CDK6 affinity is tighter than measured, due to the approach of the K_{d-app} value to the lower limit of detection. The competition assay confirmed this interpretation and showed that the interactions of the viral cyclins with CDK6 are even tighter than measured directly, while in contrast the viral cyclins appeared to only be weak competitors of Cdc37 for CDK4. One potential explanation is that CDK4 is distorted by Cdc37 and unfolded more than the weaker binding CDK6 thereby making it less competent to bind the viral cyclins. Such an explanation would be consistent with the recently determined structure of a CDK4-Cdc37-Hsp90 complex cryo-EM structure (Verba *et al.*, 2016). Comparison of the relative binding affinities for the viral cyclins to CDK4 and CDK6 compared to Cdc37 gives

a Cdc37:viral cyclin affinity ratio for CDK6 of >31 (>500 nM/<15 nM) whereas that for CDK4 is 3 (90 nM/30 nM). This ratio supports a cellular model whereby CDK6 is readily handed over from Cdc37 even at low concentrations of the viral cyclins, to form a comparatively stable CDK6-viral cyclin complex, while CDK4 would require much higher concentrations of the viral cyclins to be displaced.

These findings extend to the canonical D-type cyclins which showed a similar pattern with cyclin D3 binding more tightly to CDK6, and cyclin D1 binding with lower affinity to both CDK6 and CDK4. As with the viral cyclins, higher concentrations of cyclin D3 would be needed to displace CDK4 from Cdc37-Hsp90 than CDK6, while even higher concentrations of cyclin D1 would be required to displace both CDK4 and CDK6. It is possible that this difference in affinities allows for fine-tuning of the G1 CDK activation in a tissue-specific manner based on the D-type cyclin isoform expression profiles. The tighter interaction between CDK6 and cyclin D3 is reflected in their propensity for expression together in haematopoietic cell lines (Sicinska *et al.*, 2003; Malumbres and Barbacid, 2009) and is also reflected in the types of cancers caused by Herpesvirus saimiri (Jung *et al.*, 1994) and Kaposi's sarcoma virus (Kaldis, 2005) showing the importance of differential CDK4 and CDK6 regulation in these cell lines. Overall these results show that CDK4 and CDK6 can be distinguished by D-type cyclins and that the poor ability of the D-type cyclins to resist Cdc37 displacement when bound to CDK4 suggests a requirement for an additional assembly factor to assist D-type cyclin complex formation from the Cdc37-Hsp90 chaperone system.

p21CIP1 and p27KIP1 were shown to be able to assist CDK-cyclin D complex stabilisation suggesting a mode of action by which they could partition the CDK away from Cdc37-Hsp90 even with relatively low levels of cyclin D expression. The increased stability observed for CDK6-cyclin D3 against Cdc37 displacement suggests this complex is more likely to form independently of a p21CIP1 and p27KIP1 mechanism. However, the lowered stability of CDK4-cyclin D complexes against Cdc37 suggest either higher levels of cyclin D1 or D3 or the presence of p21CIP1 or p27KIP1 would be required before CDK4 could be displaced from the Cdc37-Hsp90 chaperone system. The catalytic activity of the ternary CDK-cyclin D-p27KIP1 complexes still needs to be confirmed to show that p21CIP1 and p27KIP1 are acting in an assembly factor role and not simply as an alternative inhibitory process. Activity would only be expected for the p27

phosphomimetic mutants (Tyr88 or Tyr89) or the p27₁₋₇₉ constructs which removes the 3₁₀ helix from the ATP binding site of the CDKs.

The competition assay with a variety of p21CIP1 and p27KIP1 fragments appeared to show a variety of affinities between CDK4 and CDK6 with in general the interactions between p27KIP1 constructs and CDK6 being weaker. The difference in affinity between them potentially highlights differences in the specific interactions between CDK4 and CDK6. This disruption of the CDK-Cdc37 complexes shows that at high concentrations p21CIP1 and p27KIP1 can disrupt the CDK-Cdc37 complex even without the D-type cyclins present, a result which was reflected in the ability of p27XS which lacks the RXL recognition site to stabilise CDK4-cyclin D3. Under closer examination of the C-terminal domain of p27KIP1, phosphomimetic mutants on Tyr88 or Tyr89 were still found to be capable of stabilising CDK4-cyclin D3 and CDK6-cyclin D3 against Cdc37. Phosphorylation on Tyr88 or Tyr89 has been shown to remove the inhibitory role of p27KIP1. Therefore, this finding that phosphorylation or even complete removal of this site still leaves p27KIP1 capable of resisting redistribution back to Cdc37-Hsp90 thereby acting as an assembly factor of the CDK-cyclin D. Further truncation of p27KIP1 residues 76-79 can no longer stabilise CDK4-cyclin D3 against Cdc37 suggesting that these residues are important in stabilising the kinase N-terminal lobe against Cdc37 interactions. This observation requires repetition to confirm the findings and it would be interesting to use it in the competition assay as we would no longer expect it to be able to displace Cdc37 from the CDKs.

Chapter 5. INK regulation

5.1 Introduction

Binding of p16^{INK4a} (p16) and Cdc37 to CDK4 is mutually exclusive, and in cells overexpression of Cdc37 is capable of reducing the levels of p16 bound to CDK4 (Stepanova *et al.*, 1996; Lamphere *et al.*, 1997). The ability of the INKs to displace CDK4 and CDK6 from the Cdc37-Hsp90 chaperone system and the potential effects of cancer-associated INK point mutants on this process have been investigated.

5.1.1 INK mutations drive cancer progression

The Inhibitors of CDK4 (INK4) proteins are potent inhibitors of CDK4 and CDK6 but not the later cell cycle regulators CDK2 or CDK1 (Hirai *et al.*, 1995; Baumgartner *et al.*, 1998). p16 was first identified as a cyclin dependent kinase inhibitor 1 in 1993 (Serrano *et al.*, 1993) and since then further members of the INK family p15^{INK4b} (p15), p18^{INK4c} (p18) and p19^{INK4d} (p19) have also been characterised. All four INKs appear to be structurally redundant and are equally potent at inhibiting both CDK4 and CDK6. However, varying expression profiles in different cell lineages suggest tissue-specific functions, a model borne out by the differing phenotypes of INK knockout mice (Ciemerych and Sicinski, 2005). INK expression usually results from cellular stress causing G1 arrest and cellular senescence, a state in which cells are no longer dividing and are insensitive to mitogenic signals, thereby fulfilling the role of a tumour suppressor (Canepa *et al.*, 2007). The INKs, unlike p21CIP1 and p27KIP1, do not require the presence of D-type cyclins to bind the CDKs, and instead actively displace them (Hirai *et al.*, 1995). They are also able to effectively compete with p21CIP1 and p27KIP1 for CDK inhibition (McConnell *et al.*, 1999).

The high level of sequence identity between the INKs is reflected in their structural homology (Figure 5-1). Only the structure of p15 remains unsolved by crystallography, however, a partial NMR structure reveals that it closely resembles the p16 fold (Yuan *et al.*, 2000). The NMR and crystal structures of p16, p18 and p19 show that the INKs form a highly ordered stack of either four (p16) or five (p18 and p19) ankyrin repeats, each connected by similarly ordered loops that make extensive β -sheet interactions between each other ((Luh *et al.*, 1997; Byeon *et al.*, 1998; Li *et al.*, 1999), Figure 5-1). The

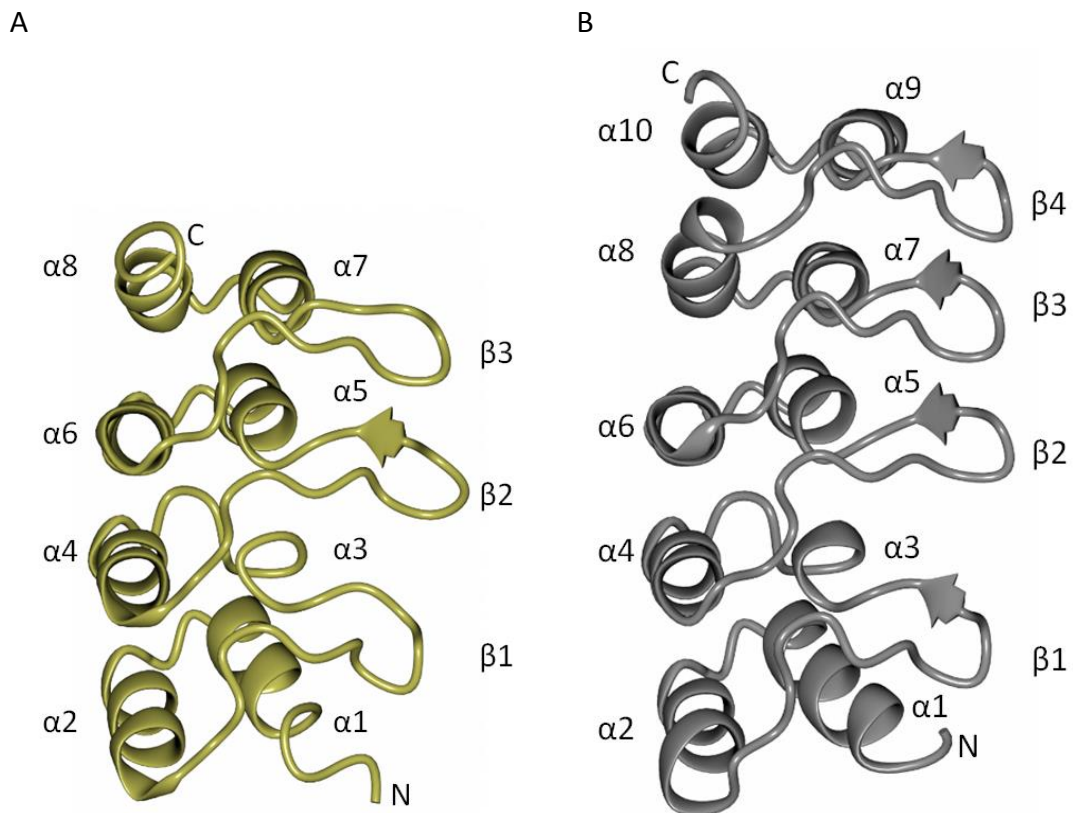


Figure 5-1 The structural makeup of p16 and p19

(A) Cartoon of p16 structure shown as ribbons (PDB: 1BI7). (B) Cartoon of p19 structure shown as ribbons (PDB: 1B18). Each ankyrin repeat is composed of two antiparallel helices separated by loops that build to a solenoid structure that generates the CDK interaction site. Image created using CCP4MG (McNicholas *et al.*, 2011).

structures reveal that the INK family possess a characteristic shorter $\alpha 3$ helix, that makes up the second ankyrin repeat, which results in a short β -sheet region and more splayed β -loops 1 and 2 compared to other Ankyrin containing proteins such as GABP β , 53BP2 and myotropin (Baumgartner *et al.*, 1998).

Crystal structures of CDK6 bound to p16 (Russo *et al.*, 1998) and to p19 (Brotherton *et al.*, 1998) revealed the mechanism of CDK inhibition imposed by the INKs. These structures show that ankyrin repeats 1-3 pack almost at a right angle to CDK6 in a cleft on the N-terminal lobe, just above the active site (Figure 5-2). The ankyrin repeats and INK β -turns 1-3 pack around the CDK N-terminal β -sheets making extensive contacts, while the INK β -turn loops 4 and 6 interact with the C-terminal domain of CDK6. This site considerably overlaps with the p27KIP1 binding site making the two inhibitors mutually exclusive (Brotherton *et al.*, 1998). As this binding site is on the opposite side of CDK6 to where the cyclin binds the inhibitory effect of the INKs is allosteric and arises from considerable distortion of the relative orientation of the CDK6 N and C-lobes pushing

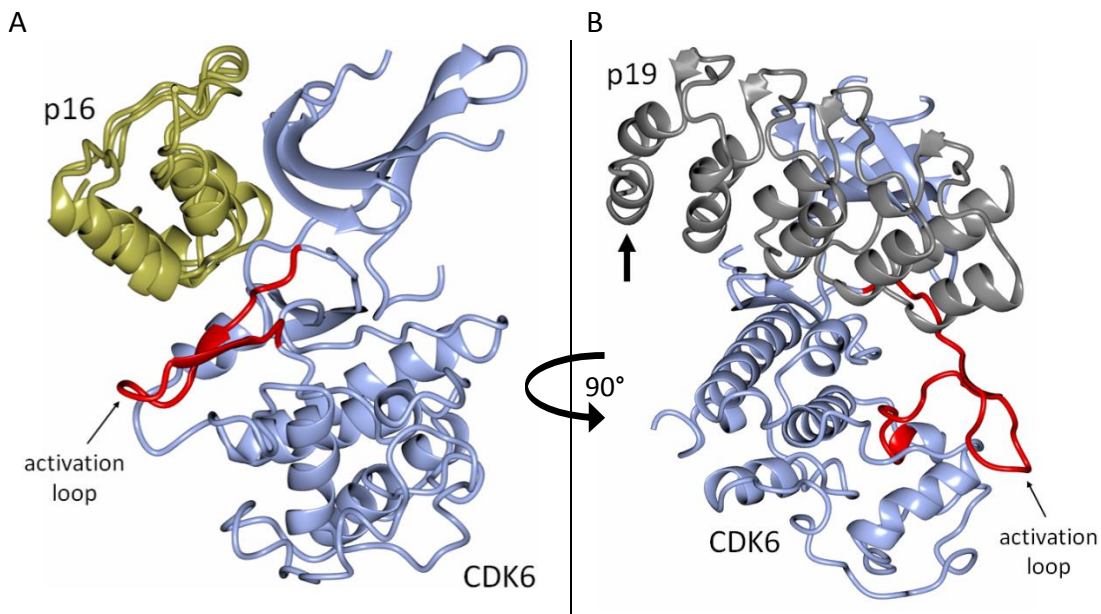


Figure 5-2 Mechanism of INK inhibition

(A) The structure of p16 bound to CDK6 shows the mechanism through which the INKs inhibit CDK activity. p16 binds to the hinge region of CDK6 distorting the two lobes. The C-helix cannot be observed in the structure as it has become disordered (PDB entry 1BI7). (B) p19 bound to CDK6 shows the additional ankyrin repeat (arrow) does not interact with the CDK (PDB: 1BLX). Proteins are displayed in ribbon form with p16 in gold, CDK6 in blue, p19 in grey and the activation loop is highlighted in red. Images created using CCP4MG (McNicholas *et al.*, 2011).

them apart and twisting them in relation to each other. This distortion in turn repositions the CDK α C-helix to the 'out' position, so that the correct orientation of key catalytic residues is precluded and the size of the exposed cyclin binding site is reduced. INK binding also causes the activation loop to become disordered and distorted back towards the INK, a modification that prevents substrate binding. Taken together, these structural changes interfere with ATP binding by disorientating key catalytic residues required for catalysis (Brotherton *et al.*, 1998; Russo *et al.*, 1998).

The strong inhibitory effect of the INKs on the G1 phase of the cell cycle highlights their role as tumour suppressors, and as such p16 and p15 have been found to be deleted in a wide range of cancers including leukemias and melanomas (Krukenberg *et al.*, 2011). In one study of melanoma samples, 56% showed reductions in p16 expression that often correlated with overexpression of either CDK4 or cyclin D1 (Young *et al.*, 2014). As such, these tumours were more sensitive to CDK4/6-specific inhibitors. The tumour suppressive role of p15 and p16 is highlighted in knockout mice which are prone to spontaneous tumours and are more susceptible to carcinogenic agents (Ciemerych and Sicinski, 2005). Mice deleted for p16 present with a similar phenotype to those deleted

for pRB strongly suggesting that the main regulatory effect of p16 is through inhibition of CDK4 or CDK6 phosphorylation of pRB (Liggett and Sidransky, 1998). While p16 mutations are common cancer alterations, mutations to p15 and p18 are significantly rarer and p19 rarer still. p19 null mice are in fact no more susceptible to tumour development than wild-type (Canepa *et al.*, 2007).

CDK inhibition is not only lost from p16 gene deletions but also through truncations or mutations. Residue Asp84 of p16 (Figure 5-3) makes a key hydrogen bond with CDK6 Arg31 (Arg24 on CDK4) and has been identified to be mutated to asparagine (D84N) in oesophagus and lung cancers (Smith-Sorensen and Hovig, 1996). The importance of this hydrogen bond is shown also by the identification of the CDK complementary mutation Arg24Cys on CDK4 (Arg31Cys in CDK6) in melanoma cases that makes them insensitive to INK inhibition but not to p21CIP1 or p27KIP1 binding (Wolfel *et al.*, 1995; Rodriguez-Diez *et al.*, 2014).

The p16 point mutant Met53Ile (M53I), (Figure 5-3) has been identified in several familial melanoma cases and is highly studied (Walker *et al.*, 1995; FitzGerald *et al.*, 1996). In some studies the M53I mutation was highly prevalent affecting around two thirds of patients (Flores *et al.*, 1997). The p16 Met53 residue (Met50 in p19) packs against loop 7 and the $\alpha 2$ helix of CDK6 and makes extensive interactions ((Brotherton *et al.*, 1998; Russo *et al.*, 1998), Figure 5-3). Previous studies have reported either that the p16^{M53I} mutant does not bind to CDK4 or CDK6 (Harland *et al.*, 1997) or that it retains a wild-type ability to bind to CDK6, but has no observable interaction with CDK4 *in vivo* (Sun *et al.*, 1997; Walker *et al.*, 1999; McKenzie *et al.*, 2010). Other p16 point mutants such as Arg24Pro have been identified in melanoma patients. They also only bind CDK6 and not CDK4, and again highlight the importance of CDK4 inhibition by p16 over CDK6 in melanomas (Jones *et al.*, 2007).

Due to the prevalence of p16 mutations in cancer a number of studies have been performed to investigate their effect and mechanisms of action. In many cases the loss of p16 binding appeared to be independent of the location of the mutants in relation to the CDK binding site suggesting that these mutations instead interfere with the packing and structure of p16 leading to defective folding and/or aggregation (Luh *et al.*, 1997; Baumgartner *et al.*, 1998; Byeon *et al.*, 1998). Indeed, in fluorescence cell based studies

A

```

p16  MEPAAGSSMEPSADWLATAAARGRVEEVRRALLEAG-ALPNAPNSYGRRP IQVMMMG SARV 59
p19  ----MLLEEVRAGDR LSGAAARCDVQEVRRLLHRELVHPDALNRF GK TALQVMMFGSTAI 56
      .  . *  * :  * * * * * * : * * * * * .  . * : * * * : * : * * * * * : * :

```

```

p16  AELLLLHGAEPNCADPATLTRPVHDAAREGF LDTLVVLHRAGARLDVRDAWGR LRPVDLAE 119
p19  ALELLKQGASPNVQDTS-GTSPVHDAARTGF LDTLTKVLVEHGADVNVDPGTGALPIHLAV 115
      *  * * : * * * * * * : *  * * * * * * * * * * * * . * * : * * . * * * : * *

```

```

p16  ELGHRDVARYLRAAAGGTR----GSNHARIDAAEGPSDIPD----- 156
p19  QEGHTAVVVSFLAAESDLHRRDARGLTPELELALQRGAQDLVDILQGHMVAPL 166
      :  * * * . : * * * : . *  *  .  . :  . * . * : *

```

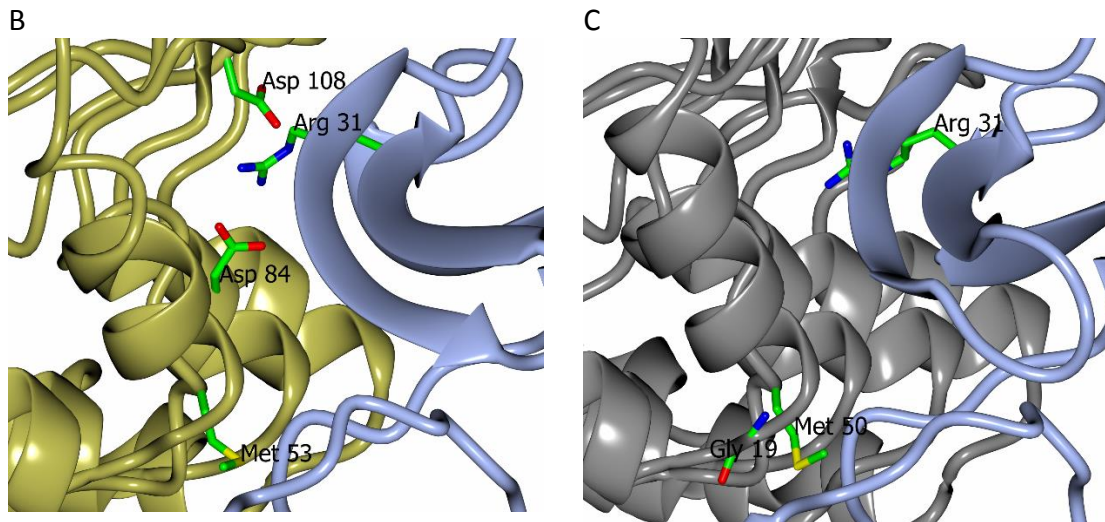


Figure 5-3 p16 point mutations map to the interface with CDK6

(A) Sequence alignment of human p16 (CDKN2A, Uniprot entry P42771) and p19 (CDKN2D, Uniprot entry P55273) sequences. Residues that are mutated in various familial cancers are highlighted. Gly19 (in p19) in red, Met53 (in p16 and p19) in orange and Asp84 (in p16) in green. (B) The structure of CDK6 bound to p16 highlighting p16 residues M53, D84 and D108 that are commonly mutated in cancers. CDK6 Arg31 is also drawn to highlight the position of the hydrogen bonding residues essential for the interaction. p16 and CDK6 are rendered in ribbon form and coloured gold and blue respectively. (PDB: 1BI7) (C) The structure of CDK6 bound to p19 highlighting p19 residues M50 and G19 that have been mutated for this study. CDK6 Arg31 is also drawn to highlight the position of the hydrogen bonding residues essential for the interaction. p19 and CDK6 are rendered in ribbon form and coloured gold and blue respectively. (PDB: 1BLX) Amino acid sidechains are coloured by atom type. Image created using CCP4MG (McNicholas *et al.*, 2011).

the p16^{M53I} mutant has been observed to clump and its localisation is altered. Both changes are indicative of instability (Walker *et al.*, 1999; McKenzie *et al.*, 2010). However, this is not the case for all non-CDK interacting residues (Jones *et al.*, 2007). For example, the p16^{D84N} mutant retains structural integrity as demonstrated by NMR, but no longer binds to CDK4 (Byeon *et al.*, 1998).

The effect of p16 point mutations on CDK handoff from the Cdc37-Hsp90 chaperone system was investigated using the clinically relevant cancer mutants M53I, D84N and

D108N (Figure 5-3). D108N was identified through the website www.tumorportal.org. This database contains the details of genetic alterations identified from thousands of tumour samples. D108N was identified in familial melanoma in several Australian families (Flores *et al.*, 1997; Goldstein *et al.*, 2006). Due to the potential destabilising effects of introducing an isoleucine at the Met53 position, a corresponding glutamic acid mutant (M53E) was also designed to ensure that any changes measured were due to side chain alterations and not through misfolding. The equivalent p16 Met53Glu mutation of p19 Met50Glu (M50E) and the Gly19Asp (G19D) mutation on the adjacent loop were also made to compare the effect on p19.

5.2 Materials and methods

All chemicals listed in the materials and methods were of analytical grade and obtained from Sigma Aldrich unless otherwise stated.

5.2.1 Protein production

CDK4 and CDK6 were expressed as N-terminal GST fusions in Sf9 insect cells, as described in Section 2.3.7. Avi-tagged p16, p19, p16^{M53I}, p16^{M53E}, p19^{G19D}, p19^{M50E} constructs were expressed with an N-terminal His₆-tag while p15, p16, p18, p19, p16^{M53I}, p16^{M53E}, p16^{D84N}, p16^{D108N}, p19^{G19D}, p19^{M50E} and Avi-tagged p16^{M53I}, p16^{D84N} and p16^{D108N} were expressed as N-terminal GST fusions. Cdc37 constructs were expressed with an N-terminal His₆-tag. All constructs were expressed in BL21STAR (DE3) *E. coli*, as described in Section 2.3.6. All proteins were purified using the standard protocols outlined in Section 2.4.

5.2.2 Biotinylation of Avi-tagged constructs

Avi-tagged proteins (Cdc37, p16, p19, p16^{M53I}, p16^{M53E}, p16^{D84N}, p16^{D108N}, p19^{G19D} and p19^{M50E}) were biotinylated *in vitro* according to the protocol outlined in Section 2.4.5.

5.2.3 HTRF in direct binding mode

For direct binding assays of wild-type INKs and mutants twofold serial dilutions were prepared from 500 nM or 1000 nM respectively. In all experiments presented the GSTCDK concentration was 10 nM. All other conditions were as described in Section 3.3.6.

5.2.4 HTRF in competition mode

For INK and INK mutant competition experiments the INKs were introduced as twofold serial dilution from 500 nM. All other conditions were as described in Section 4.2.4.

5.2.5 Microscale thermophoresis

To measure the p16-CDK6 interaction p16 was titrated in a twofold serial dilution from 500 nM against 41.6 nM of fluorescently labelled CDK6. All other parameters were as described in Section 3.3.4. Experiments were repeated in triplicate.

5.2.6 Surface plasmon resonance

All SPR experiments were performed on a Biacore S200 (GE Healthcare) at 25 °C using SPR buffer (10 mM HEPES pH 7.5, 150 mM NaCl, 0.5 mM TCEP, 3 mM EDTA and 0.05% Tween 20). Samples were centrifuged at 10000 x g at 4 °C (Beckman Coulter Allegra X22R) before use. 20 µg/mL GSTCDK4 or GSTCDK6 were captured on a surface of goat anti-GST antibody at 5 µL/min for 480 seconds. Goat anti-GST antibody was amine coupled to a CM5 BIAcore sensor chip using the standard protocol provided in the capture kit (GE Healthcare). Analyte solutions of p16 and p16 mutants at 100 nM, 25 nM, 6.25 nM, 1.56 nM and 0.4 nM were flowed over the bound GSTCDKs at 30 µL/min for 120 seconds and the dissociation was measured over 600 seconds. The bound GSTCDKs were removed from the antibody using 20 mM glycine pH 2.2 at 30 µL/min for 240 seconds. The chip was regenerated by capturing fresh GSTCDKs before each analyte concentration run. GST was loaded onto a separate lane at 10 µg/mL for 60 seconds at 30 µL/min to act as a negative control. Sensorgram readings from the GST control were subtracted from GSTCDK sensorgrams to correct for non-specific interactions and bulk effects. K_d values and dissociation rates were calculated based on the rate equation using the Biacore S200 evaluation software.

5.2.7 Differential Scanning Fluorimetry

A protein/Sypro orange mix containing 5 µM protein and a 1:5,000 dilution of dye in DMSO (as supplied by Sigma Aldrich) was prepared just before plate setup in 10 mM HEPES pH 7.5, 150 mM NaCl, 0.5 mM EDTA and 0.5 mM TCEP. 14.5 µL of the protein/Sypro orange mix was aliquoted into 384-well plates and sealed. Each experiment was done in triplicate. Thermal melting experiments were carried out using

an QuantStudio Real Time PCR machine (Applied Biosystems). The plates were first equilibrated at 25°C for 2 min in the PCR machine before starting the thermal melting experiment upon which the plates were heated at 0.05°C per second from 25 to 99°C. The fluorescence intensity was recorded using the ROX filters under continuous collection. Raw fluorescence data were extracted from the QuantStudio Real-Time PCR software and analysed using the Applied Biosystems Protein Thermal Shift software. Calculated derivative T_m values for each of the three repeats were extracted and the average values calculated.

5.3 Determining INK affinity for G1 CDKs

Before the ability of the INKs to extract the CDKs from the Cdc37-Hsp90 chaperone system could be characterised, their CDK affinity had to be determined. Preliminary pull-downs showed that all four INKs bound to both CDK4 and CDK6 (results not shown). HTRF, MST and SPR were subsequently used to quantify the affinity and to better understand the kinetics of the interaction. Full-length INKs were used for subsequent biophysical experiments.

INK binding determined by HTRF

HTRF was used in direct binding mode, as described in Section 3.3.6, to quantify the interaction between various INKs and the CDKs. First to assess whether there is any non-specific interaction between GST and the INK proteins, Avi-tagged p19 and -p16 were

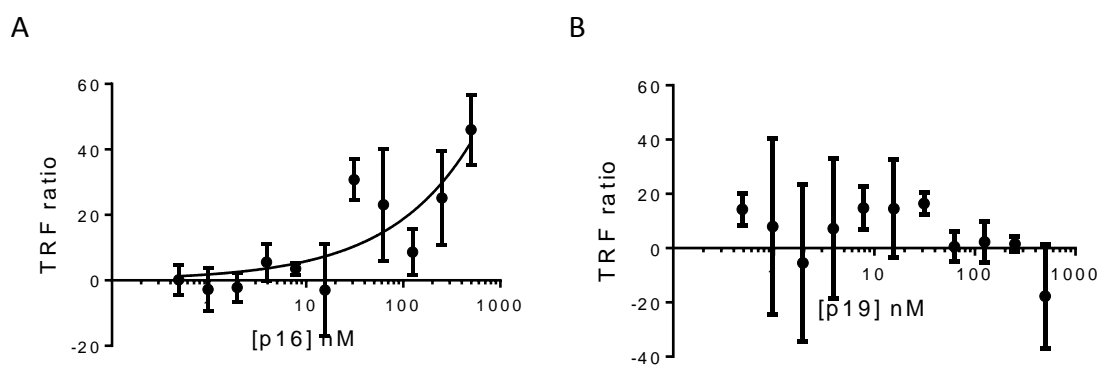


Figure 5-4 Avi-tagged INKs do not interact with GST

(A) Background binding of N-Avi p16 to GST only control. (B) Background binding of N-Avi p19 to GST only control. Measurements were only performed once in duplicate. The error bars represent the standard deviation of the measurements. Graphs were plotted using GraphPad Prism 6.

titrated against a GST-only negative control. No substantial interaction with GST was detected for either N-Avi p16 (Figure 5-4 A) or N-Avi p19 (Figure 5-4 B).

Next, GSTCDK4 or GSTCDK6 was used as the bait and titrated against a twofold serial dilution of N-Avi p16 starting at 500 nM. A clear increase in fluorescent signal was observed with increasing N-Avi p16 concentration with both CDK4 (Figure 5-5 A) and CDK6 (Figure 5-5 B) showing formation of the CDK-p16 complex. The resulting binding curves revealed that p16 bound very tightly to both CDKs so that the K_{d-app} values could not be accurately determined. The lower limit of detection for the system is 10 nM, which is determined by the concentration of the GSTCDK bait. Therefore, an upper limit of 10 nM was set for the strength of the interaction of p16 with CDK4 or CDK6 although the actual interaction may be even tighter. Hillslope evaluation from analysis gave 1.16 +/- 0.16 and 0.99 +/- 0.13 for CDK4 and CDK6 respectively.

To investigate if there was a difference in the interaction between the shorter INKs, p15 and p16, (that contain four ankyrin repeats) and the longer INKs, p18 and p19 (that contain five), the HTRF assay was repeated using the N-Avi tagged p19 construct (Figure 5-6). The fluorescent signal again increased showing the formation of the CDK-p19 complex. Binding curves determined from this interaction yielded K_{d-app} values of 29 +/- 14 nM and 30 +/- 17 nM for CDK4 and CDK6 respectively, suggesting that interaction of p19 with CDK4 or CDK6 is weaker than that of p16. Evaluation of the hillslope from analysis showed no cooperative effects with CDK4 or CDK6.

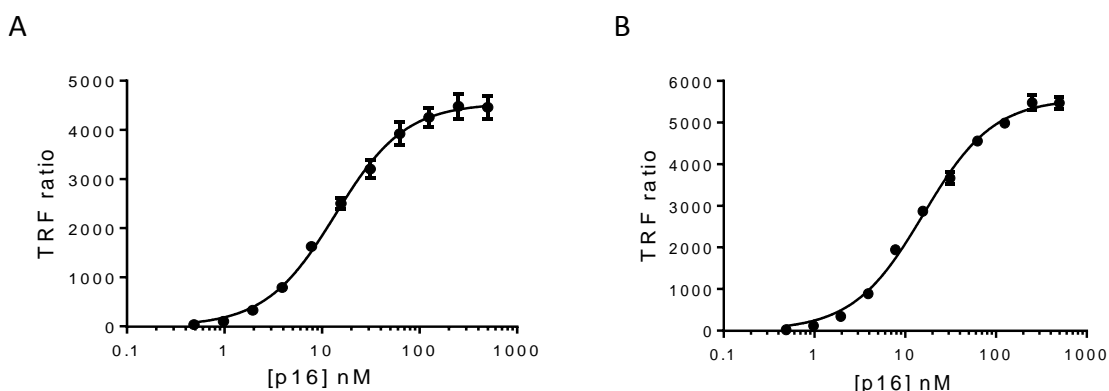


Figure 5-5 p16 bound tightly by HTRF

(A) Representative binding curve fitted for the N-Avi p16 interaction with GSTCDK4. (B) Representative binding curve fitted for the N-Avi p16 interaction with GSTCDK6. Measurements were carried out in duplicate a total of 3 and 2 times with CDK4 and CDK6 respectively performed on different days. The error bars represent the standard deviation of the measurements. Graphs were plotted using GraphPad Prism 6.

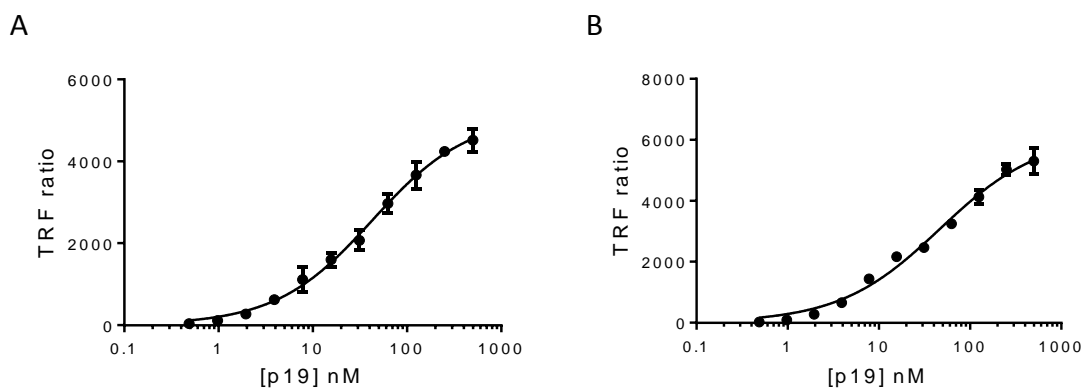


Figure 5-6 p19 binding was weaker than p16

(A) Representative binding curve fitted for the N-Avi p19 interaction with GSTCDK4. (B) Representative binding curve fitted for the N-Avi p19 interaction with GSTCDK6. Measurements were carried out in duplicate a total of 2 times with both CDKs performed on different days. The error bars represent the standard deviation of the measurements. Graphs were plotted using GraphPad Prism 6.

However, although nominally within the limits of detection, the experimental variation between runs would suggest that the value should again be treated as an upper limit for the strength of the interaction. That p16 and p19 appear have similar strengths of interaction with the CDKs is perhaps not surprising as the additional p19 ankyrin repeat does not make any additional contacts (Figure 5-2).

Microscale thermophoresis

The interactions between the CDKs and p16 were too tight to accurately determine by the HTRF assay and so other biophysical techniques were explored to more accurately measure these interactions. Microscale thermophoresis (MST) is an orthogonal solution-based fluorescent technique. CDK6 was chemically tagged with the amine coupling fluorescent dye NT-647 NHS and titrated against a twofold serial dilution series of untagged p16 starting at 500 nM. Full details of the method are described in Section 3.3.4.

Although a steady fluorescent signal could be measured and a fluorescent shift observed, a K_d for this interaction could not be accurately determined. Figure 5-7 shows the inflection point for the interaction to be sub-nanomolar indicating a tighter interaction than that observed by HTRF. This sub-nanomolar inflection was reproducible and was not a result of non-specific variations in fluorescence which were consistent across each concentration point. A binding curve could not be fitted as it was also

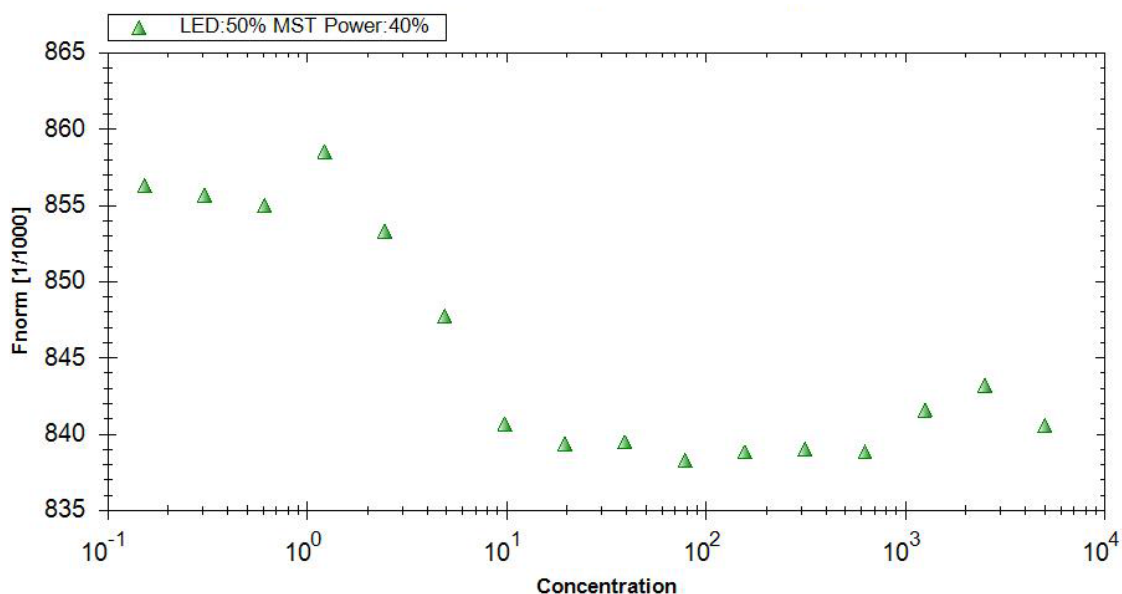


Figure 5-7 The CDK6-p16 interaction could not be accurately determined by MST

Thermophoresis change upon increasing p16 concentration to measure the CDK6-p16 interaction by MST. No binding curve could be plotted. Experiment was repeated a total of 3 times performed on different days using two independently expressed and purified p16 samples. Experiment carried out at room temperature using an LED power of 50% and thermophoresis energy of 40%.

substantially below the limits of detection, determined by the concentration of NT-647 NHS labelled CDK6, of 41.6 nM. Unfortunately, we were unable to reduce the concentration to maintain a reliable fluorescent signal below the expected p16 binding affinity. In addition, the instrument is designed to measure interactions in the nanomolar to millimolar range and as such would not have been able to accurately measure this interaction even if it had been possible to reduce the fluorescently-labelled CDK6 concentration far enough. MST was not explored further to quantify other INK-CDK interactions due to the limit of detection being higher than that of the HTRF assay.

Surface plasmon resonance

Unlike the HTRF and MST assays, SPR does not depend on a fluorescent signal for the measurement of interactions between species. The interaction is instead directly dependent on the sizes of the interacting species localised to the chip surface and as such is not subject to the same concentration-dependent limits of detection. SPR measurements are also taken in real time and so permit the kinetics of the interaction to be studied. At the time of writing only preliminary results derived from a single experiment for each interaction are available. However, kinetic analysis has revealed important insights into the interactions of p16 and selected p16 mutants with CDKs.

A summary of all the results from SPR kinetic analyses of CDK-INK interactions is provided in Table 5-1. Consistent with the HTRF analysis the interaction between the CDKs and p16 is very tight, 0.298 pM and 59.7 pM for CDK4 and CDK6 respectively. These values are far beyond the limit of detection for the HTRF assay. However, the accuracy of these K_d values, that have been determined from the micro k_{on} and k_{off} rates, are compromised by the accuracy with which k_{off} can be measured. As shown in Figure 5-8, there is no discernible dissociation of the wild-type p16 from the immobilised GSTCDK4 or GSTCDK6 over the time-scale of this experiment. The K_d determination could not be improved by using the equilibrium binding measurements as the association curves did not reach saturation. The association rates (k_a) for both CDK4 and CDK6 are similar at $69.5 \times 10^4 \text{ M}^{-1}\text{s}^{-1}$ and $152 \times 10^4 \text{ M}^{-1}\text{s}^{-1}$ respectively.

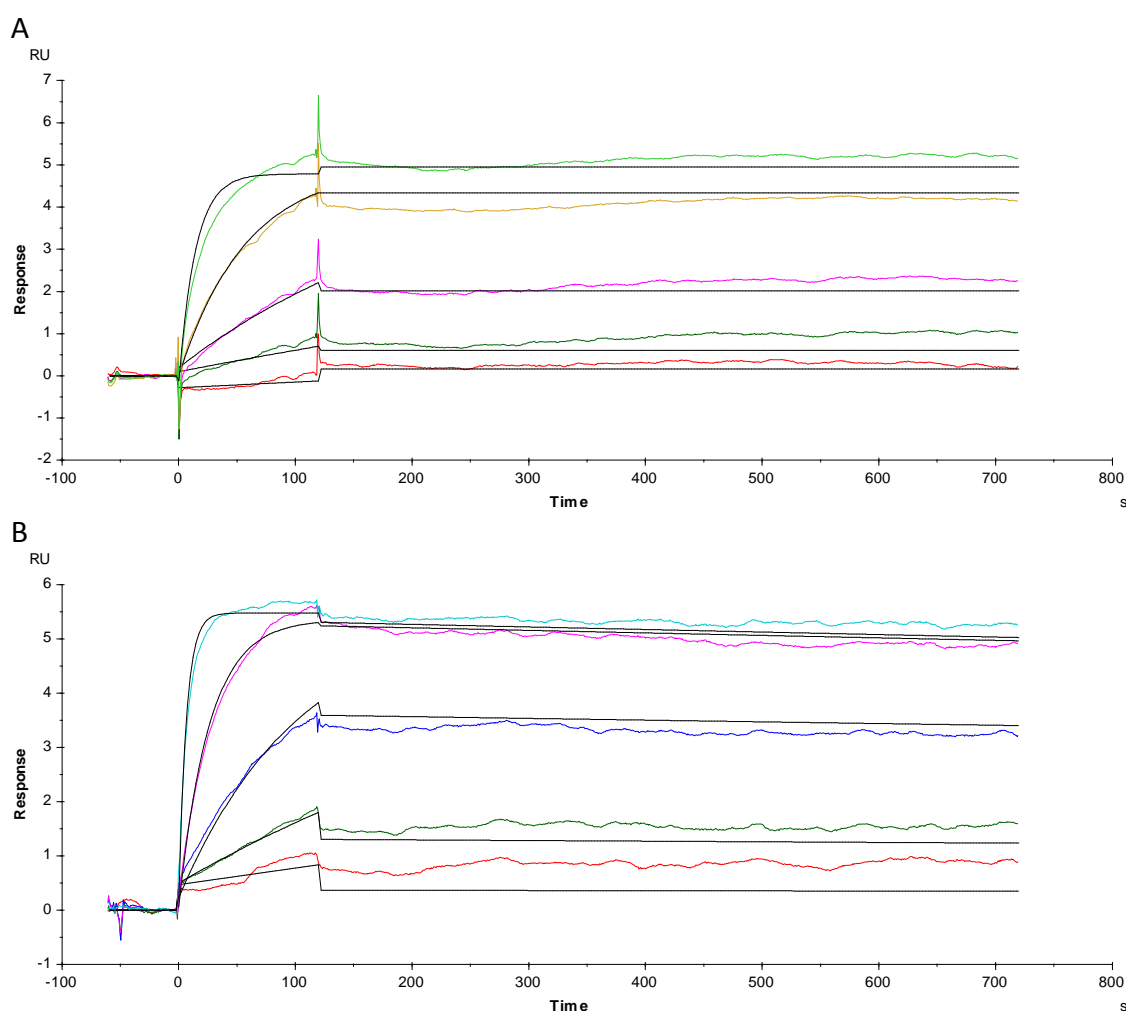


Figure 5-8 p16 binding to CDK4 and CDK6 is very tight and is characterised by a very slow off rate

(A) SPR plot of response units against time for the interaction of p16 with CDK4. (B) SPR plot of response units against time for the interaction of p16 with CDK6. Measurements performed only once.

Taken together these results show that p16 binds rapidly and tightly to both CDK4 and CDK6. Intriguingly, as determined by the HTRF assay, p19 appears to bind less tightly to its CDK partners than p16. However, due to time constraints, the interactions with p19 have not been interrogated by SPR to confirm the strength of the interaction.

5.4 INK mutants affect CDK affinity

We have established that p16 binding to the CDKs is incredibly tight. Many p16 mutants have been identified in a variety of cancers whose mechanism of action is believed to be through loss of CDK, particularly CDK4, inhibition. The model would be that these mutants show reduced binding to CDK4 or CDK6 and cannot therefore compete as effectively against other CDK partners for CDK binding. The HTRF and SPR assays have been used to investigate the effect of the p16 point mutants p16^{M53I}, p16^{M53E}, p16^{D84N} and p16^{D108N} on their ability to bind to CDK4 and CDK6. Full-length p16 mutants were used for subsequent experiments.

5.4.1 The D108N mutation had no effect on CDK binding

The p16^{D108N} point mutant was identified in several familial melanoma cases in Australia (Flores *et al.*, 1997). Although not directly involved in interactions with the CDK, the Asp108 residue is solvent exposed on the third β -loop of p16 near to several key hydrogen bonding residues (Figure 5-3). As such alterations in the structure around this loop may negatively impact the binding of these residues and the packing around the CDK N-terminal lobe.

SPR was subsequently used to try and more accurately determine the K_d for the CDK-p16^{D108N} interaction. Kinetic analysis revealed similar k_{on} values for the p16^{D108N} mutant, of $40.4 \times 10^4 \text{ M}^{-1}\text{s}^{-1}$ and $104 \times 10^4 \text{ M}^{-1}\text{s}^{-1}$ for CDK4 and CDK6 respectively. For CDK6 (Figure 5-9 B) the k_{off} was also similar to that observed for the wild-type p16: over the time-frame of this experiment there was no discernible dissociation of the p16 from the immobilised CDK6. As such the K_d of 0.354 pM determined for the CDK6- p16^{D108N} interaction is limited by the k_{off} determination and again could not be improved upon by thermodynamic analysis. A difference in affinity of p16^{D108N} compared to p16 however was observed for CDK4 (Figure 5-9 A). Although the k_{on} values for each p16 variant are similar, a considerable difference was observed in the k_{off} , as shown by the gradual loss

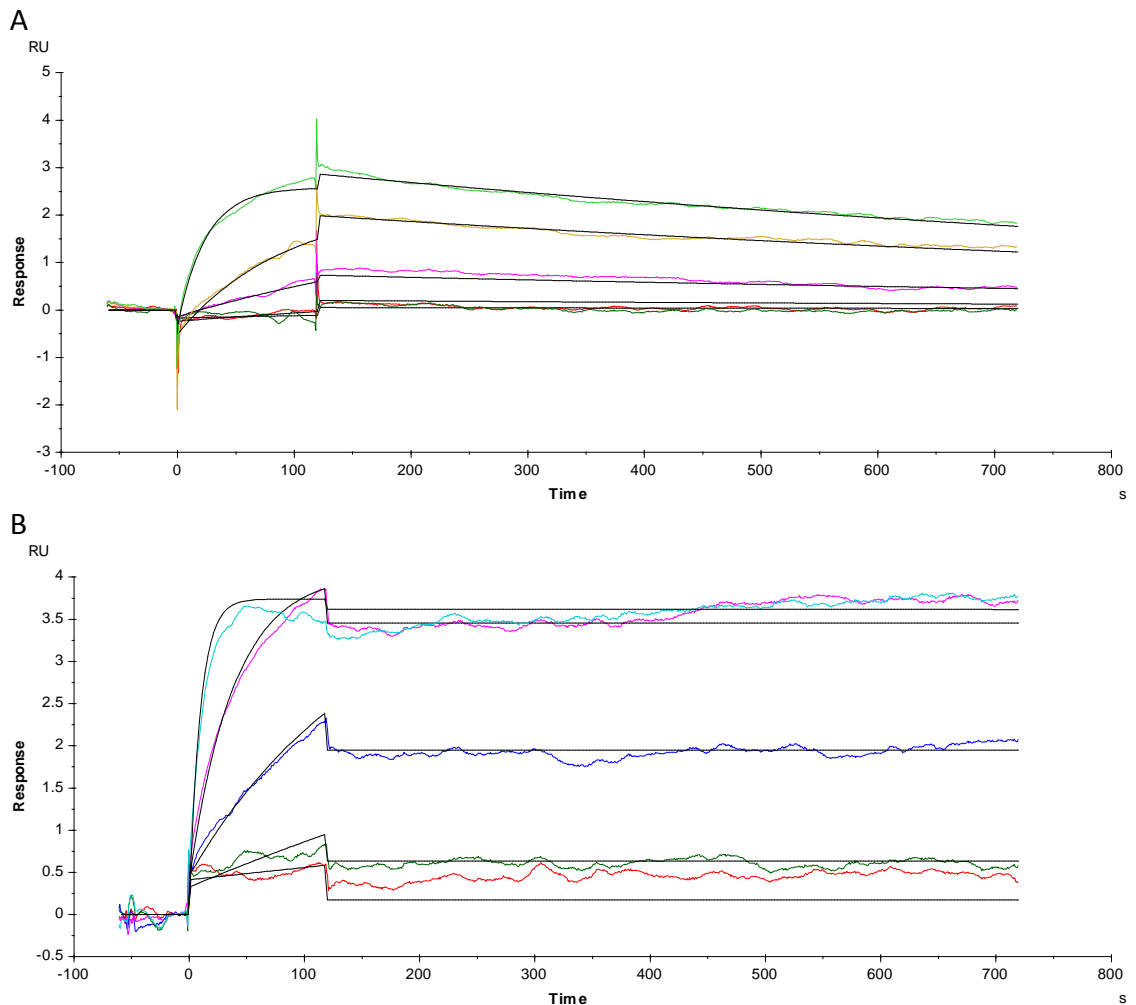


Figure 5-9 p16^{D108N} binding by SPR

(A) SPR plot of response units against time for the interaction of p16^{D108N} with CDK4. (B) SPR plot of response units against time for the interaction of p16^{D108N} with CDK6. Measurements performed only once. p16^{D108N} used in this experiment produced by Dr Martyna Pastok (Postdoc, Endicott lab, NICR).

in signal during the dissociation phase. From these dissociation curves a k_{off} of $0.8 \times 10^{-3} \text{ s}^{-1}$ was measured allowing a more accurate K_d determination of 2.0 nM for the CDK4-p16^{D108N} interaction.

Although still tight for a protein-protein interaction it is considerably weaker than wild-type p16, and therefore may be sufficiently reduced to prevent inhibition of CDK4 *in vivo*. It is also worth noting that the recombinant expression levels of p16^{D108N} were considerably lower than wild-type p16 and that of the other p16 mutants investigated, apart from p16^{M53I}. As this mutated residue makes no direct interactions with the CDK it is possible that this mutant exerts at least some of its inhibitory effect through destabilising the p16 fold leading to lower levels of expression.

5.4.2 Mutation of Asp84 to asparagine reduces the affinity of p16 for CDK4 and CDK6

Next the direct interactions of the p16^{D84N} mutant with the CDKs was explored. Residue Asp84 of p16 makes a key hydrogen bond to Arg31 of CDK6 or the equivalent Arg24 of CDK4 and has been identified in several cancer types including oesophageal and lung cancers (Smith-Sorensen and Hovig, 1996). Unlike the p16^{D108N} mutant, p16^{D84N} is expressed in high yields similar to the wild-type protein and previous NMR studies have shown this mutant is folded (Byeon *et al.*, 1998).

To confirm the HTRF result, p16^{D84N} was also subjected to SPR as described in Section 5.2.6. A clear reduction in binding was seen to both CDKs (Figure 5-10), as is evident from the rapid loss in signal once the flow of p16^{D84N} was removed after 120 seconds. Unfortunately, due to the very low response unit count using CDK4 as the bait, it has

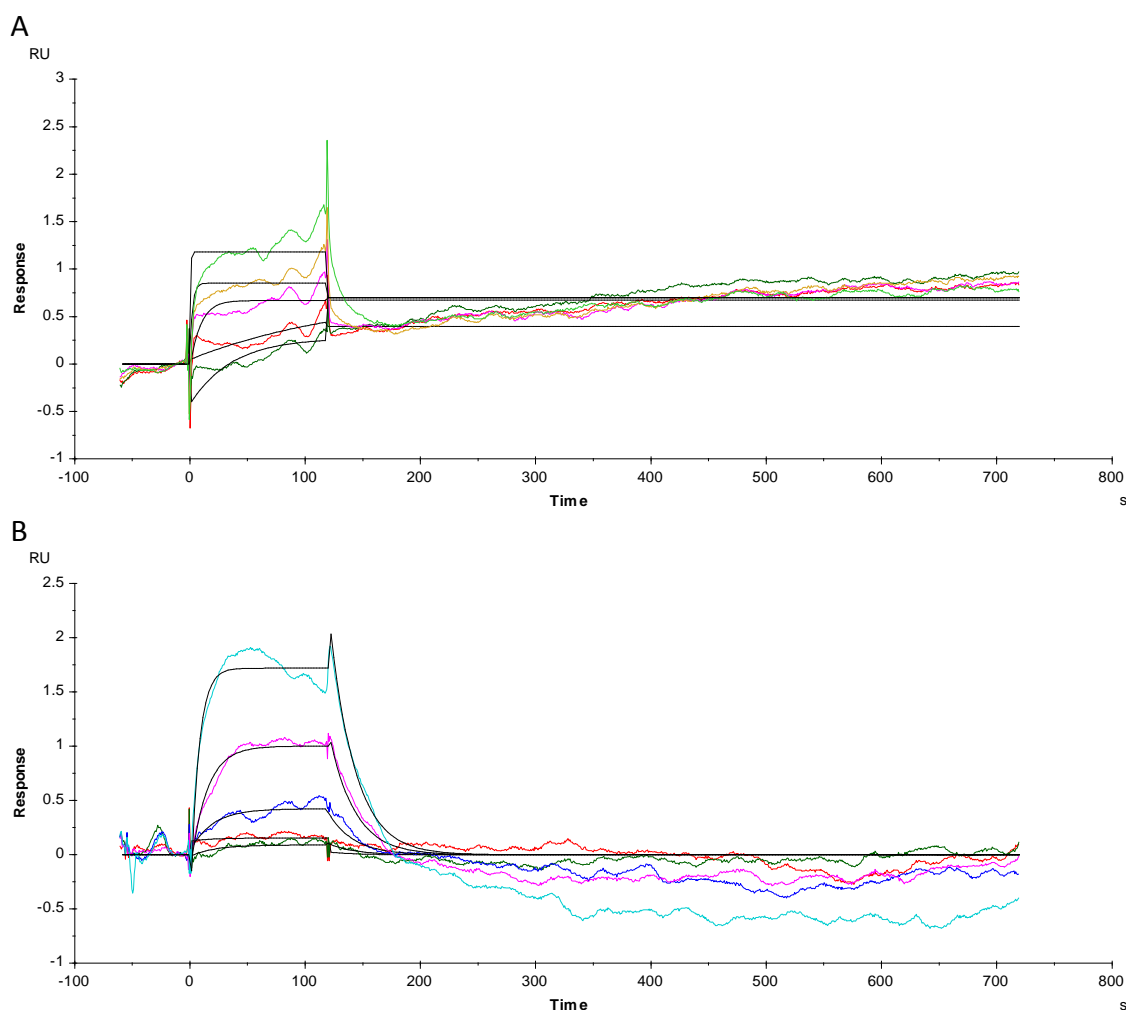


Figure 5-10 p16^{D84N} binding by SPR

(A) SPR plot of response units against time for the interaction of p16^{D84N} with CDK4. (B) SPR plot of response units against time for the interaction of p16^{D84N} with CDK6. Measurements performed only once.

been difficult to accurately fit an association and dissociation curve from which to determine a K_d . However, by visual inspection a concentration-dependent increase in binding and a more rapid dissociation rate can be observed. This experiment with CDK4 needs to be repeated to determine an accurate K_d . The measured response units when CDK6 was coupled to the chip were also small, however the signal was sufficient to determine both association and dissociation rates. This experiment showed that the k_{on} was again similar to the wild-type p16, ($97.0 \times 10^4 \text{ M}^{-1}\text{s}^{-1}$). However, the k_{off} was significantly larger at $46.1 \times 10^{-3} \text{ s}^{-1}$ resulting in a K_d of 47.5 nM.

Taken together these results show a clear reduction in the affinity of p16^{D84N} for CDK4 and CDK6. As the p16^{D84N} mutant was expressed well and has previously been shown to be stable (Byeon *et al.*, 1998) it is likely that this reduction in affinity arises through the loss of the key hydrogen bond between Asp84 and Arg31/24 on CDK6 and CDK4 respectively. This greatly diminished affinity attributed mainly to the rapid off rate likely gives rise to the loss of CDK inhibition observed in the associated cancers.

5.4.3 p16 Met53 mutants can differentiate between CDK4 and CDK6

Two p16 Met53 mutants were also investigated for alterations in affinity for CDK4 and CDK6: p16^{M53I} which has been genetically linked to familial melanoma and the analogous mutant p16^{M53E}. The Met53 residue on p16 is surface exposed and when p16 interacts with CDK6 it points towards the C terminal lobe of the CDK packing closely with CDK6 residues Asp102, Gln103, Asp104 and Thr107. The loss of these interactions is expected to account for the loss of CDK4 inhibition associated with this mutation in familial melanoma cases. Interestingly, a considerable difference was observed in the expression levels of these two Met53 mutants. p16^{M53I} was expressed in the smallest yields of any of the p16 mutants, typically only 1-2 mg/L, while p16^{M53E} expressed at effectively wild-type levels of *circa* 60 mg/L. These differences in expression and solubility suggest that this residue may have an important role in stabilising the protein structure.

Despite these problems with protein expression, both p16^{M53I} and p16^{M53E} were tested in the HTRF assay in direct binding mode. Unlike the wild-type construct a drop in signal intensity was observed after plateauing at around 100 nM. This phenomenon is most likely attributable to the Hook effect caused by a mismatch in detection reagent

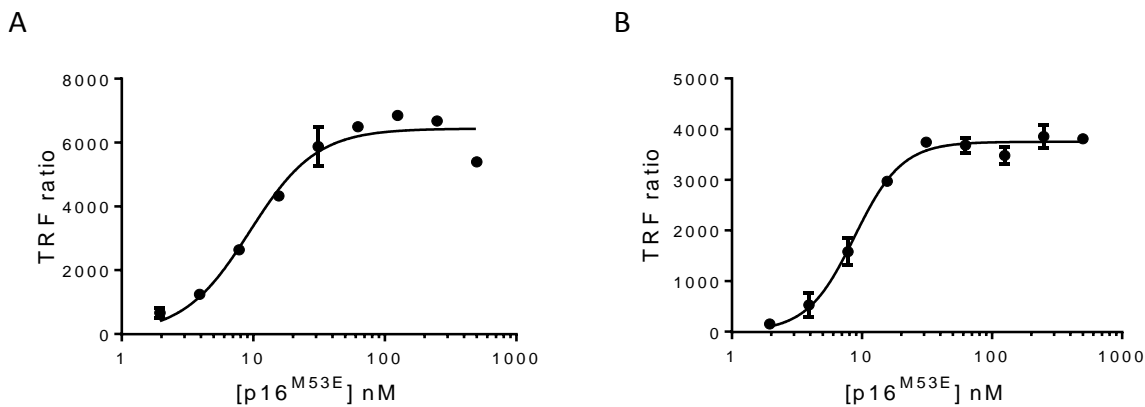


Figure 5-11 p16^{M53E} interaction by HTRF

(A, B) Representative binding curve fitted for the N-Avi p16^{M53E} interaction with GSTCDK4 (A) or GSTCDK6 (B). Measurements were carried out in duplicate a total of 5 times with both CDKs performed using two independently purified p16^{M53E} samples. The error bars represent the standard deviation of the measurements. Graphs were plotted using GraphPad prism.

compared to protein concentrations and may be a result of incomplete removal of biotin after biotinylation. These anomalous points were removed from the binding curves, a decision justified as they arose after the signal had plateaued and did not affect the binding curve. The binding curves revealed that these interactions are very tight, and the derived K_{d-app} values for both Met53 point mutants were on the 10 nM limit of detection. Hill slope evaluation from analysis gave 0.93 ± 0.23 and 1.44 ± 0.55 for CDK4 and CDK6 respectively suggesting cooperative binding with CDK6. These values are similar to those measured for wild-type p16 association with either CDK4 (Figure 5-11 A, C) or CDK6 (Figure 5-11 D, E) in this assay. Although no reduction in binding was observed in the HTRF assay, it may still be the case that these mutants can be distinguished from the wild-type p16 using SPR.

SPR was used to more accurately determine the interactions of p16^{M53I} and p16^{M53E} with CDK4 and CDK6. Using this technique, we were able to observe a considerable difference in the affinity of the Met53 mutants for CDK4 and CDK6. Figure 5-12 A and C show a considerable reduction in binding for both Met53 mutants to CDK4 with K_d values determined as 109 nM and 105 nM for p16^{M53I} and p16^{M53E} respectively. These values compare with equivalent K_d s for p16^{M53I} and p16^{M53E} binding to CDK6 of 0.81 nM and 1.31 nM (Figure 5-12 B and D). For all four of these interactions, rapid binding is observed corresponding to k_{on} values in the range of $87 \times 10^4 \text{ M}^{-1}\text{s}^{-1}$ and $138 \times 10^4 \text{ M}^{-1}\text{s}^{-1}$. These values are consistent with those obtained for wild-type p16 of $69.5 \times 10^4 \text{ M}^{-1}\text{s}^{-1}$ and $152 \times 10^4 \text{ M}^{-1}\text{s}^{-1}$ for CDK4 and CDK6 respectively. They show that all the mutants

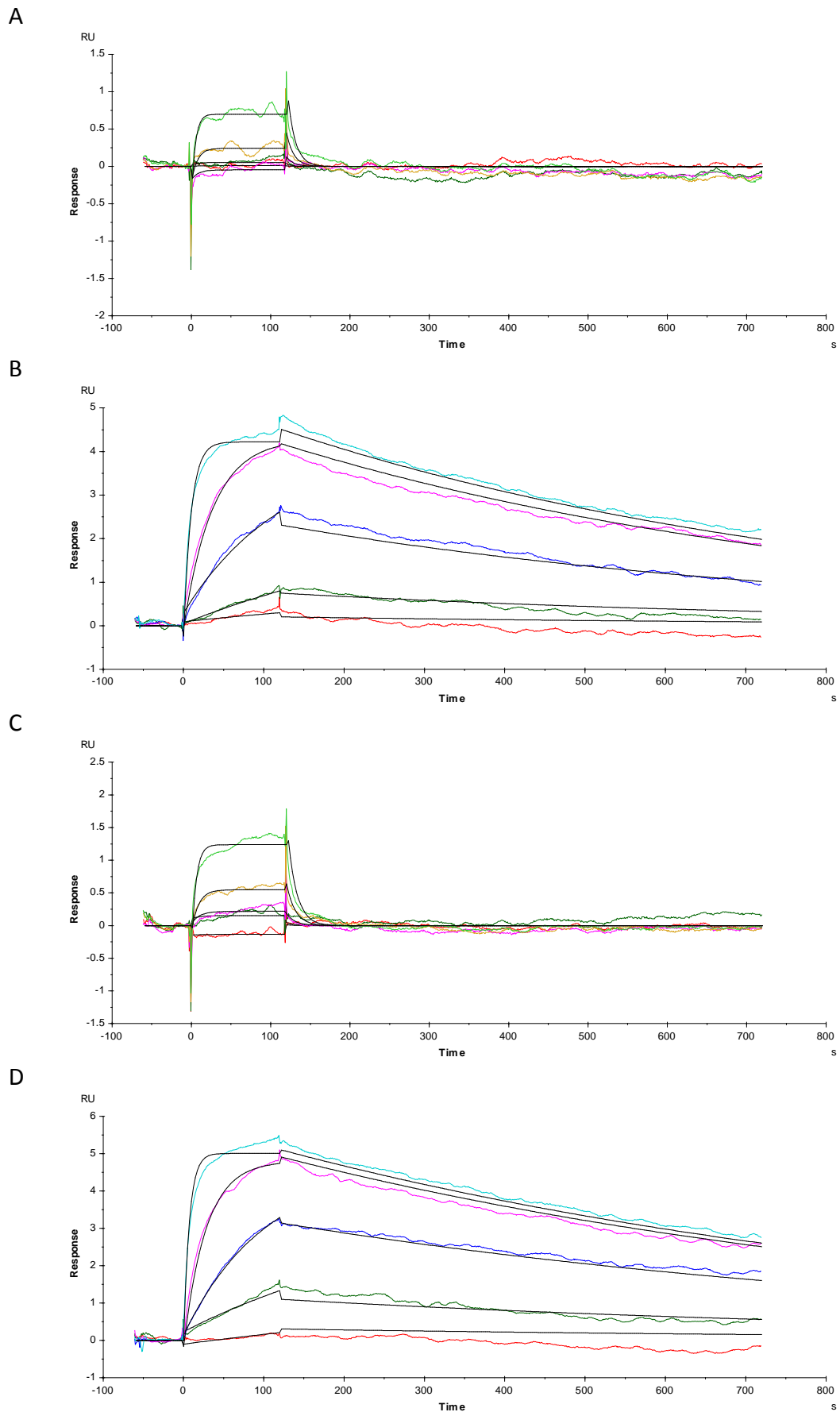


Figure 5-12 p16 Met53 mutants binding by SPR

(A, B) SPR plot of response units against time for the interaction of p16^{M53I} with CDK4 (A) and CDK6 (B). (C, D) SPR plot of response units against time for the interaction of p16^{M53E} with CDK4 (C) and CDK6 (D). Measurements performed only once.

interact rapidly with both CDK4 and CDK6, and that the difference observed in their affinities arises from considerably different dissociation rates. For the Met53 mutants with CDK4 k_{off} s were determined as $109 \times 10^{-3} \text{ s}^{-1}$ and $91.7 \times 10^{-3} \text{ s}^{-1}$ for p16^{M53I} and p16^{M53E} respectively compared to much lower k_{off} values of $1.12 \times 10^{-3} \text{ s}^{-1}$ and $1.37 \times 10^{-3} \text{ s}^{-1}$ for CDK6. This difference results in the 100-fold difference in K_d observed. The more rapid off-rates also correlate with the dissociation observed during SEC when trying to purify the CDK4-p16^{M53E} complex for crystallographic trials. In contrast, stable CDK6-p16^{M53E} and -p16^{M53I} complexes could be purified (not shown).

The K_d values for the p16 Met53 mutants with CDK6 of 1 nM determined by SPR are consistent with the tight interaction measured to have an affinity of <10 nM by HTRF. However, the SPR-derived K_d values for these interactions of nearer 100 nM should have been observed with the HTRF assay. The tighter interaction determined by the HTRF assay is likely influenced by the rapid association of these mutants with CDK4 or CDK6 which are similar to wild-type p16. Taken together, these results suggest that the altered p16 inhibition profile in familial melanoma patients carrying the M53I mutation occurs predominantly through CDK4, as shown by the 100-fold weaker affinity of this mutant for CDK4 over CDK6. However, the precise mechanism is unclear as the residues that interact with p16 Met53 are conserved between CDK4 and CDK6. One hypothesis is that

Sample	k_a ($M^{-1}s^{-1} \times 10^4$)	k_d ($s^{-1} \times 10^{-3}$)	KD
p16WT			
*CDK4	69.5	0.000207	0.298 pM
*CDK6	152	0.0907	59.7 pM
p16^{D108N}			
CDK4	40.4	0.81	2.0 nM
*CDK6	104	0.000367	0.354 pM
p16^{D84N}			
#CDK4	1770	0.00392	0.222 pM
CDK6	97.0	46.1	47.5 nM
p16^{M53I}			
CDK4	101	109	109 nM
CDK6	138	1.12	0.812 nM
p16^{M53E}			
CDK4	87.1	91.7	105 nM
CDK6	104	1.37	1.31 nM

Table 5-1 Summary of SPR kinetic analysis

Summary of kinetic data obtained from the preliminary SPR experiments with the p16 mutants. # indicates the signal was too small to accurately measure parameters, * indicates the k_{off} was too slow to be accurately determined in the timescale used.

the reduced stability of the p16^{M53I} mutant, as observed by its considerably lower recombinant expression levels, may have a larger effect on the interactions it makes with CDK4 than with CDK6. However, this model would not explain the reduced affinity observed for p16^{M53E}, the expression levels of which were not affected. An alternative hypothesis is that interactions to the second shell of residues are affected and these changes impact the interaction with CDK4 more significantly.

5.5 p19 mutants also reduce CDK binding

For comparison with p19, the equivalent p19 variant of the p16^{M53E} mutant was assayed by HTRF in direct binding mode. p19^{M50E} has not been associated with any particular cancer, but it makes a conserved set of interactions with CDK6 as revealed by a comparison of the structures of CDK6-p19 (PDB code 1BI8) and CDK6-p16 (PDB code 1BI7). As determined by HTRF, the interaction of CDK6 with wild-type p19 (30 +/- 17 nM) is considerably weaker than that with p16. The p19^{M50E} mutant showed a small reduction in affinity, if any, with K_{d-app} values for CDK4 (Figure 5-13 A) of 38 +/- 16 nM and CDK6 (Figure 5-13 A) of 55 +/- 41 nM. Hill slope evaluation from analysis suggested cooperative binding of this mutant to both CDKs, with 1.45 +/- 0.16 and 1.27 +/- 0.03 for CDK4 and CDK6 respectively. Unlike the equivalent mutation in p16, no difference was observed between CDK4 and CDK6 suggesting that the contribution of the interactions made by this methionine residue to the INK-CDK interface is different depending on its molecular context.

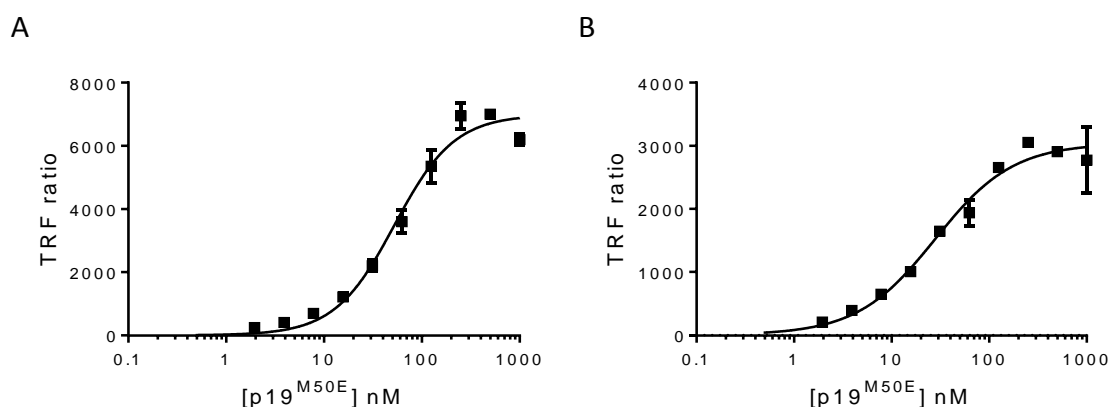


Figure 5-13 Direct binding of p19 mutant M50E to CDK4 and CDK6

(A, B) Representative binding curve fitted for the N-Avi p19^{M50E} mutant interaction with GSTCDK4 (A) and GSTCDK6 (B). Measurements were carried out in duplicate a total of 3 times with both CDKs performed on different days. The error bars represent the standard deviation of the measurements. Graphs were plotted using GraphPad prism.

An alternative p19 mutant, p19^{G19D} was also prepared and its direct binding to CDK4 and CDK6 was measured by HTRF. The p19^{G19D} mutant has also not been identified in any particular cancers, however, its key role in stabilising the first β -turn in p19 and its vicinity to the Met50 residue may both effect the stability of the p19 structure and the interactions of the neighbouring residues. Expression levels were only slightly lower than the wild-type and no obvious aggregation was observed during purification.

Interaction of the p19^{G19D} mutant with CDK4 and CDK6 was observed and the K_{d-app} values derived from the resulting binding curves were 230 +/- 180 nM for CDK4 (Figure 5-14 A) and 130 +/- 69 nM for CDK6 (Figure 5-14 B) respectively. Hill slope evaluation from analysis gave 1.31 +/- 0.14 and 1.78 +/- 0.30 for CDK4 and CDK6 respectively suggesting cooperative binding with both CDKs. Analysis may be affected by the incomplete saturation of some binding curves for these p19 mutants. These values suggest a fivefold drop in affinity for the CDKs compared to the wild-type p19. As p19 Gly19 makes no direct interactions with the CDKs it must therefore be hypothesised that its reduction in affinity arises from an altered structure causing misalignment of neighbouring interacting residues. A technique such as circular dichroism (CD) would be able to establish if this was the case.

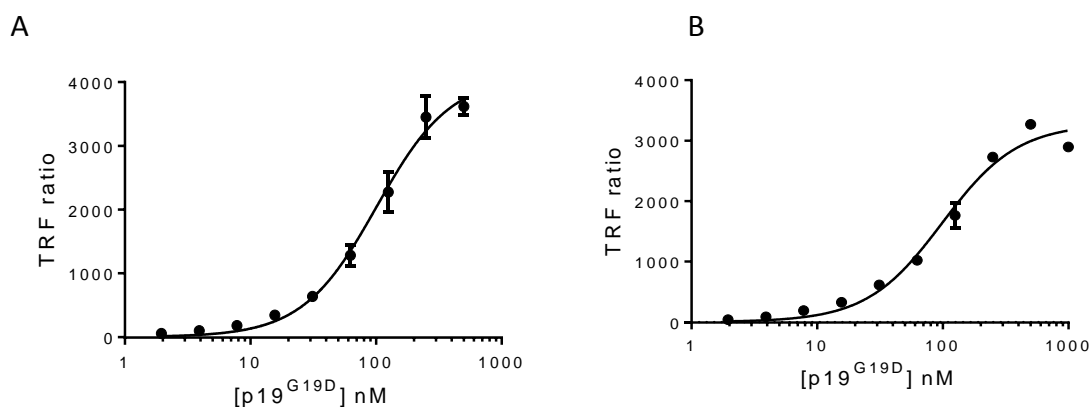


Figure 5-14 Direct binding of p19 mutant G19D to CDK4 and CDK6

(A) Representative binding curve fitted for the N-Avi p19 G19D mutant interaction with GST-CDK4. (B) Representative binding curve fitted for the N-Avi p19 G19D mutant interaction with GST-CDK6. Measurements were carried out in duplicate a total of 3 times with both CDKs performed on different days. The error bars represent the standard deviation of the measurements. Graphs were plotted using GraphPad prism.

5.6 Competition assays

To investigate if the INKs are potential binding partners to which a CDK would be relinquished by a Cdc37-Hsp90 complex, CDKs were subjected to competition assays in the presence of Cdc37. Initial competitive pull-downs were inconclusive as the presence of larger ternary complexes or multiple species could not be distinguished. The small size of the INKs and the similar size of Cdc37 and the CDKs precluded analysis by SEC. HTRF was therefore used in competition mode as described in Section 4.2.4.

5.6.1 *The INKs rapidly disrupt the CDK-Cdc37 complex*

SPR experiments revealed that p16 binds very tightly to CDK4 and CDK6, although the slow off rates hindered accurate determination of the K_d values. These results suggested that the weaker binding Cdc37, as established in Section 3.5 would be readily displaced. HTRF analysis of p19, however, suggested a weaker interaction, of 30 +/- 17 nM, which should be distinguishable by HTRF. Firstly, the abilities of untagged wild-type p15, p16, p18 and p19 to disrupt CDK4-Cdc37 and CDK6-Cdc37 complexes were investigated. All four INKs appeared to be equipotent at displacing both CDK4 (Figure 5-15 A) and CDK6 (Figure 5-15 B) from Cdc37. In all cases the K_{d-app} values determined from the inhibition curves were at or below the limit of detection: 8 nM and 6 nM for CDK4 and CDK6 respectively, and as such could not be more accurately described. Ready displacement of the CDKs from Cdc37 by the INKs highlights their roles as potent CDK4 and CDK6 inhibitors of the cell cycle as it shows that when they are expressed they would rapidly displace and sequester the CDKs from the Cdc37-Hsp90 chaperone system. The observed ready displacement was expected for p16 which showed a sub-nanomolar interaction as measured by both MST and SPR, however, the efficiency of p19 was not. One explanation for the observed difference between the competition and direct binding assay results for p19 may be inaccuracies in determining the protein concentration. p19 contains no tryptophans and so has a very low absorption at 280 nm. If the concentrations have been underestimated the K_d determined by the direct binding assay may actually be beyond the limit of detection for the system and so tighter than measured.

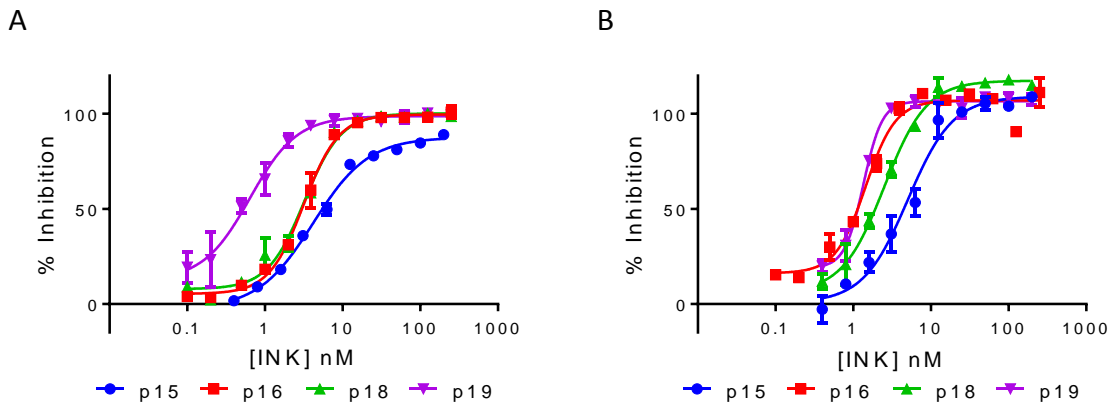


Figure 5-15 All INKs can effectively compete with Cdc37 for the CDKs

(A, B) Representative HTRF competition curves of p15 (blue), p16 (red), p18 (green) and p19 (purple) vs the GST-CDK4/C-Avi Cdc37 (A) or the GST-CDK6/C-Avi Cdc37 (B) complex. Measurements were carried out in duplicate a total of 3, 10, 3 and 6 times for p15, p16, p18 and p19 respectively with CDK4 and 3, 12, 5, and 7 times with CDK6. Measurements performed on different days with p15 and p18 or using two independently expressed and purified p16 and p19 samples. The error bars represent the standard deviation of the measurements. All curves produced using GraphPad prism.

5.6.2 The p16 M53 mutants show a difference in ability to disrupt CDK4-Cdc37 and CDK6-Cdc37 complexes

The HTRF competition assay was repeated with the p16 INK mutants p16^{M53I}, p16^{M53E}, p16^{D84N}, p16^{D108N} and compared to the activity of the wild type p16. Against CDK4 (Figure 5-16 A) a substantial reduction in the ability to displace Cdc37 was observed compared to the wild-type for all p16 mutants tested. However, as observed by SPR, the Met53 mutants still bound tightly to CDK6 (Figure 5-16 B orange and green curves) with a greater affinity than can be determined by the HTRF assay and so showed no reduction in CDK displacement over wild-type p16 (red curve). This result shows that p16^{M53I} and p16^{M53E} would still be able to displace CDK6 from the Cdc37-Hsp90 complex while their ability would be greatly reduced for CDK4. The reduced binding to the CDKs in general correlates with the reduction in mutant affinities observed by SPR, and although the affinities for CDK4 appear to be slightly weaker than expected they cannot be determined from this experiment. The ability of p16^{D108N} to disrupt the CDK-Cdc37 complexes, however, does not match the SPR results which suggested binding of 2 nM to CDK4 and near wild-type for CDK6. It can be hypothesized that the observed difference may be attributed to the reduced structural stability of the p16^{D108N} mutant, as shown by its poor levels of expression. This lowered stability may lead to protein destabilisation which would leave a smaller competent pool to bind the CDKs, although an effect on the CDK fold caused by Cdc37 binding may also contribute. Although the

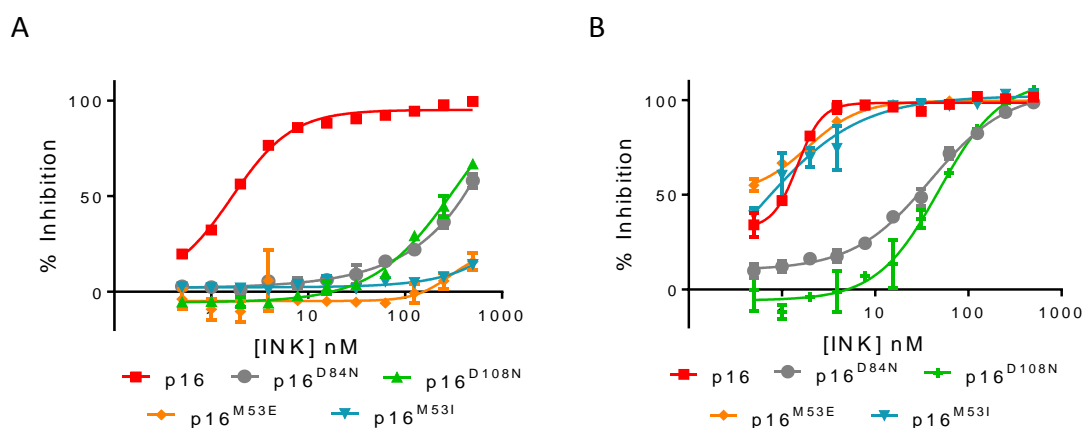


Figure 5-16 INK4 mutants show a weakened ability to displace Cdc37

(A) Representative HTRF inhibition curves of p16 (red), p16 M53I (turquoise), p16 M53E (orange) and p16 D84N (grey) vs the GSTCDK4-C-Avi Cdc37 complex. (B) Representative HTRF inhibition curves of p16 (red), p16 M53I (turquoise), p16 M53E (orange) and p16 D84N (grey) vs the GSTCDK6-C-Avi Cdc37 complex. Measurements were carried out in duplicate a total of 9, 8, 7 and 8 times for p16^{M53I}, p16^{M53E}, p16^{D84N} and p16^{D108N} respectively with CDK4 and 7, 5, 5, and 6 times with CDK6. Experiments were performed using two independently expressed and purified samples of each mutant. p16^{D108N} used in two repeats was produced by Dr Martyna Pastok (Postdoc, Endicott lab, NICR). The errors bars represent the standard deviation of the measurements. All curves produced using GraphPad prism.

p16^{M53I} expression levels were considerably lower than the wild-type the consistency of these results with the p16^{M53E} mutant, which showed no reduced expression, suggests that an additional impact on the interaction with the CDKs must also be taking place.

A thermal melt assay, as described in Section 5.2.7, was performed on p16 and the clinically identified point mutants investigated in this study. A summary of the results is shown in Table 5-2 which show that only a small decrease in thermal stability of 2.5°C is

<i>Mutant</i>	<i>T_m (°C)</i>	<i>ΔT_m (vs. p16) (°C)</i>
p16WT	47.5 (+/- 1.94)	0.0
p16 ^{M53E}	43.2 (+/- 0.38)	-4.3
p16 ^{M53I}	42.7 (+/- 0.47)	-4.9
p16 ^{D84N}	45.1 (+/- 1.92)	-2.5
p16 ^{D108N}	36.4 (+/- 3.21)	-11.2

Table 5-2 Thermal stability of p16 point mutants

Summary of p16 mutant melting temperatures determined by DSF. Values displayed are calculated from three separate experiments, performed in triplicate, using two independently expressed and purified protein samples.

observed for p16^{D84N}, when compared with the wildtype, while the M53 mutants are less stable shown by a further decrease of 1.8-2.4°C. The p16^{D108N} mutant, however, is considerably less stable than the wildtype by 11.2°C and may therefore be more prone to aggregation. This may account for the lower expression levels of this mutant and may be partially responsible for the reduced activity in cancer.

5.6.3 p19 displaces CDK4 from Cdc37

For comparison, the HTRF competition assays were also performed with the p19 mutants p19^{M50E} and p19^{G19D} and compared to wild-type p19 for their ability to disrupt the CDK4-Cdc37 complex. Figure 5-17 shows that as observed with the previous HTRF competition assay, the wild-type p19 (purple curve) displaced Cdc37 at a concentration below the limit of detection (8 nM). Both p19^{M50E} (gold curve) and p19^{G19D} (blue curve) showed a reduced ability to displace Cdc37 compared to authentic p19. For the p19 mutants, the measured affinities for CDK4 in the presence of Cdc37 (133.3 +/- 63.3 nM and 177.4 +/- 83.6 nM for p19^{M50E} and p19^{G19D} respectively) appeared to be in a similar range to those observed for the direct interaction. However, incomplete saturation effects the fitting of these binding curves and limits the accuracy of these estimates.

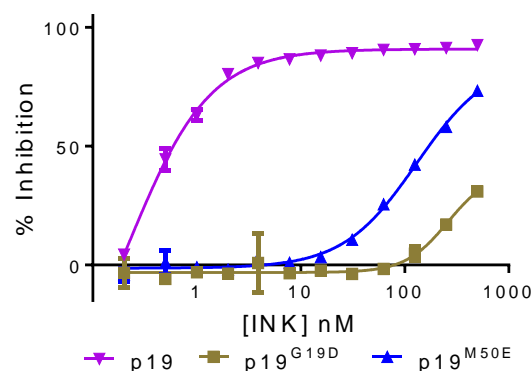


Figure 5-17 p19 mutants showed a reduced ability to displace CDK4 from Cdc37

Representative HTRF inhibition curves of p19 (purple), p19 G19D (gold) and p19 M50E (dark blue) vs the GST-CDK4-C-Avi Cdc37 complex. Measurements were carried out in duplicate a total of 4 times for p19^{G19D} and p19^{M50E} using two independently expressed and purified samples of each mutant. The error bars represent the standard deviation of the measurements. All curves produced using GraphPad prism.

5.7 Discussion

The affinities of the INKs for CDK4 and CDK6 were found to be very tight at 10 nM and 41.6 nM by HTRF and MST respectively. Although measurements were limited by the concentrations of GSTCDK used, the subsequent MST thermophoresis shift and SPR analyses confirmed tight binding, measuring affinities in the sub-nanomolar range. Repetition of the SPR analysis is currently underway to more accurately determine the K_d values which was hampered by the very slow dissociation rates. This potency of at least 100-fold magnitude greater than the Cdc37 interaction is reflected in the ability of the INKs to rapidly displace the CDKs from a CDK-Cdc37 complex. Surprisingly, the K_{d-app} values determined for p19 binding to the CDKs by the HTRF direct binding assay, of *circa* 30 nM, were significantly weaker than was observed in the competition assay and were also considerably weaker than were measured for p16. These results may be due to poor protein stability or aggregation within the assay. Overall, these results highlight the role of the INKs as potent inhibitors of both CDK4 and CDK6 and show that they are suitable binding partners for handoff from the Cdc37-Hsp90 complex and would readily sequester the CDKs away in normal cells, even at very low concentrations. The sub-nanomolar affinities determined by SPR suggest that CDK-INK complexes cannot be readily disrupted by the introduction of alternative binding partners. Instead the resulting cell cycle arrest is only likely to be relieved by CDK-INK degradation and subsequent CDK synthesis providing a potent inhibitory mechanism.

The loss of inhibition observed for a selection of p16 point mutants was shown to arise through a combination of reduced affinity, as observed by SPR, and protein instability as reflected in the expression levels of some mutants, although analysis through a technique such as DSF or CD is needed to confirm the loss in stability or structure. The SPR kinetic analysis revealed that the difference in affinity between the p16 mutants arises from a considerable increase in the mutant dissociation rates compared to the wild-type, whose dissociation could not be determined within the timescale of the assay design. This increased dissociation rate of p16^{M53E} was confirmed by subsequent attempts to purify a CDK4-p16^{M53E} complex which were hampered by complex stability during the size-exclusion chromatography step. The K_d values obtained by SPR were reduced to between 2 and 100 nM, although the exact magnitude of the reduction in mutant affinity cannot be determined until more accurate K_d values for the wild-type

p16 interaction with the CDKs are established. The range in affinities for the INK mutants p16^{D84N}, p16^{M53I} and p16^{M53E} were reflected in the reduced ability to disrupt the CDK-Cdc37 complex, observed in the HTRF competition assay, as the rapid dissociation rates allow CDK redistribution with Cdc37.

The loss of affinity of the p16^{D108N} mutant was attributed to reduced protein stability associated with its poor expression levels. This residue makes no direct contact with the CDK- which may also explain why the magnitude of the disruption in the HTRF assay was considerably less than expected given the K_d s determined by SPR for the interactions. Aggregation would result in a lower active concentration than expected although the possible effect of Cdc37 interactions on the CDK fold may also attribute to weaker displacements observed in the HTRF competition assay. However, the reduction in affinity of p16^{D84N}, which expressed well, is more likely attributed to the loss in hydrogen bonding to Arg31 in CDK6 or Arg24 in CDK4, as it had equally deleterious effects on both CDK4 and CDK6 association.

Interestingly, the SPR revealed a 100-fold difference in affinity of both p16 Met53 mutants between CDK4 and CDK6 due to a substantially faster dissociation rate with CDK4. The mismatch in affinity between the SPR and the HTRF direct binding assay for the p16 Met53 mutants for CDK4 were attributed to the rapid association rate, of *circa* $100 \times 10^4 \text{ M}^{-1}\text{s}^{-1}$, which was consistent across all the p16 constructs tested showing that the INK mutants are still capable of binding. The p19 mutants p19^{M50E} and p19^{G19D} also showed a reduction in affinity towards the CDKs by HTRF suggesting their binding was compromised. This explanation could be substantiated by further SPR analysis.

In a cancer setting CDK inhibition by these INK mutants would be lost as the rapid dissociation rates would mean they would not be able to efficiently displace the CDKs from the Cdc37-Hsp90 complex and maintain inhibition. Additionally, aggregation of poorly folded mutants would result in a lower active concentration in the cell resulting in the loss of effective inhibition. These results also highlight the importance of CDK4 in driving familial melanoma progression over CDK6 as the p16 Met53 mutants, identified in this disease state, are still able to bind CDK6 to a considerable extent while CDK4 binding is dramatically reduced.

Chapter 6. CDK-cyclin inhibition by ATP-competitive inhibitors

6.1 Introduction

6.1.1 Structure based design of kinase inhibitors

Kinases are key participants in virtually all signalling cascades that regulate cellular processes from growth to promoting angiogenesis. For this reason, upregulated or aberrant kinase activities are frequently associated with cancer progression as a result of deregulation of the associated pathways (Asghar *et al.*, 2015). Cancers are often described as being addicted to these oncogenic kinases leaving them susceptible to their inhibition (Weinstein, 2002). As such, considerable research has been performed to design potent and selective inhibitors that has resulted in a number of ATP-competitive kinase inhibitors reaching the clinic (Kelland, 2000; O'Leary *et al.*, 2016; Roskoski, 2016).

To date all kinase inhibitors in the clinic work through binding tightly to the ATP binding site and displacing ATP. However, with around 518 predicted kinases in the human genome, along with many other ATPases including chaperones and motor proteins that require ATP binding for activity, the design of selective inhibitors for a particular target is no easy task (Zhang *et al.*, 2009; Muller *et al.*, 2015). Small molecule inhibitors can also take advantage of the large structural rearrangements that occur within kinases as they transform from an inactive to an active state (Endicott *et al.*, 2012). Inhibitors can trap the kinase in an inactive form thereby preventing alignment of key catalytic residues and substrate binding (Wang *et al.*, 2014). As inactive kinases show greater variation of exposed residues when inactive, the design of selective inhibitors should be more successful if they target the inactive conformation (Echalier *et al.*, 2014).

All kinases contain the same conserved features required for ATP binding and phosphate transfer (Figure 6-1). ATP binds in a large cleft between the N and C lobes making significant interactions with the hinge region, through multiple hydrogen bonds to the backbone moieties. Above this pocket sits a glycine-rich loop (the P-loop, highlighted in coral in Figure 6-1), composed of the residues between $\beta 1$ and $\beta 2$ and including the GXGXXG motif that interacts with the ATP phosphates. This region has also been associated with the Cdc37 interaction (Zhao *et al.*, 2004; Terasawa *et al.*, 2006). The highly-conserved Asp-Phe-Gly (DFG) motif (purple) is highly conserved and contains the

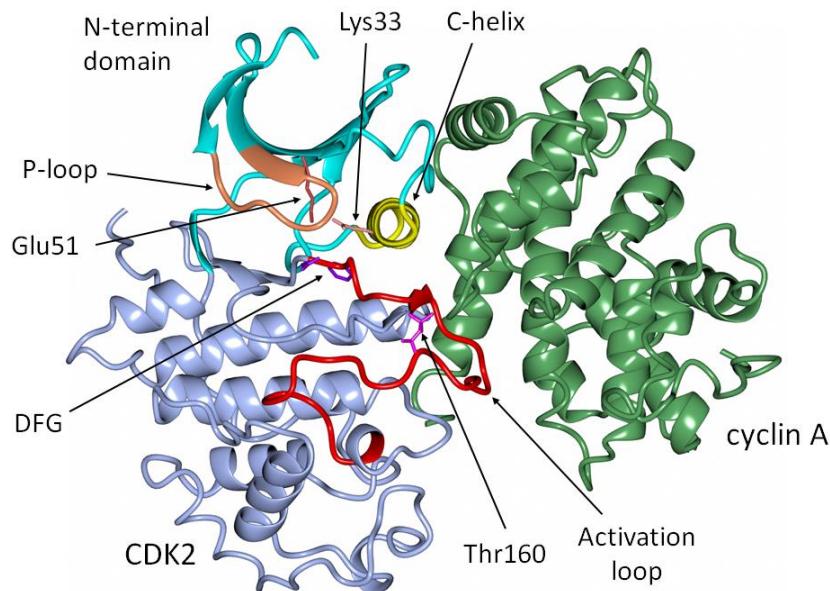


Figure 6-1 The structure of CDK2-cyclin A to highlight key conserved structural elements

Key structural elements of CDKs shown using CDK2-cyclin A (PDB: 1JST) displayed in ribbon form. CDK2 N lobe in cyan, C lobe in ice blue, P-loop in coral, activation loop in red, DFG in purple, Glu51 in pink, Lys33 in pale crimson, C-helix in yellow, phosphorylated Thr160 in magenta and cyclin A in lawn green. Figure prepared using CCP4MG (McNicholas *et al.*, 2011).

key aspartate that coordinates Mg^{2+} which, along with a lysine on $\beta 3$ (pale crimson) and a glutamate (pink) on the αC helix (yellow), orientates the ATP phosphates for efficient transfer to the substrate. The DFG motif is located at the beginning of the activation segment (red) which when not phosphorylated folds back and blocks ATP and substrate access. The DFG motif exists in two distinct states the so called 'in' and 'out' states. The DFG 'in' state, which has a more strained conformation and so is less favoured, has the key aspartate orientated towards the magnesium for catalysis while in the 'out' state the aspartate is rotated by almost 180° and points away (Jura *et al.*, 2011). Through repositioning of the αC helix to orientate the glutamate for phosphate binding and restructuring the activation loop by phosphorylation to orientate the DFG motif the activity of kinases can be tightly controlled (Zhang *et al.*, 1994).

Kinase inhibitors can be classified into three classes ((Dar and Shokat, 2011), Figure 6-2). Type I inhibitors are the most common and inhibit the active kinase conformation by mimicking ATP binding. They interact with the hinge and can also extend towards a hydrophobic pocket at the back of the ATP binding site and towards a hydrophobic pocket at the solvent exposed front of the pocket. Type II inhibitors recognise the inactive conformation and bind in the ATP pocket in a manner reminiscent of the Type I

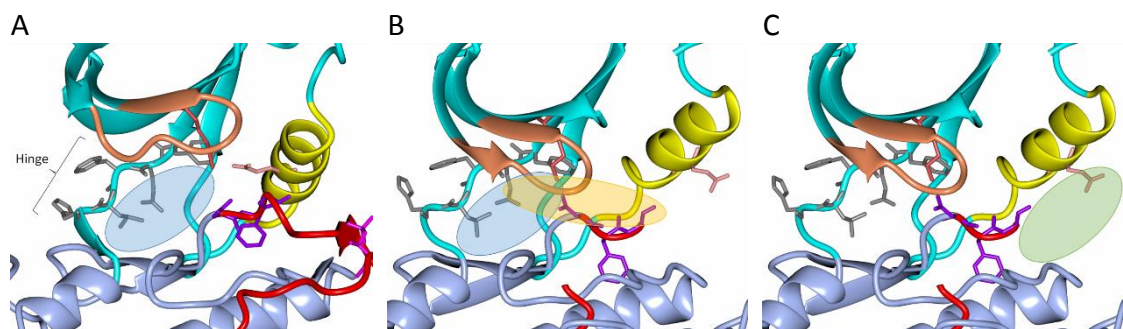


Figure 6-2 Classification of protein kinase ATP-competitive inhibitors

(A) Type I inhibitors are ATP-competitive and occupy the substrate binding site (delineated by light blue oval). (B) Type II inhibitor binding mode. Within the active site, this inhibitor type explores regions not occupied by ATP (yellow oval) and promotes an inactive conformation. (C) Type II inhibitors occupy an allosteric binding pocket (lime green oval) and so indirectly disrupt the ATP binding pocket. (A) PDB: 1JST. (B) and (C) PDB: 1HCK. Activation segment removed for clarity.

inhibitors, but also extend past the DFG 'out' motif towards a third hydrophobic site beneath the C-helix. Finally, Type III inhibitors are allosteric and do not compete with ATP; instead they interact with regions outside the ATP site and prevent rearrangement of the kinase to the active state (Zhang *et al.*, 2012). Allosteric inhibitors may offer an even greater degree of selectivity due to the higher diversity of residues in sites other than the ATP binding site (Wang *et al.*, 2014).

Since the identification of the first kinase inhibitor Staurosporine, which potently inhibits over 90% of kinases, much effort has been made towards producing inhibitors that are more specific by taking advantage of subtle differences between non-conserved residues around the ATP binding pocket (Dar and Shokat, 2011). Structure-informed design using bioinformatics and structure determination by crystallography or NMR have provided major advances in improving specificity (Dar and Shokat, 2011; Zhang *et al.*, 2012). Fragment-based screening, for example, has led to great success in this field by allowing the identification of multiple smaller fragments that bind to a target (Murray and Blundell, 2010). These fragments can then be interlinked and extended to optimise surrounding ionic or hydrophobic interactions both improving specificity and potency (Cho *et al.*, 2012; Erlanson *et al.*, 2016). Inhibitors can even be designed to better target specific mutations associated with some oncogenic kinases (Jia *et al.*, 2016).

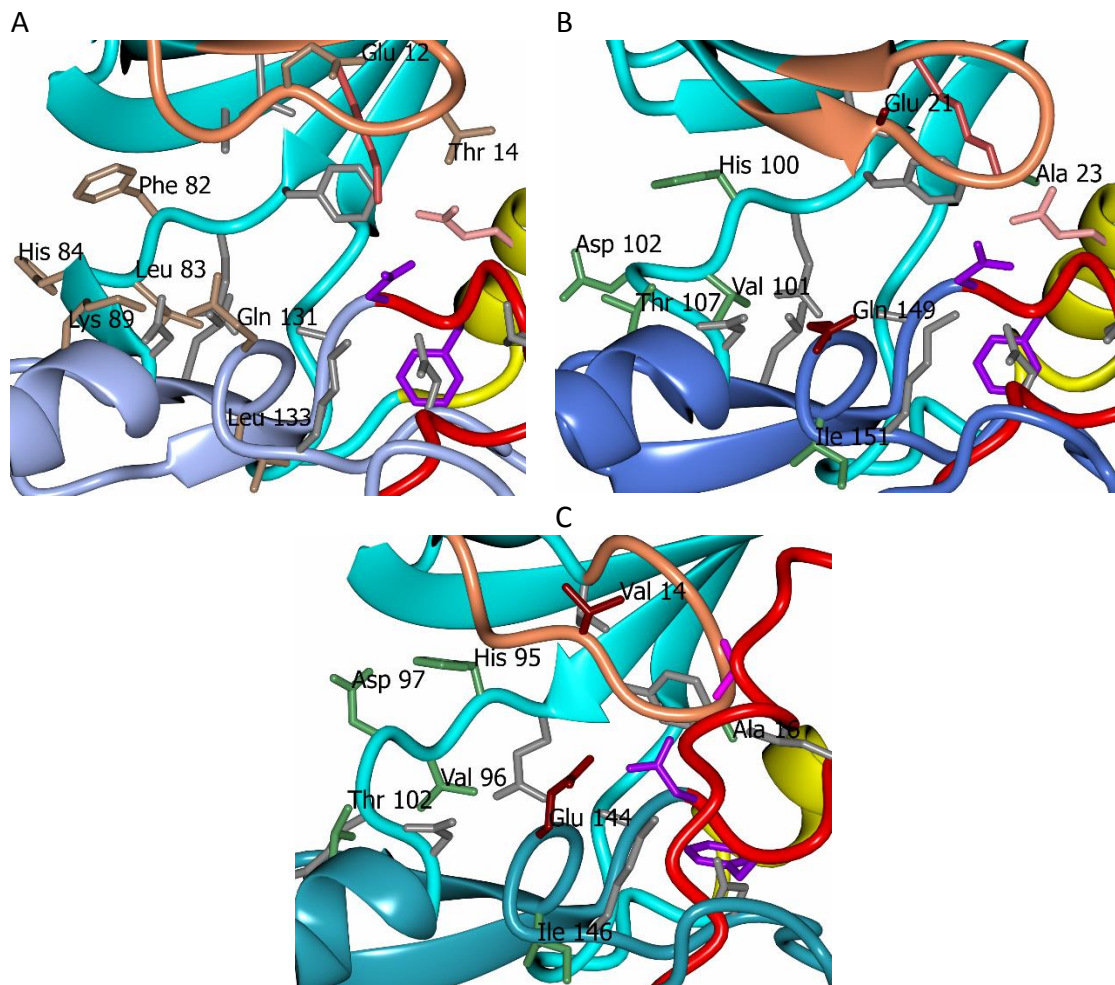


Figure 6-4 Conserved sequence features in the CDK2, CDK4 and CDK6 ATP binding sites residues

The ATP binding site with interacting residues of (A) CDK2-cyclin A2 (PDB: 1JSU) (B) CDK6-Vcyclin (PDB: 2EUF) and (D) CDK4-cyclin D3 (PDB: 3G33). The residues in grey are interaction residues that are conserved between all three, those that are different to CDK4/6 are brown, green are different to CDK2 and dark tan are different between CDK4 and CDK6. The remaining colours are the N lobe in cyan, C lobe in ice blue, P-loop in coral, activation loop in red, DFG in purple, Glu51 in pink, Lys33 in pale crimson, C-helix in yellow, phosphorylated Thr160 in magenta. Residue selection based on (Echalier *et al.*, 2014). Image created using CCP4MG (McNicholas *et al.*, 2011).

Three CDK4/6 specific ATP-competitive inhibitors; PD0332991 (Palbociclib), LEE011, (Ribociclib) and LY2835219 (Abemaciclib) are currently in phase 3 clinical trials for the treatment of a variety of cancer targets (O'Sullivan, 2016). PD0332991 has been granted FDA approval for the treatment of ER-positive HER2-negative breast cancer in combination with Letrozole (O'Leary *et al.*, 2016). All three are highly potent with measured IC₅₀ values against CDK4/6-cyclin D complexes of 11/15 nM, 10/39 nM and 2/5 nM respectively and offer at least 1000-fold selectivity over CDK1 and CDK2. (Gelbert *et al.*, 2014; O'Leary *et al.*, 2016).

6.1.3 ATP-competitive inhibitors cause kinase-Cdc37-Hsp90 complex disruption

Hsp90 is essential to the regulation of many of the protein kinases known to be overexpressed or mutated in human cancers, including BRAf, ErbB2, PKB and CDK4. These kinases and others when aberrantly expressed or regulated result in insensitivity to anti-growth signals, evading apoptosis or sustaining angiogenesis, all hallmarks of cancer. When overexpressed Hsp90 acts as a buffer against the increasingly stressed environment of cancer cells (Neckers and Workman, 2012). The key role of Hsp90 in the regulation of so many oncogenic targets has highlighted it as a potential target for the development of a broad-spectrum inhibitor what could be used to treat a multitude of cancers (Butler *et al.*, 2015). Studies of Hsp90 inhibition have shown that targeting Hsp90 both prevents client association and therefore activation but also leads to proteasomal degradation or aggregation of the clients (Pearl *et al.*, 2008; Taipale *et al.*, 2012). Despite initial concerns of the potential catastrophic side effects of inhibiting such a vital regulator of so many members of the proteome, Hsp90 has become a key anticancer target with a number of inhibitors now in clinical trials (Sidera and Patsavoudi, 2014).

Intriguingly it has also been shown that ATP-competitive inhibitors specific to client kinases and not Hsp90 are also capable of preventing kinase interactions with the Cdc37-Hsp90 complex (Nakatani *et al.*, 2005; Taipale *et al.*, 2012; Polier *et al.*, 2013). Instead of blocking Hsp90 ATPase activity it is thought that kinase inhibitors prevent the recruitment of the kinase to Cdc37 thereby preventing kinase entry into the Cdc37-Hsp90 system. This mechanism of inhibiting client kinases may be an alternative mechanism through which clinical kinase inhibitors impart at least part of their action (Polier *et al.*, 2013).

An in-depth study into this process by Polier *et al.* has shown that kinase-specific inhibitors for B-Raf can prevent Cdc37 association *in vitro*, although ATP alone was insufficient to disrupt Cdc37 binding due to its substantially weaker affinity. Using a selection of clinically approved B-Raf^{V600E} inhibitors they were also able to show concentration- and time-dependent dissociation of Cdc37 and Hsp90 *in vivo* (Figure 6-5). This observation was repeated with two other Hsp90 client kinases ErbB2 and EGFR^{G719S}.

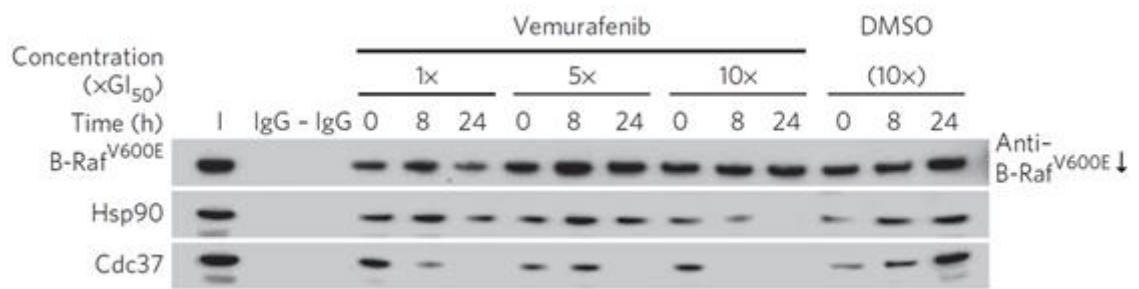


Figure 6-5 ATP-competitive inhibitors can disrupt the Hsp90 complex in vivo

Taken from (Polier *et al.*, 2013). B-Raf^{V600E} immunoprecipitation from cell lysates with subsequent western blotting analysis for Hsp90 and Cdc37. HT29 human colon cancer cells were dosed with a variety of Vemurafenib concentrations (1, 5 and 10 times the GI₅₀) and harvested after either 0, 8 or 24 hours.

As had been observed for Hsp90 inhibition, the prevention of client binding to the chaperone complex results in ubiquitin targeted degradation of the client via the ubiquitin-proteasome pathway (Citri *et al.*, 2002), Figure 6-6). Overexpression of Cdc37 resulted in higher concentrations of inhibitor being required for the same effect confirming the role of Cdc37 in this process (Polier *et al.*, 2013). It can be hypothesized that given the substantial unfolding of the kinase that accompanies binding to Cdc37, the tight binding ATP-competitive inhibitors stabilise the kinase fold preventing extensive Cdc37 interactions (Verba *et al.*, 2016) (Taipale *et al.*, 2013).

The clinically relevant CDK4/6 specific ATP-competitive inhibitors; PD0332991 (Palbociclib), LEE011, (Ribociclib) and LY2835219 (Abemaciclib) were investigated for their abilities to disrupt CDK4/6-Cdc37 complexes using the HTRF competition assay. CDK2-cyclin A2 was subsequently used as a structural surrogate in crystallographic studies to investigate and compare the interactions of these clinically relevant inhibitors.

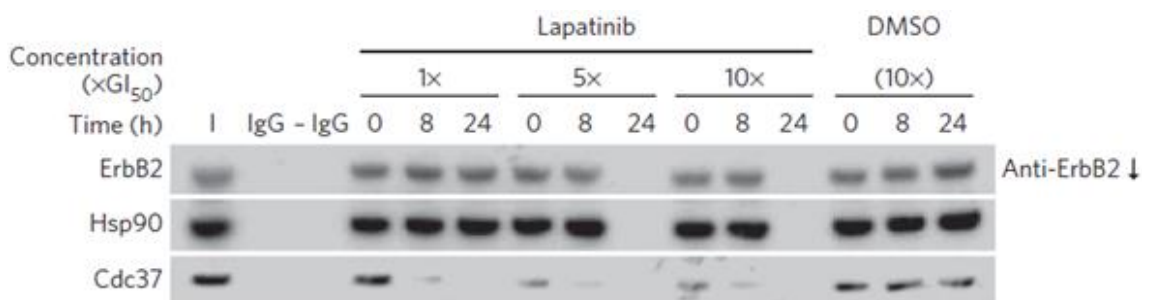


Figure 6-6 kinases not bound to the Hsp90 complex are degraded

Taken from (Polier *et al.*, 2013). ErbB2 immunoprecipitation from cell lysates with subsequent western blotting analysis for Hsp90 and Cdc37. BT474 breast cancer cells were dosed with a variety of Lapatinib concentrations (1, 5 and 10 times the GI₅₀) and harvested after either 0, 8 or 24 hours. The association of Cdc37 with ErbB2 is considerably reduced on drug treatment.

6.2 Materials and methods

Reagents

All chemicals listed in the materials and methods were of analytical grade and obtained from Sigma Aldrich unless otherwise stated. CDK4/6 inhibitors PD0332991 Palbociclib) was purchased from Sigma Aldrich while LY2835219 (Abemaciclib) and LEE011 (Ribociclib) were obtained from MedChem Express. AMP-PNP was obtained from Sigma Aldrich.

6.2.2 Protein production

CDK4 and CDK6 were expressed as N-terminal GST fusions in Sf9 insect cells, as described in section 2.3.7. C-Avi Cdc37 was expressed with an N-terminal His₆-tag, CDK2 was expressed as an N-terminal GST fusion and cyclin A2 was expressed with a C-terminal His₆-tag, but was co-purified exploiting the GST-tag on CDK2. These proteins were expressed in BL21STAR (DE3) *E. coli*, as described in Section 2.3.6. Proteins were purified using the standard protocols outlined in Section 2.4 with the exception that the buffer used for purification of CDK2-cyclin A2 was modified to mHBS2A (40 mM HEPES, pH 7.0, 200 mM NaCl and 1 mM DTT).

6.2.3 Biotinylation of Avi-tagged constructs

C-Avi Cdc37 was biotinylated *in vitro* per the protocol outlined in Section 2.4.5.

6.2.4 HTRF in competition mode

All direct binding HTRF assays were carried out as described in Section 4.1.3. A twofold serial dilution of Lee011 was prepared from a 20 μ M stock in HTRF buffer A (50 mM HEPES, 100 mM NaCl, 1 mM DTT and 0.1 mg/ml BSA) with 0.1% DMSO. PD0332991 and LY2835219 were prepared as twofold serial dilutions from 5 μ M or 500 nM stocks for CDK4 and CDK6 respectively in HTRF buffer A.

6.2.5 Crystallisation trials and structure determination

For co-crystallisation trials of CDK6-cyclin D with ATP-competitive inhibitors (PD0332991, LY2835219, Lee011 or AMP-PNP). 1 mM of the inhibitor was incubated with purified CDK6-cyclin D3, at around 1 mg/ml, for 1 hour at 4 °C before being

concentrated, using 2 mL Ultracel® 30 kDa centrifugal filters (Amicon® Ultra), to between 4-7 mg/ml. Samples were subsequently filtered through 0.22µm Ultrafree® centrifugal filters (Millipore) to remove any precipitate. CDK6-p16^{M53I}, CDK6-p16^{M53E}, CDK6-cyclin D3-p27M, CDK6-cyclin D3-p27S and CDK6-cyclin D3-p27S co-purified complexes were concentrated and filtered as described above to 8 mg/mL for the INK mutant-containing complexes or 4-5 mg/mL for the CIP/KIP-containing complexes. CDK2-cyclin A2 was concentrated to 10 mg/ml before incubation with 1 mM of the inhibitor and incubated for 1 hour at 4 °C before being filtered through 0.22µm Ultrafree® centrifugal filters (Millipore).

All crystallisation trials were carried out in 96-well crystallisation sitting drop vapour diffusion trays (MRC two-well plate, Molecular Dimensions) using a range of commercially available screens: Index (Hampton Research), JCSG+, Morpheus, Structure, PACT and ProPlex (all from Molecular Dimensions) and AmSO₄ suite (Qiagen). A previously designed CDK2-cyclin A2 optimised crystallisation screen (Echalier *et al.*, 2008), outlined in Appendix A, was prepared in a deep-well block using a Biomek (Beckman Coulter) liquid handling station. 80µl of solution was pipetted into each reservoir and crystallisation trays were subsequently prepared using a Mosquito LCP liquid handler (TTP Labtech) using ratios of 100 nl: 100 nl and 200 nl: 100 nl protein complex to reservoir solution. The plates were incubated at 4°C and examined regularly over 30 days.

Lee011 did not co-crystallise with CDK2-cyclin A2 and so was soaked into Apo CDK2-cyclin A2 crystals. A variety of methods were implemented as the inhibitor readily precipitated in the AmSO₄ based CDK2-cyclin A2 optimised crystallisation screen. 1 mM Lee011 in 30% PEG400 was added to drops containing Apo-CDK2-cyclin A2 crystals and crystals were added to drops of mother liquor containing 1 µM Lee011. The structure was determined from crystals soaked in Lee011 powder that was introduced directly to the drop by acupuncture needle and incubated at 4 °C overnight before harvesting. Crystals were harvested using CryoLoops (Hampton Research) and cryoprotected in saturated (>3.5M AmSO₄) before flash freezing in liquid nitrogen. A summary of the various crystallisation trials is provided in Table 6-1.

Protein complex	Ligand	Growth conditions
CDK2-cyclin A2	LY2835219	100 mM HEPES, pH 7.5, 1.3 M ammonium sulfate, 650 mM potassium chloride
CDK2-cyclin A2	Lee011	100 mM HEPES, pH 7.5, 1.3 M ammonium sulfate, 700 mM potassium chloride
CDK6-cyclin D3	PD0332991	2 M ammonium sulfate, 0.1 M sodium acetate

Table 6-1 Crystal growth conditions

Growth conditions for CDK2-cyclin A2 and CDK6-cyclin D3 crystals used for structure determination.

6.2.6 Data collection and processing.

Data collection was performed at the Diamond Light Source (Didcot, UK) on beamline IO4-1 at 100 K. Typically, 2000 images were collected from a single crystal with an oscillation of 0.1° per image and an exposure of 0.01 s. Data imported from Xia2 (Winter, 2010) and scaled using Aimless (Evans, 2006). Molecular replacement was performed using MolRep (Vagin and Teplyakov, 1997), part of the CCP4i2 suite (Winn *et al.*, 2011), using the previously determined CDK2-cyclin A2 structure (1H1S) as a search model. The structure was refined by rounds of refinement using COOT (Emsley *et al.*, 2010) and REFMAC5 (Murshudov *et al.*, 1997) with non-crystallographic symmetry (NCS) restraints. Inhibitor coordinates were prepared using Make Ligand (Moriarty *et al.*, 2009). The final structural parameters were evaluated using Molprobability (Chen *et al.*, 2010) and COOT. All figures were produced using CCP4MG (McNicholas *et al.*, 2011).

6.3 CDK4/6-specific inhibitors disrupt Cdc37 complex formation

The three clinically relevant CDK4/6 specific ATP-competitive inhibitors; PD0332991 (Palbociclib), LEE011 (Ribociclib) and LY2835219 (Abemaciclib) were investigated for their abilities to disrupt the CDK4/6-Cdc37 interaction. Preliminary pull-downs and SEC experiments were inconclusive as the weak interaction between CDK6 and Cdc37 precluded reproducible detection of the complex. Instead HTRF was used in competition mode, as describe in Section 4.2.4, as a more sensitive method.

Before testing the CDK4/6-selective inhibitors, titration experiments were carried out with the natural ligand ATP. If the ability of the ATP-competitive inhibitors to displace Cdc37 from the CDK is a mechanism of action then ATP at physiologically relevant concentrations should not be able to displace either CDK4 or CDK6 from Cdc37. ATP was titrated against the CDK-Cdc37 complexes up to physiological concentrations (2mM). As shown in Figure 6-7, ATP was unable to significantly disrupt either the CDK4-Cdc37 (A) or CDK6-Cdc37 (B) complexes even at the highest concentrations.

These results show that CDK4-Cdc37 and CDK6-Cdc37 complexes are not disrupted by ATP at concentrations that would be present in the cell. Next, the abilities of the three CDK4/6-selective inhibitors to displace Cdc37 from CDK4 or CDK6 were tested. While a more biologically relevant K_d could be determined in the presence of physiological concentrations of ATP, by mimicking conditions present in the cell, this was not included to minimise sources of error between measurements. Inhibition curves revealed a substantial difference between the abilities of the three compounds to disrupt the CDK-Cdc37 interaction as well as a difference between CDK4 and CDK6. Figure 6-8 shows that PD0332991 (blue curves) readily displaced Cdc37 from both CDK4 and CDK6 with K_{d-app} values of 98.9 +/-22.6 nM and 11.1 +/-3.7 nM respectively. For CDK6 this K_{d-app} was very near the lower limit of detection (6 nM). Lee011 (red curves) displaced both CDK4 and CDK6 from Cdc37 with K_{d-app} values of 1094 +/-60.5 nM and 320 +/-110 nM for CDK4 and CDK6 respectively, showing over a 10-fold weaker ability to disrupt the CDK4 complex and a 30-fold weaker ability to disrupt the CDK6 complex than PD0332991.

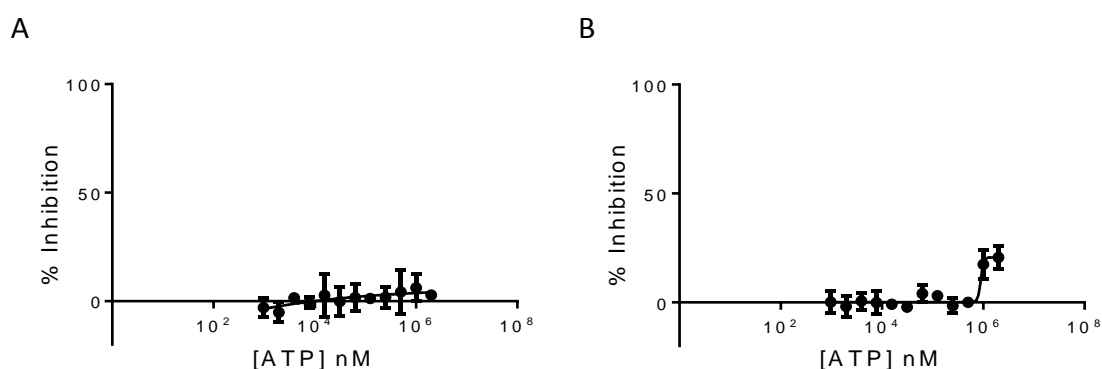


Figure 6-7 ATP does not disrupt the interaction of CDK4/6 with Cdc37

(A) Representative curve of CDK4-Cdc37 complex disruption by ATP. (B) Representative curve of CDK6-Cdc37 complex disruption by ATP. HTRF measurements were carried out in duplicate a total of 3 times for both CDKs using different stock solutions on performed on different days. Error bars represent the standard deviation of the measurements. Graphs were plotted using GraphPad Prism 6.

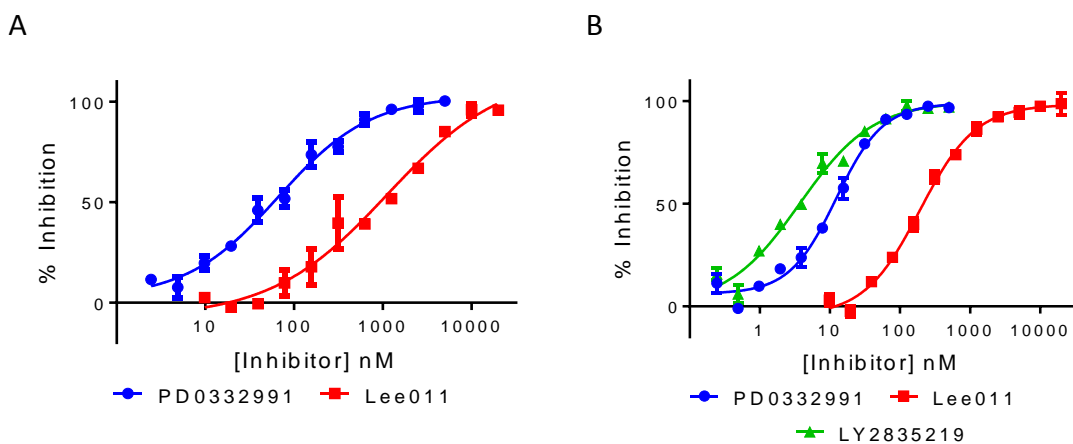


Figure 6-8 ATP-competitive inhibitors disrupt CDK-Cdc37 complexes

(A) Representative curve of CDK4-Cdc37 complex disruption by CDK4/6 specific ATP-competitive inhibitors. PD0332991 (blue) and Lee011 (red). (B) Representative curve of CDK6-Cdc37 complex disruption by CDK4/6 specific ATP-competitive inhibitors. PD0332991 (blue), Lee011 (red) and LY2835219 (green). HTRF measurements were carried out in duplicate a total of 3 and 4 times for PD0332991 and Lee011 with CDK4 and 3, 4 and 3 for PD0332991, Lee011 and LY2835219 with CDK6 respectively. Measurements were performed using two independent stock solutions of each compound and on different days. Error bars represent the standard deviation of the measurements. Graphs were plotted using GraphPad Prism 6.

The K_{d-app} values associated with disruption of the CDK4-Cdc37 complex are substantially weaker than the published IC_{50} values. PD0332991 and Lee011 are potent inhibitors of the CDK4 catalytic activity with measured IC_{50} s of 11 nM and 10 nM respectively. This difference may simply reflect differences in compound affinities for the CDK-cyclin D complexes, (used to determine the IC_{50} values) and the inactive monomeric kinase conformation (the kinase state used in this assay). The substantially higher concentrations required for CDK4-Cdc37 disruption may also reflect the ability of Cdc37 to more greatly affect the CDK4 structure, compared to the more stable structure of CDK6. It can be hypothesized that *in vivo*, at lower inhibitor concentrations, CDK6 would be more readily displaced from Cdc37 than CDK4, leading to greater levels of inhibition.

For both CDKs Lee011 was far less able to displace Cdc37 despite having a similar inhibitory potency to the other inhibitors (IC_{50} values of 10/39 nM for CDK4/6 respectively). This difference in ability to disrupt Cdc37 binding may reflect an alternative binding mode of Lee011 which is less able to stabilise the kinase N-terminal domain against Cdc37. However, it should also be noted that Lee011 was the least soluble compound and required DMSO to dissolve the concentrated stock. The reduction in inhibition observed might therefore reflect a lower soluble concentration

than expected. It would be interesting to see if this correlation of weaker CDK-Cdc37 disruption by Lee011 matched clinical results presenting as a reduced effectiveness of Lee011 inhibition through a reduction of this alternative inhibitory pathway via Hsp90 inhibition.

LY2835219 is a highly potent agonist of CDK6-Cdc37 complex formation (Figure 6-8 B green curve). Its ability to displace Cdc37 is similar to PD0332991 (blue curve), although the K_{d-app} value determined for this interaction at 6.12 ± 2.37 nM is again on the limit of detection for the assay. As such, this interaction may be even tighter than determined, though it should be noted it agrees very well with the published IC_{50} value of 5 nM. Inhibition curves for LY2835219 displacement of Cdc37 from CDK4 could not be reliably measured. This interaction produced a linear plot between roughly 20 and 80% inhibition (Figure 6-9). As the compound is soluble in water and disrupted the CDK6-Cdc37 complex this result was unexpected. The difference in the ability of LY2835219 to displace CDK4 may be due to a different LY2835219 binding mode thereby making the competition no longer mutually exclusive with Cdc37. To better understand the inhibitor interactions which give rise to these differences in Cdc37 displacement, complexes of CDK2-cyclin A2 bound to LY2835219 and Lee011 were crystallised as structural surrogates. Similar biophysical analysis to those described above could not be performed on CDK2 as it does not form a stable complex with Cdc37.

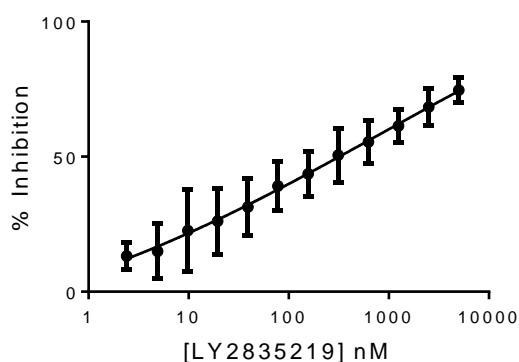


Figure 6-9 Determination of the ability of LY2835219 to displace CDK4 from CDK4-Cdc37

The displacement assay was repeated on seven occasions from two independent stocks using the standard assay conditions. Despite repeated attempts, the experiment did not generate conventional displacement curves. Error bars represent the standard deviation of all the measurements. Graphs were plotted using GraphPad Prism 6.

The structure of PD0332991 bound to CDK2-cyclin A2 had previously been determined (Hallett, 2013).

6.4 CDK6 crystallisation trials

Throughout the project multiple crystallisation trials were performed on CDK6-cyclin D3 using the previously described CDK4/6 ATP-competitive inhibitors; PD0332991, LY2835219 and Lee011 and the non-hydrolysable ATP analogue AMP-PNP. Addition of inhibitors that stabilise the kinase fold has been reported as a route to help bring order to the complex for better crystal packing (Eswaran and Knapp, 2010). Despite considerable improvements in CDK6-cyclin D3 expression levels, quality and purity (Figure 6-10 A) no crystal hits were obtained. One potential crystal lead for CDK6-cyclin D3 in complex with PD0332991 in the JCSG⁺ commercial screen (Molecular Dimensions) formed in 2 M ammonium sulfate, 0.1 M sodium acetate. A small rod like crystal was observed after 10 days and slowly grew to almost 200 μm in length after a further 10 days (Figure 6-10 B). The crystal was harvested, as described in Section 6.2.5, revealing it was fragile to the touch, however no diffraction was observed at the synchrotron. Further, optimisation around this condition is currently underway.

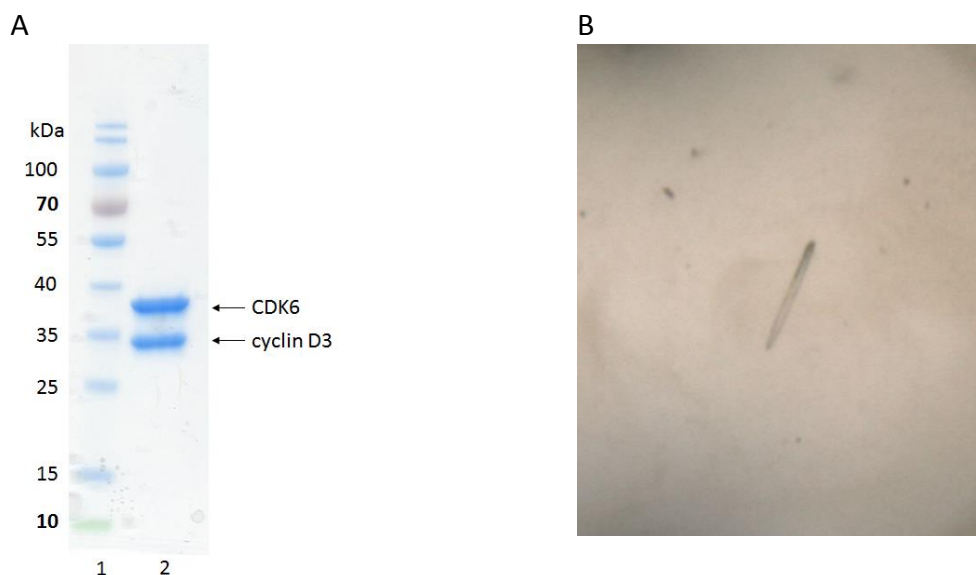


Figure 6-10 CDK6-cyclin D3 crystallisation trials

(A) CDK6-cyclin D3 used for crystallisation. 12% SDS-PAGE stained using InstantBlue. Lane 1, PageRuler protein ladder; Lane 2, CDK6-cyclin D3. (B) Image of potential CDK6-cyclin D3-PD0332991 crystal hit taken by the Minstrel automated imaging system (Rigaku). The crystal is 200 μm in length.

Additional CDK6 crystallisation trials were performed using members of the INK family. Crystallisation trials of CDK6-p16^{M53I}, CDK6-p16^{M53E}, CDK6-cyclin D3-p27M, CDK6-cyclin D3-p27S and CDK6-cyclin D3-p21S complexes were prepared, as outlined in Section 6.2.5, using a range of commercially available screens. However, no crystals were obtained. A range of truncated CDK6, cyclin D1 and cyclin D3 constructs were also designed, as described in Section 2.1.3, to remove flexible regions at both the N and C-termini for improved crystal packing. However, expression of these constructs was not successful.

6.5 ATP-competitive inhibitor crystallisation trials using a CDK2 surrogate

The readily crystallisable CDK2-cyclin A2 complex was used as a structural surrogate to investigate the interactions of CDK4/6 selective ATP-competitive inhibitors. Whilst having far higher affinity towards CDK4/6 (low nanomolar) compared to CDK2 (tens of micromolar) incubation with millimolar concentrations of the inhibitors, with the highly homologous CDK2, can allow ligand bound structures to be determined. Structural analysis may lead to better understanding of their selectivity towards CDK4/6 and potential consequences on the Cdc37 interaction. CDK2-cyclin A2 was expressed and purified in a phosphorylated form (Figure 6-11) as described in Sections 2.3.6 and 2.4.

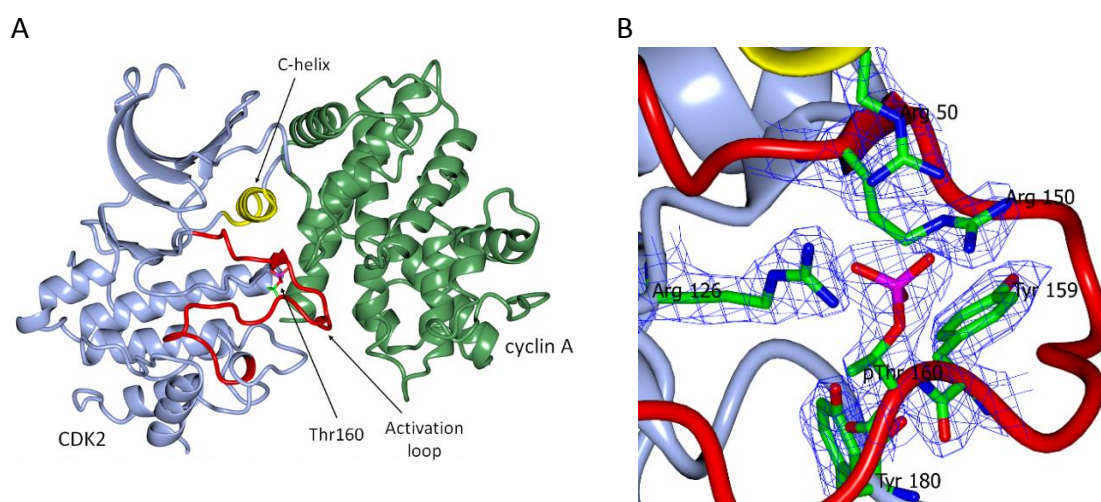


Figure 6-11 CDK2-cyclin A2 used in crystallisation trials was phosphorylated on Thr160. (A) CDK2-cyclin A2 used in crystallisation trials, shown in ribbon form, is present in the 'active' conformation. CDK2 is shown in ice blue, cyclin A in green, the C-helix in yellow and the activation loop in red. The phosphorylated Thr160 residue is also highlighted. (B) A close up of phosphorylated Thr160 and surrounding residues displayed with $2F_o - F_c$ electron density (blue mesh) contoured at 0.32 electrons/ \AA^3 . Residues are displayed in cylinder form and coloured by atom type. Images created in CCP4MG (McNicholas *et al.*, 2011).

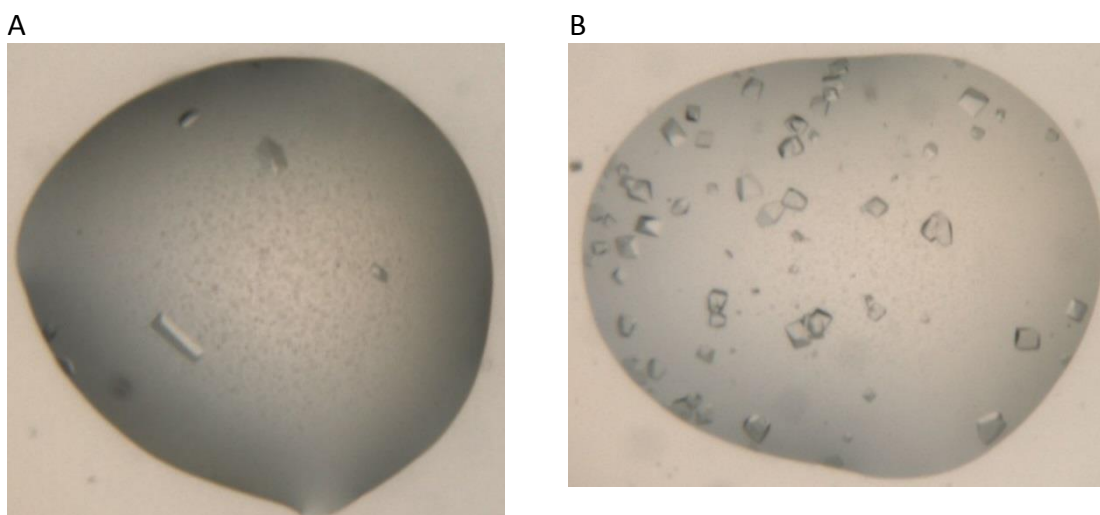


Figure 6-12 Images of CDK2-cyclin A2 crystals used for structure determination

(A) CDK2-cyclin A-LY2835219 crystals (B) CDK2-cyclin A apo crystals used for Lee011 soaking. Crystals were grown in 96 well plates and incubated and imaged at 4 °C in a Rigaku Minstrel.

Co-crystallisation trials of CDK2-cyclin A2 using both LY2835219 and Lee011 were set up using an optimised ammonium sulphate and potassium chloride buffer screen (Appendix A). Co-crystals were obtained with LY2835219 in a variety of conditions (Figure 6-12 A). Co-crystallisation attempts with Lee011 proved unsuccessful, most likely due to the requirement of DMSO to maintain Lee011 solubility. Therefore, Lee011 was soaked into apo-CDK2-cyclin A2 crystals (Figure 6-12 B) as described in Section 6.2.5. Crystals used for structure determination were grown in the conditions outlined in Table 6-1. Most hits formed small tetragonal crystals after three days of between 100-150 μm in length. Crystals were harvested using saturated ammonium sulphate as a cryoprotectant and flash frozen in liquid nitrogen.

Data collection was performed at the Diamond Light Source (Didcot, UK) on beamline IO4-1 at 100 K using an oscillation range of 0.1° for a total oscillation of 200°. Data processed using Xia2 (Winter, 2010) and programmes from the CCP4i2 suite (Winn *et al.*, 2011) and the structures determined by molecular replacement using Molrep (Vagin and Teplyakov, 1997) with the previously determined CDK2-cyclin A2 structure (PDB: 1H1S) as a search model followed by rounds of refinement using COOT (Emsley *et al.*, 2010) and REFMAC5 (Murshudov *et al.*, 1997). The final structures were validated using MolProbity (Chen *et al.*, 2010). CDK2-cyclin A2 structures containing LY2835219 and Lee011 were determined to 2.07 Å and 2.65 Å and the data collection and processing statistics are provided in Table 6-2 and Table 6-3 respectively.

CDK2-cyclin A2-LY2835219

Wavelength (Å)	0.92		
Space Group	P 21 21 21		
a, b, c, (Å)	74.9, 136.3, 151.5		
α , β , γ (°)	90.0 90.0 90.0		
Resolution (Å)	68.2 - 2.07 (2.11 - 2.07)		
I/ σ I	8.4 (1.5)		
R _{merge}	0.124 (1.388)		
Completeness (%)	100 (100)		
Multiplicity	7.2 (6.7)		
Refinement		Molprobitry	
R _{work} /R _{free}	0.225 / 0.253	Clashscore (All atoms)	0.92 (100 th percentile - 2.07 Å +/- 0.25 Å)
Mean B-Value (Å ²) (Chains; A, B, C, D)	36.3, 39.9, 51.5, 58.1	Poor rotomers	5 (0.53 %)
Water	32.9	Ramachandran outliers	2 (0.19 %)
LY2835219	40.7, 49.2	Ramachandran favoured	912 (98.58 %)
No. of atoms		No of CB deviations (> 0.25 Å)	1 (0.10 %)
Protein	4744, 4137, 4247, 4092	Molprobitry score	0.78 (100 th percentile - 2.07 Å +/- 0.25 Å)
Water	109	Residues with bad bonds	4 (0.05 %)
LY2835219	69, 69	Residues with bad Angles	0 (0.00 %)
Rmsd			
Bond lengths (Å)	0.0109		
Angles (°)	1.384		

Table 6-2 Data collection and refinement statistics for determination of the CDK2-cyclin A2-LY2835219 complex structure

Data collection statistics for CDK2-cyclin A2 co-crystals with LY2835219. The data was collected from a single crystal at 100 K on beamline IO4-1 at Diamond Light Source (DLS). The data was processed using xia2 (3daii-run). Statistics are presented as averages with values for the highest resolution shell in parentheses. Refinement statistics were generated using Refmac5, and Validation statistics by the Molprobitry web server.

CDK2-cyclin A2-Lee011

Wavelength (Å)	0.92		
Space Group	P 21 21 21		
a, b, c, (Å)	74.8 135.5 151.7		
α , β , γ (°)	90.0 90.0 90.0		
Resolution (Å)	67.7 - 2.65 (2.74 - 2.65)		
I/ σ	9.3 (1.6)		
Rmerge	0.177 (1.121)		
Completeness (%)	100 (100)		
Multiplicity	7.2 (7.6)		
Refinement		Molprobit	
R _{work} /R _{free}	0.212 / 0.265	Clashscore (All atoms)	1.87 (100 th percentile - 2.65 Å +/- 0.25 Å)
Mean B-Value (Å ²) (Chains; A, B, C, D)	58.8, 59.7, 89.9, 92.7	Poor rotomers	28 (2.92 %)
Water LY2835219	48.1 67.4, 87.9	Ramachandran outliers	4 (0.38 %)
No. of atoms Protein	4746, 4137, 4707, 3879	Ramachandran favoured	1025 (96.24 %)
Water LY2835219	22 62, 62	No of CB deviations (> 0.25 Å)	4 (0.39 %)
Rmsd Bond lengths (Å)	0.0124	Molprobit score	1.56 (100 th percentile - 2.65 Å +/- 0.25 Å)
Angles (°)	1.612	Residues with bad bonds	4 (0.04 %)
		Residues with bad Angles	1 (0.04 %)

Table 6-3 Data collection and refinement statistics for determination of the CDK2-cyclin A2-Lee011 complex structure

Data collection statistics for CDK2-cyclin A2 crystals soaked with Lee011. The data was collected from a single crystal at 100 K on beamline IO4-1 at Diamond Light Source (DLS). The data was processed using xia2 (3daii-run). Statistics are presented as averages with values for the highest resolution shell in parentheses. Refinement statistics were generated using Refmac5, and Validation statistics by the Molprobit web server.

The space group of $P2_1 2_1 2_1$ was determined with 81.5% and 72.5% probability for LY2835219 and Lee011 respectively by Pointless. Lower symmetry space groups for each had less than a 1% likelihood as they are prohibited by the 90° angles determined for all three unit cell dimensions. The three-fold screw axis was confirmed by systematic absence analysis which had over 92% probability of a 2-fold access for each dimension, except for one dimension for Lee011 which was 83%. The next most probable space groups, with a two-fold screw axis, were only 7.5% and 14.7% likely. Both structures contained two complexes of CDK2-cyclin A2 in the unit cell, however, the electron density for chains A and B (one CDK2-cyclin A2 complex) in both cases was more extensive than for the alternative complex (chains C and D) suggesting improved ordering of the first complex through crystal contacts. This difference in electron density was also observed in a native crystal collected, which was also $P2_1 2_1 2_1$ and possessed almost identical unit cell dimensions, suggesting that the overall protein structure and subsequent packing is not significantly altered by inhibitor binding.

6.6 Comparison of CDK4/6 inhibitor interactions

The electron density for LY2835219 (Figure 6-14 A) and Lee011 (Figure 6-14 B) was clearly visible in the CDK2 ATP binding pocket allowing the inhibitors to be modelled into the sites. Ligand presence was confirmed by composite omit map (Figure 6-14 C and D). The chemical structures of each of these compounds are provided in Figure 6-13.

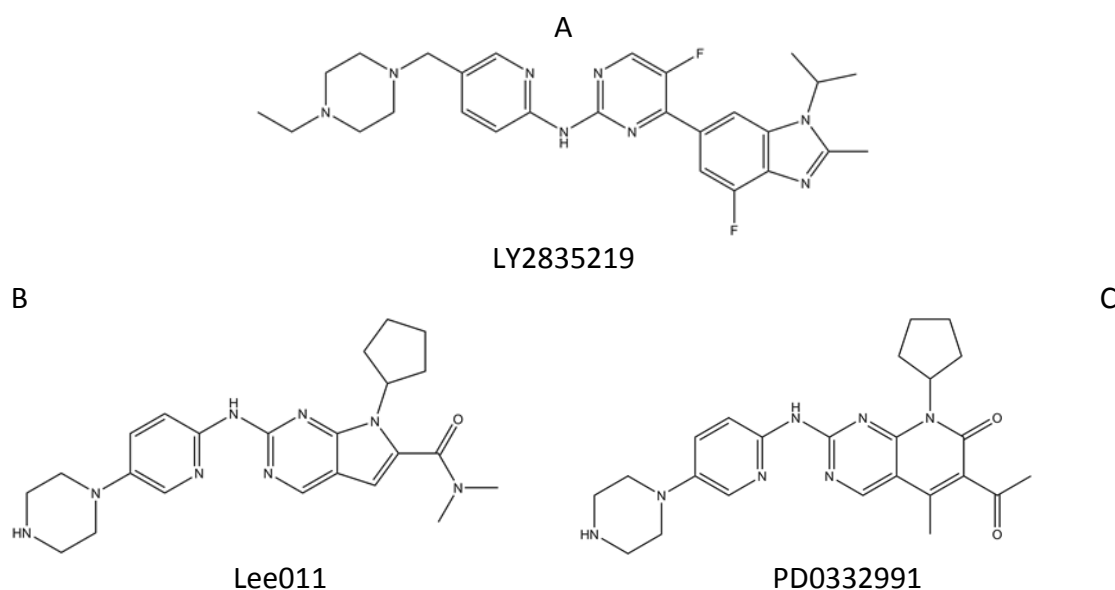


Figure 6-13 Chemical structures of LY2835219, Lee011 and PD0332991

Structures were drawn in Chemdraw.

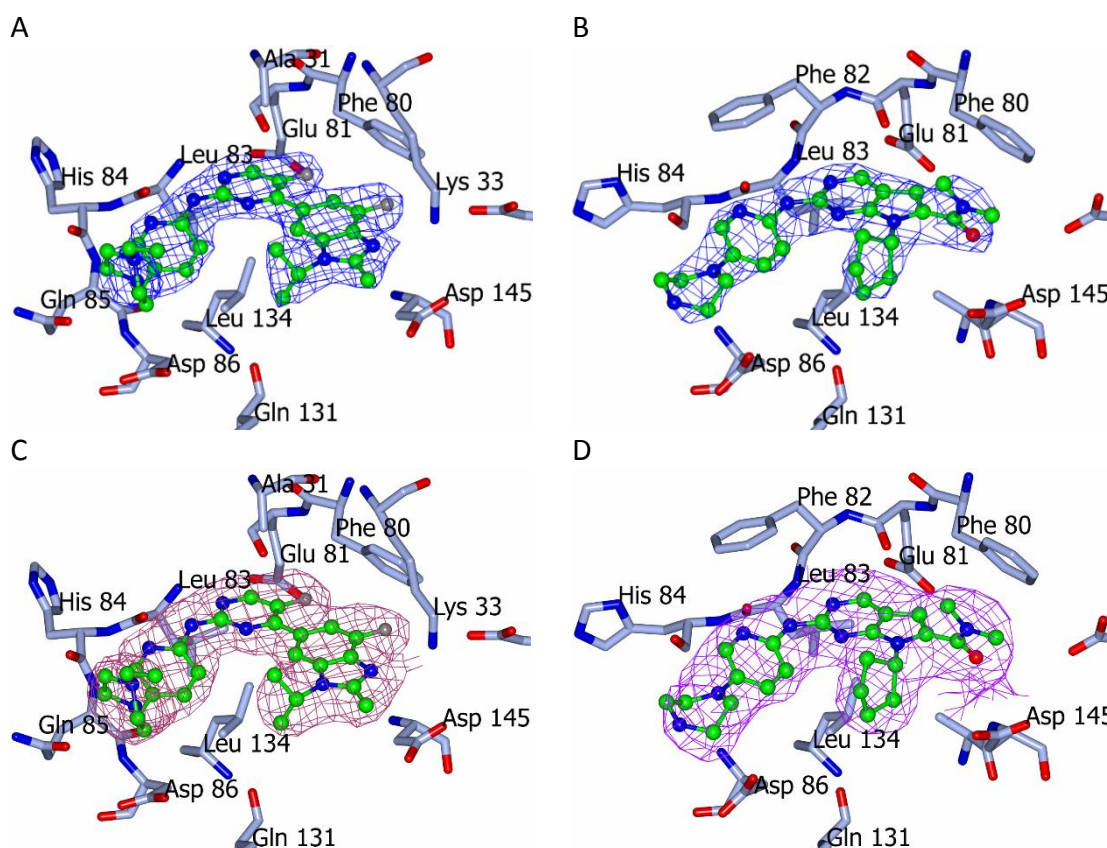


Figure 6-14 Structures of LY2835219 and Lee011 bound to the CDK2-cyclin A2 ATP binding site

(A) LY2835219 bound to the active site of CDK2. Amino acids within 4 Å are displayed and coloured by atom type. $2F_o - F_c$ maps contoured at 0.32 electrons/Å³ (B) Lee011 bound to the active site of CDK2. Amino acids within 4 Å are displayed and coloured by atom type. $2F_o - F_c$ maps contoured at 0.23 electrons/Å³. (C) Composite omit map of LY2835219 contoured at 0.32 electrons/Å³. (D) Composite omit map of Lee011 contoured at 0.23 electrons/Å³. Omit maps generated using Composite omit map in Phenix (Terwilliger *et al.*, 2008). In each panel, some residues have been removed for clarity. Images created in CCP4MG (McNicholas *et al.*, 2011).

The structure of CDK2-cyclin A2-PD0332991 has previously been determined (Hallett, 2013) allowing for comparison of the binding modes of these three inhibitors. PD0332991, LEE011 and LY2835219 share a very similar binding mode and are typical Type I kinase inhibitors. All three compounds sit in the same plane and share an orientation such that their 2-pyrimidinamine-benzimidazole pyrimidine-based scaffolds pack towards the back of the pocket against the gatekeeper (Phe80). All three inhibitors form a conserved hydrogen bond to the hinge. The specific interactions of these compounds were investigated to better understand which differences, if any, may underlie the observed differences in their abilities to disrupt the CDK-Cdc37 complexes. Interactions were analysed using CCP4MG based on residues which fell within a distance of 4 Å from the compound. Hydrogen bonds were assigned by CCPMG based on the

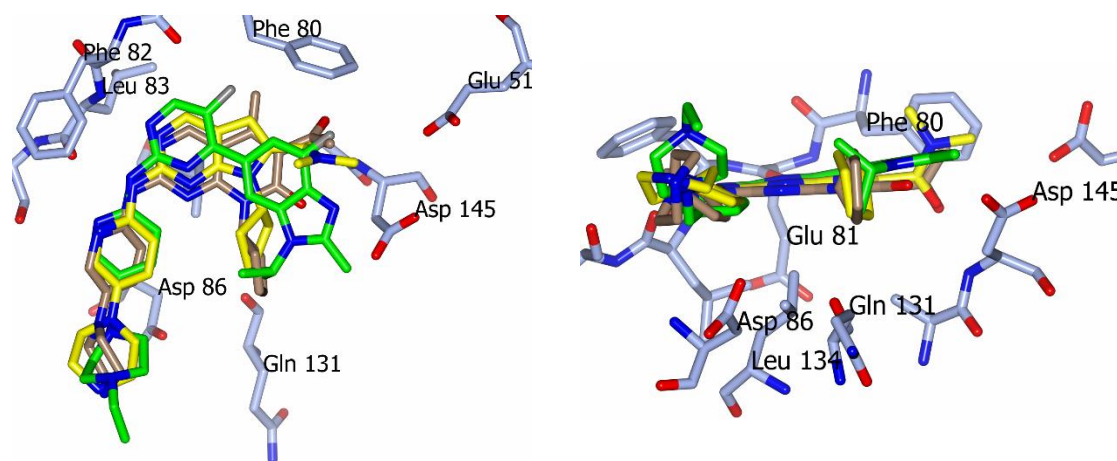


Figure 6-15 Inhibitor overlay

Overlay of all three inhibitors in the ATP binding pocket from two angles. Residues displayed are from the Lee011 containing CDK2-cyclin A structure. Bonds are displayed in cylinder form with oxygens in red, nitrogen in blue, fluorine in grey and carbon in light blue, green, yellow and brown for the CDK2, LY2835219, Lee011 and PD0332991 respectively. Images created in CCP4MG (McNicholas *et al.*, 2011).

optimum distance of a hydrogen bond of 3 Å. Binding modes were further analysed using Poseview to provide a 2D representation of the key interactions.

6.6.1 LY2835219 vs Lee011 binding to CDK2-cyclin A

LY2835219 makes one hydrogen bond to the carbonyl moiety of Leu83, a hinge backbone interaction that is not made by the authentic ligand ATP. In addition, there is an extensive network of interactions between a fluorine and two water molecules occupying a cavity at the back of the binding site that is lined by the sidechains of Lys33 and Glu51 (Figure 6-16 A). Lee011 also makes this hydrogen bond (Figure 6-16 B). However, for both inhibitors the hydrogen bonding network between the 2-aminopyridine group and the remainder of hinge region backbone (Phe82, Leu83, His84, Gln85) appears to be inefficient due to longer than optimum bond distances of around 3.2 Å to Leu83 and 3.8 Å to Gln85.

Both compounds pack tightly against the gatekeeper residue (Phe80) at the back of the pocket forming hydrophobic interactions with it and Val64. Additional hydrophobic interactions are formed with Leu134 beneath the inhibitor, from the C lobe, while Ala31 and Ile10 form additional hydrophobic interactions from above. Comparison of the pocket's size and shape also shows that LY2835219 pushes Glu81 back (Figure 6-16 E), by around 1 Å, forming a larger pocket than observed with Lee011 (Figure 6-16 F), reflecting the larger size of LY2835219. Additional interactions are observed between

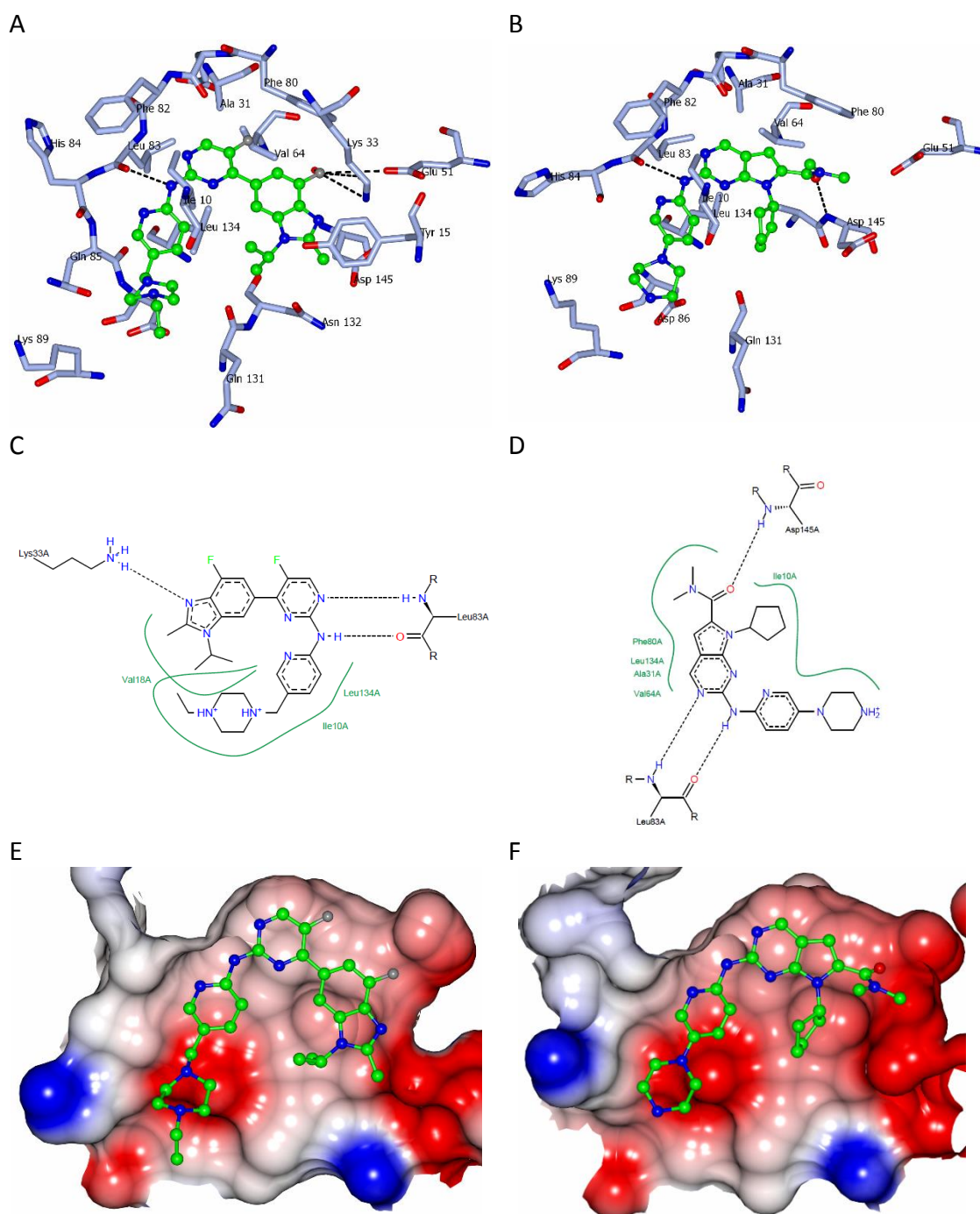


Figure 6-16 A structural comparison of the binding of LY2835219 and Lee011 to CDK2 (A) LY2835219 bound to the active site of CDK2. Amino acids within 4 Å are displayed in cylinder form and coloured by atom type with carbon (light blue), oxygen (red), nitrogen (blue) and fluorine (grey). Inhibitor displayed in ball and stick form and hydrogen bonds are shown by dashed lines. (B) Lee011 bound to the active site of CDK2. Amino acids within 4 Å are displayed in cylinder form and coloured by atom type. Inhibitor displayed in ball and stick form and hydrogen bonds are shown by dashed lines. (C) 2D representation of LY2835219 interactions with CDK2 created by Poseview. (D) 2D representation of Lee011 interactions with CDK2 created by Poseview. (E) The protein surface of LY2835219 bound to the active site of CDK2 coloured by electrostatic potential with negative in red and positive in blue. Inhibitor atoms are displayed as ball and stick form. (F) The protein surface of Lee011 bound to the active site of CDK2 coloured by electrostatic potential. Inhibitor atoms are displayed as ball and stick models. Structural images were created in CCP4MG (McNicholas *et al.*, 2011).

the dimethylamide of Lee011 which packs against Asp145 and Ala144 at the back of the pocket between the gatekeeper (Phe80) and the catalytic Asp145 that forms the beginning of the DFG motif.

Each compound contains a solubilising moiety, a piperazine on Lee011 (and PD0332991) and the slightly bulkier ethyl-piperazinyl group on LY2835219. These groups protrude out of the pocket, following the line of the hinge, into the solvent. While the piperazine group on Lee011 remains in the same plane as the rest of the molecule the ethyl-piperazinyl on LY2835219 is kinked upwards towards the N lobe (Figure 6-16 A, E). While this potentially brings the nitrogen on the ethyl-piperazinyl within range to make a weak hydrogen bond (3.4 Å) with the backbone oxygen of Ile10, the incomplete electron density for this group suggests a degree of mobility still exists. This orientation may be partially caused by the close location of Lys89 which sits just outside the mouth of the pocket, and which may sterically hinder optimal binding. However, this residue is disordered and is not visible in the electron density.

6.6.2 Alternate packing of the P-loop

In the LY2835219-bound structure Tyr15 on the P-loop of CDK2 is folded back towards the inhibitor and stacks on top of a methyl group of LY2835219 (Figure 6-17 A). Interestingly, this is not observed in either of the other inhibitor structures for which there is little to no electron density in this region showing that this loop remains, comparatively, disordered. In the Lee011 structure (Figure 6-17 B) only the electron density for the carbon backbone is visible, whereas in the structure of PD0332991 the side chain of Thr14 has not been built due to the lack of density present. This region contains the GXGXXG sequence that is involved in the interaction with Cdc37 (Zhao *et al.*, 2004; Terasawa *et al.*, 2006; Verba *et al.*, 2016). It can be hypothesized that this stabilisation of the P-loop would lead to LY2835219 being a more potent inhibitor and that this behaviour would also make it an effective inhibitor of the CDK-Cdc37 interaction. Such behaviour was observed in the HTRF competition assay with CDK6 (Figure 6-8 B). However, it does not explain the result observed with CDK4 (Figure 6-9).

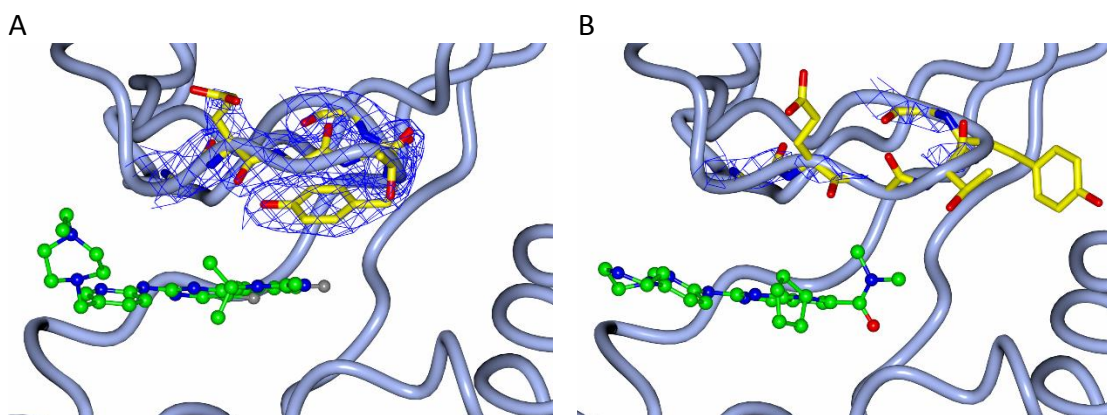


Figure 6-17 LY2835219 orders the CDK2 P-loop

(A) The ordered structure of the P-loop of CDK2 with LY2835219 bound. The $2F_o-F_c$ map is contoured at $0.25 \text{ electrons}/\text{\AA}^3$. (B) The disordered structure of the P-loop of CDK2 with Lee011 bound with only the carbon backbone distinguished. The $2F_o-F_c$ map is contoured at $0.25 \text{ electrons}/\text{\AA}^3$. In each panel, the carbon backbone of CDK2 is displayed in worm form in blue and the inhibitor is displayed in ball and stick form with the carbons (green), nitrogen (blue), oxygen (red). Sidechains are displayed in cylinder form with carbon (yellow), nitrogen (blue) and oxygen (red). Images created in CCP4MG (McNicholas *et al.*, 2011).

6.6.3 Comparison of Lee011 and PD0332991 binding to CDK2-cyclin A2

The structure of PD0332991 bound to CDK2 has been determined and the interactions it makes described (Hallett, 2013). Comparison of this structure with that of the CDK2-cyclin A2-Lee011 complex reveals an almost identical binding mode for the two inhibitors. However, PD0332991 makes an additional hydrogen bond between the acetyl oxygen and the backbone amide of Asp145 (Figure 6-18 A), and Lee011 packs slightly tighter to Phe80 and Glu81 at the back corner of the pocket, likely due to the presence of the bulkier dimethylamide group and the lack of the methyl group on PD0332991.

The structure of PD0332991 bound to CDK6-Vcyclin has been determined (PDB: 2EUF) and is in the active conformation due to viral cyclin binding. Here PD0332991 makes more efficient hydrogen bonds with the hinge region backbone (Val101, Asp102, Gln103) due to improved packing against the hinge shortening the bond distances (Figure 6-18 B). An additional hydrogen bond is also made between the ketone group and the amide of Asp163 (Asp145 in CDK2) due to slightly better packing of the inhibitor in the pocket. The tighter packing is caused by a shift in the P-loop causing residues Ile19, Gly20 and Val27 to pack closer on top of PD0332991 closing the pocket more efficiently around the inhibitor (Figure 6-18 F).

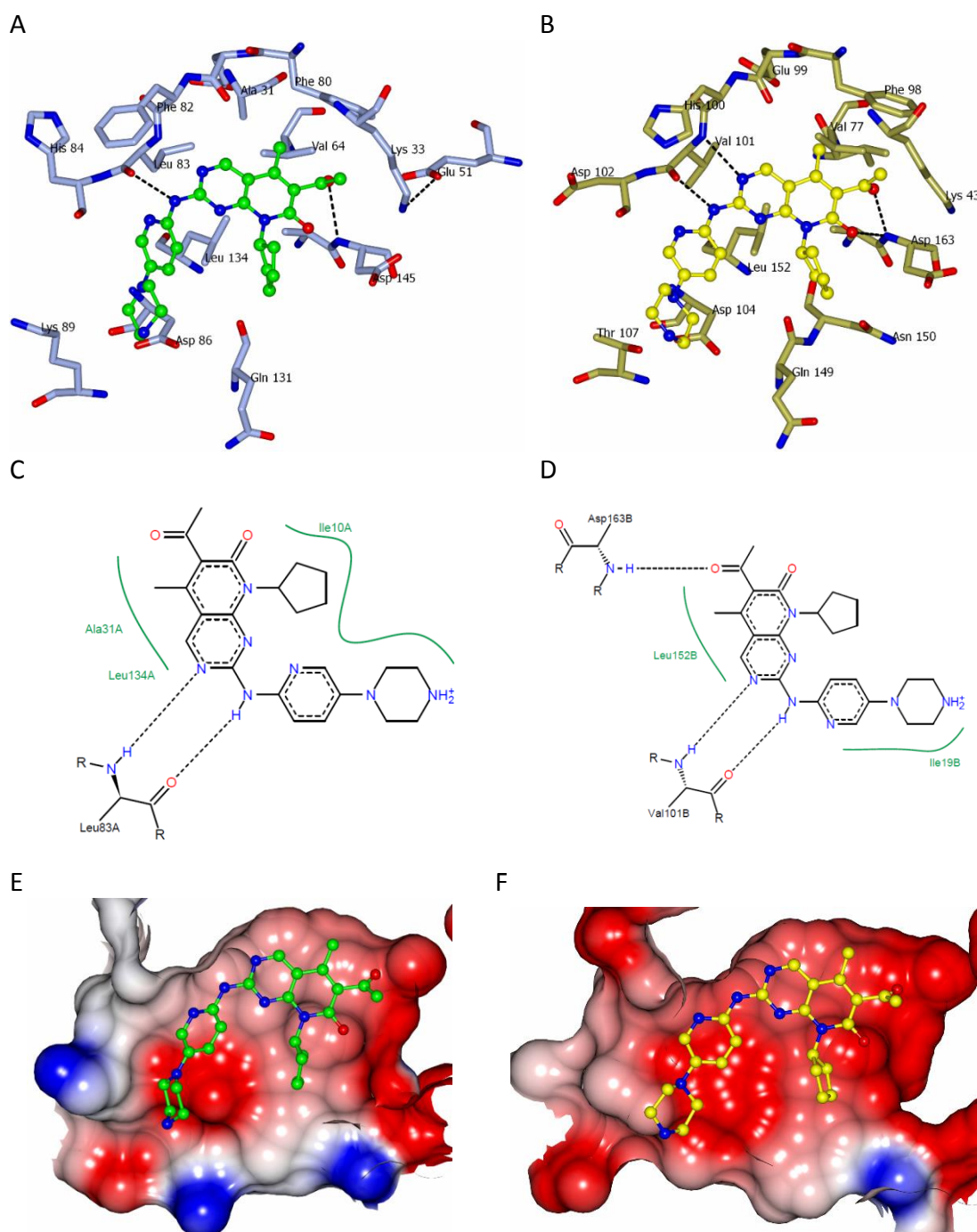


Figure 6-18 A comparison PD0332991 binding to CDK2-cyclin A2 and CDK6-Vcyclin
 (A) PD0332991 bound to the active site of CDK2. Amino acids within 4 Å are displayed in cylinder form and coloured by atom type with carbon (light blue), oxygen (red) and nitrogen (blue). Inhibitor displayed in ball and stick form and hydrogen bonds are shown by dashed lines. (B) PD0332991 bound to the active site of CDK6. Amino acids within 4 Å are displayed in cylinder form and coloured by atom type. Inhibitor displayed in ball and stick form with carbon (yellow) and hydrogen bonds are shown by dashed lines. (C) 2D representation of PD0332991 interactions with CDK2 created by Poseview. (D) 2D representation of PD0332991 interactions with CDK6 created by Poseview. (E) The protein surface of PD0332991 bound to the active site of CDK2 coloured by electrostatic potential with negative in red and positive in blue. Inhibitor atoms are displayed as ball and stick form. (F) The protein surface of PD0332991 bound to the active site of CDK6 coloured by electrostatic potential. Inhibitor atoms are displayed as ball and stick form. Images were created in CCP4MG (McNicholas *et al.*, 2011).

6.6.4 Modelling PD0332991 into CDK6 active site

The PD0332991-CDK6-Vcyclin structure was then used as a template to compare the binding modes of PD0332991, LEE011 and LY2835219 between CDK2 and CDK6. The sequences of CDK2 and CDK6 were aligned using the conserved residue ranges 56-67 and 98-163 (of CDK6) and then the three inhibitors bound to CDK2 were displayed over the CDK6 binding site bound to PD0332991. Bound to CDK6, PD0332991 sits around 1 Å lower in the binding pocket, towards the C-terminal lobe, than each of the CDK2 bound inhibitors. This binding mode is most likely caused by the tighter packing of the P-loop from above.

As observed previously, the positions of PD0332991 in both CDKs overlap well with only a slight variation in the piperazine group orientation which now packs closer towards the hinge in the CDK6-bound structure (Figure 6-19 A). This combination of piperazine group shift and the tighter clamping down by the P-loop on PD0332991 in CDK6 better aligns the hinge hydrogen bonding groups. The 2-pyrimidinamine group of LY2835219 in this position would pack too closely with Glu99 (2.24 Å) and therefore form unfavourable van der Waals interactions (Figure 6-19 B). Comparison of the conserved 2-pyridinyl groups which form the hydrogen bonds with the hinge, reflects this movement showing on average a 1.3 Å shift further towards the front of the pocket for PD0332991 bound to CDK6. The equivalent shift in Lee011 is smaller, just under 1 Å, reflecting the slightly smaller size of the pyrrolo[2,3-d]pyrimidine scaffold (Figure 6-19 C). The removal of the methyl group present on PD0332991 would also allow closer packing to Phe98. Comparison of the position of the solvent-exposed piperazine groups shows a comparable shift of between 1.3 Å and 1.8 Å for the three compounds bound to CDK2 compared to CDK6. As a result, the PD0332991 piperazine packs more closely with Thr107 allowing better alignment along the hinge, perhaps due to the loss of steric hindrance from Lys89, the equivalent residue in CDK2. The combination of the shift of the solvent exposed piperazine group towards Thr107, helping to align the hinge hydrogen bonds, assisted by the tighter clamping down of the P-loop likely give rise to the specificity of these compounds towards CDK4/6 over CDK2.

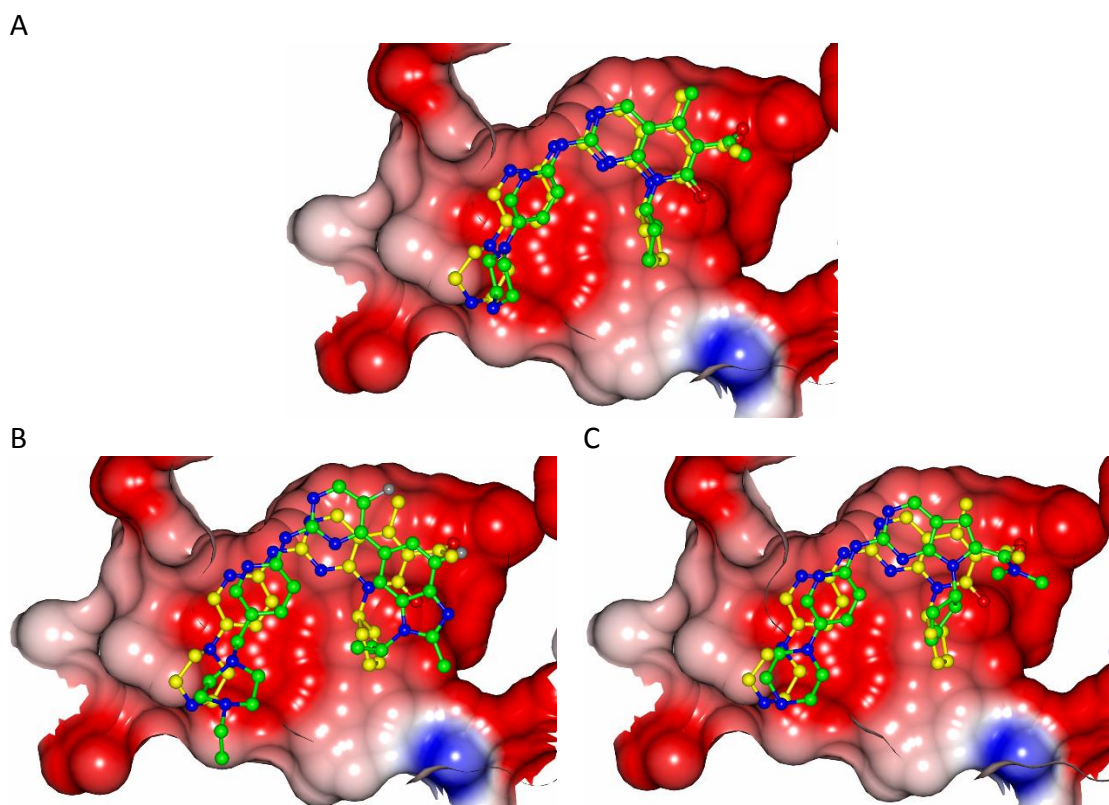


Figure 6-19 Comparative inhibitor interactions between CDK active sites

(A) The protein surface of PD0332991 is modelled over the active site of CDK6 with PD0332991 bound. The surface is coloured by electrostatic potential with negative in red and positive in blue. CDK2 inhibitor atoms are displayed as ball and stick form with carbon (green), nitrogen (blue) and oxygen (red). CDK6 PD0332991 atoms are displayed as ball and stick form with carbon in yellow. (B) The protein surface of LY2835219 modelled over the active site of CDK6 with PD0332991 bound coloured by electrostatic potential. CDK2 inhibitor atoms are displayed as ball and stick form with carbon in green (fluorine in grey). CDK6 PD0332991 atoms are displayed as ball and stick form with carbon in yellow. (C) The protein surface of Lee011 modelled over the active site of CDK6 with PD0332991 bound coloured by electrostatic potential. CDK2 inhibitor atoms are displayed as ball and stick form with carbon in green. CDK6 PD0332991 atoms are displayed as ball and stick form with carbon in yellow. Images were created in CCP4MG (McNicholas *et al.*, 2011).

6.6.5 Why is Lee011 so much weaker a competitor?

Given the similarities in binding position and interactions between the two very analogous inhibitors PD0332991 and Lee011, and CDK2, it is difficult to see why Lee011 appears considerably less potent at disrupting the CDK-Cdc37 interaction. The only difference observed in inhibitor binding was slightly tighter packing to the back of the pocket due to the lack of the methyl group present on PD0332991. However, comparison of the position of the P-loop also reveals a more open pocket for Lee011 (Figure 6-20 B) compared to that of PD0332991 (Figure 6-20 C). This region is different again in the LY2835219-bound CDK2 structure, which showed tight packing of Tyr15 and

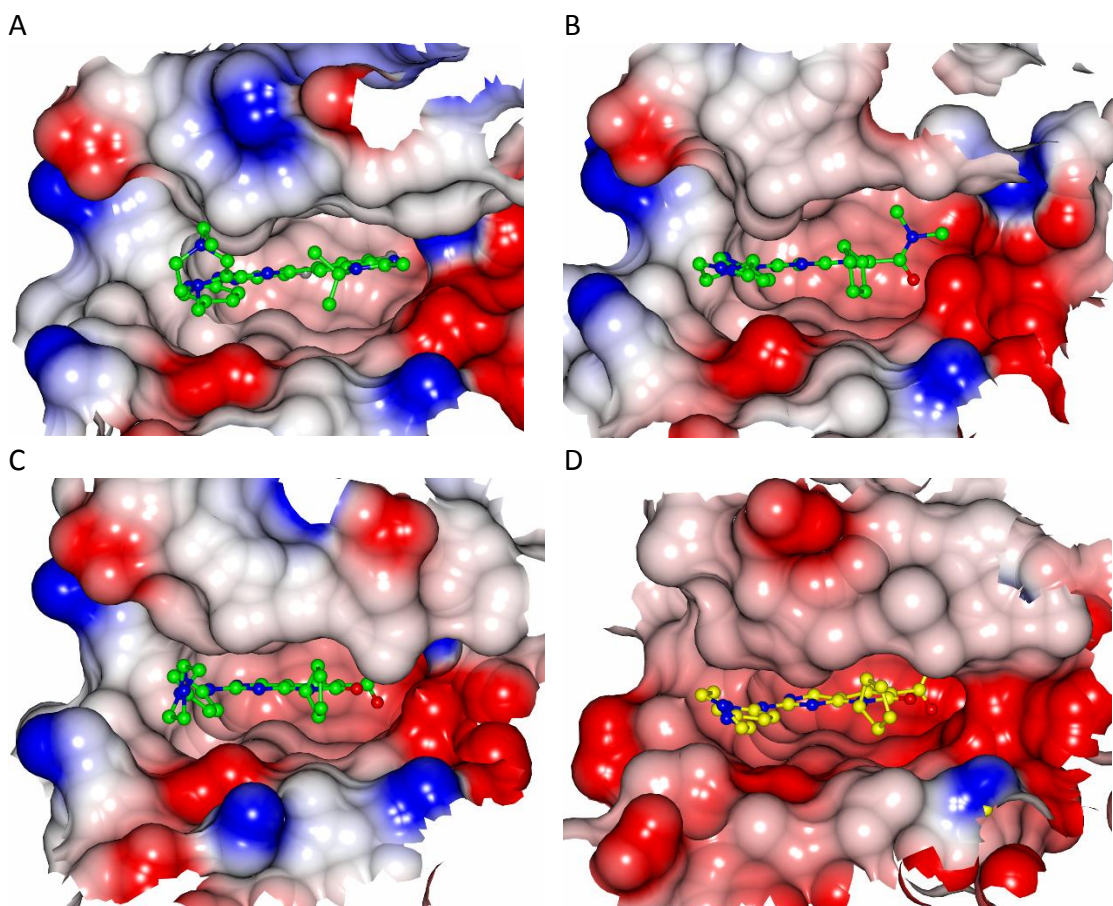


Figure 6-20 Comparison of the binding of LY2835219, Lee011 and PD0332991 to CDK2-cyclin A

For each panel the view is taken looking in to the CDK2 (A, B, C) or CDK6 (D) ATP binding pocket and the CDK surface is coloured by electrostatic potential with negative in red and positive in blue. All inhibitors are drawn in ball and stick mode. (A, B, C) LY2835219 (A), Lee011 (B) and PD0332991 (C) bound to CDK2. Inhibitor atoms are coloured by atom type: carbon (green), nitrogen (blue), oxygen (red) and fluorine (grey). (D) PD0332991 bound to CDK6. PD0332991 atoms are coloured by atom type with carbon in yellow. Images were created in CCP4MG (McNicholas *et al.*, 2011).

an ordered P-loop (Figure 6-20 A). The packing of the P-loop was observed to be tighter still in CDK6 (Figure 6-20 D). It is possible that this more open and accessible structure, through poorer packing of the P-loop, gives rise to the easier disruption of the kinase N lobe by Cdc37 and hence the poorer ability of this inhibitor to compete.

A small shift in the position of Lys33 of around 2.3 Å (Figure 6-21 orange) was also observed in the CDK2-Lee011 complex when compared to the structure of CDK2 bound to LY2835219 (blue), PD0332991 (grey) and the equivalent Lys43 in CDK6 (gold). This loss of an extended hydrogen bonding network instigated by its interaction with Glu51, may be sufficient to weaken the kinase N-terminal lobe and improve Cdc37 binding. The dimethylamide that interacts with this corner of the ATP binding pocket appears to

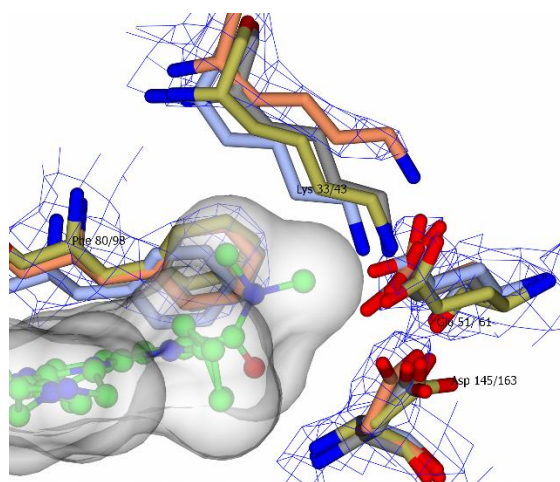


Figure 6-21 Lee011 binding to CDK2 is accompanied by a shift in Lys33

Lys33 of CDK2 in the Lee011 containing structure is out of line compared with the corresponding residue in other structures. Lee011 atoms are displayed as ball and stick models with carbon (green), nitrogen (blue) and oxygen (red). Amino acids are displayed in cylinder form with CDK2-LY2835219 (light blue), CDK2-Lee011 (coral), CDK2-PD0332991 (grey), CDK6-PD0332991 (gold). 2Fo-Fc maps contoured at 0.22 electrons/Å³ for the residues corresponding to the Lee011 bound structure.

intrude into this site which may be sufficient to cause steric hindrance of the lysine hydrogen bonding network. However, the movement of this residue may also reflect a general weakening of the N lobe stability due to weakened inhibitor packing in the binding site.

6.7 Discussion

The ability to disrupt CDK-Cdc37 complexes using clinically relevant CDK4/6-specific inhibitors was investigated using the HTRF competition assay. A clear 10-fold difference was observed in the ability of PD0332991 and Lee011 to disrupt the complex despite their seemingly similar structures. Additionally, the inhibitors were less active towards CDK4, although this may simply reflect the difference in stability between these two proteins as revealed by their differing Cdc37 affinities.

Despite improvements in CDK6 expression and purification attempts to crystallise a number of CDK6-containing complexes proved unsuccessful. Although multiple chemical and protein binding partners were explored to attempt to stabilise CDK6 complexes, the use of CAK to phosphorylate and order the CDK6 activation segment was not explored and would be the next step for crystallisation trials. CDK2-cyclin A2 was instead used as a structural surrogate to investigate the binding modes of CDK4/6-specific inhibitors to better understand the difference observed in their ability to disrupt

CDK-Cdc37 complexes. X-ray structure determination revealed only minor differences in the overall positioning and orientations of the three compounds. However, a substantial difference in the ordering of the P-loop was observed upon LY2835219 binding because of inhibitor-Tyr15 packing. The CDK6-Vcyclin-PD0332991 structure also shows that tight packing of the P-loop is a key feature of tight binding inhibitors. Ideally comparison with an inhibitor-bound CDK4 structure is needed to determine whether P-loop disordering is one of the factors that gives rise to the differing activities of the CDK4- and CDK6-Cdc37 complexes in the HTRF assay.

Comparison with the CDK6-Vcyclin-PD0332991 structure suggested that compound selectivity between CDK6 and CDK2 could be provided by substitution of Lys89 (in CDK2) with Thr107 in CDK6/4 resulting in the loss of potential steric hindrance with the inhibitor piperazine groups. Better alignment of the compound with the hinge and improved hydrogen bonding would then result. It is also possible that the nitrogen atoms in the piperazine group could form additional hydrogen bonds to the sidechain of Thr107 further stabilising this position. Other studies, however, have suggested that the altered flexibility of the hinge region, due to sequence differences, is what gives rise to the difference in selectivity between CDK4 and CDK2 (Honma *et al.*, 2001; Lu and Schulze-Gahmen, 2006). While writing this manuscript a paper was published describing the interactions of these three inhibitors determined structurally in the binding pocket of CDK6 (Chen *et al.*, 2016). They also noted the substitution of Lys89 in CDK2 with Thr107 as key to providing the specificity of these compounds towards CDK4/6 however they also noticed stabilising hydrogen bonds to the sidechain of His100 on CDK6, which are not possible to Phe82 of CDK2. Direct comparison with CDK4 is difficult as there are no structures of CDK4 in the active conformation. There are only two sequence differences between CDK4 and CDK6 in the ATP binding site. The substitution of Val14 on the P-loop of CDK4 for Glu21 in CDK6, although not directly involved in inhibitor interactions, may have a larger effect on the overall packing and flexibility of this loop.

It was less clear as to what gave rise to the significantly weaker ability of Lee011 to disrupt CDK-Cdc37 complexes, as its binding appears highly comparable to PD0332991. The tighter packing of Lee011 to the back of the pocket may reduce its interaction with the P-loop and so reduce its potential to stabilise. Misalignment of Lys33 with Glu51 was only observed in the CDK2-Lee011 structure and suggests Lee011 binding may

destabilise the N-lobe fold. A thermal melt assay would determine if these compounds varied in their abilities to stabilise CDK4 and CDK6. A reduction in stability would suggest Cdc37 would be better able to bind, due to the observed propensity for Cdc37 to interact with less stable proteins (Keramisanou *et al.*, 2016). Determination of the K_d values of the inhibitors with the monomeric CDKs, for example using SPR, would determine if the observed weakened interaction, compared to the published IC_{50} values, is simply due to a difference in affinity to the monomeric state. However, the reduced solubility of Lee011 may preclude straightforward analysis.

It would be interesting to see if this difference in ability to destabilise the CDK-Cdc37 complexes by these inhibitors could be observed *in vivo* or even in the clinic. The HTRF results suggest that LY2835219 and PD0332991 would be more effective at downregulating CDK4/6 than Lee011 due to better inhibition of the Hsp90 pathway leading to higher levels of degradation. However, in contrast to BRAf inhibitors (Polier *et al.*, 2013), PD0332991 has been shown to stabilise CDK4-cyclin D complexes against degradation (Paternot *et al.*, 2014).

Chapter 7. Conclusions and future directions

The transition of cells through the early G1 stage of the cell cycle is co-ordinated by CDK4 and CDK6 following mitogen-dependent expression of D-type cyclins. This process is tightly controlled as irregular CDK activity results in abnormal cell cycle control and is a significant indicator of poor cancer prognosis. Hsp90 and the kinase specific co-chaperone Cdc37 form stable complexes with both CDK4 and CDK6 *in vivo* however the mechanism of client regulation and subsequent CDK4(6)-cyclin D complex formation is not fully understood. A range of biophysical and biochemical techniques have been used to investigate the mechanism of CDK4(6)-cyclin D complex formation and regulation via the Hsp90 chaperone system by both the D-type cyclins and CKIs.

In cells, the CDKs are predominantly distributed into either chaperone complexes with Hsp90, active cyclin-bound complexes or inhibited CKI-bound complexes (Stepanova *et al.*, 1996). The CDK distribution will depend on the relative concentrations and affinities of each CDK binding partner. The affinities of multiple CDK clients have therefore been determined using re-constituted *in vitro* assays and their abilities to displace Cdc37 compared. Firstly, CDK4 and CDK6 were shown to differ considerably in their affinity for Cdc37 and Hsp90 with K_{d-app} values determined as 92 +/- 29 nM and >500 nM for CDK4 and CDK6 respectively. This difference, first observed *in vivo*, has been suggested to reflect the inherent stability of the client kinase fold (Taipale *et al.*, 2012) with clients undergoing repeated rounds of capture and release of the chaperone system until an appropriate stabilising binding partner is found (Krukenberg *et al.*, 2011). The higher affinity of CDK4 may simply reflect the difference in protein stability between CDK4 and CDK6 or it may show tighter regulation of CDK4 by Hsp90 is required to prevent unwanted interactions within cells, suggesting a predominance of CDK4 activity in driving the G1 phase of the cell cycle.

The D-type cyclins displayed a wide range of abilities to redistribute the CDKs from Cdc37 and appeared to differ considerably in their affinities for CDK4 and CDK6. CDK6 complexes containing the viral cyclins or cyclin D3 formed more stable complexes against Cdc37 than those containing CDK4. The ability of the viral cyclins to disrupt the CDK6-Cdc37 complex correlated with the <10 nM affinity measured for the direct interaction. Cyclin D3 also bound tightly to CDK6, forming a stable complex against

Cdc37, while cyclin D1 binding was insufficient to prevent redistribution. In contrast CDK4, the stronger Cdc37-Hsp90 client, readily redistributed to a Cdc37 complex from all D-type cyclins. These results show that the D-type cyclin isoforms can distinguish between CDK4 and CDK6 when bound to Cdc37-Hsp90. As both CDK6 and cyclin D3 are required for lymphocyte development this difference in affinity may reflect an interaction which would allow preferential tissue specific fine tuning of CDK6 complex formation over CDK4 in these cells. Cyclin D2 has not been investigated in this thesis as it does not express in a soluble form, however, it would be interesting to see if it also showed a CDK preference.

The inability of any of the D-type cyclins to displace CDK4 from Cdc37 led to the investigation of p21CIP1 and p27KIP1 as potential assembly factors to assist D-type cyclin displacement of CDK4. Previous evidence for an assembly role function comes from studies on mouse embryonic fibroblasts (MEFs) which are far less efficient at assembling CDK4/6-cyclin D complexes *in vivo* when p21CIP1 and p27KIP1 are knocked down (Cheng *et al.*, 1999) and from isolated ternary CDK4-cyclin D-p27KIP1 complexes which retain kinase activity (Blain *et al.*, 1997). The *in vitro* HTRF experiments carried out here showed that the CIP/KIP family were inefficient at displacing both CDK4 and CDK6 from Cdc37 alone whilst in the presence of either cyclin D1 or cyclin D3 they formed stable ternary complexes that were highly resistant to Cdc37. From these results, it can be inferred that the reverse mechanism of this equilibrium process, whereby the presence of p21CIP1 or p27KIP1 would assist the D-type cyclins to partition the CDKs away from the Cdc37-Hsp90 complex, must also be true. With the assistance of either p21CIP1 or p27KIP1 the D-type cyclins would be able to rapidly extract the CDKs from the Hsp90 complex, speeding up the entry into the cell-cycle upon D-type cyclin expression and when the cellular concentrations of p21CIP1 and p27KIP1 are still high.

The ability of p27KIP1 to stabilise against Cdc37 displacement was explored using further truncated constructs and phosphomimetic point mutants at residues Tyr88 and Tyr89. Both of these point mutants and the p27₁₋₇₉ truncate, all of which removes the 3₁₀ helix from the active site, were still able to stabilise the CDK-cyclin complexes against Cdc37. This result is functionally significant as the displacement of the 3₁₀ helix from the ATP binding pocket of CDK4/6 is required for CDK activity (James *et al.*, 2008). CDK4/6-cyclin D bound to p27KIP1 phosphorylated on Tyr88 or Tyr89 would still be stable against

redistribution to Cdc37 while remaining active, supporting the idea of an assembly role for p27KIP1 and not just as an inhibitory mechanism.

Further truncation of a β -sheet on p27KIP1, which packs against $\beta 2$ of the CDK N-terminal lobe, showed a marked reduction in ability to stabilise CDK-cyclin complexes against Cdc37. This loss of stabilisation is likely a result of a severe reduction in affinity for the CDKs by the removal of this β -sheet. The direct affinity of the CIP/KIP constructs, however, were not determined by either HTRF or SPR and are the work of ongoing experiments. These experiments would confirm if the loss of this region has a detrimental effect on affinity as suggested. To establish if p21CIP1 and p27KIP1 are acting in an assembly role in this system, not as an inhibitory mechanism, the activity of Tyr88/Tyr89 phosphorylated ternary complexes extracted from Cdc37-Hsp90 would need to be established. The ADP-Glo assay, which measures ATP turnover and therefore kinase activity, could be used to determine this activity in future analysis.

The INKs proved to be highly potent CDK binding partners, by HTRF and SPR experiments, as might be expected for inhibitors that preferentially bind to CDK4 and CDK6 to halt the cell cycle. The INKs were measured by SPR to have sub-nanomolar affinity for the CDKs, predominantly a result of their very slow off rates, although experiments are currently being repeated to more accurately determine the strength of this interaction. The high affinity of the INKs to the CDKs was reflected in the HTRF competition assay, shown by the ready displacement of Cdc37, and predicts that INK expression in cells would result in the rapid redistribution of the CDKs from Cdc37-Hsp90-bound complexes to inhibited INK-bound complexes.

The introduction of a subset of cancer associated p16 point mutants resulted in a considerable reduction in their direct affinity to the CDKs, as determined by SPR, from sub-nanomolar to over 100 nM although the Met53 point mutants showed a marked difference in their affinities for CDK4 and CDK6. This difference would suggest a possible alternative binding mode of these mutants with CDK4 and CDK6, however, crystallisation trials of these mutants to explore this observation are still ongoing. The ability of the p16^{M53I} mutant to distinguish between CDK4 and CDK6 highlights the CDK-specific dependency of the Melanocyte cell lines affected in these cancers. This mutation

in CDK6 dependent cell lines would not show the same loss of inhibition and cancer progression.

This loss in potency of the p16^{D84N} mutant was ascribed to a loss of a key hydrogen bond to Arg24/Arg31 of CDK4/CDK6 respectively. However, low expression levels of p16^{D108N} would suggest that this mutant is unstable causing a reduction in affinity due to a loss in protein concentration from aggregation. A thermal melt assay confirmed a large decrease in thermal stability of 11.2 °C for p16^{D108N} compared to wildtype p16. Aggregation of unstable mutants in cells would lead to the reduced ability to inhibit CDK4/6 observed in the derived cancers from an effective drop in inhibitor concentration. The reduced potency of some of these point mutants with the CDKs correlated with their abilities to disrupt the CDK-Cdc37 complex. Together these results show that p16^{D84N} and p16^{D108N} would be less able to redistribute CDK6 from Cdc37-Hsp90 into inhibitory complexes than the wild-type protein, while all four mutants investigated would be less able to redistribute CDK4. This reduced ability *in vivo* would result in the loss of CDK inhibition and continued cancer proliferation.

Finally, the mechanism of CDK-Cdc37 disruption by three CDK4/6 selective ATP-competitive inhibitors currently in clinical trials was reconstituted *in vitro*. It has previously been reported that the chaperone cycle can be blocked by ATP-competitive kinase inhibitors (Polier *et al.*, 2013) resulting in ubiquitin mediated proteasomal degradation of the client kinase (Butler *et al.*, 2015), potentially providing a secondary mechanism for kinase inhibitory activity (Polier *et al.*, 2013). All three inhibitors disrupted the interaction with Cdc37, although with a range of abilities, with LY2835219 and PD0332991 being more potent than Lee011. Crystallographic studies of these inhibitors, using CDK2-cylin A as a surrogate, suggested that the difference in ability to disrupt the CDK6-Cdc37 complex is reflective of the extent of interactions made with the ATP binding pocket. The difference in ability to displace Cdc37 could be seen in clinical potencies as the more potent disruptors should result in higher levels of kinase degradation through the ubiquitin proteasome pathway and therefore would have a greater therapeutic benefit. However, current clinical trials have not been compared to investigate this difference.

Taken together the *in vitro* experiments performed in this thesis provide a quantitative assessment of the molecular interactions involved in CDK regulation and handoff by the Hsp90 chaperone system. The results support a model whereby inactive CDK clients are protected by the Hsp90 complex until an appropriate binding partner is found. In this model CDK6 would be readily handed over to cyclin D3 or the viral cyclins from the Hsp90 complex whereas the comparatively weaker CDK4-cyclin D1, CDK4-cyclin D3 and CDK6-cyclin D1 complexes would require either a higher cyclin concentration or the presence of an assembly factor, such as p27KIP1, for formation. The range of cyclin affinities towards the two CDKs, the potential role of p21CIP1 and p27KIP1 as assembly factors to assist complex formation and the high affinity of the INKs provide multiple opportunities for Cdc37-Hsp90 to fine-tune the activities of CDK4 and CDK6. Additional CDK binding partners, not investigated in this study, or phosphorylation of the CDKs or Cdc37-Hsp90 may provide further opportunities to tailor the release of the CDKs for specific roles in regulating G1 phase activity.

Further development of the HTRF assay is still required to allow the assessment of CDK handoff from the full Hsp90 containing complex as this interaction proved to be poorly reproducible. Better understanding and monitoring of the posttranslational modifications that regulate this interaction may help to achieve this. A key unmet aim of the project was to determine the structure of CDK6-cyclin D. While a potential crystal hit was observed, of CDK6-cyclin D3 with PD0332991, insufficient time remained to optimise around these conditions to see if the crystal could be repeated or improved upon. To improve the chances of crystallisation the truncated CDK6 and cyclin D construct transfections need to be repeated to remove the predicted disordered regions that may be preventing packing and crystal formation. This technique has proven successful for several published CDK6 containing structures. Point mutations could also be made to make CDK6 or cyclin D more like other previously crystallised CDKs and cyclins in the hope of making them more crystallisable. In addition, CAK phosphorylation of CDK6 on Thr177, thought by mass spectrometry to be non-phosphorylated, could further order the protein structure by bringing order to the activation segment. Similarly, the use of a peptide substrate mimic may help to order the peptide binding site. Given more time a combination of these techniques, along with those already attempted, would allow structural determination of CDK6-cyclin D.

Appendix A.

A.1 Additional techniques

A.1.1 Polymerase chain reaction

PCR reactions contained 1x Phusion buffer, 200 μ M dNTPs, 0.5 μ M forward primer and 0.5 μ M reverse primer, 100 ng template DNA, 3% DMSO, 1U Phusion Hot Start DNA Polymerase The PCR reaction was heating to 98°C for 30 seconds then consisted of 30 cycles of 98°C for 10sec, 50°C for 30sec and 72°C for 30sec. The final extension was carried out at 72°C for 10 minutes then the reaction held at 4°C. PCR products were cleaned using Qiagen QIAquick PCR purification kit and DNA concentrations were measured using the Nanodrop.

A.1.2 Transformations

50 μ l competent cells stored at -80°C were thawed slowly on ice and then 2 μ l of DNA was added, mixed by gentle tapping, and then left on ice for 15 minutes. Heat-shock cells at 42°C for 1 minute and then return to ice. Add 400 μ l SOC media, (or LB), to cells and incubate at 37°C, with shaking, for 1 hour. Cells then spread on Ampicillin (50 μ g/ml) agar plates and incubated at 37°C overnight.

A.1.3 Agarose gels

0.4g of Ultrapure agarose was dissolved in 40ml of TAE by heating then 0.4 μ l of SYBR Safe (Invitrogen) was added once cooled. 5 μ l of 1kb ladder or 10 μ l of PCR product was mixed with 2 μ l of loading dye and loaded onto the gel and run at 100V for 40 minutes.

A.1.4 Sequencing

Plasmids were extracted for sequencing using a Qiagen QIA prep spin Miniprep kit following manufacturer's instructions from the pellets of 10ml cultures grown in Ampicillin (50 μ g/ml) containing LB media at 37°C overnight. Pellets were harvested by centrifugation at 1610 g for 10 mins. Sequencing was performed by Eurofins and the results analysed using the EXPASy translate tool and Clustal Omega

A.1.5 SDS-PAGE

Expedeon precast gels were run using SDS run buffer and stained with instant blue. 2µl of lysate or unbound fraction was added to 10µl of loading dye or 10µl of purified protein was added to 3µl of loading buffer and boiled at 95°C for 5 minutes. 5µl of PageRuler pre-stained protein ladder (Thermo Scientific) or 12µl of each sample were loaded onto the gel and run at 180V for 60 minutes. Proteins were visualised by InstantBlue staining.

A.1.6 Determining protein concentration

Protein concentrations were determined using a NanoDrop2000 UV-Vis Spectrophotometer (Thermo Scientific).

A.2 Primers

Primer name	Forward primer	Reverse primer
N-Avi 16	AGGAGATATAACCATGGAACCGGCAGC GGGGTC	GTTAGCAGCCACTAGTTTAATCGGGA ATGTCGCTCG
N-Avi 19	AGGAGATATA CCATGGCCCTGCTGGAGGAGGTTTCG	GTTAGCAGCCACTAGTTCACAGCGGG GCCA CCATGT
N-Avi- Cdc37 ₁ - 348	AGGAGATATAACCATGGTGGACTACAG CGTGTG	GTTAGCAGCC ACTAGTTTAG GCCTTAGAGT TGGGGACCCA GAGGC
C-Avi- Cdc37 ₁ - 348	AGGAGATATAACCATGGTGGACTACAG CGTGTG	GTTAGCAGCCACTAGTTCATTCATGCC ATTCAATTTTCTGCGCTTCGAAAATAT CGTTCAGGCCCATGGCCTTAGAGTTG GGGACCCAGAGGC
N-Avi- Cdc37 ₃₀ - 348	AGGAGATATAACCATGGCACGCTGGCG GCATCAGGCCCGGGTGG	GTTAGCAGCC ACTAGTTTAG GCCTTAGAGT TGGGGACCCA GAGGC
C-Avi- Cdc37 ₃₀ - 348	AGGAGATATAACCATGGCACGCTGGCG GCATCAGGCCCGGGTGG	GTTAGCAGCCACTAGTTCATTCATGCC ATTCAATTTTCTGCGCTTCGAAAATAT CGTTCAGGCCCATGGCCTTAGAGTTG GGGACCCAGAGGC
N-Avi- Cdc37 ₁ - 378	AGGAGATATAACCATGGTGGACTACAG CGTGTG	GTTAGCAGCCACTAGTTCACACACTGA CATCCTTCTCATCGCC
C-Avi- Cdc37 ₁ - 378	AGGAGATATAACCATGGTGGACTACAG CGTGTG	GTTAGCAGCCACTAGTTCATTCATGCC ATTCAATTTTCTGCGCTTCGAAAATAT CGTTCAGGCCCATCACACTGACATCCT TCTCATCGCC

N-Avi- Cdc37 ₃₀₋₃₇₈	AGGAGATATACCATGGCACGCTGGCG GCATCAGGCCCGGGTGG	GTTAGCAGCCACTAGTTCACACACTGA CATCCTTCTCATCGCC
N-Avi- Cdc37 ₃₀₋₃₇₈	AGGAGATATACCATGGCACGCTGGCG GCATCAGGCCCGGGTGG	GTTAGCAGCCACTAGTTCATTTCATGCC ATTCAATTTTCTGCGCTTCGAAAATAT CGTTCAGGCCCATCACACTGACATCCT TCTCATCGCC
C-Avi Cdc37 ^{S13} E	AGGAGATATACCATGGTGGACTACAG CGTGTG	GTTAGCAGCCACTAGTTCATTTCATGCC ATTCAATTTTCTGCGCTTCGAAAATAT CGTTCAGGCCCATCACACTGACATCCT TCTCATCGCC
N-Avi Hsp90	TGGCATGAAGCCATGCCTGAGGAAGT GCACCATGGAG	GTTAGCAGCC ACTAGTCTAA TCGACTTCTT CCATGCGAG

Table A-1 Primers for Avi-tagged constructs

Construct	Forward primer	Reverse primer
CDK6 1-326	ATCGGGCGCGGATCCATGTCCCCT ATACTAGGTTA	TAGGCCTTTGAATTCTCAGGCTGTAT TCAGCTCCGAG
CDK6 1-301	ATCGGGCGCGGATCCATGTCCCCT ATACTAGGTTA	GTTAGCAGCC ACTAGTTTAC TGGAAGTATG GGTGAGACAG
CDK6 10-301	TTCCAGGGGC CCATGGACCA GCAGTACGAA TGCGTG	GTTAGCAGCC ACTAGTTTAC TGGAAGTATG GGTGAGACAG
CDK6 10-326	TTCCAGGGGC CCATGGACCA GCAGTACGAA TGCGTG	TAGGCCTTTGAATTCTCAGGCTGTAT TCAGCTCCGAG
cyclin D1 1-295	ACCCGGGATCTCGAGATGGAACA CCAGCTCCTGTGC	GCATCAGCTGCTAGCTCAGATGTCCA CGTCCCGCAC
cyclin D1 15-295	TCACCCGGGATCTCGATGCGCGCG TACCCCGATGCCAAC	GCATCAGCTGCTAGCTCAGATGTCCA CGTCCCGCAC
cyclin D1 20-295	TCACCCGGGATCTCGATGGCCAAC CTCCTCAACGACCGG	GCATCAGCTGCTAGCTCAGATGTCCA CGTCCCGCAC
cyclin D1 1-271	ACCCGGGATCTCGAGATGGAACA CCAGCTCCTGTGC	GCATCAGCTGCTAGCTTAGGCGGCCT TGGGGTCCATGTT
cyclin D1 15-271	TCACCCGGGATCTCGATGCGCGCG TACCCCGATGCCAAC	GCATCAGCTGCTAGCTTAGGCGGCCT TGGGGTCCATGTT
cyclin D1 20-271	TCACCCGGGATCTCGATGGCCAAC CTCCTCAACGACCGG	GCATCAGCTGCTAGCTTAGGCGGCCT TGGGGTCCATGTT
cyclin D1 1-255	ACCCGGGATCTCGAGATGGAACA CCAGCTCCTGTGC	GCATCAGCTGCTAGCTTACAGCAGG GCTTCGATCTGCTC
cyclin D1 15-255	TCACCCGGGATCTCGATGCGCGCG TACCCCGATGCCAAC	GCATCAGCTGCTAGCTTACAGCAGG GCTTCGATCTGCTC

cyclin D1 20-255	TCACCCGGGATCTCGATGGCCAAC CTCCTCAACGACCGG	GCATCAGCTGCTAGCTTACAGCAGG GCTTCGATCTGCTC
cyclin D3 1-292	ACCCGGGATCTCGAGATGGAGCT GCTGTGTTGCGAAG	GCATCAGCTGCTAGCCTACAGGTGTA TGGCTGTGAC
cyclin D3 20-292	TCACCCGGGATCTCGATGCGGCTG CTGGGGGACCAGCGT	GCATCAGCTGCTAGCCTACAGGTGTA TGGCTGTGAC
cyclin D3 1-260	ACCCGGGATCTCGAGATGGAGCT GCTGTGTTGCGAAG	GCATCAGCTGCTAGCTTACTGAGCGG CTCCCTGAGGCT
cyclin D3 20-260	TCACCCGGGATCTCGATGCGGCTG CTGGGGGACCAGCGT	GCATCAGCTGCTAGCTTACTGAGCGG CTCCCTGAGGCT
cyclin D3 1-255	ACCCGGGATCTCGAGATGGAGCT GCTGTGTTGCGAAG	GCATCAGCTGCTAGCTTAGAGGCTCT CCCTGAGTGCAGC
cyclin D3 20-255	TCACCCGGGATCTCGATGCGGCTG CTGGGGGACCAGCGT	GCATCAGCTGCTAGCTTAGAGGCTCT CCCTGAGTGCAGC

Table A-2 Primers for truncated CDK6 and D-type cyclins for MultiBac™ system

A.2.1 Additional constructs

cDNA of p15, p16, p18 and p19 were obtained from Dharmacon (GE) and codon optimised p16 were synthesised by Eurofins. P16 mutants were synthesised and cloned into pGEX6P1 by GeneScrit. Vcyclin and Kcyclin were synthesised by IDT (Integrated DNA Technologies).

A.3 Table of protein constructs

<i>Uniprot name</i>	<i>Referred to as</i>	<i>Residue range</i>	<i>Molecular weight</i>
<i>CDK6</i>	CDK6	1-326	36 938
	GSTCDK6		63 426
<i>CDK4</i>	CDK4	1-308	34 141
	GSTCDK4		60 554
<i>CCND1</i>	cyclin D1	1-295	33729
<i>CCND3</i>	cyclin D3	1-292	32 519
<i>CDK2</i>	CDK2	1-298	33930
<i>CCNA2</i>	cyclin A2	173-432	29833

<i>Uniprot name</i>	<i>Referred to as</i>	<i>Residue range</i>	<i>Molecular weight</i>
<i>CDKN2B</i>	p15	1-138	14722
	<i>CDKN2A</i>	p16	1-156
	N-Avi p16	1-176	18771
	p16 ^{M53I}	1-156	16515
	p16 ^{M53E}	1-156	16531
	N-Avi p16 ^{M53E}	1-176	18551
	p16 ^{D84N}	1-156	16532
	p16 ^{D108N}	1-156	16532
<i>CDKN2C</i>	p18	1-168	18128
<i>CDKN2D</i>	p19	1-166	17700
	N-Avi p19	1-186	19939
	p19 ^{G19D}	1-166	17758
	N-Avi p19 ^{G19D}	1-186	19778
	p19 ^{M50E}	1-166	17698
	N-Avi p19 ^{M50E}	1-186	19718

CDKN1B	p27KIP1	1-198	22 073
	p27M	1-106	12368
	p27 ^{Y88E}	1-106	12334
	p27 ^{Y88E/Y89E}	1-106	12301
	p27S	23-106	9952
	p27XS	34-106	8701
	p27 ₁₋₇₉	1-79	9354
	p27 ₁₋₇₅	1-75	8812
CDKN1A	p21M	1-87	9800
	p21S	9-87	7067
	p21XS	23-87	8684
72 (Herpesvirus saimiri)	Vcyclin	1-254	28637
	C-Avi Vcyclin		30657
ORF72 (Kaposi's sarcoma- associated herpesvirus)	Kcyclin	1-257	28100
	C-Avi Kcyclin		30120
<i>Uniprot name</i>	<i>Referred to as</i>	<i>Residue range</i>	<i>Molecular weight</i>
Hsp90AB1	Hsp90	1-724	83264
	N-Avi Hsp90	1-744	85502
Cdc37	Cdc37 ₁₋₃₄₈	1-348	41432
	Cdc37 ₃₀₋₃₄₈	30-348	38070
	His-Avi-1-348 (N)	1-348	43671
	His-1-348-Avi (C)	1-348	43528
	His-Avi-30-348 (N)	30-348	40510

His-30-348-Avi (C)	30-348	40440
Cdc37	1-378	44468
Cdc37	30-378	
His-Avi-1-FL (N)	1-378	46707
His-1-FL-Avi (C)	1-378	46565
His-Avi-30-FL (N)	30-378	43547
His-30-FL-Avi (C)	30-378	43404
Cdc37 ^{S13E}	1-378	44510
N-Avi Cdc37 ^{S13E}	1-378	46530
Cdc37 ^{Q247R}	1-378	44496
N-Avi Cdc37 ^{Q247R}	1-378	46516

Table A-3 Protein constructs produced

A table of all the protein constructs discussed in this thesis.

A.4 Media and buffers

Buffer	Components
mHBS	10 mM HEPES pH7.5, 150 mM NaCl, 0.5 mM EDTA, 0.5 mM TCEP
mHBS2A	40mM HEPES pH 7.0, 200 mM NaCl, 1mM DTT
HTRF buffer A	50 mM HEPES pH 7.5, 100 mM NaCl, 1mM DTT, 0.1 mg/ml BSA
HTRF buffer B	50 mM HEPES pH 7.5, 100 mM NaCl, 0.1 mg/ml BSA
MST buffer	10 mM HEPES pH7.5, 150 mM NaCl, 0.5 mM EDTA, 0.5 mM TCEP, 0.05% Triton-X-100
SPR buffer	10 mM HEPES pH7.5, 150 mM NaCl, 3 mM EDTA, 0.05% Tween
Lysis buffer	10 mM HEPES pH7.5, 150 mM NaCl, 0.5 mM EDTA, 0.5 mM TCEP, 0.01 mg/mL DNase, 0.05 mg/mL RNase, 0.25 mg/mL

	Lysozyme, 5 mM MgCl ₂ , 1 EDTA-free complete™ protease inhibitor tablet (Roche),
Biotinylation buffer	0.5 M bicine pH 8.3, 100 mM ATP, 100 mM MgOAc and 500 μM d-biotin
LB	Prepared from premade powder; 25g per litre
2YT	1.6 % Trypton, 1% Yeast Extract, 0.5% NaCl

Table A-4 Table of media and buffer components

A.5 CDK2-cyclin A2 optimised crystallisation screen

All wells contain 0.1 M HEPES pH 7.0. KCl increases in 0.05 M increments from 0.6 M to 0.95 M down tray (A-H). (NH₄)₂SO₄ increases in 0.1 M increments from 0.8 M to 1.3 M across half the tray (1-6 and 7-12)

	1	2	3	4	5	6	7	8	9	10	11	12
A	Water	500mM NaCl	150mM NaCl	150mM KCl	150mM NH4Cl	150mM MgCl2	150mM NH4SO4	2 mM CHAPS, 150 mM NaCl	150mM NaCl, 0.5M TMAO	150 mM NaCl, 50mM Glu/Arg	150mM NaCl, 10% Glycerol	150 mM NaCl, 200mM Sucrose
B	Bis-Tris pH 6.0	Bis-Tris pH 6.0, 500mM NaCl	Bis-Tris pH 6.0, 150mM NaCl	Bis-Tris pH 6.0, 150mM KCl	Bis-Tris pH 6.0, 150mM NH4Cl	Bis-Tris pH 6.0, 150mM MgCl2	Bis-Tris pH 6.0, 150mM NH4SO4	Bis-Tris pH 6.0, 2 mM CHAPS, 150 mM NaCl	Bis-Tris pH 6.0, 150mM NaCl, 0.5M TMAO	Bis-Tris pH 6.0, 150 mM NaCl, 50mM Glu/Arg	Bis-Tris pH 6.0, 150mM NaCl, 10% Glycerol	Bis-Tris pH 6.0, 150 mM NaCl, 200mM Sucrose
C	Na Cacodylate pH 6.5	Na Cacodylate pH 6.5, 500mM NaCl	Na Cacodylate pH 6.5, 150mM NaCl	Na Cacodylate pH 6.5, 150mM KCl	Na Cacodylate pH 6.5, 150mM NH4Cl	Na Cacodylate pH 6.5, 150mM MgCl2	Na Cacodylate pH 6.5, 150mM NH4SO4	Na Cacodylate pH 6.5, 2 mM CHAPS, 150 mM NaCl	Na Cacodylate pH 6.5, 150mM NaCl, 0.5M TMAO	Na Cacodylate pH 6.5, 150 mM NaCl, 50mM Glu/Arg	Na Cacodylate pH 6.5, 150mM NaCl, 10% Glycerol	Na Cacodylate pH 6.5, 150 mM NaCl, 200mM Sucrose
D	MES pH 6.5	MES pH 6.5, 500mM NaCl	MES pH 6.5, 150mM NaCl	MES pH 6.5, 150mM KCl	MES pH 6.5, 150mM NH4Cl	MES pH 6.5, 150mM MgCl2	MES pH 6.5, 150mM NH4SO4	MES pH 6.5, 2 mM CHAPS, 150 mM NaCl	MES pH 6.5, 150mM NaCl, 0.5M TMAO	MES pH 6.5, 150 mM NaCl, 50mM Glu/Arg	MES pH 6.5, 150mM NaCl, 10% Glycerol	MES pH 6.5, 150 mM NaCl, 200mM Sucrose
E	Na Phosphate pH 7.0	Na Phosphate pH 7.0, 500mM NaCl	Na Phosphate pH 7.0, 150mM NaCl	Na Phosphate pH 7.0, 150mM KCl	Na Phosphate pH 7.0, 150mM NH4Cl	Na Phosphate pH 7.0, 150mM MgCl2	Na Phosphate pH 7.0, 150mM NH4SO4	Na Phosphate pH 7.0, 2 mM CHAPS, 150 mM NaCl	Na Phosphate pH 7.0, 150mM NaCl, 0.5M TMAO	Na Phosphate pH 7.0, 150 mM NaCl, 50mM Glu/Arg	Na Phosphate pH 7.0, 150mM NaCl, 10% Glycerol	Na Phosphate pH 7.0, 150 mM NaCl, 200mM Sucrose
F	MOPS pH 7.0	MOPS pH 7.0, 500mM NaCl	MOPS pH 7.0, 150mM NaCl	MOPS pH 7.0, 150mM KCl	MOPS pH 7.0, 150mM NH4Cl	MOPS pH 7.0, 150mM MgCl2	MOPS pH 7.0, 150mM NH4SO4	MOPS pH 7.0, 2 mM CHAPS, 150 mM NaCl	MOPS pH 7.0, 150mM NaCl, 0.5M TMAO	MOPS pH 7.0, 150 mM NaCl, 50mM Glu/Arg	MOPS pH 7.0, 150mM NaCl, 10% Glycerol	MOPS pH 7.0, 150 mM NaCl, 200mM Sucrose
G	HEPES pH 7.5	HEPES pH 7.5, 500mM NaCl	HEPES pH 7.5, 150mM NaCl	HEPES pH 7.5, 150mM KCl	HEPES pH 7.5, 150mM NH4Cl	HEPES pH 7.5, 150mM MgCl2	HEPES pH 7.5, 150mM NH4SO4	HEPES pH 7.5, 2 mM CHAPS, 150 mM NaCl	HEPES pH 7.5, 150mM NaCl, 0.5M TMAO	HEPES pH 7.5, 150 mM NaCl, 50mM Glu/Arg	HEPES pH 7.5, 150mM NaCl, 10% Glycerol	HEPES pH 7.5, 150 mM NaCl, 200mM Sucrose
H	Tris pH 8.0	Tris pH 8.0, 500mM NaCl	Tris pH 8.0, 150mM NaCl	Tris pH 8.0, 150mM KCl	Tris pH 8.0, 150mM NH4Cl	Tris pH 8.0, 150mM MgCl2	Tris pH 8.0, 150mM NH4SO4	Tris pH 8.0, 2 mM CHAPS, 150 mM NaCl	Tris pH 8.0, 150mM NaCl, 0.5M TMAO	Tris pH 8.0, 150 mM NaCl, 50mM Glu/Arg	Tris pH 8.0, 150mM NaCl, 10% Glycerol	Tris pH 8.0, 150 mM NaCl, 200mM Sucrose

Table A-5 DSF buffer screen conditions

Bibliography

- Adams, P.D., Sellers, W.R., Sharma, S.K., Wu, A.D., Nalin, C.M. and Kaelin, W.G. (1996) 'Identification of a cyclin-cdk2 recognition motif present in substrates and p21-like cyclin-dependent kinase inhibitors', *Molecular and Cellular Biology*, 16(12), pp. 6623-6633.
- Alberts, B. (1998) 'The cell as a collection of protein machines: Preparing the next generation of molecular biologists', *Cell*, 92(3), pp. 291-294.
- Aligue, R., Wu, L. and Russell, P. (1997) 'Regulation of Schizosaccharomyces pombe Wee1 tyrosine kinase', *Journal of Biological Chemistry*, 272(20), pp. 13320-13325.
- Andersen, D.C. and Krummen, L. (2002) 'Recombinant protein expression for therapeutic applications', *Current Opinion in Biotechnology*, 13(2), pp. 117-123.
- Antony-Debre, I. and Steidl, U. (2014) 'CDK6, a new target in MLL-driven leukemia', *Blood*, 124(1), pp. 5-6.
- Arellano, M. and Moreno, S. (1997) 'Regulation of CDK/cyclin complexes during the cell cycle', *Int J Biochem Cell Biol*, 29(4), pp. 559-73.
- Arooz, T., Yam, C.H., Siu, W.Y., Lau, A., Li, K.K. and Poon, R.Y. (2000) 'On the concentrations of cyclins and cyclin-dependent kinases in extracts of cultured human cells', *Biochemistry*, 39(31), pp. 9494-501.
- Asghar, U., Witkiewicz, A.K., Turner, N.C. and Knudsen, E.S. (2015) 'The history and future of targeting cyclin-dependent kinases in cancer therapy', *Nat Rev Drug Discov*, 14(2), pp. 130-46.
- Baneyx, F. (1999) 'Recombinant protein expression in Escherichia coli', *Current Opinion in Biotechnology*, 10(5), pp. 411-421.
- Bartek, J., Bartkova, J. and Lukas, J. (2007) 'DNA damage signalling guards against activated oncogenes and tumour progression', *Oncogene*, 26(56), pp. 7773-7779.
- Bartek, J. and Lukas, J. (2001) 'Mammalian G1- and S-phase checkpoints in response to DNA damage', *Curr Opin Cell Biol*, 13(6), pp. 738-47.
- Bartek, J. and Lukas, J. (2007) 'DNA damage checkpoints: from initiation to recovery or adaptation', *Curr Opin Cell Biol*, 19(2), pp. 238-45.
- Baumgartner, R., Fernandez-Catalan, C., Winoto, A., Huber, R., Engh, R.A. and Holak, T.A. (1998) 'Structure of human cyclin-dependent kinase inhibitor p19INK4d: comparison to known ankyrin-repeat-containing structures and implications for the dysfunction of tumor suppressor p16INK4a', *Structure*, 6(10), pp. 1279-90.
- Baumli, S., Lolli, G., Lowe, E.D., Troiani, S., Rusconi, L., Bullock, A.N., Debreczeni, J.E., Knapp, S. and Johnson, L.N. (2008) 'The structure of P-TEFb (CDK9/cyclin T1), its complex with flavopiridol and regulation by phosphorylation', *EMBO J*, 27(13), pp. 1907-18.
- Bazin, H., Preaudat, M., Trinquet, E. and Mathis, G. (2001) 'Homogeneous time resolved fluorescence resonance energy transfer using rare earth cryptates as a tool for probing molecular interactions in biology', *Spectrochim Acta A Mol Biomol Spectrosc*, 57(11), pp. 2197-2111.
- Beach, D., Durkacz, B. and Nurse, P. (1982) 'Functionally homologous cell cycle control genes in budding and fission yeast', *Nature*, 300(5894), pp. 706-9.
- Beljelarskaya, S.N. (2011) 'Baculovirus expression systems for production of recombinant proteins in insect and mammalian cells', *Molecular Biology*, 45(1), pp. 123-138.

Berthet, C., Aleem, E., Coppola, V., Tessarollo, L. and Kaldis, P. (2003) 'Cdk2 knockout mice are viable', *Current Biology*, 13(20), pp. 1775-1785.

Bertoni, F., Rinaldi, A., Zucca, E. and Cavalli, F. (2006) 'Update on the molecular biology of mantle cell lymphoma', *Hematol Oncol*, 24(1), pp. 22-7.

Blain, S.W. (2008) 'Switching cyclin D-Cdk4 kinase activity on and off', *Cell Cycle*, 7(7), pp. 892-8.

Blain, S.W., Montalvo, E. and Massague, J. (1997) 'Differential interaction of the cyclin-dependent kinase (Cdk) inhibitor p27(Kip1) with cyclin A-Cdk2 and cyclin D2-Cdk4', *Journal of Biological Chemistry*, 272(41), pp. 25863-25872.

Boczek, E.E., Reefschlager, L.G., Dehling, M., Struller, T.J., Hausler, E., Seidl, A., Kaila, V.R.I. and Buchner, J. (2015) 'Conformational processing of oncogenic v-Src kinase by the molecular chaperone Hsp90', *Proceedings of the National Academy of Sciences of the United States of America*, 112(25), pp. 7626-7626.

Brotherton, D.H., Dhanaraj, V., Wick, S., Brizuela, L., Domaille, P.J., Volyanik, E., Xu, X., Parisini, E., Smith, B.O., Archer, S.J., Serrano, M., Brenner, S.L., Blundell, T.L. and Laue, E.D. (1998) 'Crystal structure of the complex of the cyclin D-dependent kinase Cdk6 bound to the cell-cycle inhibitor p19INK4d', *Nature*, 395(6699), pp. 244-50.

Brown, N.R., Korolchuk, S., Martin, M.P., Stanley, W.A., Moukhametzianov, R., Noble, M.E.M. and Endicott, J.A. (2015) 'CDK1 structures reveal conserved and unique features of the essential cell cycle CDK', *Nature Communications*, 6.

Brown, N.R., Noble, M.E.M., Endicott, J.A., Garman, E.F., Wakatsuki, S., Mitchell, E., Rasmussen, B., Hunt, T. and Johnson, L.N. (1995) 'The Crystal-Structure of Cyclin-A', *Structure*, 3(11), pp. 1235-1247.

Brown, N.R., Noble, M.E.M., Endicott, J.A. and Johnson, L.N. (1999a) 'The structural basis for specificity of substrate and recruitment peptides for cyclin-dependent kinases', *Nature Cell Biology*, 1(7), pp. 438-443.

Brown, N.R., Noble, M.E.M., Lawrie, A.M., Morris, M.C., Tunnah, P., Divita, G., Johnson, L.N. and Endicott, J.A. (1999b) 'Effects of phosphorylation of threonine 160 on cyclin-dependent kinase 2 structure and activity', *Journal of Biological Chemistry*, 274(13), pp. 8746-8756.

Butler, L.M., Ferraldeschi, R., Armstrong, H.K., Centenera, M.M. and Workman, P. (2015) 'Maximizing the Therapeutic Potential of HSP90 Inhibitors', *Molecular Cancer Research*, 13(11), pp. 1445-1451.

Byeon, I.J., Li, J., Ericson, K., Selby, T.L., Tevelev, A., Kim, H.J., O'Maille, P. and Tsai, M.D. (1998) 'Tumor suppressor p16INK4A: determination of solution structure and analyses of its interaction with cyclin-dependent kinase 4', *Mol Cell*, 1(3), pp. 421-31.

Cancer Genome Atlas Research, N. (2008) 'Comprehensive genomic characterization defines human glioblastoma genes and core pathways', *Nature*, 455(7216), pp. 1061-8.

Canepa, E.T., Scassa, M.E., Ceruti, J.M., Marazita, M.C., Carcagno, A.L., Sirkin, P.F. and Ogara, M.F. (2007) 'INK4 proteins, a family of mammalian CDK inhibitors with novel biological functions', *IUBMB Life*, 59(7), pp. 419-26.

Casimiro, M.C., Velasco-Velazquez, M., Aguirre-Alvarado, C. and Pestell, R.G. (2014) 'Overview of cyclins D1 function in cancer and the CDK inhibitor landscape: past and present', *Expert Opin Investig Drugs*, 23(3), pp. 295-304.

Cerqueira, A., Martin, A., Symonds, C.E., Odajima, J., Dubus, P., Barbacid, M. and Santamaria, D. (2014) 'Genetic Characterization of the Role of the Cip/Kip Family of Proteins as Cyclin-Dependent Kinase Inhibitors and Assembly Factors', *Molecular and Cellular Biology*, 34(8), pp. 1452-1459.

Chang, J.Y. (1985) 'Thrombin specificity. Requirement for apolar amino acids adjacent to the thrombin cleavage site of polypeptide substrate', *Eur J Biochem*, 151(2), pp. 217-24.

Chauhan, S., Diril, M.K., Lee, J.H., Bisteau, X., Manoharan, V., Adhikari, D., Ratnacaram, C.K., Janela, B., Noffke, J., Ginhoux, F., Coppola, V., Liu, K., Tessarollo, L. and Kaldis, P. (2016) 'Cdk2 catalytic activity is essential for meiotic cell division in vivo', *Biochem J*.

Chen, P., Lee, N., Hu, W., Xu, M., Ferre, R.A., Lam, H., Bergqvist, S., Solowiej, J., Diehl, W., He, Y.A., Yu, X., Nagata, A., VanArsdale, T. and Murray, B.W. (2016) 'Spectrum and Degree of CDK Drug Interactions Predicts Clinical Performance', *Mol Cancer Ther*.

Chen, V.B., Arendall, W.B., Headd, J.J., Keedy, D.A., Immormino, R.M., Kapral, G.J., Murray, L.W., Richardson, J.S. and Richardson, D.C. (2010) 'MolProbity: all-atom structure validation for macromolecular crystallography', *Acta Crystallographica Section D-Biological Crystallography*, 66, pp. 12-21.

Cheng, M., Olivier, P., Diehl, J.A., Fero, M., Roussel, M.F., Roberts, J.M. and Sherr, C.J. (1999) 'The p21(Cip1) and p27(Kip1) CDK 'inhibitors' are essential activators of cyclin D-dependent kinases in murine fibroblasts', *EMBO J*, 18(6), pp. 1571-83.

Cho, Y.S., Angove, H., Brain, C., Chen, C.H., Cheng, H., Cheng, R., Chopra, R., Chung, K., Congreve, M., Dagostin, C., Davis, D.J., Feltell, R., Giraldes, J., Hiscock, S.D., Kim, S., Kovats, S., Lagu, B., Lewry, K., Loo, A., Lu, Y., Luzzio, M., Maniara, W., McMenemy, R., Mortenson, P.N., Benning, R., O'Reilly, M., Rees, D.C., Shen, J., Smith, T., Wang, Y., Williams, G., Woolford, A.J., Wrona, W., Xu, M., Yang, F. and Howard, S. (2012) 'Fragment-Based Discovery of 7-Azabenzimidazoles as Potent, Highly Selective, and Orally Active CDK4/6 Inhibitors', *ACS Med Chem Lett*, 3(6), pp. 445-9.

Chou, P.Y. and Fasman, G.D. (1974) 'Prediction of Protein Conformation', *Biochemistry*, 13(2), pp. 222-245.

Ciemerych, M.A. and Sicinski, P. (2005) 'Cell cycle in mouse development', *Oncogene*, 24(17), pp. 2877-2898.

Citri, A., Alroy, I., Lavi, S., Rubin, C., Xu, W.P., Grammatikakis, N., Patterson, C., Neckers, L., Fry, D.W. and Yarden, Y. (2002) 'Drug-induced ubiquitylation and degradation of ErbB receptor tyrosine kinases: implications for cancer therapy', *Embo Journal*, 21(10), pp. 2407-2417.

Citri, A., Harari, D., Shohat, G., Ramakrishnan, P., Gan, J., Lavi, S., Eisenstein, M., Kimchi, A., Wallach, D., Pietrokovski, S. and Yarden, Y. (2006) 'Hsp90 recognizes a common surface on client kinases', *Journal of Biological Chemistry*, 281(20), pp. 14361-14369.

Coleman, M.L., Marshall, C.J. and Olson, M.F. (2004) 'RAS and RHO GTPases in G1-phase cell-cycle regulation', *Nat Rev Mol Cell Biol*, 5(5), pp. 355-66.

Cregg, J.M., Cereghino, J.L., Shi, J.Y. and Higgins, D.R. (2000) 'Recombinant protein expression in *Pichia pastoris*', *Molecular Biotechnology*, 16(1), pp. 23-52.

Cutforth, T. and Rubin, G.M. (1994) 'Mutations in Hsp83 and Cdc37 Impair Signaling by the Sevenless Receptor Tyrosine Kinase in *Drosophila*', *Cell*, 77(7), pp. 1027-1036.

Dai, K., Kobayashi, R. and Beach, D. (1996) 'Physical interaction of mammalian CDC37 with CDK4', *J Biol Chem*, 271(36), pp. 22030-4.

Dar, A.C. and Shokat, K.M. (2011) 'The evolution of protein kinase inhibitors from antagonists to agonists of cellular signaling', *Annu Rev Biochem*, 80, pp. 769-95.

Day, P.J., Cleasby, A., Tickle, I.J., O'Reilly, M., Coyle, J.E., Holding, F.P., McMenemy, R.L., Yon, J., Chopra, R., Lengauer, C. and Jhoti, H. (2009) 'Crystal structure of human CDK4 in complex with a D-type cyclin', *Proc Natl Acad Sci U S A*, 106(11), pp. 4166-70.

Debondt, H.L., Rosenblatt, J., Jancarik, J., Jones, H.D., Morgan, D.O. and Kim, S.H. (1993) 'Crystal-Structure of Cyclin-Dependent Kinase-2', *Nature*, 363(6430), pp. 595-602.

Devault, A., Martinez, A.M., Fesquet, D., Labbe, J.C., Morin, N., Tassan, J.P., Nigg, E.A., Cavadore, J.C. and Doree, M. (1995) 'Mat1 (Menage-a-Trois) a New Ring Finger Protein Subunit Stabilizing Cyclin H-Cdk7 Complexes in Starfish and *Xenopus Cak*', *Embo Journal*, 14(20), pp. 5027-5036.

Doran, P.M. (2000) 'Foreign protein production in plant tissue cultures', *Curr Opin Biotechnol*, 11(2), pp. 199-204.

Drozdetskiy, A., Cole, C., Procter, J. and Barton, G.J. (2015) 'JPred4: a protein secondary structure prediction server', *Nucleic Acids Res*, 43(W1), pp. W389-94.

Duffy, C.M., Hilbert, B.J. and Kelch, B.A. (2016) 'A Disease-Causing Variant in PCNA Disrupts a Promiscuous Protein Binding Site', *Journal of Molecular Biology*, 428(6), pp. 1023-1040.

Dyson, N.J. (2016) 'RB1: a prototype tumor suppressor and an enigma', *Genes & Development*, 30(13), pp. 1492-1502.

Echalier, A., Bettayeb, K., Ferandin, Y., Lozach, O., Clement, M., Valette, A., Liger, F., Marquet, B., Morris, J.C., Endicott, J.A., Joseph, B. and Meijer, L. (2008) 'Meriolins (3-(pyrimidin-4-yl)-7-azaindoles): synthesis, kinase inhibitory activity, cellular effects, and structure of a CDK2/cyclin A/meriolin complex', *J Med Chem*, 51(4), pp. 737-51.

Echalier, A., Hole, A.J., Lolli, G., Endicott, J.A. and Noble, M.E. (2014) 'An inhibitor's-eye view of the ATP-binding site of CDKs in different regulatory states', *ACS Chem Biol*, 9(6), pp. 1251-6.

Emsley, P., Lohkamp, B., Scott, W.G. and Cowtan, K. (2010) 'Features and development of Coot', *Acta Crystallogr D Biol Crystallogr*, 66(Pt 4), pp. 486-501.

Endicott, J.A., Noble, M.E. and Johnson, L.N. (2012) 'The structural basis for control of eukaryotic protein kinases', *Annu Rev Biochem*, 81, pp. 587-613.

Ericsson, U.B., Hallberg, B.M., DeTitta, G.T., Dekker, N. and Nordlund, P. (2006) 'Thermofluor-based high-throughput stability optimization of proteins for structural studies', *Analytical Biochemistry*, 357(2), pp. 289-298.

Erlanson, D.A., Fesik, S.W., Hubbard, R.E., Jahnke, W. and Jhoti, H. (2016) 'Twenty years on: the impact of fragments on drug discovery', *Nat Rev Drug Discov*, 15(9), pp. 605-19.

Esteller, M., Corn, P.G., Baylin, S.B. and Herman, J.G. (2001) 'A gene hypermethylation profile of human cancer', *Cancer Res*, 61(8), pp. 3225-9.

Eswaran, J. and Knapp, S. (2010) 'Insights into protein kinase regulation and inhibition by large scale structural comparison', *Biochimica Et Biophysica Acta-Proteins and Proteomics*, 1804(3), pp. 429-432.

Evans, P. (2006) 'Scaling and assessment of data quality', *Acta Crystallogr D Biol Crystallogr*, 62(Pt 1), pp. 72-82.

Evans, T., Rosenthal, E.T., Youngblom, J., Distel, D. and Hunt, T. (1983) 'Cyclin - a Protein Specified by Maternal Messenger-Rna in Sea-Urchin Eggs That Is Destroyed at Each Cleavage Division', *Cell*, 33(2), pp. 389-396.

Fesquet, D., Labbe, J.C., Derancourt, J., Capony, J.P., Galas, S., Girard, F., Lorca, T., Shuttleworth, J., Doree, M. and Cavadore, J.C. (1993) 'The Mo15 Gene Encodes the Catalytic Subunit of a Protein-Kinase That Activates Cdc2 and Other Cyclin-Dependent Kinases (Cdks) through Phosphorylation of Thr161 and Its Homologs', *Embo Journal*, 12(8), pp. 3111-3121.

Fitzgerald, D.J., Berger, P., Schaffitzel, C., Yamada, K., Richmond, T.J. and Berger, I. (2006) 'Protein complex expression by using multigene baculoviral vectors', *Nat Methods*, 3(12), pp. 1021-32.

FitzGerald, M.G., Harkin, D.P., Silva-Arrieta, S., MacDonald, D.J., Lucchina, L.C., Unsal, H., O'Neill, E., Koh, J., Finkelstein, D.M., Isselbacher, K.J., Sober, A.J. and Haber, D.A. (1996)

'Prevalence of germ-line mutations in p16, p19ARF, and CDK4 in familial melanoma: analysis of a clinic-based population', *Proc Natl Acad Sci U S A*, 93(16), pp. 8541-5.

Fleuren, E.D.G., Zhang, L.X., Wu, J.M. and Daly, R.J. (2016) 'The kinome 'at large' in cancer', *Nature Reviews Cancer*, 16(2), pp. 83-98.

Flores, J.F., Pollock, P.M., Walker, G.J., Glendening, J.M., Lin, A.H., Palmer, J.M., Walters, M.K., Hayward, N.K. and Fountain, J.W. (1997) 'Analysis of the CDKN2A, CDKN2B and CDK4 genes in 48 Australian melanoma kindreds', *Oncogene*, 15(24), pp. 2999-3005.

Förster, T. (1948) 'Zwischenmolekulare Energiewanderung und Fluoreszenz Annalen der Physik Volume 437, Issue 1-2', *Annalen der Physik*, 437(1-2), pp. 55-75 [Online]. Available at: <http://onlinelibrary.wiley.com/doi/10.1002/andp.19484370105/abstract> (Accessed: 01).

Franklin, D.S. and Xiong, Y. (1996) 'Induction of p18(INK4c) and its predominant association with CDK4 and CDK6 during myogenic differentiation', *Molecular Biology of the Cell*, 7(10), pp. 1587-1599.

Gasteiger, E., Gattiker, A., Hoogland, C., Ivanyi, I., Appel, R.D. and Bairoch, A. (2003) 'ExpASY: the proteomics server for in-depth protein knowledge and analysis', *Nucleic Acids Research*, 31(13), pp. 3784-3788.

Gelbert, L.M., Cai, S.F., Lin, X., Sanchez-Martinez, C., del Prado, M., Lallena, M.J., Torres, R., Ajamie, R.T., Wishart, G.N., Flack, R.S., Neubauer, B.L., Young, J., Chan, E.M., Iversen, P., Cronier, D., Kreklau, E. and de Dios, A. (2014) 'Preclinical characterization of the CDK4/6 inhibitor LY2835219: in-vivo cell cycle-dependent/independent anti-tumor activities alone/in combination with gemcitabine', *Investigational New Drugs*, 32(5), pp. 825-837.

Gerber, M.R., Farrell, A., Deshaies, R.J., Herskowitz, I. and Morgan, D.O. (1995) 'Cdc37 Is Required for Association of the Protein-Kinase Cdc28 with G(1) and Mitotic Cyclins', *Proceedings of the National Academy of Sciences of the United States of America*, 92(10), pp. 4651-4655.

Ghaemmaghani, S., Huh, W.K., Bower, K., Howson, R.W., Belle, A., Dephoure, N., O'Shea, E.K. and Weissman, J.S. (2003) 'Global analysis of protein expression in yeast', *Nature*, 425(6959), pp. 737-41.

Giacinti, C. and Giordano, A. (2006) 'RB and cell cycle progression', *Oncogene*, 25(38), pp. 5220-5227.

GoddenKent, D., Talbot, S.J., Boshoff, C., Chang, Y., Moore, P., Weiss, R.A. and Mitnacht, S. (1997) 'The cyclin encoded by Kaposi's sarcoma-associated herpesvirus stimulates cdk6 to phosphorylate the retinoblastoma protein and histone H1', *Journal of Virology*, 71(6), pp. 4193-4198.

Goldstein, A.M., Chan, M., Harland, M., Gillanders, E.M., Hayward, N.K., Avril, M.F., Azizi, E., Bianchi-Scarra, G., Bishop, D.T., Bressac-de Paillerets, B., Bruno, W., Calista, D., Cannon Albright, L.A., Demenais, F., Elder, D.E., Ghiorzo, P., Gruis, N.A., Hansson, J., Hogg, D., Holland, E.A., Kanetsky, P.A., Kefford, R.F., Landi, M.T., Lang, J., Leachman, S.A., Mackie, R.M., Magnusson, V., Mann, G.J., Niendorf, K., Newton Bishop, J., Palmer, J.M., Puig, S., Puig-Buttille, J.A., de Snoo, F.A., Stark, M., Tsao, H., Tucker, M.A., Whitaker, L., Yakobson, E. and Melanoma Genetics, C. (2006) 'High-risk melanoma susceptibility genes and pancreatic cancer, neural system tumors, and uveal melanoma across GenoMEL', *Cancer Res*, 66(20), pp. 9818-28.

Gould, C.M., Kannan, N., Taylor, S.S. and Newton, A.C. (2009) 'The chaperones Hsp90 and Cdc37 mediate the maturation and stabilization of protein kinase C through a conserved PXXP motif in the C-terminal tail', *J Biol Chem*, 284(8), pp. 4921-35.

Grimmler, M., Wang, Y., Mund, T., Cilensek, Z., Keidel, E.M., Waddell, M.B., Jakel, H., Kullmann, M., Kriwacki, R.W. and Hengst, L. (2007) 'Cdk-inhibitory activity and stability of p27Kip1 are directly regulated by oncogenic tyrosine kinases', *Cell*, 128(2), pp. 269-80.

Grossel, M.J. and Hinds, P.W. (2006) 'From cell cycle to differentiation: an expanding role for cdk6', *Cell Cycle*, 5(3), pp. 266-70.

Gu, J.Y., Babayeva, N.D., Suwa, Y., Baranovskiy, A.G., Price, D.H. and Tahirov, T.H. (2014) 'Crystal structure of HIV-1 Tat complexed with human P-TEFb and AFF4', *Cell Cycle*, 13(11).

Gu, Y., Rosenblatt, J. and Morgan, D.O. (1992) 'Cell-Cycle Regulation of Cdk2 Activity by Phosphorylation of Thr160 and Tyr15', *Embo Journal*, 11(11), pp. 3995-4005.

Guan, K.L., Jenkins, C.W., Li, Y., Nichols, M.A., Wu, X.Y., Okeefe, C.L., Matera, A.G. and Xiong, Y. (1994) 'Growth Suppression by P18, a P16(Ink4/Mts1)-Related and P14(Ink4b/Mts2)-Related Cdk6 Inhibitor, Correlates with Wild-Type Prb Function', *Genes & Development*, 8(24), pp. 2939-2952.

Guan, K.L., Jenkins, C.W., Li, Y., OKeefe, C.L., Noh, S., Wu, X.Y., Zariwala, M., Matera, A.G. and Xiong, Y. (1996) 'Isolation and characterization of p19(INK4d), a p16-related inhibitor specific to CDK6 and CDK4', *Molecular Biology of the Cell*, 7(1), pp. 57-70.

Hagopian, J.C., Kirtley, M.P., Stevenson, L.M., Gergis, R.M., Russo, A.A., Pavletich, N.P., Parsons, S.M. and Lew, J. (2001) 'Kinetic basis for activation of CDK2/cyclin A by phosphorylation', *J Biol Chem*, 276(1), pp. 275-80.

Hallett, S. (2013) 'Structural and functional characterisation of CDK6/cyclin D complexes', *MRes*.

Hanahan, D. and Weinberg, R.A. (2011) 'Hallmarks of Cancer: The Next Generation', *Cell*, 144(5), pp. 646-674.

Hannon, G.J. and Beach, D. (1994) 'P15(Ink4b) Is a Potential Effector of Tgf-Beta-Induced Cell-Cycle Arrest', *Nature*, 371(6494), pp. 257-261.

Harland, M., Meloni, R., Gruis, N., Pinney, E., Brookes, S., Spurr, N.K., Frischauf, A.M., Bataille, V., Peters, G., Cuzick, J., Selby, P., Bishop, D.T. and Bishop, J.N. (1997) 'Germline mutations of the CDKN2 gene in UK melanoma families', *Hum Mol Genet*, 6(12), pp. 2061-7.

Hartl, F.U., Bracher, A. and Hayer-Hartl, M. (2011) 'Molecular chaperones in protein folding and proteostasis', *Nature*, 475(7356), pp. 324-32.

Hirai, H., Roussel, M.F., Kato, J.Y., Ashmun, R.A. and Sherr, C.J. (1995) 'Novel Ink4 Proteins, P19 and P18, Are Specific Inhibitors of the Cyclin D-Dependent Kinases Cdk4 and Cdk6', *Molecular and Cellular Biology*, 15(5), pp. 2672-2681.

Honda, R., Lowe, E.D., Dubinina, E., Skamnaki, V., Cook, A., Brown, N.R. and Johnson, L.N. (2005) 'The structure of cyclin E1/CDK2: implications for CDK2 activation and CDK2-independent roles', *EMBO J*, 24(3), pp. 452-63.

Honma, T., Yoshizumi, T., Hashimoto, N., Hayashi, K., Kawanishi, N., Fukasawa, K., Takaki, T., Ikeura, C., Ikuta, M., Suzuki-Takahashi, I., Hayama, T., Nishimura, S. and Morishima, H. (2001) 'A novel approach for the development of selective Cdk4 inhibitors: Library design based on locations of Cdk4 specific amino acid residues', *Journal of Medicinal Chemistry*, 44(26), pp. 4628-4640.

Hughes, B.T., Sidorova, J., Swanger, J., Monnat, R.J. and Clurman, B.E. (2013) 'Essential role for Cdk2 inhibitory phosphorylation during replication stress revealed by a human Cdk2 knockin mutation', *Proceedings of the National Academy of Sciences of the United States of America*, 110(22), pp. 8954-8959.

Hydbring, P., Malumbres, M. and Sicinski, P. (2016) 'Non-canonical functions of cell cycle cyclins and cyclin-dependent kinases', *Nat Rev Mol Cell Biol*, 17(5), pp. 280-92.

Jakob, U., Kriwacki, R. and Uversky, V.N. (2014) 'Conditionally and transiently disordered proteins: awakening cryptic disorder to regulate protein function', *Chem Rev*, 114(13), pp. 6779-805.

James, M.K., Ray, A., Leznova, D. and Blain, S.W. (2008) 'Differential modification of p27Kip1 controls its cyclin D-cdk4 inhibitory activity', *Mol Cell Biol*, 28(1), pp. 498-510.

Jarviluoma, A., Koopal, S., Rasanen, S., Makela, T.P. and Ojala, P.M. (2004) 'KSHV viral cyclin binds to p27KIP1 in primary effusion lymphomas', *Blood*, 104(10), pp. 3349-3354.

Jeffrey, P.D., Ruso, A.A., Polyak, K., Gibbs, E., Hurwitz, J., Massague, J. and Pavletich, N.P. (1995) 'Mechanism of Cdk Activation Revealed by the Structure of a Cyclin-Cdk2 Complex', *Nature*, 376(6538), pp. 313-320.

Jeffrey, P.D., Tong, L. and Pavletich, N.P. (2000) 'Structural basis of inhibition of CDK-cyclin complexes by INK4 inhibitors', *Genes Dev*, 14(24), pp. 3115-25.

Jerabek-Willemsen, M., Wienken, C.J., Braun, D., Baaske, P. and Duhr, S. (2011) 'Molecular Interaction Studies Using Microscale Thermophoresis', *Assay and Drug Development Technologies*, 9(4), pp. 342-353.

Jia, Y., Quinn, C.M., Gagnon, A.I. and Talanian, R. (2006) 'Homogeneous time-resolved fluorescence and its applications for kinase assays in drug discovery', *Anal Biochem*, 356(2), pp. 273-81.

Jia, Y., Yun, C.H., Park, E., Ercan, D., Manuia, M., Juarez, J., Xu, C., Rhee, K., Chen, T., Zhang, H., Palakurthi, S., Jang, J., Lelais, G., DiDonato, M., Bursulaya, B., Michellys, P.Y., Epple, R., Marsilje, T.H., McNeill, M., Lu, W., Harris, J., Bender, S., Wong, K.K., Janne, P.A. and Eck, M.J. (2016) 'Overcoming EGFR(T790M) and EGFR(C797S) resistance with mutant-selective allosteric inhibitors', *Nature*, 534(7605), pp. 129-32.

Jirawatnotai, S., Sharma, S., Michowski, W., Suktitipat, B., Geng, Y., Quackenbush, J., Elias, J.E., Gygi, S.P., Wang, Y.Y.E. and Sicinski, P. (2014) 'The cyclin D1-CDK4 oncogenic interactome enables identification of potential novel oncogenes and clinical prognosis', *Cell Cycle*, 13(18), pp. 2889-2900.

Jones, R., Ruas, M., Gregory, F., Moulin, S., Delia, D., Manoukian, S., Rowe, J., Brookes, S. and Peters, G. (2007) 'A CDKN2A mutation in familial melanoma that abrogates binding of p16(INK4a) to CDK4 but not CDK6', *Cancer Research*, 67(19), pp. 9134-9141.

Jorgensen, P., Nishikawa, J.L., Breitkreutz, B.J. and Tyers, M. (2002) 'Systematic identification of pathways that couple cell growth and division in yeast', *Science*, 297(5580), pp. 395-400.

Jung, J.U., Stager, M. and Desrosiers, R.C. (1994) 'Virus-Encoded Cyclin', *Molecular and Cellular Biology*, 14(11), pp. 7235-7244.

Jura, N., Zhang, X., Endres, N.F., Seeliger, M.A., Schindler, T. and Kuriyan, J. (2011) 'Catalytic control in the EGF receptor and its connection to general kinase regulatory mechanisms', *Mol Cell*, 42(1), pp. 9-22.

Kaldis, P. (2005) 'The N-terminal peptide of the Kaposi's sarcoma-associated herpesvirus (KSHV)-cyclin determines substrate specificity', *J Biol Chem*, 280(12), pp. 11165-74.

Kaldis, P., Ojala, P.M., Tong, L., Makela, T.P. and Solomon, M.J. (2001) 'CAK-independent activation of CDK6 by a viral cyclin', *Mol Biol Cell*, 12(12), pp. 3987-99.

Karimian, A., Ahmadi, Y. and Yousefi, B. (2016) 'Multiple functions of p21 in cell cycle, apoptosis and transcriptional regulation after DNA damage', *DNA Repair (Amst)*, 42, pp. 63-71.

Kato, J.Y., Matsuoka, M., Strom, D.K. and Sherr, C.J. (1994) 'Regulation of Cyclin D-Dependent Kinase-4 (Cdk4) by Cdk4-Activating Kinase', *Molecular and Cellular Biology*, 14(4), pp. 2713-2721.

Kelland, L.R. (2000) 'Flavopiridol, the first cyclin-dependent kinase inhibitor to enter the clinic: current status', *Expert Opinion on Investigational Drugs*, 9(12), pp. 2903-2911.

Keramisanou, D., Aboalroub, A., Zhang, Z., Liu, W., Marshall, D., Diviney, A., Larsen, R.W., Landgraf, R. and Gelis, I. (2016) 'Molecular Mechanism of Protein Kinase Recognition and Sorting by the Hsp90 Kinome-Specific Cochaperone Cdc37', *Mol Cell*, 62(2), pp. 260-71.

Khatib, Z.A., Matsushime, H., Valentine, M., Shapiro, D.N., Sherr, C.J. and Look, A.T. (1993) 'Coamplification of the Cdk4 Gene with Mdm2 and Gli in Human Sarcomas', *Cancer Research*, 53(22), pp. 5535-5541.

Kohrt, D., Crary, J., Zimmer, M., Patrick, A.N., Ford, H.L., Hinds, P.W. and Grossel, M.J. (2014) 'CDK6 binds and promotes the degradation of the EYA2 protein', *Cell Cycle*, 13(1), pp. 62-71.

Kollmann, K., Heller, G., Schneckenleithner, C., Warsch, W., Scheicher, R., Ott, R.G., Schafer, M., Fajmann, S., Schleder, M., Schiefer, A.I., Reichart, U., Mayerhofer, M., Hoeller, C., Zochbauer-Muller, S., Kerjaschki, D., Bock, C., Kenner, L., Hoefler, G., Freissmuth, M., Green, A.R., Moriggl, R., Busslinger, M., Malumbres, M. and Sexl, V. (2013) 'A kinase-independent function of CDK6 links the cell cycle to tumor angiogenesis', *Cancer Cell*, 24(2), pp. 167-81.

Kornev, A.P. and Taylor, S.S. (2010) 'Defining the conserved internal architecture of a protein kinase', *Biochim Biophys Acta*, 1804(3), pp. 440-4.

Kozar, K., Ciemerych, M.A., Rebel, V.I., Shigematsu, H., Zagozdou, A., Sicinska, E., Geng, Y., Yu, Q.Y., Bhattacharya, S., Bronson, R.T., Akashi, K. and Sicinski, P. (2004) 'Mouse development and cell proliferation in the absence of D-cyclins', *Cell*, 118(4), pp. 477-491.

Krukenberg, K.A., Street, T.O., Lavery, L.A. and Agard, D.A. (2011) 'Conformational dynamics of the molecular chaperone Hsp90', *Quarterly Reviews of Biophysics*, 44(2), pp. 229-255.

Kung, J.E. and Jura, N. (2016) 'Structural Basis for the Non-catalytic Functions of Protein Kinases', *Structure*, 24(1), pp. 7-24.

LaBaer, J., Garrett, M.D., Stevenson, L.F., Slingerland, J.M., Sandhu, C., Chou, H.S., Fattaey, A. and Harlow, E. (1997) 'New functional activities for the p21 family of CDK inhibitors', *Genes Dev*, 11(7), pp. 847-62.

Laman, H., Coverley, D., Krude, T., Laskey, R. and Jones, N. (2001) 'Viral cyclin-cyclin-dependent kinase 6 complexes initiate nuclear DNA replication', *Molecular and Cellular Biology*, 21(2), pp. 624-635.

Lamphere, L., Fiore, F., Xu, X., Brizuela, L., Keezer, S., Sardet, C., Draetta, G.F. and Gyuris, J. (1997) 'Interaction between Cdc37 and Cdk4 in human cells', *Oncogene*, 14(16), pp. 1999-2004.

Larrea, M.D., Liang, J., Da Silva, T., Hong, F., Shao, S.H., Han, K., Dumont, D. and Slingerland, J.M. (2008) 'Phosphorylation of p27Kip1 regulates assembly and activation of cyclin D1-Cdk4', *Mol Cell Biol*, 28(20), pp. 6462-72.

Li, J., Byeon, I.J., Ericson, K., Poi, M.J., O'Maille, P., Selby, T. and Tsai, M.D. (1999) 'Tumor suppressor INK4: determination of the solution structure of p18INK4C and demonstration of the functional significance of loops in p18INK4C and p16INK4A', *Biochemistry*, 38(10), pp. 2930-40.

Li, M.T., Lee, H.R., Yoon, D.W., Albrecht, J.C., Fleckenstein, B., Neipel, F. and Jung, J.U. (1997) 'Kaposi's sarcoma-associated herpesvirus encodes a functional cyclin', *Journal of Virology*, 71(3), pp. 1984-1991.

Liedberg, B., Nylander, C. and Lundstrom, I. (1983) 'Surface-Plasmon Resonance for Gas-Detection and Biosensing', *Sensors and Actuators*, 4(2), pp. 299-304.

Liggett, W.H., Jr. and Sidransky, D. (1998) 'Role of the p16 tumor suppressor gene in cancer', *J Clin Oncol*, 16(3), pp. 1197-206.

Lim, J.T., Mansukhani, M. and Weinstein, I.B. (2005) 'Cyclin-dependent kinase 6 associates with the androgen receptor and enhances its transcriptional activity in prostate cancer cells', *Proc Natl Acad Sci U S A*, 102(14), pp. 5156-61.

Lin, J.Y., Reichner, C., Wu, X.W. and Levine, A.J. (1996) 'Analysis of wild-type and mutant p21(WAF-1) gene activities', *Molecular and Cellular Biology*, 16(4), pp. 1786-1793.

Liu, W. and Landgraf, R. (2015) 'Phosphorylated and unphosphorylated serine 13 of CDC37 stabilize distinct interactions between its client and HSP90 binding domains', *Biochemistry*, 54(7), pp. 1493-504.

Lu, H. and Schulze-Gahmen, U. (2006) 'Toward understanding the structural basis of cyclin-dependent kinase 6 specific inhibition', *J Med Chem*, 49(13), pp. 3826-31.

Luckow, V.A. and Summers, M.D. (1988) 'Trends in the Development of Baculovirus Expression Vectors', *Bio-Technology*, 6(1), pp. 47-55.

Luh, F.Y., Archer, S.J., Domaille, P.J., Smith, B.O., Owen, D., Brotherton, D.H., Raine, A.R., Xu, X., Brizuela, L., Brenner, S.L. and Laue, E.D. (1997) 'Structure of the cyclin-dependent kinase inhibitor p19Ink4d', *Nature*, 389(6654), pp. 999-1003.

Makrides, S.C. (1996) 'Strategies for achieving high-level expression of genes in Escherichia coli', *Microbiological Reviews*, 60(3), pp. 512-+.

Malmqvist, M. (1993) 'Biospecific interaction analysis using biosensor technology', *Nature*, 361(6408), pp. 186-7.

Malumbres, M. (2011) 'Physiological relevance of cell cycle kinases', *Physiol Rev*, 91(3), pp. 973-1007.

Malumbres, M. and Barbacid, M. (2001) 'To cycle or not to cycle: a critical decision in cancer', *Nat Rev Cancer*, 1(3), pp. 222-31.

Malumbres, M. and Barbacid, M. (2007) 'Cell cycle kinases in cancer', *Curr Opin Genet Dev*, 17(1), pp. 60-5.

Malumbres, M. and Barbacid, M. (2009) 'Cell cycle, CDKs and cancer: a changing paradigm', *Nat Rev Cancer*, 9(3), pp. 153-66.

Malumbres, M., Sotillo, R., Santamaria, D., Galan, J., Cerezo, A., Ortega, S., Dubus, P. and Barbacid, M. (2004) 'Mammalian cells cycle without the D-type cyclin-dependent kinases Cdk4 and Cdk6', *Cell*, 118(4), pp. 493-504.

Mann, D.J., Child, E.S., Swanton, C., Laman, H. and Jones, N. (1999) 'Modulation of p27(Kip1) levels by the cyclin encoded by Kaposi's sarcoma-associated herpesvirus', *Embo Journal*, 18(3), pp. 654-663.

Mann, M., Hendrickson, R.C. and Pandey, A. (2001) 'Analysis of proteins and proteomes by mass spectrometry', *Annu Rev Biochem*, 70, pp. 437-73.

Mao, Y.X., Yu, L.L., Yang, R., Qu, L.B. and Harrington, P.D. (2015) 'A novel method for the study of molecular interaction by using microscale thermophoresis', *Talanta*, 132, pp. 894-901.

Mathis, G. (1993) 'Rare earth cryptates and homogeneous fluoroimmunoassays with human sera', *Clin Chem*, 39(9), pp. 1953-9.

Mathis, G. (1995) 'Probing molecular interactions with homogeneous techniques based on rare earth cryptates and fluorescence energy transfer', *Clin Chem*, 41(9), pp. 1391-7.

Mathis, G. (1999) 'HTRF(R) Technology', *J Biomol Screen*, 4(6), pp. 309-314.

Matsushime, H., Ewen, M.E., Strom, D.K., Kato, J.Y., Hanks, S.K., Roussel, M.F. and Sherr, C.J. (1992) 'Identification and Properties of an Atypical Catalytic Subunit (P34(Psk-J3)/Cdk4) for Mammalian-D Type-G1 Cyclins', *Cell*, 71(2), pp. 323-334.

Matsushime, H., Quelle, D.E., Shurtleff, S.A., Shibuya, M., Sherr, C.J. and Kato, J.Y. (1994) 'D-type cyclin-dependent kinase activity in mammalian cells', *Mol Cell Biol*, 14(3), pp. 2066-76.

McConnell, B.B., Gregory, F.J., Stott, F.J., Hara, E. and Peters, G. (1999) 'Induced expression of p16(INK4a) inhibits both CDK4- and CDK2-associated kinase activity by reassortment of cyclin-CDK-inhibitor complexes', *Molecular and Cellular Biology*, 19(3), pp. 1981-1989.

McDonnell, J.M. (2001) 'Surface plasmon resonance: towards an understanding of the mechanisms of biological molecular recognition', *Curr Opin Chem Biol*, 5(5), pp. 572-7.

McGrath, D.A., Balog, E.R.M., Koivomagi, M., Lucena, R., Mai, M.V., Hirschi, A., Kellogg, D.R., Loog, M. and Rubin, S.M. (2013) 'Cks confers specificity to phosphorylation-dependent CDK signaling pathways', *Nature Structural & Molecular Biology*, 20(12), pp. 1407-1414.

McKenzie, H.A., Fung, C., Becker, T.M., Irvine, M., Mann, G.J., Kefford, R.F. and Rizos, H. (2010) 'Predicting Functional Significance of Cancer-Associated p16(INK4a) Mutations in CDKN2A', *Human Mutation*, 31(6), pp. 692-701.

McLachlin, D.T. and Chait, B.T. (2001) 'Analysis of phosphorylated proteins and peptides by mass spectrometry', *Curr Opin Chem Biol*, 5(5), pp. 591-602.

McNicholas, S., Potterton, E., Wilson, K.S. and Noble, M.E.M. (2011) 'Presenting your structures: the CCP4mg molecular-graphics software', *Acta Crystallographica Section D-Biological Crystallography*, 67, pp. 386-394.

Meyerson, M. and Harlow, E. (1994) 'Identification of G(1) Kinase-Activity for Cdk6, a Novel Cyclin-D Partner', *Molecular and Cellular Biology*, 14(3), pp. 2077-2086.

Mirzaa, G.M., Parry, D.A., Fry, A.E., Giamanco, K.A., Schwartzentruber, J., Vanstone, M., Logan, C.V., Roberts, N., Johnson, C.A., Singh, S., Kholmanskikh, S.S., Adams, C., Hodge, R.D., Hevner, R.F., Bonthron, D.T., Braun, K.P.J., Faivre, L., Riviere, J.B., St-Onge, J., Gripp, K.W., Mancini, G.M.S., Pang, K., Sweeney, E., van Esch, H., Verbeek, N., Wiczorek, D., Steinraths, M., Majewski, J., Boycott, K.M., Pilz, D.T., Ross, M.E., Dobyns, W.B., Sheridan, E.G. and Consortium, F.C. (2014) 'De novo CCND2 mutations leading to stabilization of cyclin D2 cause megalencephaly-polymicrogyriapolydactyly-hydrocephalus syndrome', *Nature Genetics*, 46(5), pp. 510-515.

Mitrea, D.M., Yoon, M.K., Ou, L. and Kriwacki, R.W. (2012) 'Disorder-function relationships for the cell cycle regulatory proteins p21 and p27', *Biol Chem*, 393(4), pp. 259-74.

Miyata, Y. and Nishida, E. (2004) 'CK2 controls multiple protein kinases by phosphorylating a kinase-targeting molecular chaperone, Cdc37', *Mol Cell Biol*, 24(9), pp. 4065-74.

Morgan, D.O. (2006) *The cell cycle : principles of control*. London: New Science Press.

Moriarty, N.W., Grosse-Kunstleve, R.W. and Adams, P.D. (2009) 'electronic Ligand Builder and Optimization Workbench (eLBOW): a tool for ligand coordinate and restraint generation', *Acta Crystallogr D Biol Crystallogr*, 65(Pt 10), pp. 1074-80.

Mullany, L.K., White, P., Hanse, E.A., Nelsen, C.J., Goggin, M.M., Mullany, J.E., Anttila, C.K., Greenbaum, L.E., Kaestner, K.H. and Albrecht, J.H. (2008) 'Distinct proliferative and transcriptional effects of the D-type cyclins in vivo', *Cell Cycle*, 7(14), pp. 2215-24.

Muller, S., Chaikuad, A., Gray, N.S. and Knapp, S. (2015) 'The ins and outs of selective kinase inhibitor development', *Nature Chemical Biology*, 11(11), pp. 818-821.

Murray, C.W. and Blundell, T.L. (2010) 'Structural biology in fragment-based drug design', *Curr Opin Struct Biol*, 20(4), pp. 497-507.

Murshudov, G.N., Vagin, A.A. and Dodson, E.J. (1997) 'Refinement of macromolecular structures by the maximum-likelihood method', *Acta Crystallogr D Biol Crystallogr*, 53(Pt 3), pp. 240-55.

Musgrove, E.A., Caldon, C.E., Barraclough, J., Stone, A. and Sutherland, R.L. (2011) 'Cyclin D as a therapeutic target in cancer', *Nat Rev Cancer*, 11(8), pp. 558-72.

Nakatani, H., Kobayashi, M., Jin, T.F., Taguchi, T., Sugimoto, T., Nakano, T., Hamada, S. and Araki, K. (2005) 'STI571 (Glivec) inhibits the interaction between c-KIT and heat shock protein 90 of the gastrointestinal stromal tumor cell line, GIST-T1', *Cancer Science*, 96(2), pp. 116-119.

Narasimha, A.M., Kaulich, M., Shapiro, G.S., Choi, Y.J., Sicinski, P. and Dowdy, S.F. (2014) 'Cyclin D activates the Rb tumor suppressor by mono-phosphorylation', *Elife*, 3.

Neckers, L. and Workman, P. (2012) 'Hsp90 Molecular Chaperone Inhibitors: Are We There Yet?', *Clinical Cancer Research*, 18(1), pp. 64-76.

Niesen, F.H., Berglund, H. and Vedadi, M. (2007) 'The use of differential scanning fluorimetry to detect ligand interactions that promote protein stability', *Nature Protocols*, 2(9), pp. 2212-2221.

O'Leary, B., Finn, R.S. and Turner, N.C. (2016) 'Treating cancer with selective CDK4/6 inhibitors', *Nat Rev Clin Oncol*, 13(7), pp. 417-30.

O'Sullivan, C.C. (2016) 'CDK4/6 inhibitors for the treatment of advanced hormone receptor positive breast cancer and beyond: 2016 update', *Expert Opin Pharmacother*, 17(12), pp. 1657-67.

Oberoi, J., Dunn, D.M., Woodford, M.R., Mariotti, L., Schulman, J., Bourboulia, D., Mollapour, M. and Vaughan, C.K. (2016) 'Structural and functional basis of protein phosphatase 5 substrate specificity', *Proc Natl Acad Sci U S A*, 113(32), pp. 9009-14.

Olesen, S.H., Ingles, D.J., Zhu, J.Y., Martin, M.P., Betzi, S., Georg, G.I., Tash, J.S. and Schonbrunn, E. (2015) 'Stability of the human Hsp90-p50Cdc37 chaperone complex against nucleotides and Hsp90 inhibitors, and the influence of phosphorylation by casein kinase 2', *Molecules*, 20(1), pp. 1643-60.

Ortega, S., Prieto, I., Odajima, J., Martin, A., Dubus, P., Sotillo, R., Barbero, J.L., Malumbres, M. and Barbacid, M. (2003) 'Cyclin-dependent kinase 2 is essential for meiosis but not for mitotic cell division in mice', *Nature Genetics*, 35(1), pp. 25-31.

Ou, L., Ferreira, A.M., Otieno, S., Xiao, L.M., Bashford, D. and Kriwacki, R.W. (2011) 'Incomplete Folding upon Binding Mediates Cdk4/Cyclin D Complex Activation by Tyrosine Phosphorylation of Inhibitor p27 Protein', *Journal of Biological Chemistry*, 286(34), pp. 30142-30151.

Pardee, A.B. (1974) 'A restriction point for control of normal animal cell proliferation', *Proc Natl Acad Sci U S A*, 71(4), pp. 1286-90.

Parry, D., Mahony, D., Wills, K. and Lees, E. (1999) 'Cyclin D-CDK subunit arrangement is dependent on the availability of competing INK4 and p21 class inhibitors', *Molecular and Cellular Biology*, 19(3), pp. 1775-1783.

Paternot, S., Colleoni, B., Bisteau, X. and Roger, P.P. (2014) 'The CDK4/CDK6 inhibitor PD0332991 paradoxically stabilizes activated cyclin D3-CDK4/6 complexes', *Cell Cycle*, 13(18), pp. 2879-88.

Pearl, L.H. (2005) 'Hsp90 and Cdc37 -- a chaperone cancer conspiracy', *Curr Opin Genet Dev*, 15(1), pp. 55-61.

Pearl, L.H. and Prodromou, C. (2006) 'Structure and mechanism of the Hsp90 molecular chaperone machinery', *Annu Rev Biochem*, 75, pp. 271-94.

Pearl, L.H., Prodromou, C. and Workman, P. (2008) 'The Hsp90 molecular chaperone: an open and shut case for treatment', *Biochemical Journal*, 410, pp. 439-453.

Pestell, R.G. (2013) 'New roles of cyclin D1', *Am J Pathol*, 183(1), pp. 3-9.

Petri, E.T., Errico, A., Escobedo, L., Hunt, T. and Basavappa, R. (2007) 'The crystal structure of human cyclin B', *Cell Cycle*, 6(11), pp. 1342-9.

Pick, E., Kluger, Y., Giltneane, J.M., Moeder, C., Camp, R.L., Rimm, D.L. and Kluger, H.M. (2007) 'High HSP90 expression is associated with decreased survival in breast cancer', *Cancer Research*, 67(7), pp. 2932-2937.

Pines, J. (1993) 'Cyclins and Their Associated Cyclin-Dependent Kinases in the Human Cell-Cycle', *Biochemical Society Transactions*, 21(4), pp. 921-925.

Pitarke, J.M., Silkin, V.M., Chulkov, E.V. and Echenique, P.M. (2007) 'Theory of surface plasmons and surface-plasmon polaritons', *Reports on Progress in Physics*, 70(1), pp. 1-87.

Placke, T., Faber, K., Nonami, A., Putwain, S.L., Salih, H.R., Heidel, F.H., Kramer, A., Root, D.E., Barbie, D.A., Krivtsov, A.V., Armstrong, S.A., Hahn, W.C., Huntly, B.J., Sykes, S.M., Milsom, M.D., Scholl, C. and Frohling, S. (2014) 'Requirement for CDK6 in MLL-rearranged acute myeloid leukemia', *Blood*, 124(1), pp. 13-23.

Polier, S., Samant, R.S., Clarke, P.A., Workman, P., Prodromou, C. and Pearl, L.H. (2013) 'ATP-competitive inhibitors block protein kinase recruitment to the Hsp90-Cdc37 system (vol 9, pg 307, 2013)', *Nature Chemical Biology*, 9(6), pp. 406-406.

Potterton, E., McNicholas, S., Krissinel, E., Cowtan, K. and Noble, M. (2002) 'The CCP4 molecular-graphics project', *Acta Crystallogr D Biol Crystallogr*, 58(Pt 11), pp. 1955-7.

Rane, S.G., Dubus, P., Mettus, R.V., Galbreath, E.J., Boden, G., Reddy, E.P. and Barbacid, M. (1999) 'Loss of Cdk4 expression causes insulin-deficient diabetes and Cdk4 activation results in beta-islet cell hyperplasia', *Nature Genetics*, 22(1), pp. 44-52.

Reed, S.I., Bailly, E., Dulic, V., Hengst, L., Resnitzky, D. and Slingerland, J. (1994) 'G1 control in mammalian cells', *J Cell Sci Suppl*, 18, pp. 69-73.

Reutens, A.T., Fu, M., Wang, C., Albanese, C., McPhaul, M.J., Sun, Z., Balk, S.P., Janne, O.A., Palvimo, J.J. and Pestell, R.G. (2001) 'Cyclin D1 binds the androgen receptor and regulates hormone-dependent signaling in a p300/CBP-associated factor (P/CAF)-dependent manner', *Mol Endocrinol*, 15(5), pp. 797-811.

Rodriguez-Diez, E., Quereda, V., Bellutti, F., Prchal-Murphy, M., Partida, D., Eguren, M., Kollmann, K., Gomez de Cedron, M., Dubus, P., Canamero, M., Martinez, D., Sexl, V. and Malumbres, M. (2014) 'Cdk4 and Cdk6 cooperate in counteracting the INK4 family of inhibitors during murine leukemogenesis', *Blood*, 124(15), pp. 2380-90.

Roe, S.M., Ali, M.M.U., Meyer, P., Vaughan, C.K., Panaretou, B., Piper, P.W., Prodromou, C. and Pearl, L.H. (2004) 'The mechanism of Hsp90 regulation by the protein kinase-specific cochaperone p50(cdc37)', *Cell*, 116(1), pp. 87-98.

Roskoski, R., Jr. (2016) 'Cyclin-dependent protein kinase inhibitors including palbociclib as anticancer drugs', *Pharmacol Res*, 107, pp. 249-75.

Ruas, M. and Peters, G. (1998) 'The p16(INK4a)/CDKN2A tumor suppressor and its relatives', *Biochimica Et Biophysica Acta-Reviews on Cancer*, 1378(2), pp. F115-F177.

Russo, A.A., Jeffrey, P.D., Patten, A.K., Massague, J. and Pavletich, N.P. (1996a) 'Crystal structure of the p27Kip1 cyclin-dependent-kinase inhibitor bound to the cyclin A-Cdk2 complex', *Nature*, 382(6589), pp. 325-31.

Russo, A.A., Jeffrey, P.D. and Pavletich, N.P. (1996b) 'Structural basis of cyclin-dependent kinase activation by phosphorylation', *Nature Structural Biology*, 3(8), pp. 696-700.

Russo, A.A., Tong, L., Lee, J.O., Jeffrey, P.D. and Pavletich, N.P. (1998) 'Structural basis for inhibition of the cyclin-dependent kinase Cdk6 by the tumour suppressor p16INK4a', *Nature*, 395(6699), pp. 237-43.

Saibil, H. (2013) 'Chaperone machines for protein folding, unfolding and disaggregation', *Nat Rev Mol Cell Biol*, 14(10), pp. 630-42.

Sanchez-Aguilera, A., Delgado, J., Camacho, F.I., Sanchez-Beato, M., Sanchez, L., Montalban, C., Fresno, M.F., Martin, C., Piris, M.A. and Garcia, J.F. (2004) 'Silencing of the p18(INK4c) gene by promoter hypermethylation in Reed-Sternberg cells in Hodgkin lymphomas', *Blood*, 103(6), pp. 2351-2357.

Santamaria, D., Barriere, C., Cerqueira, A., Hunt, S., Tardy, C., Newton, K., Caceres, J.F., Dubus, P., Malumbres, M. and Barbacid, M. (2007) 'Cdk1 is sufficient to drive the mammalian cell cycle', *Nature*, 448(7155), pp. 811-U8.

Sari, D., Gupta, K., Thimiri Govinda Raj, D.B., Aubert, A., Drncova, P., Garzoni, F., Fitzgerald, D. and Berger, I. (2016) 'The MultiBac Baculovirus/Insect Cell Expression Vector System for Producing Complex Protein Biologics', *Adv Exp Med Biol*, 896, pp. 199-215.

Satyanarayana, A., Berthet, C., Lopez-Molina, J., Coppola, V., Tessarollo, L. and Kaldis, P. (2008) 'Genetic substitution of Cdk1 by Cdk2 leads to embryonic lethality and loss of meiotic function of Cdk2', *Development*, 135(20), pp. 3389-3400.

Satyanarayana, A. and Kaldis, P. (2009) 'Mammalian cell-cycle regulation: several Cdks, numerous cyclins and diverse compensatory mechanisms', *Oncogene*, 28(33), pp. 2925-2939.

Schatz, P.J. (1993) 'Use of Peptide Libraries to Map the Substrate-Specificity of a Peptide-Modifying Enzyme - a 13 Residue Consensus Peptide Specifies Biotinylation in Escherichia-Coli', *Bio-Technology*, 11(10), pp. 1138-1143.

Schulze-Gahmen, U., Jung, J.U. and Kim, S.H. (1999) 'Crystal structure of a viral cyclin, a positive regulator of cyclin-dependent kinase 6', *Structure*, 7(3), pp. 245-54.

Schulze-Gahmen, U. and Kim, S.H. (2001) 'Crystallization of a complex between human CDK6 and a virus-encoded cyclin is critically dependent on the addition of small charged organic molecules', *Acta Crystallogr D Biol Crystallogr*, 57(Pt 9), pp. 1287-9.

Schulze-Gahmen, U. and Kim, S.H. (2002) 'Structural basis for CDK6 activation by a virus-encoded cyclin', *Nature Structural Biology*, 9(3), pp. 177-181.

Seidel, S.A., Dijkman, P.M., Lea, W.A., van den Bogaart, G., Jerabek-Willemsen, M., Lazic, A., Joseph, J.S., Srinivasan, P., Baaske, P., Simeonov, A., Katritch, I., Melo, F.A., Ladbury, J.E., Schreiber, G., Watts, A., Braun, D. and Duhr, S. (2013) 'Microscale thermophoresis quantifies biomolecular interactions under previously challenging conditions', *Methods*, 59(3), pp. 301-15.

Serrano, M., Hannon, G.J. and Beach, D. (1993) 'A New Regulatory Motif in Cell-Cycle Control Causing Specific-Inhibition of Cyclin-D/Cdk4', *Nature*, 366(6456), pp. 704-707.

Shao, J., Irwin, A., Hartson, S.D. and Matts, R.L. (2003) 'Functional dissection of cdc37: characterization of domain structure and amino acid residues critical for protein kinase binding', *Biochemistry*, 42(43), pp. 12577-88.

Sherr, C.J. (2012) 'Ink4-Arf locus in cancer and aging', *Wiley Interdiscip Rev Dev Biol*, 1(5), pp. 731-41.

Sherr, C.J. and Roberts, J.M. (1999) 'CDK inhibitors: positive and negative regulators of G1-phase progression', *Genes Dev*, 13(12), pp. 1501-12.

Shiau, A.K., Harris, S.F., Southworth, D.R. and Agard, D.A. (2006) 'Structural Analysis of E. coli hsp90 reveals dramatic nucleotide-dependent conformational rearrangements', *Cell*, 127(2), pp. 329-40.

Sicinska, E., Aifantis, I., Le Cam, L., Swat, W., Borowski, C., Yu, Q., Ferrando, A.A., Levin, S.D., Geng, Y., von Boehmer, H. and Sicinski, P. (2003) 'Requirement for cyclin D3 in lymphocyte development and T cell leukemias', *Cancer Cell*, 4(6), pp. 451-61.

Sicinski, P., Donaher, J.L., Geng, Y., Parker, S.B., Gardner, H., Park, M.Y., Robker, R.L., Richards, J.S., McGinnis, L.K., Biggers, J.D., Eppig, J.J., Bronson, R.T., Elledge, S.J. and Weinberg, R.A. (1996) 'Cyclin D2 is an FSH-responsive gene involved in gonadal cell proliferation and oncogenesis', *Nature*, 384(6608), pp. 470-4.

Sicinski, P., Donaher, J.L., Parker, S.B., Li, T.S., Gardner, H., Haslam, S.Z., Bronson, R.T., Elledge, S.J. and Weinberg, R.A. (1995) 'Cyclin D1 Provides a Link between Development and Oncogenesis in the Retina and Breast', *Cell*, 82(4), pp. 621-630.

Sidera, K. and Patsavoudi, E. (2014) 'HSP90 inhibitors: current development and potential in cancer therapy', *Recent Pat Anticancer Drug Discov*, 9(1), pp. 1-20.

Sievers, F., Wilm, A., Dineen, D., Gibson, T.J., Karplus, K., Li, W., Lopez, R., McWilliam, H., Remmert, M., Soding, J., Thompson, J.D. and Higgins, D.G. (2011) 'Fast, scalable generation of high-quality protein multiple sequence alignments using Clustal Omega', *Mol Syst Biol*, 7, p. 539.

Slabinski, L., Jaroszewski, L., Rychlewski, L., Wilson, I.A., Lesley, S.A. and Godzik, A. (2007) 'XtalPred: a web server for prediction of protein crystallizability', *Bioinformatics*, 23(24), pp. 3403-3405.

Smith-Sorensen, B. and Hovig, E. (1996) 'CDKN2A (p16INK4A) somatic and germline mutations', *Hum Mutat*, 7(4), pp. 294-303.

Smith, J.R., de Billy, E., Hobbs, S., Powers, M., Prodromou, C., Pearl, L., Clarke, P.A. and Workman, P. (2015) 'Restricting direct interaction of CDC37 with HSP90 does not compromise chaperoning of client proteins', *Oncogene*, 34(1), pp. 15-26.

Smith, J.R. and Workman, P. (2009) 'Targeting CDC37: an alternative, kinase-directed strategy for disruption of oncogenic chaperoning', *Cell Cycle*, 8(3), pp. 362-72.

Soding, J., Biegert, A. and Lupas, A.N. (2005) 'The HHpred interactive server for protein homology detection and structure prediction', *Nucleic Acids Research*, 33, pp. W244-W248.

Stepanova, L., Leng, X.H., Parker, S.B. and Harper, J.W. (1996) 'Mammalian p50(Cdc37) is a protein kinase-targeting subunit of Hsp90 that binds and stabilizes Cdk4', *Genes & Development*, 10(12), pp. 1491-1502.

Sugimoto, M., Martin, N., Wilks, D.P., Tamai, K., Huot, T.J.G., Pantoja, C., Okumura, K., Serrano, M. and Hara, E. (2002) 'Activation of cyclin D1-kinase in murine fibroblasts lacking both p21(Cip1) and P27(Kip1)', *Oncogene*, 21(53), pp. 8067-8074.

Sun, S., Pollock, P.M., Liu, L., Karimi, S., Jothy, S., Milner, B.J., Renwick, A., Lassam, N.J., Hayward, N.K., Hogg, D., Narod, S.A. and Foulkes, W.D. (1997) 'CDKN2A mutation in a non-FAMMM kindred with cancers at multiple sites results in a functionally abnormal protein', *International Journal of Cancer*, 73(4), pp. 531-536.

Swanton, C., Mann, D.J., Fleckenstein, B., Neipel, F., Peters, G. and Jones, N. (1997) 'Herpes viral cyclin/Cdk6 complexes evade inhibition by CDK inhibitor proteins', *Nature*, 390(6656), pp. 184-187.

Taipale, M., Krykbaeva, I., Koeva, M., Kayatekin, C., Westover, K.D., Karras, G.I. and Lindquist, S. (2012) 'Quantitative analysis of HSP90-client interactions reveals principles of substrate recognition', *Cell*, 150(5), pp. 987-1001.

Taipale, M., Krykbaeva, I., Whitesell, L., Santagata, S., Zhang, J., Liu, Q., Gray, N.S. and Lindquist, S. (2013) 'Chaperones as thermodynamic sensors of drug-target interactions reveal kinase inhibitor specificities in living cells', *Nat Biotechnol*, 31(7), pp. 630-7.

Takaki, T., Echaliier, A., Brown, N.R., Hunt, T., Endicott, J.A. and Noble, M.E.M. (2009) 'The structure of CDK4/cyclin D3 has implications for models of CDK activation', *Proceedings of the National Academy of Sciences of the United States of America*, 106(11), pp. 4171-4176.

Tassan, J.P., Jaquenoud, M., Fry, A.M., Frutiger, S., Hughes, G.J. and Nigg, E.A. (1995) 'In-Vitro Assembly of a Functional Human Cdk7-Cyclin-H Complex Requires Mat1, a Novel 36 Kda Ring Finger Protein', *Embo Journal*, 14(22), pp. 5608-5617.

Terasawa, K., Yoshimatsu, K., Iemura, S., Natsume, T., Tanaka, K. and Minami, Y. (2006) 'Cdc37 interacts with the glycine-rich loop of Hsp90 client kinases', *Mol Cell Biol*, 26(9), pp. 3378-89.

Terpe, K. (2003) 'Overview of tag protein fusions: from molecular and biochemical fundamentals to commercial systems', *Applied Microbiology and Biotechnology*, 60(5), pp. 523-533.

Terwilliger, T.C., Grosse-Kunstleve, R.W., Afonine, P.V., Moriarty, N.W., Adams, P.D., Read, R.J., Zwart, P.H. and Hung, L.W. (2008) 'Iterative-build OMIT maps: map improvement by iterative model building and refinement without model bias', *Acta Crystallogr D Biol Crystallogr*, 64(Pt 5), pp. 515-24.

Toyoshima, H. and Hunter, T. (1994) 'P27, a Novel Inhibitor of G1 Cyclin-Cdk Protein-Kinase Activity, Is Related to P21', *Cell*, 78(1), pp. 67-74.

Trimarchi, J.M. and Lees, J.A. (2002) 'Sibling rivalry in the E2F family', *Nat Rev Mol Cell Biol*, 3(1), pp. 11-20.

Trowitzsch, S., Bieniossek, C., Nie, Y., Garzoni, F. and Berger, I. (2010) 'New baculovirus expression tools for recombinant protein complex production', *Journal of Structural Biology*, 172(1), pp. 45-54.

Tsutsui, T., Hesabi, B., Moons, D.S., Pandolfi, P.P., Hansel, K.S., Koff, A. and Kiyokawa, H. (1999) 'Targeted disruption of CDK4 delays cell cycle entry with enhanced p27(Kip1) activity', *Molecular and Cellular Biology*, 19(10), pp. 7011-7019.

Uziel, T., Zindy, F., Xie, S., Lee, Y., Forget, A., Magdaleno, S., Rehg, J.E., Calabrese, C., Solecki, D., Eberhart, C.G., Sherr, S.E., Plimner, S., Clifford, S.C., Hatten, M.E., McKinnon, P.J., Gilbertson, R.J., Curran, T., Sherr, C.J. and Roussel, M.F. (2005) 'The tumor suppressors Ink4c and p53 collaborate independently with Patched to suppress medulloblastoma formation', *Genes Dev*, 19(22), pp. 2656-67.

Vagin, A. and Teplyakov, A. (1997) 'MOLREP: an automated program for molecular replacement', *Journal of Applied Crystallography*, 30, pp. 1022-1025.

van den Burg, B. and Eijsink, V.G.H. (2002) 'Selection of mutations for increased protein stability', *Current Opinion in Biotechnology*, 13(4), pp. 333-337.

van der Lee, R., Buljan, M., Lang, B., Weatheritt, R.J., Daughdrill, G.W., Dunker, A.K., Fuxreiter, M., Gough, J., Gsponer, J., Jones, D.T., Kim, P.M., Kriwacki, R.W., Oldfield, C.J., Pappu, R.V., Tompa, P., Uversky, V.N., Wright, P.E. and Babu, M.M. (2014) 'Classification of Intrinsically Disordered Regions and Proteins', *Chemical Reviews*, 114(13), pp. 6589-6631.

Vaughan, C.K., Gohlke, U., Sobott, F., Good, V.M., Ali, M.M.U., Prodromou, C., Robinson, C.V., Saibil, H.R. and Pearl, L.H. (2006) 'Structure of an Hsp90-Cdc37-Cdk4 complex', *Molecular Cell*, 23(5), pp. 697-707.

Verba, K.A., Wang, R.Y., Arakawa, A., Liu, Y., Shirouzu, M., Yokoyama, S. and Agard, D.A. (2016) 'Atomic structure of Hsp90-Cdc37-Cdk4 reveals that Hsp90 traps and stabilizes an unfolded kinase', *Science*, 352(6293), pp. 1542-7.

Vermeulen, K., Van Bockstaele, D.R. and Berneman, Z.N. (2003) 'The cell cycle: a review of regulation, deregulation and therapeutic targets in cancer', *Cell Proliferation*, 36(3), pp. 131-149.

Walker, G.J., Gabrielli, B.G., Castellano, M. and Hayward, N.K. (1999) 'Functional reassessment of p16 variants using a transfection-based assay', *International Journal of Cancer*, 82(2), pp. 305-312.

Walker, G.J., Hussussian, C.J., Flore, J.F., Glendening, J.M., Haluska, F.G., Dracopoli, N.C., Hayward, N.K. and Fountain, J.W. (1995) 'Mutations of the Cdkn2/P16(Ink4) Gene in Australian Melanoma Kindreds', *Human Molecular Genetics*, 4(10), pp. 1845-1852.

Wang, Q., Zorn, J.A. and Kuriyan, J. (2014) 'A structural atlas of kinases inhibited by clinically approved drugs', *Methods Enzymol*, 548, pp. 23-67.

Weinstein, I.B. (2002) 'Cancer. Addiction to oncogenes--the Achilles heel of cancer', *Science*, 297(5578), pp. 63-4.

Whitesell, L. and Lindquist, S.L. (2005) 'HSP90 and the chaperoning of cancer', *Nature Reviews Cancer*, 5(10), pp. 761-772.

Wienken, C.J., Baaske, P., Rothbauer, U., Braun, D. and Duhr, S. (2010) 'Protein-binding assays in biological liquids using microscale thermophoresis', *Nature Communications*, 1.

Winn, M.D., Ballard, C.C., Cowtan, K.D., Dodson, E.J., Emsley, P., Evans, P.R., Keegan, R.M., Krissinel, E.B., Leslie, A.G., McCoy, A., McNicholas, S.J., Murshudov, G.N., Pannu, N.S., Potterton, E.A., Powell, H.R., Read, R.J., Vagin, A. and Wilson, K.S. (2011) 'Overview of the CCP4 suite and current developments', *Acta Crystallogr D Biol Crystallogr*, 67(Pt 4), pp. 235-42.

Winter, G. (2010) 'xia2: an expert system for macromolecular crystallography data reduction', *Journal of Applied Crystallography*, 43, pp. 186-190.

Wolfel, T., Hauer, M., Schneider, J., Serrano, M., Wolfel, C., Klehmann-Hieb, E., De Plaen, E., Hankeln, T., Meyer zum Buschenfelde, K.H. and Beach, D. (1995) 'A p16INK4a-insensitive CDK4 mutant targeted by cytolytic T lymphocytes in a human melanoma', *Science*, 269(5228), pp. 1281-4.

Wu, L.T., Yee, A., Liu, L., Carbonarohall, D., Venkatesan, N., Tolo, V.T. and Hall, F.L. (1994) 'Molecular-Cloning of the Human Cak1 Gene Encoding a Cyclin-Dependent Kinase-Activating Kinase', *Oncogene*, 9(7), pp. 2089-2096.

Xu, W.P., Mollapour, M., Prodromou, C., Wang, S.Q., Scroggins, B.T., Palchick, Z., Beebe, K., Siderius, M., Lee, M.J., Couvillon, A., Trepel, J.B., Miyata, Y., Matts, R. and Neckers, L. (2012) 'Dynamic Tyrosine Phosphorylation Modulates Cycling of the HSP90-P50(CDC37)-AHA1 Chaperone Machine', *Molecular Cell*, 47(3), pp. 434-443.

Xu, W.P., Yuan, X.T., Xiang, Z.X., Mimnaugh, E., Marcu, M. and Neckers, L. (2005) 'Surface charge and hydrophobicity determine ErbB2 binding to the Hsp90 chaperone complex', *Nature Structural & Molecular Biology*, 12(2), pp. 120-126.

Yamak, A., Latinkic, B.V., Dali, R., Temsah, R. and Nemer, M. (2014) 'Cyclin D2 is a GATA4 cofactor in cardiogenesis', *Proc Natl Acad Sci U S A*, 111(4), pp. 1415-20.

Yoon, M.K., Mitrea, D.M., Ou, L. and Kriwacki, R.W. (2012) 'Cell cycle regulation by the intrinsically disordered proteins p21 and p27', *Biochem Soc Trans*, 40(5), pp. 981-8.

Young, R.J., Waldeck, K., Martin, C., Foo, J.H., Cameron, D.P., Kirby, L., Do, H., Mitchell, C., Cullinane, C., Liu, W., Fox, S.B., Dutton-Regester, K., Hayward, N.K., Jene, N., Dobrovic, A., Pearson, R.B., Christensen, J.G., Randolph, S., McArthur, G.A. and Sheppard, K.E. (2014) 'Loss of CDKN2A expression is a frequent event in primary invasive melanoma and correlates with sensitivity to the CDK4/6 inhibitor PD0332991 in melanoma cell lines', *Pigment Cell Melanoma Res*, 27(4), pp. 590-600.

- Yu, Z., Wang, L., Wang, C., Ju, X., Wang, M., Chen, K., Loro, E., Li, Z., Zhang, Y., Wu, K., Casimiro, M.C., Gormley, M., Ertel, A., Fortina, P., Chen, Y., Tozeren, A., Liu, Z. and Pestell, R.G. (2013) 'Cyclin D1 induction of Dicer governs microRNA processing and expression in breast cancer', *Nat Commun*, 4, p. 2812.
- Yuan, C., Selby, T.L., Li, J., Byeon, I.J. and Tsai, M.D. (2000) 'Tumor suppressor INK4: refinement of p16INK4A structure and determination of p15INK4B structure by comparative modeling and NMR data', *Protein Sci*, 9(6), pp. 1120-8.
- Zarkowska, T. and Mitnacht, S. (1997) 'Differential phosphorylation of the retinoblastoma protein by G(1)/S cyclin-dependent kinases', *Journal of Biological Chemistry*, 272(19), pp. 12738-12746.
- Zhang, H., Hannon, G.J. and Beach, D. (1994) 'p21-containing cyclin kinases exist in both active and inactive states', *Genes Dev*, 8(15), pp. 1750-8.
- Zhang, J., Yang, P.L. and Gray, N.S. (2009) 'Targeting cancer with small molecule kinase inhibitors', *Nat Rev Cancer*, 9(1), pp. 28-39.
- Zhang, Y., Kim, K.H., Zhang, W., Guo, Y., Kim, S.H. and Lu, J. (2012) 'Galbanic acid decreases androgen receptor abundance and signaling and induces G1 arrest in prostate cancer cells', *Int J Cancer*, 130(1), pp. 200-12.
- Zhao, Q., Boschelli, F., Caplan, A.J. and Arndt, K.T. (2004) 'Identification of a conserved sequence motif that promotes Cdc37 and cyclin D1 binding to Cdk4', *Journal of Biological Chemistry*, 279(13), pp. 12560-12564.
- Zhou, Q., Li, T. and Price, D.H. (2012) 'RNA polymerase II elongation control', *Annu Rev Biochem*, 81, pp. 119-43.
- Zwijsen, R.M.L., Buckle, R.S., Hijmans, E.M., Loomans, C.J.M. and Bernards, R. (1998) 'Ligand-independent recruitment of steroid receptor coactivators to estrogen receptor by cyclin D1', *Genes & Development*, 12(22), pp. 3488-3498.